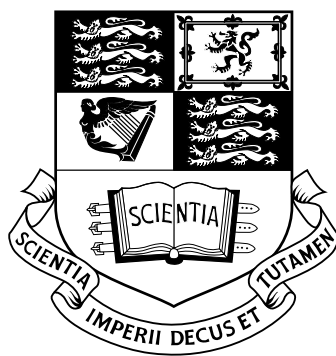# SUPRAMOLECULAR INTERACTIONS INVESTIGATED BY SOLID-STATE NMR

Thesis towards the award of Doctor of Philosophy (Ph.D.)

Matthew John Parkinson, M.Sci. ARCS

Imperial College, London, UK

Abstract

The hydrogen bonding of polybenzoxazines was investigated using a number of oligomeric model systems using advanced solid-state NMR techniques. Both intermolecular and intramolecular hydrogen-bonding interactions were probed using dipolar-recoupling, multiple quantum coherence and fast-MAS. Insight into the supramolecular structure was gained exploiting the proximity dependent nature of the nuclear dipole-dipole interaction via ^{1}H–^{1}H homonuclear and ^{1}H–^{13}C heteronuclear 2D NMR methods. The supramolecular structure of the model dimers was shown to be influenced by both ring and amine-substituents, with steric hindrance found to strongly affect hydrogen bond strength. Such an influence of the amine-substituent was also demonstrated for the model trimers, however with more complex supramolecular structures suggested. All model systems showed a general propensity to form strong N··H-O and O··H-O hydrogen bonds, with evidence of polymorphism seen for many systems. Interpretation of experimental results were complemented by ab-initio electronic structure methods combined with chemical shift calculation, allowing possible geometries to be tested and refined.

Preface

By three methods we may approach wisdom:
First by reflection, which is nobelest;
second by imitation, which is the easiest;
and third, by experience, which is the bitterest.

<div align="right">

CONFUCIOUS 551–479 BC

</div>

<div align="right">

M.J.PARKINSON 2006 AD

</div>

External referee: Prof. Malcolm. H. Levitt
School of Chemistry, University of Southampton, UK

Internal referee: Dr. Robert. G. Hill
Department of Materials, Imperial College, London, UK

Examination date: 20$^{\text{th}}$ March 2006

for
M.H.W.

Contents

List of Figures

List of Tables

Chapter 1

Introduction

Just as there is a field of molecular chemistry based on the covalent bond, there is a field of supramolecular chemistry, the chemistry of molecular assemblies and of the intermolecular bond.

JEAN-MARIE LEHN 1978 AD
[Lehn 78]

Since the introduction of the term supramolecular chemistry in 1978 by Jean-Marie Lehn, the field of supramolecular chemistry has developed into a rapidly growing, highly interdisciplinary, field of science. The key aim of this field is the controlled formation and characterisation of organised polymolecular systems held together by non-covalent interactions such as electrostatic interactions, hydrogen bonding or van der Waals forces [Lehn 95]. The increasing complexity of such systems demands increasingly more sophisticated characterisation methods. Comprehensive analysis only becoming possible through the development of powerful analytical techniques.

The aim of this work was the investigation of the supramolecular structure found in hydrogen bonded systems related to polybenzoxazines by means of advanced solid-state NMR techniques [Brown 01b]. The research presented here builds upon investigations carried out by, and was conducted in collaboration with, the group of Professor Hans Wolfgang Spiess at the Max Planck Institute for Polymer Research, Mainz, Germany. In particular this work extends upon the research carried out by Ingo Schnell and Gillian Goward[†] [Schnell 98a, Goward 01, Goward 03].

[†]currently at McMaster University, Hamilton, Canada

1.1 Polybenzoxazines

The compounds investigated here serve as model compounds for polybenzoxazines; a new class of phenolic resins. Such materials have been extensively investigated in the past 10 years [Ning 94, Shen 96, Lui 96, Ishida 96, Ishida 97]. Polybenzoxazines are formed by cationic ring-opening polymerisation of azamethylene phenol monomers (Figure 1.1). Although the basic benzoxazine monomers produce linear polymers, resins are formed by either the addition of small quantities of cross-linker or by the use of diamine-based monomer systems [Ishida 95]. Studies have focused both on the synthesis of new members of this family of compounds and on the characterisation of the unique properties of these materials. This research effort has been motivated by the observation that polybenzoxazines exhibit a number of unusual properties, such as low volumetric shrinkage or expansion upon curing [Ishida 97], lack of water absorption and excellent resistance to chemicals and ultra-violet (UV) light [Kim 01, Macko 00], as well as surprisingly high glass transition temperatures (T_g), given the low crosslinking density [Ishida 95]. These properties make polybenzoxazines attractive candidates for many commercial applications. However, because of these properties analysis in the bulk state is difficult.
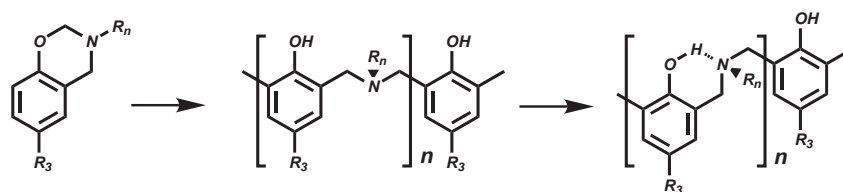
Figure 1.1: Formation of polybenzoxazines and suspected N··H-O hydrogen bonding.

The key structural feature presumed to be responsible for the remarkable behaviour of these polymers is the formation of co-operative N··H-O and O··H-O hydrogen bonds. It has been previously suggested that the network structure of polybenzoxazines is partially supported by hydrogen bond mediated interaction between chains [Wirasate 98] (Figure 1.1). Supramolecular structures influenced by such interactions are frequently observed in polymeric architectures [Percec 98, Ezuhara 99, Chino 01, Berl 02, Monkman 02]. Polybenzoxazines are a classic example of such structures. The role of hydrogen bonding is thought to be of great importance due to the low concentrations of chemical cross-linkers used. Thus, a better understanding of the hydrogen bonding within these systems is of importance.

1.2 Models for polybenzoxazines

With complex behaviour seen for polybenzoxazines, synthesis and characterisation of model compounds was undertaken, first as model dimers [Dunkers 95, Dunkers 96, Ishida 98, Schnell 98a, Laobuthee 01, Goward 01] and later as model trimers and tetramers [Kim 03b, Kim 03c, Goward 03, Hemvichian 05]. The hydrogen bonding in these model systems has been investigated by infrared (IR) spectroscopy [Dunkers 95], X-ray diffraction [Dunkers 96, Laobuthee 01], molecular modelling [Dunkers 96, Goward 03] and solid-state nuclear magnetic resonance NMR [Schnell 98a, Goward 01, Goward 03]. Although the model compounds are relatively small the growth of suitable crystals for X-ray diffraction has proven extremely difficult, despite their high propensity to form both intra- and inter-molecular hydrogen bonds. Presently, only two high-quality X-ray structures are known: that of the 3,5-dimethyl-methylamine dimer (Me,Me-N-Me) (Figure 1.2a) [Dunkers 96] and the 5-methyl-cyclohexylamine dimer (H,Me-N-Cy) (Figure 1.2b) [Laobuthee 01].
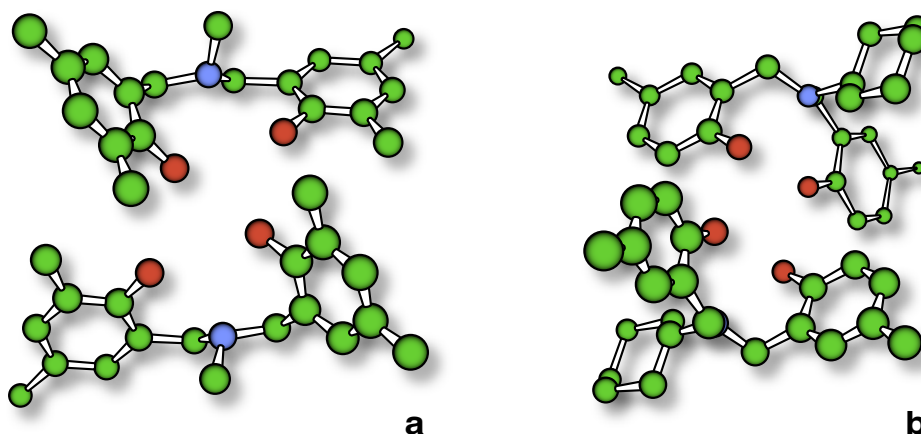
Figure 1.2: *The two known X-ray structures: (a) Me,Me-N-Me and (b) H,Me-N-Cy. (Only heavy atoms shown)*

Although these two model dimers organise themselves into a regular paired lattice (a dimeric supramolecular structure of dimers) the X-ray model cannot be extended to account for the unique properties of the parent polymer. Therefore, synthetic effort was made to procure higher oligomers to bridge the gap between the fully determined dimer structure and the unknown polymer structure [Ishida 98]. No such X-ray structures are currently known for the model trimers or tetramer. Hence, structure determination by methods both sensitive to hydrogen bonding, and not limited by a lack of long-range order, was needed.

1.3 Characterisation of supramolecular systems

Supramolecular structures often suffer from a lack of long-range order and crystallinity. This being due to the comparatively weak interactions that determine their structures, e.g. hydrogen bonding [Jeffrey 91, Lehn 93, Sijbesma 97, Brunsfeld 01, Schmuck 01, Brunsveld 02, Yamauchi 02b] and π-stacking [Brown 99, Lahiri 00, Ajayaghosh 01].

The investigation of hydrogen bonding and its role in supramolecular chemistry represents one of the current frontiers of scientific endeavour. The motivating factor behind these studies is the structure stabilising or structure-directing role played by hydrogen bonds [Sijbesma 97, Brunet 97, Castellano 98]. Information about hydrogen bonding in solids can be obtained by a variety of methods [Hamilton 68]. In particular, X-ray and neutron diffraction [Jeffrey 75, Jeffrey 86], NMR [Becker 96] and IR spectroscopy [McQuade 97]. Of these techniques, solid-state NMR has the great advantage of not requiring long-range order to provide structural information. Thus, solid-state NMR shows great promise for the analysis of systems containing hydrogen bonds and π-stacking, the building blocks of supramolecular architecures (Figure 1.3). Indeed, both interactions can clearly be seen in high-resolution solid-state ^{1}H NMR studies [Wei 99, Brown 01b, Percec 02]. In contrast to diffraction methods, NMR allows accurate location of the protons involved in these interactions. Proton positions of small organic molecules are generally determined by Fourier difference mapping in X-ray diffraction studies, or by a combination of deuterium labelling and neutron diffraction [Inabe 94, Jeffrey 75]. Variable temperature X-ray and neutron diffraction on non-deuterated systems have also recently provided insight into hydrogen bonding [Wilson 96, Parkin 04, Wilson 04, Harte 05]. Although the more reliable results are achieved by neutron scattering, access to a nuclear reactor is required. In contrast solid-state NMR is more routinely available and offers superior sensitivity, with specific isotope enrichment only required in special cases.
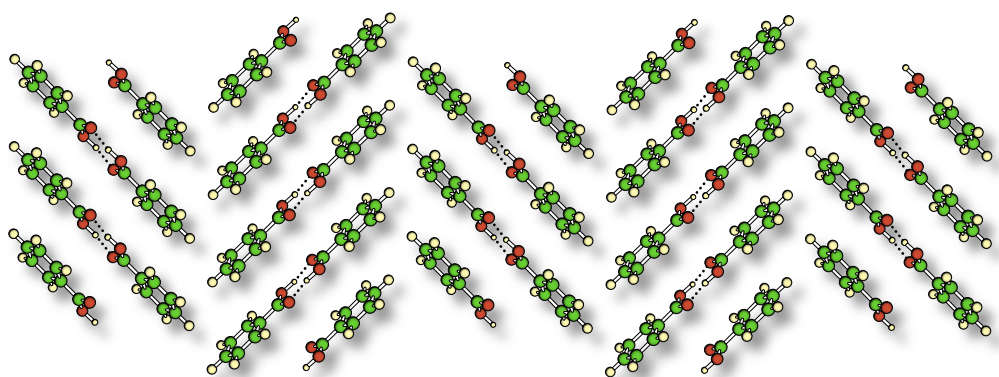
Figure 1.3: *Neutron diffraction crystal structure of benzoic acid [Wilson 96]. The 'herring-bone' packing is driven by intermolecular O··H-O hydrogen bonding forming benzoic acid dimers and π-stacking between dimers.*

Information about hydrogen bonded structures has been obtained by NMR experiments utilising cross polarisation from ^{1}H to dilute nuclei such as ^{13}C and ^{29}Si [Chuang 96, Gu 96]. Alternatively quantification of the quadrupolar coupling constants of deuterons involved in hydrogen bonding has also been shown to correlate with hydrogen bond strength [Hunt 74].

Another important factor regarding the supramolecular structure of crystalline solids is polymorphism [Bernstein 02]. This is defined as the ability of a substance to exist in two or more crystalline forms that differ in the arrangement and/or conformation of the molecules in the crystal lattice. The polymorphic form of a compound may significantly affect both physical and thermodynamic properties. Many compounds exist in multiple polymorphic forms for which the crystal structures are not known. The phenomenon of polymorphism is of great interest and importance to several industries attempting to control the production, processing, and development of organic materials in environments in which a particular polymorph is desirable over another. Polymorphism presents a significant problem to the pharmaceutical industry as many drugs are administered in crystalline form. With different polymorphs having different solubilities, residence times and therapeutic values approval by regulatory bodies is only granted for a specific crystal structure or polymorph.

Crystallisation conditions, such as the solvent from which crystallisation occurs, commonly dictate the polymorph formed but inter-conversion between polymorphs may also occur. For example, the artificial sweetener aspartame exists in three distinct forms at room temperature and can change from a hemihydrate to a dihemihydrate polymorph by being placed into a high relative humidity ($>98\%$) for 5 days [Zell 99]. Thus the environmental history of a polymorphic system is also important.

Since conformational differences result in variations in local electron density, chemical shift information from solid-state NMR is a powerful method to probe polymorphism [Tishmack 03]. Valuable information about the number of crystallographically inequivalent sites per unit cell and the molecular conformations/arrangements possible for different polymorphs can be provided by multinuclear solid-state NMR spectroscopy [Medek 00]. This is of particular interest for mixtures of polymorphs where powder X-ray diffraction is problematic. For example, although cortisone acetate only contains three carbonyl groups per molecule, six sites are observed in the ^{13}C solid-state NMR spectrum (Figure 1.4). Assignment can be made by comparison to spectra of the pure polymorphs and a ratio of polymorphs can be determined [Harris 90, Christopher 92].
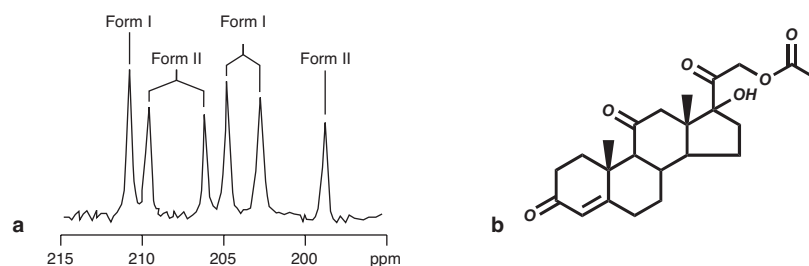
Figure 1.4: *The (a) ketone region of a soild-state ^{13}C NMR spectrum of polymorphic (b) cortisone acetate. A total of six ketons sites are resolved with three sites from each polymorph.*

Polymorphic behaviour of the model polybenzoxazines was suggested by the variation of proton chemical shift with synthetic batch [Brown 02a], especially that of the protons involved in hydrogen bonding. Further evidence was seen in the ^{1}H−^{1}H DQ spectra with both dimeric and continuous forms observed for the same system [Schnell 98a]. However, investigation of this phenomenon was not further pursued for these systems.

1.3.1 Proton solid-state NMR

In principle, ^{1}H NMR spectroscopy has the advantage of directly probing the hydrogen bonded protons themselves. However, ^{1}H NMR spectroscopy of rigid solids is complicated by the homonuclear ^{1}H−^{1}H dipolar interaction, this leading to substantial homogeneous broadening of the resonances [Abragam 61, Mehring 83, Schmidt-Rohr 94]. In rigid solids the strength of this interaction is usually strong enough to obscure all chemical shift information (Figure 1.5). Generally, in order to obtain high-resolution spectra of rigid solids both the homogeneous and inhomogeneous broadening, associated with the dipolar interaction and the chemical shift anisotropy (CSA) respectively, have to be removed first. A number of ingenious methods have been developed to gain sufficient proton spectral resolution in solid-state NMR [Brown 01b].

The application of multiple-pulse methods, such as WAHUHA [Waugh 68], to single-crystal samples, and the combination of multiple-pulse methods with magic-angle spinning (MAS) [Andrew 58, Lowe 59] in the combined rotation and multiple-pulse (CRAMPS) approach [Gerstein 77, Scheler 81, Maciel 90] have allowed access to proton chemical shift information in the solid-state. However, such 'windowed' homonuclear decoupling schemes are sensitive to pulse flip angle and phase setting and are prone to the introduction of spectral artefacts. Significantly narrower proton linewidths can be obtained via the application of windowless homonuclear decoupling sequences, such as the Lee-Goldburg (LG) technique [Lee 65]. Further success has been found with the refinements of the LG approach, such as frequency-switched Lee-Goldburg (FSLG) [Bielecki 89, Bielecki 90] and

phase-modulated Lee-Goldburg (PMLG) [Vinogradov 99] sequences. Recently linewidths as low as 60 Hz have been obtained for the aliphatic resonances of *l*-alanine using a constant-time (CT) CRAMPS experiment [Lesage 01]. Currently the best proton resolution is achieved using the computer-optimized sequence DUMBO [Sakellariou 00] and its experimentally optimised equivalent eDUMBO [Elena 04].
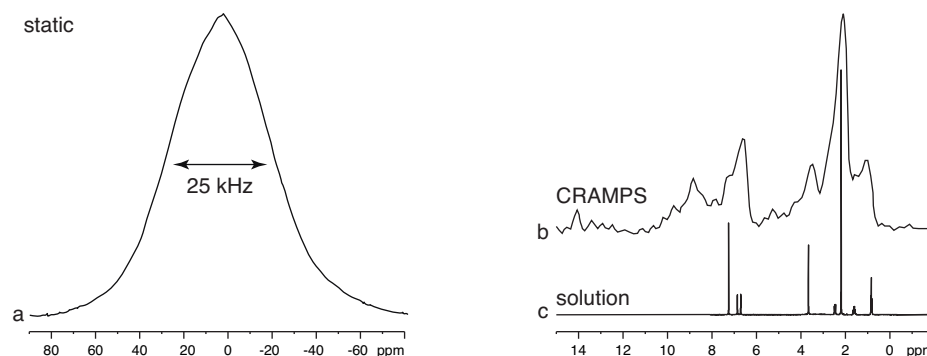
***Figure 1.5**: Typical ^{1}H NMR spectra of a rigid solid; (a) static, (b) CRAMPS and (c) solution-state.*

The reason for such effort to gain proton resolution lies with the chemical shift of a proton involved in hydrogen bonding containing valuable information about the strength of the hydrogen bonding itself. The degree to which a ^{1}H resonance is shifted to higher frequency has been found to correlate with the strength of the hydrogen bond in which it is involved. This correlation has been established for a range of O··H-O hydrogen bonds, e.g. in carboxylic acids, through comparison of the ^{1}H chemical shift to O··O [Berglund 80] or O··H [Jeffrey 86] distances determined by X-ray and neutron diffraction respectively. In another study, ^{1}H CRAMPS was used to provide further resolution of the hydrogen bonding protons in carboxylic acids [Harris 88]. Through the analysis of dipolar sideband patterns, obtained at low spinning speeds, CRAMPS can also be used to measure N··H distances in the solid state. In a recent example, the N··H distance in ^{15}N labelled poly(*l*-aniline) was measured using ^{1}H CRAMPS [Kimura 00]. Differing bond lengths were determined for the α-helical (112 pm) and β-sheet (109 pm) morphologies, and attributed to stronger hydrogen bonds in the latter case.

Over the past decade, much progress has been made in the field of fast MAS [Jakobsen 96, Samoson 02a], with probeheads capable of a rotation frequency of $\omega_r/2\pi = 35$ kHz now commercially available [Bruker 97]. Through the use of custom-built MAS probeheads, Samoson *et al.* have demonstrated stable rotational frequencies of 70 kHz [Samoson 03, Samoson 05]. Comparison of different external magnetic fields and spinning speeds have suggested that at high fields (25 T) and fast MAS speed (>40 kHz) the ^{1}H linewidth approaches an intrinsic limit determined by the anisotropy of magnetic susceptibility [Samoson 01a]. Under such conditions the mechanical dynamics are comparable to the spin-dynamics in coupled spin systems allowing unique experiments to be undertaken such as ramped-speed cross-polarisation [Samoson 01b] or rotation-sweep NMR [Samoson 02b].
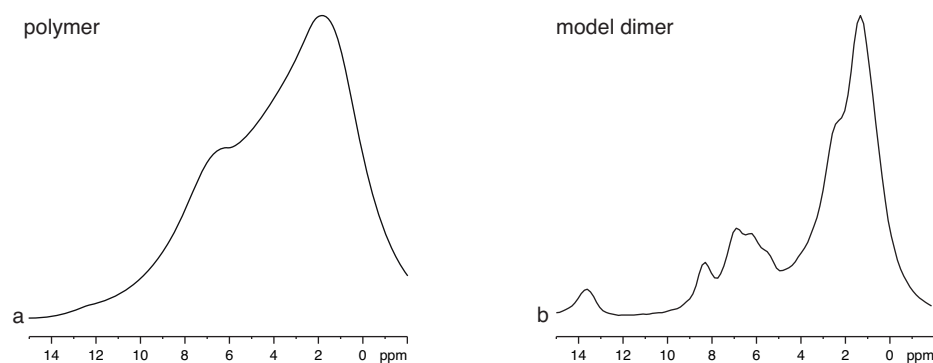
Figure 1.6: *MAS ^{1}H NMR spectra at 30 kHz of a (a) polybenzoxazine and (b) model polybenzoxazine dimer. The presence of protons involved in N··H-O (13.5 ppm) and O··H-O (8.2 ppm) hydrogen bonds can be clearly seen in the model system.*

The resolution afforded by such fast MAS means that important information about hydrogen bonding can now be obtained by MAS alone (Figure 1.6). The improvements in ^{1}H resolution of hydrogen bonded protons afforded by MAS at such fast rotation frequencies is illustrated by Yamauchi *et al.* [Yamauchi 02a], Schnell *et al.* [Schnell 98a], Brown *et al.* [Brown 01c] and Goward *et al.* [Goward 03]. Proton solid-state NMR has developed into a versatile tool for the investigation of hydrogen bonding structures in organic solids and peptides [Wei 99, Schnell 01a, Brown 01a, Schnell 04a]. Recently a study of amide protons involved in N··H-O hydrogen bonding, in glycine containing peptides and poly-peptides, correlated the N··O distances with ^{1}H chemical shift information obtained at high magnetic field and under fast MAS [Yamauchi 00]. A trend towards high-frequency shifts for shorter N··O distances was observed and confirmed by ab-initio calculations. Another approach involved the study of the dynamics in ^{15}N-^{n}H··^{15}N low-barrier hydrogen bonds[†] examining the two N··H distances using solid-state ^{15}N NMR and quantum chemical calculations [Benedict 98].

1.3.2 Two dimensional (2D) proton solid-state NMR

In addition to achieving high resolution, and hence proton chemical shift information, it is desirable to access the structural and dynamic information inherent to the ^{1}H–^{1}H dipolar coupling. In the solution-state additional information about through-bond and through-space proton distances has been gained by extending the NMR experiment into a second dimension [Jeener 71, Ernst 87]. Similar information about the through-space proximity of dipolar coupled nuclei in the solid-state can be gained using double-quantum (DQ) MAS spectroscopy [Geen 94, Sommer 95, Gottwald 95, Feike 96b, Graf 97]. More specificically, ^{1}H–^{1}H DQ spectroscopy [Geen 94, Lee 95, Schnell 98a, Brown 01b, Schnell 01b]. The method relies on the generation of double quantum coherence between proximal ^{1}H

[†]where ^{n}H represents either hydrogen or deuterium

spins, covering a $^1H-^1H$ distance range of up to approximately 3.5 Å, thereby prob-ing the spatial arrangement of protons based on the strength of the through-space dipolar coupling [Lee 95, Hohwy 98, Brinkmann 00, Schnell 01b]. The ability to harness such $^1H-^1H$ DQ information is however highly dependent on the resolution in both frequency dimensions [Schnell 98b]. It has been shown that valuable insight into the hydrogen bonded structures adopted by different alkylsubstituted model polybenzoxazine dimers could be obtained [Schnell 98a]. Insight into a quadrupole hydrogen bonding system, formed by dimers of 2-ureido-4-pyrimidone upon a ketoenol tautomerism, could also be obtained [Schnell 01a]. It has also been demonstrated that quantitative determination of $^1H-^1H$ distances in the complex hydrogen bonded arrangement adopted by bilirubin was possible through the analysis of ^1H DQ MAS sideband patterns [Brown 01c]. Furthermore, the kinetics of the hydrogen bond formation process could also be followed by the changes in signal intensity of a DQ filtered experiment [Brown 00].
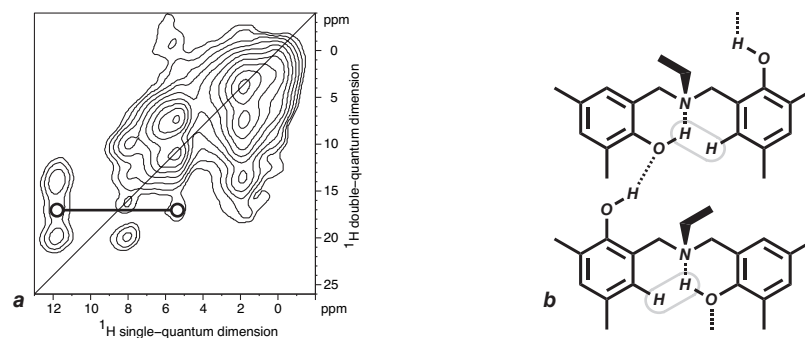
Figure 1.7: *Proton correlation in (a) ^1H double-quantum (DQ) NMR spectra suggested (b) continuous structure of model dimers.*

Considerable insight has been provided into the supramolecular structure of model polybenzoxazines by $^1H-^1H$ DQ MAS spectroscopy. For the model dimers, proton solid-state NMR showed different structures depending on the amine substituent. With a methyl amine substituent resulting in an exclusive dimeric geometry of two dimers, whereas a continuous 'ladder-like' structure was seen for N-Et, N-Pr, and N-Bu substituents, resulting from a twist about the amine [Schnell 98a]. These dif-ferences were suggested solely by $^1H-^1H$ DQ solid-state NMR, demonstrating the power of solid-state ^1H NMR (Figure 1.7).

1.3.3 Heteronuclear methods for hydrogen bond quantification

Although mostly qualitative information about the hydrogen bonding is gained from proton solid-state NMR, quantitative information, via the $^{15}N-^1H$ heteronu-clear dioplar coupling present in N··H-O hydrogen bonds, is also possible. Most solid-state NMR studies have focused on the measurement of relatively short N··H-O hydrogen bonds (≈ 110 pm). Through the use of advanced techniques, such as heteronuclear dipolar recoupling and fast MAS, access to comparatively long

hydrogen bonds has recently been demonstrated for model polybenzoxaxines, even in the presence of further perturbing protons [Goward 01, Goward 03].

The heteronuclear ^{1}H–^{15}N approaches used were based on REDOR-type [Gullion 89b, Gullion 98] dipolar recoupling methods. These methods generate heteronuclear single quantum correlation (HSQC) spectra and allow the observation of rotor-encoded MAS sideband patterns, the latter serving as a sensitive measure for the underlying dipolar coupling [Saalwächter 99, Saalwächter 01a, Saalwächter 01b]. Although other methods for heteronuclear dipolar recoupling have been demonstrated for N··H distance measurement [Brinkmann 01, Zhao 01b], the REDOR-type methods have been found to have a more robust performance under fast MAS.
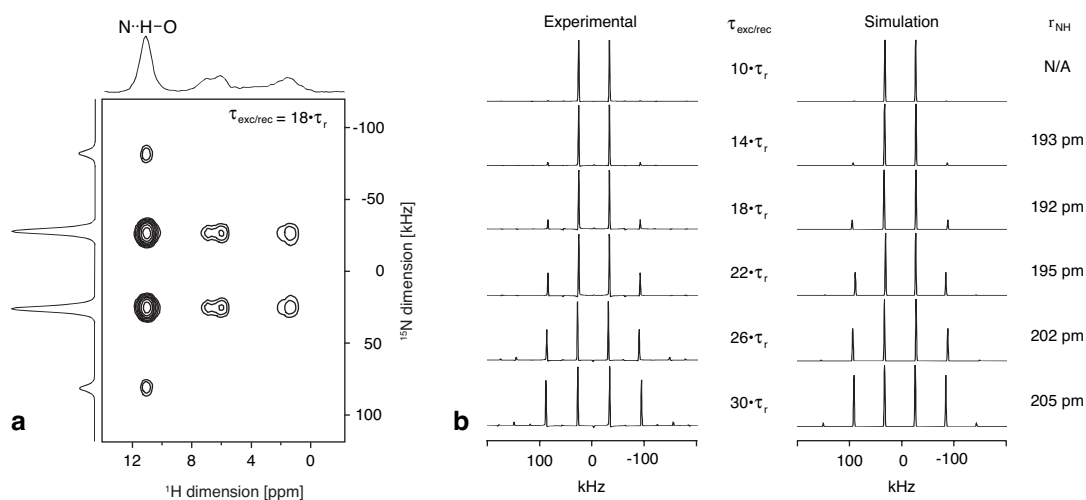
Figure 1.8: *(a)* ^{1}*H detected DIP-HSQC spectra of* ^{15}*N labelled model dimer. (b) Fitting of the rotor-encoded sideband patterns allowed quantification of the N··H distance in the N··H-O hydrogen bonds. (adapted from [Goward 01])*

Concerning polybenzoxazines, an N··H distance of 195 pm was measured for the N··H-O hydrogen bond in a ^{15}N labelled polybenzoxazine model N-Me dimer [Goward 01] and distances of 170, 179 and 184 pm determined for the three N··H-O hydrogen bonds in a ^{15}N labelled polybenzoxazine model N-Me tetramer [Goward 03]. However, to allow access to these systems advanced solid-state techniques, such as inverse detection [Goward 01, Schnell 01a] and spoil-gradients (G_z) [Schnell 02], were needed. The application of these methods to other hydrogen bonded systems, with shorter N··H-O hydrogen bonds, allowed N··H distances of $\approx$ 110 pm to be determined with ^{15}N in natural abundance [Schnell 01a]. Despite these advances in sensitivity, for the relatively long N··H distances found in polybenzoxazines, excitation of adequate signal under such natural abundance conditions was not found to be possible.

1.3.4 Molecular modelling and NMR simulation

Molecular modelling has enabled further insight into the essential structural features of polybenzoxazine oligomers [Dunkers 96, Ishida 97, Goward 03]. Recently it has become possible to calculate chemical shifts for extended systems, such as amorphous or crystalline solids [Sebastiani 01], as well as isolated molecules, within the framework of density functional theory (DFT) [Jones 89]. Such combination of experimental NMR results and geometry optimisation followed by simulation of NMR chemical shift values has previously been found to be extremely powerful for supramolecular systems [Ochsenfeld 97, Ochsenfeld 00, Ochsenfeld 01, Goward 02, Sebastiani 02a]. These methods were of particular importance for the polybenzoxazine dimers as these were known to have strong intermolecular O··H‒O hydrogen bonds [Dunkers 95, Dunkers 96, Schnell 98a].
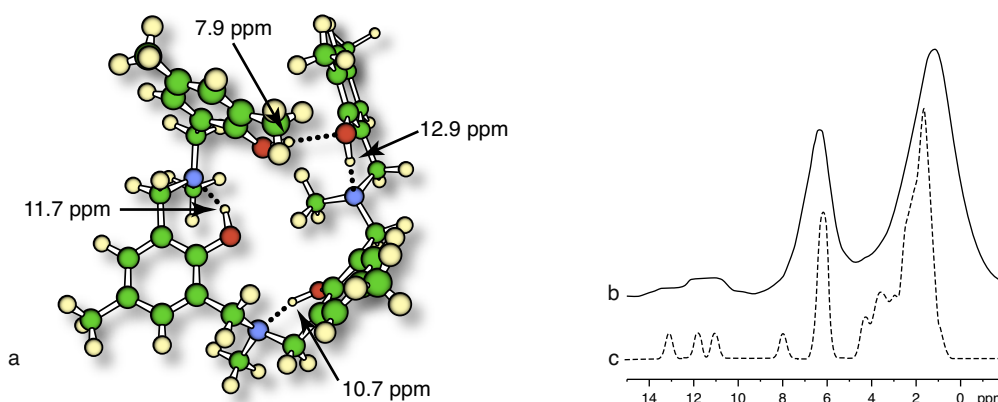
Figure 1.9: *Results of (a) geometry optimisation and comparison of (b) experimental and (c) simulated ^1H chemical shifts. (adapted from [Goward 03])*

Goward *et al.* showed that good agreement was seen between the experimental and predicted NMR spectra of an N‒Me model polybenzoxazine dimer, trimer and tetramer [Goward 03]. The dimer was found to have strong intramolecular N··H‒O and strong intermolecular O··H‒O hydrogen bonding, with the geometry based on the known dimeric X-ray structure. In contrast, with no X-ray crystal structures known, the trimer and tetramer were simulated *in-vacuo*. Thus, only intramolecular hydrogen bonding, consisting of strong N··H‒O and weak O··H‒O hydrogen bonds, was modelled. These simulations resulted in a closed ring-like geometry for the trimer and semi-helical geometry for the tetramer (Figure 1.9). Further stabilisation of these geometries is expected in the condensed phase due to packing effects, such as van der Waals interactions between phenyl rings of neighbouring molecules or intermolecular hydrogen bonding. However, these effects were assumed to be of only moderate strength due to these materials not readily forming large crystals.

1.4 Materials studied

Throughout previous ^{1}H solid-state NMR studies all oligomers examined carried the same aromatic ring substituents [Schnell 98a, Goward 01, Goward 03], i.e two methyl groups ortho and para to the hydroxyl. Thus, the question remains as to the effect of these ring substituents on the extended structures of these systems. Similarly, with the amine substituents having previously been shown to strongly effect the hydrogen bonding structure [Schnell 98a] it is presently unclear if the cyclic structures suggested for the N-Me trimer would also be found in similar systems with different amine substituents. The general challenge presented is the determination of the hydrogen bonded supramolecular structure of systems whose heavy-atom geometry is not known.

In this work a number of materials associated with polybenzoxazines were studied, both small molecules and polymers. All materials were synthesised in the group of Prof. Hatsuo Ishida at Case Western Reserve University, Cleveland, USA, and used without further purification.

In Chapter 4 nine polybenzoxazine model-dimers, with various ring and amine substituents, are studied. Although not true dimers of their associated polymers, i.e not an oligomer consisting of two monomer units, they are referred to as dimers for simplicity throughout this work. The effects of ring and amine substituents on hydrogen bonding and supramolecular structure of these systems were investigated.

The differences between methyl and ethyl amine substituted model dimers and trimers are studied in Chapter 5. As with the dimers, although not true trimers they are referred to as such for simplicity. Comparison of the trimers, and their related dimers, illustrated how subtle chemical differences can affect the hydrogen bonding, and thus overall supramolecular structure, of this class of material in this type of system.

More diverse systems related to polybenzoxazines are investigated in Chapter 6. These included a novel phenylamine dimer, two 'asymmetric-dimers' and a number of diamine-based polymers. These systems illustrated the high propensity for hydrogen bond formation.

The chemical structures and the abbreviated nomenclature of the specific systems investigated is now introduced.

1.4.1 Model polybenzoxazine dimers

In total eleven dimers, all having the same general chemical structure were studied (Figure 1.10). An abbreviated nomenclature was used for convenience, for example *N*,*N*-bis(3,5-dimethyl-2-hydroxybenzyl)-methylamine was shortened to Me,Me-N-Me, reflecting the two ring and single amine substituents (Table 1.1). When a subset of the dimers needed to be described further abbreviation was made, i.e. when considering all methyl amine substituted system the term N-Me was used.
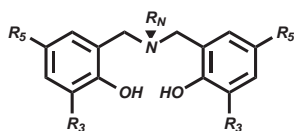
Figure 1.10: General structure of the model dimers.

Table 1.1: Abbreviated nomenclature of dimers based on ring (R_3,R_5) and amine (R_N) substituent.

R_3	R_5	R_N	abbreviation	chapter
Me	Me	Me	Me,Me-N-Me	4,5
H	Me	Me	H,Me-N-Me	4
H	Et	Me	H,Et-N-Me	4
Me	Me	Et	Me,Me-N-Et	5
Me	Me	Pr	Me,Me-N-Pr	4
H	Me	Pr	H,Me-N-Pr	4
H	Et	Pr	Et,Me-N-Pr	4
Me	Me	Cy	Me,Me-N-Cy	4
H	Me	Cy	H,Me-N-Cy	4
H	Et	Cy	Et,Me-N-Cy	4
Me	Me	Ph	Me,Me-N-Ph	6

1.4.2 Model polybenzoxazine trimers

Two trimers were investigated (Figure 1.11). The abbreviated nomenclature used for the model dimers was adapted for these compounds. For example, 2,6-bis[*N*-(3,5-dimethyl-2-hydroxybenzyl)-*N*-methylamino-methyl]-*p*-cresol was shortened to Me,Me-(N-Me)$_2$, reflecting that two amine substituent were present for each trimer (Table 1.2).
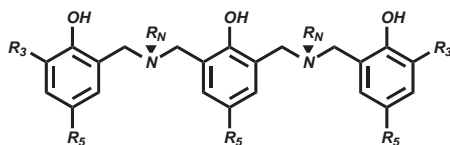
Figure 1.11: General structure of model trimers.

Table 1.2: Abbreviated nomenclature of trimers based on amine (R_N) substituent.

R_3	R_5	R_N	abbreviation	chapter
Me	Me	Me	Me,Me-(N-Me)$_2$	5
Me	Me	Et	Me,Me-(N-Et)$_2$	5

1.4.3   Model asymmetric dimers

The asymetric dimers were similar in structure to the dimers but with only one aromatic ring substituted, resulting in a benzyl amine substituent (Figure 1.12). The abbreviated nomenclature of the dimers was adapted for these compounds, for example *N*-(3,5-dimethyl-2-hydroxybenzyl)-*N*-(benzyl)-*t*-butylamine was shortened to N-Bz-N-*t*Bu as only the amine substituents varied between asymetric dimers (Table 1.3).
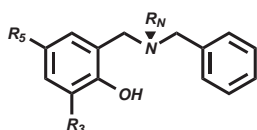
Figure 1.12: *General structure of asymmetric dimers.*

Table 1.3: *Abbreviated nomenclature of asymetric dimers based on amine (R_N) substituent.*

R_3	R_5	R_N	Abbreviation	Chapter
Me	Me	Cy	N-Cy-N-Bz	6
Me	Me	*t*Bu	N-*t*Bu-N-Bz	6

1.4.4   Diamine-based polymers

Two types of diamine-based polymers were studied in Chapter 6, these being based on either linear or cyclic diamines. The topology of the polymer formed from the linear diamine monomers (Figure 1.13) was unknown. The abbreviated nomenclature of the linear diamine systems pertained to the length of the diamine in the monomer (Table 1.4).
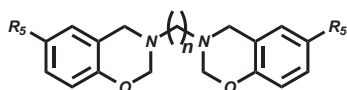
Figure 1.13: *General structure of diamine monomer.*

Table 1.4: *Abbreviated nomenclature of linear diamine polymers based on diamine length (C_n).*

R_5	C_n	Abbreviation
H	12	Poly-C_{12}
H	6	Poly-C_6
H	4	Poly-C_4
H	2	Poly-C_2
Me	2	Poly-C_{2p}

The single cyclic diamine polymer based on piperazine was also studied, this polymer was designated Poly-P (Figure 1.14).
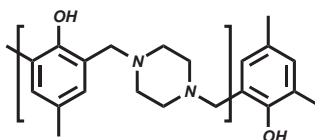
Figure 1.14: *General structure of the cyclic diamine polymer based on piperazine.*

1.5 Outline

The general theory behind NMR will be described in Chapter 2 and the basic solid-state NMR techniques used introduced. Particular attention is paid to the areas of chemical shift, dipolar coupling and magic-angle spinning (MAS). The advanced solid-state NMR methods of dipolar recouping and multiple-quantum coherence, used throughout this work, will be introduced in Chapter 3. The concept and theory as well as the practical implementation and possible limitations of each method will be discussed.

The supramolecular structure of nine model polybenzoxazine dimers will be investigated using a combination of basic and advanced solid-state NMR methods in Chapter 4. Experimental proton spectra will also be compared to simulated spectra calculated from possible three dimensional geometries using electronic structure methods. The role of both amine and ring substituents on supramolecular structure are discussed providing insight into the structure-property relationships of polybenzoxazines.

The strong structure determining role of the amine-substitutent will be further investigated in Chapter 5. The supramolecular structure of both dimers and trimers based on methyl and ethyl amine substituents will be discussed. Experimental measurements will again be complemented by simulated spectra allowing the likelihood of possible geometries to be assessed.

A number of other model polybenzoxazines will be introduced in Chapter 6 and their hydrogen bonding discussed. These systems vary from further model dimers to crosslinked polybenzoxazine macromolecules and show the prevalence of hydrogen bonding in this class of material.

A summary of the findings will be given at the end of each section and chapter. A general summary of the findings of Chapters 4, 5 and 6 will be given in Chapter 7. Conclusions will be drawn regarding the hydrogen bonding seen in the model systems and the implications to polybenzoxazines in general will be discussed.

Chapter 2

General NMR Theory

Nuclear magnetic resonance is the investigation of nuclear-spin dynamics. To do this, the time-dependent Schrödinger equation needs to be solved for the nuclei. The first step towards achieving this is to construct a Hamiltonian operator. In this chapter the form of the nuclear spin Hamiltonian will be described. The power of NMR lies in the ability to manipulate this nuclear spin Hamiltonian by external means.

2.1 NMR interactions

The quantum state of a sample is fully described by a wavefunction $|\psi_{full}\rangle$, which contains position, velocity, and spin information of all electrons and nuclei. The wavefunction obeys the time-dependent Schrödinger equation:

$$\frac{\mathrm{d}}{\mathrm{d}t}|\psi_{full}(t)\rangle = -i\hat{\mathcal{H}}_{full}|\psi_{full}(t)\rangle \tag{2.1}$$

where the Hamiltonian $\hat{\mathcal{H}}_{full}$ contains all the interactions present in the system. Although complete, it is useless, as it can never be solved for a realistic situation. However, a simplified form can be used where only the nuclear spin states are considered:

$$\frac{\mathrm{d}}{\mathrm{d}t}|\psi_{spin}(t)\rangle = -i\hat{\mathcal{H}}_{spin}|\psi_{spin}(t)\rangle \tag{2.2}$$

where $|\psi_{spin}\rangle$ is the spin state of the nuclei and $\hat{\mathcal{H}}_{spin}$ is the nuclear spin Hamiltonian, the latter only containing information about the direction of the nuclear spin polarisation. By doing so it is assumed that the rapid motion of the electrons can regarded as an average, with these average interactions taken into account by the spin Hamiltonian $\hat{\mathcal{H}}_{spin}$. This massive simplification is known as the spin Hamiltonian hy-

pothesis and holds for almost all systems at ordinary temperatures. From this point on the operator $\mathcal{H}$ will be assumed to be the nuclear spin Hamiltonian $\mathcal{H}_{spin}$ and the quantum state $|\psi\rangle$ to imply the nuclear spin state $|\psi_{spin}\rangle$.

The NMR interactions contributing to the spin Hamiltonian may originate from the external apparatus or from the sample itself and are classified as *external spin interactions* or *internal spin interactions* accordingly. The nuclear spin Hamiltonian can thus be written:

$$\mathcal{H} = \mathcal{H}_{ext} + \mathcal{H}_{int} \tag{2.3}$$

External spin interactions are purely magnetic in origin and hence magnetic fields can be used to manipulate nuclear spins. The external spin Hamiltonian $\mathcal{H}_{ext}$ contains the following terms:

Zeeman Interaction: $\mathcal{H}_Z$
> these represent the direct magnetic interaction of a static external magnetic field and nuclear spins.

RF Interaction: $\mathcal{H}_{RF}$
> these represent the direct magnetic interaction of a transverse-oscillating external magnetic field and nuclear spins

In contrast, the internal interactions originate from the sample itself and thus carry information regarding the nuclear environment. The internal spin Hamiltonian $\mathcal{H}_{int}$ contains the following terms:

Quadrupolar Couplings: $\mathcal{H}_Q$
> these represent the electronic interactions of spin $I > \frac{1}{2}$ nuclei with the surrounding electric field gradients.

Chemical Shift: $\mathcal{H}_{CS}$
> these represent the indirect magnetic interaction of the static external magnetic field and the nuclear spins, through the involvement of the electrons.

Dipole-Dipole Couplings: $\mathcal{H}_D$
> these represent the direct magnetic interactions of nuclear spins with each other.

J-Coupling: $\hat{\mathcal{H}}_J$

> these represent the indirect magnetic interaction of nuclear spins with each other, through the involvement of electrons.

Spin-Rotation Interactions: $\hat{\mathcal{H}}_R$

> these represent the interactions of the nuclear spins with magnetic fields generated by rotational motion of the molecules.

The most important interactions influencing the spin Hamiltonian $\hat{\mathcal{H}}$ are, in order of typical strength; the Zeeman-interaction, quadrupolar coupling, interaction with RF pulses, chemical shift, dipole-dipole coupling, J-coupling, and spin-rotation interaction (Equation 2.4).

$$\hat{\mathcal{H}} = \hat{\mathcal{H}}_Z + \hat{\mathcal{H}}_Q + \hat{\mathcal{H}}_{RF} + \hat{\mathcal{H}}_{CS} + \hat{\mathcal{H}}_D + \hat{\mathcal{H}}_J + \hat{\mathcal{H}}_R \qquad (2.4)$$

The mathematical forms of the nuclear spin Hamiltonians can be complicated however simplification can occur due to the secular approximation and by considering motional averaging. The secular approximation arises due to the interactions being dominated by the largest interaction with the static external magnetic field. In the secular approximation some components of the internal spin interaction $\hat{\mathcal{H}}_{int}$ can be replaced by a simplified form, $\hat{\mathcal{H}}_{int}^0$. If the molecules undergo rapid molecular motion, then the interaction terms fluctuate with time. If the molecular motion is sufficiently fast, the fluctuating interaction $\hat{\mathcal{H}}_{int}^0$ may be replaced by a motional averaged value $\overline{\hat{\mathcal{H}}}_{int}^0$. The parts of $\hat{\mathcal{H}}_{int}^0$ which have a zero time-average can then also be discarded. The motionally averaged spin Hamiltonian is usually a good approximation in gases and liquids, unless the molecular motion is slow. The discarded parts of the internal spin Hamiltonian terms then become partially responsible for the relaxation of the nuclear spin system:

$$\hat{\mathcal{H}}_{int} \xrightarrow[\text{relaxation}]{} \hat{\mathcal{H}}_{int}^0 \xrightarrow[\text{relaxation}]{} \overline{\hat{\mathcal{H}}}_{int}^0 \qquad (2.5)$$

The effect of J-coupling $\hat{\mathcal{H}}_J$ and spin-rotation interaction $\hat{\mathcal{H}}_R$ in the solid-state is usually negligible. Although still present the J-coupling is typically too weak to be detected in the presence of the stronger interactions such as dipolar coupling. Recently however the J-coupling has been exploited in the solid-state [Brown 02b].

It is interesting to note that for NMR the external interactions are usually much larger than the internal interactions, or the nuclear spins are more strongly coupled to the external apparatus than to their own molecular environment. This is in contrast to most other forms of spectroscopy, where the behaviour of the system is set by the molecular structure itself and the information is gained by a relatively weak external perturbation [Levitt 01].

Interaction representations

In general, the NMR interactions exhibit an orientation dependence with respect to the external static magnetic field $\boldsymbol{B}_0$, and are thus anisotropic. The part of an interaction Hamiltonian $\mathcal{H}_\lambda$ that describes this orientation dependence can thus be represented as a second rank tensor $\underline{A}_\lambda$, allowing $\mathcal{H}_\lambda$ to be represented as a bilinear product [Mehring 83]:

$$\mathcal{H}_\lambda = \hat{\boldsymbol{I}}_j \cdot \underline{A}_\lambda \cdot \hat{\boldsymbol{S}}_k \tag{2.6}$$

The spin angular momentum vector operators $\hat{\boldsymbol{I}}$ and $\hat{\boldsymbol{S}}$ can belong to: like spins (homonuclear dipolar coupling), unlike spins (hetronuclear dipolar coupling), the same spin (quadrupolar coupling) or one can represent a spin and the other a Cartesian vector of the $\boldsymbol{B}_0$ field (chemical shift). The most intuitive representation of the interaction tensor $\underline{A}$ is as a (3×3) spatial Cartesian matrix:

$$\underline{A} = \begin{pmatrix} A_{xx} & A_{xy} & A_{xz} \\ A_{yx} & A_{yy} & A_{yz} \\ A_{zx} & A_{zy} & A_{zz} \end{pmatrix} \tag{2.7}$$

such a matrix can always be decomposed into three contributions:

$$\underline{A} = a + \begin{pmatrix} 0 & b & c \\ -b & 0 & d \\ -c & -d & 0 \end{pmatrix} + \begin{pmatrix} e & g & h \\ g & f & i \\ h & i & (-e-f) \end{pmatrix} \tag{2.8}$$

where the first term a denotes the isotropic part and is equivalent to one third the trace of the spatial Cartesian matrix:

$$a = \frac{1}{3}\text{Tr}\{\underline{A}\} = \frac{1}{3}\{A_{xx} + A_{yy} + A_{zz}\} \tag{2.9}$$

The second term of Equation 2.8 being a traceless antisymmetric matrix of three components, and the third term a traceless symmetric matrix of five components. Alternatively the interaction tensor $\underline{A}$ can be described by the irreducible spherical tensor representation, consisting of a scalar, and two vectors of dimension (3×1) and (5×1):

$$\underline{A} = A_0 + \left(A_{1-1}, A_{10}, A_{11}\right) + \left(A_{2-2}, A_{2-1}, A_{20}, A_{21}, A_{22}\right) \tag{2.10}$$

The reason for using the irreducible spherical tensor representation lies in the favourable transformation behaviour of the spherical tensor components, which transform identically to the spherical harmonics Y_{Lm}, with familiar multiplicity of $2L + 1$ and $m = -L, -L + 1 \ldots + L$. This greatly simplifies the mathematical description of rotations inevitable in solid-state NMR by allowing only linear combinations of terms to be needed.

The interaction Hamiltonian in the spherical tensor representation reads:

$$\hat{\mathcal{H}}_\lambda = \sum_{k=0}^{2} \sum_{q=-k}^{k} (-1)^q \mathcal{A}_{kq} \hat{\mathcal{T}}_{k-q} \tag{2.11}$$

where $\hat{\mathcal{T}}_{k-q}$ are the irreducible spherical spin tensor operators of rank k and order $-q$. Another advantage of this mathematical description arises from the separation of rotations in *real-space* caused by physical motion, and those of the spins in *spin-space* caused by RF-pulses. Thus separating the space part $\mathcal{A}_{kq}$ and spin part $\hat{\mathcal{T}}_{k-q}$ of an interaction Hamiltonian:

$$\hat{\mathcal{H}}_\lambda = \mathcal{A} \cdot \hat{\mathcal{T}} \tag{2.12}$$

The density operator $\hat{\rho}$

The description of the spin state of a nuclei is given by the wavefunction:

$$|\psi\rangle = c_\alpha |\alpha\rangle + c_\beta |\beta\rangle \tag{2.13}$$

where c_α and c_β are the normalised superposition coefficients for the eigenstates $|\alpha\rangle$ and $|\beta\rangle$ respectively. For an ensemble of spins the measurable bulk magnetisation M is proportional to the coefficients of the eigenstates. If all the spins had identical wavefunctions, thus being in a so-called *pure-state*, the various components of the bulk magnetisation are given by:

$$M_x \quad \propto \quad N\big(c_\alpha c_\beta^* + c_\beta c_\alpha^*\big) = N|c_\alpha||c_\beta| \cos\phi \tag{2.14}$$

$$M_y \quad \propto \quad N\big(c_\alpha c_\beta^* - c_\beta c_\alpha^*\big) = N|c_\alpha||c_\beta| \sin\phi \tag{2.15}$$

$$M_z \quad \propto \quad N\big(c_\alpha c_\alpha^* - c_\beta c_\beta^*\big) \tag{2.16}$$

where N_i is the number of spins in the ensemble. However such a pure-state is highly unlikely and an ensemble of spins is much more likely to exist in a so-called *mixed-state* with different wavefunctions ψ_i. This state can be thought of as consisting of n sub-ensembles, each with the same wavefunction $|\phi_i\rangle$. The number of spins in each sub-ensemble is related to the total number of spins by the probability p_i, such that $p_i \leq 1$. In the mixed-state the c_α and c_β terms of Equation 2.16 can be replaced by their weighted averages:

$$\overline{c_a c_b^*} = \sum_{i=1}^{n} p_i \big(c_a c_b^*\big) \tag{2.17}$$

These average terms can then be used to describe the motion of the bulk magnetisation M from an ensemble of spins with respect to time. This is most conveniently done by defining a spin density operator $\hat{\rho}$, this being most intuitively represented as the density matrix:

$$\hat{\rho} = \begin{pmatrix} \overline{c_\alpha c_\alpha^*} & \overline{c_\alpha c_\beta^*} \\ \overline{c_\beta c_\alpha^*} & \overline{c_\beta c_\beta^*} \end{pmatrix} \tag{2.18}$$

The diagonal elements of $\hat{\rho}$ are the populations[†] of the states $|\alpha\rangle$ and $|\beta\rangle$. The off-diagonal elements are called coherences between the states $|\alpha\rangle$ and $|\beta\rangle$. The difference between the two populations is the polarisation of the system. Upon spin coupling the number of eigenstates increases. In general the number of spin states n_H for a given number of coupled spins n is related to the spin quantum number I:

$$n_H = \prod_{i=1}^{n} (2I + 1) \tag{2.19}$$

Thus the value n_H also dictates the dimensions of the density matrix. If we consider two coupled spin $I = \frac{1}{2}$ nuclei, four eigenstates are possibe (Figure 2.1) resulting in a (4×4) density matrix, each element of which represents one of the sixteen possible superpositions of eigenstates:

$$\hat{\rho}_{ab}(t) = \langle a | \hat{\rho}(t) | b \rangle = \overline{c_a^*(t) c_b(t)} \tag{2.20}$$

Thus the density matrix for such a spin system would be:

$$\hat{\rho} = \begin{pmatrix} \overline{c_{\alpha\alpha} c_{\alpha\alpha}^*} & \overline{c_{\alpha\alpha} c_{\alpha\beta}^*} & \overline{c_{\alpha\alpha} c_{\beta\alpha}^*} & \overline{c_{\alpha\alpha} c_{\beta\beta}^*} \\ \overline{c_{\alpha\beta} c_{\alpha\alpha}^*} & \overline{c_{\alpha\beta} c_{\alpha\beta}^*} & \overline{c_{\alpha\beta} c_{\beta\alpha}^*} & \overline{c_{\alpha\beta} c_{\beta\beta}^*} \\ \overline{c_{\beta\alpha} c_{\alpha\alpha}^*} & \overline{c_{\beta\alpha} c_{\alpha\beta}^*} & \overline{c_{\beta\alpha} c_{\beta\alpha}^*} & \overline{c_{\beta\alpha} c_{\beta\beta}^*} \\ \overline{c_{\beta\beta} c_{\alpha\alpha}^*} & \overline{c_{\beta\beta} c_{\alpha\beta}^*} & \overline{c_{\beta\beta} c_{\beta\alpha}^*} & \overline{c_{\beta\beta} c_{\beta\beta}^*} \end{pmatrix} \tag{2.21}$$

The density matrix now having four populations P_{ab} and twelve coherences. The coherences correspond to the six transitions possible in the spin system. It is thus useful to classify these coherences with a quantum number called the *coherence order* ρ_{ab}. With each eigenstate having well defined angular momentum in the secular approximation such that if:

$$\hat{I}_z | a \rangle = M | a \rangle \tag{2.22}$$

the order of coherence can then be defined as:

$$\rho_{ab} = M_a - M_b \tag{2.23}$$

[†]Technically these are fractional populations, as the sum over all populations is normalised to unity.
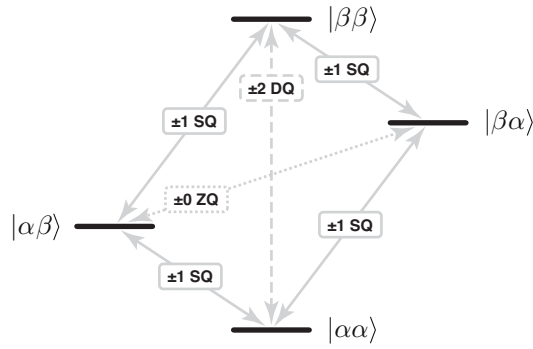
Figure 2.1: *The four eigenstates for a coupled two spin system showing the four SQ transitions (solid), one DQ transition (dashed) and one ZQ transition (dotted). Positive coherence orders point down.*

Coherence of order ± 1 is termed single quantum (SQ) coherence, and is the only order of coherence which results in transverse magnetisation. Because of this only SQ coherence can be directly excited and directly detected.[†] However, once SQ coherence has been generated it can be converted into other orders of coherence by the further application of RF pulses. By doing so it becomes possible to probe the double-quantum (DQ) and zero-quantum (ZQ) coherence of a coupled two spin system. Collectivly, orders of coherence not equal to 1 are termed multiple-quantum (MQ) coherence and need to be converted into SQ coherence prior to detection. The density matrix can then be written as:

$$
\hat{\boldsymbol{\rho}} =
\begin{pmatrix}
\alpha\alpha & +1 & +1 & +2 \\
-1 & \alpha\beta & +0 & +1 \\
-1 & -0 & \beta\alpha & +1 \\
-2 & -1 & -1 & \beta\beta
\end{pmatrix}
=
\begin{pmatrix}
\mathsf{P}_{\alpha\alpha} & \mathsf{SQ} & \mathsf{SQ} & \mathsf{DQ} \\
\mathsf{SQ} & \mathsf{P}_{\alpha\beta} & \mathsf{ZQ} & \mathsf{SQ} \\
\mathsf{SQ} & \mathsf{ZQ} & \mathsf{P}_{\beta\alpha} & \mathsf{SQ} \\
\mathsf{DQ} & \mathsf{SQ} & \mathsf{SQ} & \mathsf{P}_{\beta\beta}
\end{pmatrix}
\tag{2.24}
$$

Each transition is represented by two elements of opposite sign of coherence order, symmetric about the diagonal. These elements are complex conjugates with the absolute value of the complex number being the amplitude of the coherence and the ratio of the real and imaginary part related to the phase ϕ. The sign of the coherence order represents the direction in which the coherence is maintained, i.e. the $\overline{c_{\alpha\alpha} c^*_{\beta\beta}}$ element corresponds to a +2 quantum coherence from $|\beta\beta\rangle$ to $|\alpha\alpha\rangle$. The importance of MQ coherence lies in the ability of NMR to prove that two spins are coupled and to possibly even quantify the magnitude of the mediating coupling interaction.

The equation of motion for the time evolution of the density matrix can be derived from the time-dependent Schrödinger equation after showing that the density operator can be defined as:

$$
\hat{\boldsymbol{\rho}} = \sum_{i=1}^{n} p_i |\psi\rangle\langle\psi|
\tag{2.25}
$$

[†]due to the nature of quadrature detection only the -1 SQ coherence is detected. If the phase offset between the real and imaginary channels is not set correctly however the +1 SQ coherence is also detected at $-\omega$.

The time-evolution of $\hat{\boldsymbol{\rho}}$ is described by the Liouville-von-Neumann equation:

$$\frac{\partial \hat{\boldsymbol{\rho}}}{\partial t} = -i[\hat{\mathcal{H}}(t), \hat{\boldsymbol{\rho}}(t)]. \tag{2.26}$$

where $[\hat{\mathcal{H}}(t), \hat{\boldsymbol{\rho}}(t)]$ is the commutator of the Hamiltonian and density operators:

$$[\hat{\mathcal{H}}(t), \hat{\boldsymbol{\rho}}(t)] = \hat{\mathcal{H}}(t)\hat{\boldsymbol{\rho}}(t) - \hat{\boldsymbol{\rho}}(t)\hat{\mathcal{H}}(t) \tag{2.27}$$

The general solution of the Liouville-von-Neumann Equation is:

$$\hat{\boldsymbol{\rho}}(t) = \hat{U}(t)\,\hat{\boldsymbol{\rho}}(0)\,\hat{U}^{-1}(t) \tag{2.28}$$

where $\hat{U}$ is the so-called propagator. If $\hat{\mathcal{H}}$ is time independent, i.e. $\hat{U} = e^{-i\hat{\mathcal{H}}t}$, the solution of the Liouville-von-Neumann equation simplifies to:

$$\hat{\boldsymbol{\rho}}(t) = \exp\{-i\hat{\mathcal{H}}t\}\,\hat{\boldsymbol{\rho}}_0\,\exp\{i\hat{\mathcal{H}}t\} \tag{2.29}$$

Further simplification also arises if the components of the time independent Hamiltonian commute:

$$\hat{U} = \exp\{-i(\hat{\mathcal{H}}_1 + \hat{\mathcal{H}}_2 + \ldots + \hat{\mathcal{H}}_n)t\} \tag{2.30}$$

$$= \exp\{-i\hat{\mathcal{H}}_1 t\}\exp\{-i\hat{\mathcal{H}}_2 t\}\ldots\exp\{-i\hat{\mathcal{H}}_n t\} \tag{2.31}$$

thus allowing separate calculation of the different contributions. A known starting point $\hat{\rho}_0$ has also been assumed in Equation 2.29 for the evolution of the density matrix. For a spin ensemble in thermal equilibrium, i.e. $\frac{d\hat{\rho}}{dt} = 0$, this initial state is given by the Boltzmann distribution of the individual spins among the energy levels of the system. The spin system can then be described by [Abragam 61]:

$$\hat{\boldsymbol{\rho}}_B = \frac{\exp\left\{-\frac{\hbar}{kT} \cdot \hat{\overline{\mathcal{H}}}\right\}}{\mathrm{Tr}\left\{\exp\left\{-\frac{\hbar}{kT} \cdot \hat{\overline{\mathcal{H}}}\right\}\right\}} \tag{2.32}$$

When only the contributions from the Zeeman interaction $\hat{\mathcal{H}}_Z = -\gamma B_0 \hat{I}_z$ are taken into account the density matrix reduces to:

$$\hat{\boldsymbol{\rho}}_B = \frac{\exp\left\{\frac{\hbar}{kT} \cdot \gamma B_0 \hat{I}_z\right\}}{\mathrm{Tr}\left\{\exp\left\{\frac{\hbar}{kT} \cdot \gamma B_0 \hat{I}_z\right\}\right\}} \tag{2.33}$$

After Taylor expansion, truncation to first order terms only[†] and assuming constant energy, the equilibrium density matrix is obtained:

$$\hat{\boldsymbol{\rho}}_{eq} \sim \hat{\mathbb{1}} + \frac{\gamma \hbar \boldsymbol{B}_0}{kT} \hat{I}_z \tag{2.34}$$

Since the unitary operator $\hat{\mathbb{1}}$ commutes with the internal interaction operators it does not evolve in time and can therefore be neglected. Thus the initial equilibrium state in a static magnetic field, oriented along the z-axis, is given by a sum of the individual z-angular momentum operators $\hat{I}_z$ weighted by their different Larmor frequencies (Section 2.1.1). In the following sections the equilibrium state will be described as $\hat{I}_z$ for convenience.

The transverse magnetisation measured in an NMR experiment corresponds to the expectation values of the $\hat{I}_x$ and $\hat{I}_y$ spin operators for each of the spins. In order to predict the outcome of an experiment these expectation values $\langle \hat{I}_x \rangle$ and $\langle \hat{I}_y \rangle$ need to be calculated. In general, for a given operator $\hat{A}$ the expectation value $\langle \hat{A} \rangle$ is given by:

$$\langle \hat{A} \rangle = \mathsf{Tr}\{ \hat{\boldsymbol{\rho}} \cdot \hat{A} \} \tag{2.35}$$

[†]Possible as $T > 1$ K and only moderate $\boldsymbol{B}_0$ fields are applied

2.1.1 Zeeman interaction

The strongest and inherently most important interaction to NMR is the Zeeman interaction, the interaction of a nuclear spin I with an external static magnetic field $\boldsymbol{B}$ for nuclei with spin quantum number $I \geq \frac{1}{2}$. In the presence of a magnetic field, this interaction causes the normally degenerate $2I + 1$ nuclear spin energy levels, defined by the magnetic nuclear spin quantum number $m_I = -I, -I + 1, \ldots + I$, to have different energies. The breakdown of this degeneracy enables the absorption and emission of energy in the form of electromagnetic radiation (Figure 2.2).
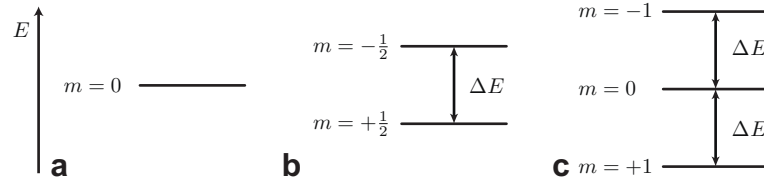
Figure 2.2: *Energy level diagram illustrating the breakdown of nuclear spin degeneracy upon the application of a magnetic field for (a) $I = 0$, (b) $I = \frac{1}{2}$ and (c) $I = 1$.*

The individual energies of the Zeeman levels are given by:

$$E_m = -m\gamma_j\hbar B \tag{2.36}$$

For nuclei with $I = \frac{1}{2}$, the energy difference between the two Zeeman levels is $\Delta E = -\gamma\hbar B = \hbar\omega_L$, where ω_L is the so-called Larmor frequency. This means that the species of nuclei can have different Larmor frequencies depending on the magnet used for NMR. For example, a proton in a 7 T magnetic field has a Larmor frequency of ≈ 300 MHz whereas in a 16.4 T magnet it has a Larmor frequency of ≈ 700 MHz.

If the external magnetic field is oriented along the z-axis, the corresponding Hamiltonian $\hat{\mathcal{H}}_Z$ is:

$$\hat{\mathcal{H}}_Z = -\gamma_j\hbar\boldsymbol{B}\hat{I}_z \tag{2.37}$$

Secular approximation

For strong external magnetic fields $\boldsymbol{B}$ the influence of the B_x and B_y components of $\boldsymbol{B}$ can be considered negligible when compared to the B_z-component. The magnetic field vector can thus be approximated to:

$$\boldsymbol{B} \approx \begin{pmatrix} 0 & 0 & B_z \end{pmatrix} = \boldsymbol{B}_0 \tag{2.38}$$

Under such conditions the Zeeman interaction exceeds all other interactions by a large degree. This allows the weaker interactions to be treated as perturbations of the Zeeman interaction in the z direction. The secular approximation leads to some

components of the internal spin interactions being masked by the strong Zeeman interaction, thus simplifying the internal interaction Hamiltonians $\hat{\mathcal{H}}_{int}$. This can be understood by considering the energy-level diagram of a spin systems. Within the secular approximation it may be possible for some near-degenerate energy levels to be considered fully degenerate, thus simplify the energy level diagram. The interaction Hamiltonian may now be divided into a *secular* and *non-secular* part, depending if their components commute with I_z or not. Only the secular Hamiltonians $\hat{\mathcal{H}}_0$ are now considered to contribute to the observable spectrum:

$$\hat{\mathcal{H}} = \hat{\mathcal{H}}_0 + \hat{\mathcal{H}}^{'} \approx \hat{\mathcal{H}}_0 \tag{2.39}$$

The secular, or high-field approximation is valid for all cases presented in this body of work. The secular Hamiltonians for the internal interactions $\hat{\mathcal{H}}_\lambda^0$ will be discussed for each interaction separately. A breakdown of the secular approximation would arise for quadrupolar nuclei $I \geq 1$ with very strong quadrupolar couplings, such that they even exceed the Zeeman interaction.

Using the spherical tensor representation, with all the terms which do not commute with $\hat{\mathcal{H}}_0$ vanishing from Equation 2.11 due to the secular approximation, the secular part of an interaction Hamiltonian simplifies to:

$$\hat{\mathcal{H}}_\lambda^0 = \mathcal{A}_{00}\hat{\mathcal{T}}_{00} + \mathcal{A}_{10}\hat{\mathcal{T}}_{10} + \mathcal{A}_{20}\hat{\mathcal{T}}_{20} \tag{2.40}$$

2.1.2 The effect of radio frequency pulses

The application of a radio frequency (RF) pulse does not merely excite the spin system, it does so in a well-defined manner. Understanding this interaction allows detailed manipulation of the spin system, and facilitates access to much more information than the chemical shift of the nuclei and their relative abundance alone. This has led to a huge number of 'pulse-sequences' being developed, and the continued interest in Fourier-transform (FT) NMR spectroscopy.

The RF coil generates a magnetic field along the *x*-axis of the laboratory reference frame. During a pulse the magnitude of the field oscillates at the Larmor frequency ω_L, and between pulses the field is equal to zero:

$$
\begin{aligned}
\boldsymbol{B}_{on}^{RF}(t) &= B_{RF} \cdot \cos(\omega_L t + \phi_p)\boldsymbol{e}_x & (2.41) \\
\boldsymbol{B}_{off}^{RF}(t) &= 0 & (2.42)
\end{aligned}
$$

where B_{RF} is the maximum amplitude of the transverse magnetic field during the pulse. It is convenient to visualise this oscillating field as two counter rotating vectors representing the resonant and non-resonant components. The resonant component rotates with the Larmor precession and the non-resonant component in the opposite direction:

$$
\boldsymbol{B}_{RF}(t) = \boldsymbol{B}_{res}^{RF}(t) + \boldsymbol{B}_{non\text{-}res}^{RF}(t) \tag{2.43}
$$

where:

$$
\begin{aligned}
\boldsymbol{B}_{res}^{RF}(t) &= -\frac{1}{2}\gamma_j B_{RF}\{\cos(\omega_L t + \phi_p)\boldsymbol{e}_x + \sin(\omega_L t + \phi_p)\boldsymbol{e}_y\} & (2.44) \\
\boldsymbol{B}_{non\text{-}res}^{RF}(t) &= -\frac{1}{2}\gamma_j B_{RF}\{\cos(\omega_L t + \phi_p)\boldsymbol{e}_x - \sin(\omega_L t + \phi_p)\boldsymbol{e}_y\} & (2.45)
\end{aligned}
$$

The non-resonant component has almost no influence on the spins, and may be neglected. The corresponding Hamiltonian for the effect of an RF pulse is therefore:

$$
\hat{\mathcal{H}}_{RF}(t) \approx -\frac{1}{2}\gamma_j B_{RF}\{\cos(\omega_L t + \phi_p)\hat{I}_x + \sin(\omega_L t + \phi_p)\hat{I}_y\} \tag{2.46}
$$

The quantity $|\frac{1}{2}\gamma_j B_{RF}|$ is proportional to the maximum RF field created by the coil. This is called the nutation frequency ω_{nut}^j and is a measure of how strong the RF field influences the spins. Typically the nutation frequency is in the range 1–200 kHz. Even under the strongest RF pulses this is still three to four orders of magnitude less than the Larmor frequency.

When describing the interaction of RF pulses on a spin system it is convenient to use the rotating frame of reference. This frame of reference can be described by a constant rotation of the laboratory frame about B_0 at the Larmor frequency.
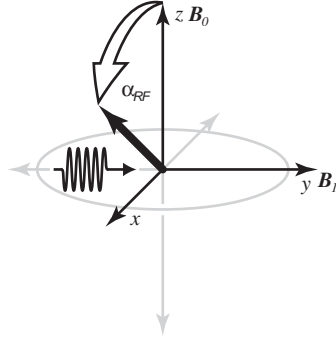
Figure 2.3: The effect of an α_y pulse on the equilibrium state $\hat{I}_z$.

When the RF field is created by the coil, an oscillating magnetic field B_{RF} is applied perpendicular to B_0. In the rotating frame the oscillating field B_{RF} appears static, thus simplifying the treatment of RF pulses. The static field B_1 associated with B_{RF} applies a torque to the magnetisation, which in the initial equilibrium state is aligned along the z-axis. The applied field causes the initial equilibrium state to turn about the axis of the applied field towards the xy plane. The effect of a pulse of the length t_{RF} is a rotation of the magnetisation by an angle α_{RF}:

$$\alpha_{RF} = -\gamma B_1 \cdot t_{RF} = \omega_1 \cdot t_{RF} \tag{2.47}$$

Consequently pulses are described by their resulting effect, i.e. a pulse applied along the y-axis resulting in a tip of the magnetisation from the z-axis into the x-axis according to the right-hand rule[†] is denoted as a $90°_y$, or $\left(\frac{\pi}{2}\right)_y$ pulse (Figure 2.3). The phase of the RF irradiation ϕ_p is directly related to the phase of the pulse, i.e. if the phase of the RF irradiation was shifted by $\frac{\pi}{2}$ it would result in a $90°_{-x}$ or $\left(\frac{\pi}{2}\right)_{-x}$ pulse, placing the magnetisation along the y-axis.

Product operator formalism

More generally the effect of a radio frequency pulse on the spin system is calculated via the density matrix formalism, with the Hamiltonian operator of a pulse on the y-axis given by $\hat{\mathcal{H}} \propto \alpha_{RF}\hat{I}_y$. Substitution of this into Equation 2.29 gives the time evolution of the equilibrium density matrix during a α_y pulse:

$$\hat{\rho}(t) \propto \exp\{-i\alpha_{RF}\hat{I}_y\}\,\hat{I}_z\,\exp\{i\alpha_{RF}\hat{I}_y\} \tag{2.48}$$

To simplify determining the outcome of a pulse on a system the *product operator formalism* was introduced by Ernst and co-workers [Sørensen 83], and is based on the fact that propagators of the general form $\hat{U}(t)\,\hat{\rho}(0)\,\hat{U}^{-1}(t)$ describe rotations in spin space. Within the product operator formalism the effect on the equilibrium magnetisation $\hat{I}_z$ during an α_y pulse simplifies to:

$$\hat{I}_z \xrightarrow{\ \ \alpha\hat{I}_y\ \ } \hat{I}_z\cos\alpha + \hat{I}_x\sin\alpha \tag{2.49}$$

[†]Whether the pulse applies a clockwise or anticlockwise torque is arbitrary, however once chosen the convention must be retained throughout a description of an NMR experiment.

with the common rotations listed in Table 2.1. The product operator formalism is not only restricted to the description of RF-pulses, but can describe the time evolutions of most NMR interactions provided the corresponding Hamiltonian is time independent or time averaged.

Table 2.1: The effect of propagators by the product operator formalism.

	$\alpha \hat{I}_x$	$\alpha \hat{I}_y$	$\alpha \hat{I}_z$
$\hat{I}_x$	$\hat{I}_x$	$\hat{I}_x \cos\alpha - \hat{I}_z \sin\alpha$	$\hat{I}_x \cos\alpha + \hat{I}_y \sin\alpha$
$\hat{I}_y$	$\hat{I}_y \cos\alpha + \hat{I}_z \sin\alpha$	$\hat{I}_y$	$\hat{I}_y \cos\alpha - \hat{I}_x \sin\alpha$
$\hat{I}_z$	$\hat{I}_z \cos\alpha - \hat{I}_y \sin\alpha$	$\hat{I}_z \cos\alpha + \hat{I}_x \sin\alpha$	$\hat{I}_z$

2.1.3 Quadrupolar coupling

Nuclei with a spin $I \geq 1$ exhibit a nuclear electric quadrupole moment which interacts with the local electric field gradient of the molecule. It is quite extraordinary that all nuclei with $I < 1$, no matter how many nucleons are present, do not interact with the electric field and can be treated as a single point charge. The Hamiltonian for the quadrupolar coupling is given by:

$$\mathcal{H}_Q = \hat{I}_i \cdot \underline{Q} \cdot \hat{I}_i \tag{2.50}$$

where $\underline{Q}$ is the quadrupolar interaction tensor defined as:

$$\underline{Q} = \frac{e \cdot Q}{2I(2I-1)\hbar} \cdot \underline{V} \tag{2.51}$$

where $\underline{V}$ is the local electric field gradient tensor. For deuterons ($I = 1$) the quadrupolar splitting is about 125 kHz, which is sufficiently lower than the Larmor frequency such that the secular approximation remains valid. The NMR spectra of deuterons are however dominated by the quadrupolar interaction. If the polar orientation of the $\boldsymbol{B}_0$-field is given by θ and ϕ, with respect to the quadrupolar coupling tensor principal axis system (PAS) the quadrupolar frequency is given by:

$$\omega_Q = \pm \frac{\delta_Q}{2} \left(3\cos^2\theta - 1 - \eta_Q \sin^2\theta \cos 2\phi \right) \tag{2.52}$$

−δ   −δ/2   0   δ/2   +δ
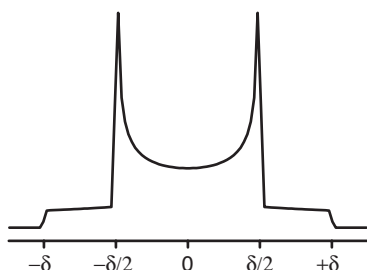
Figure 2.4: *Pake powder pattern.*

where δ_Q and η_Q are the quadrupolar anisotropy and asymmetry parameters respectively. The orientation dependence of the quadrupolar coupling with the second Legendre polynomial, $P_2(\theta)$, leads to the well-known Pake-pattern in the solid state [Pake 48]. Due to an isotropic distribution of nuclei amongst all possible orientations this is also known as a powder average of the quadrupolar coupling, resulting in a powder pattern (Figure 2.4). Molecular motion leads to a characteristic narrowing of the powder pattern yielding information on the geometry and timescale of the process.

2.1.4   Chemical shift

The chemical shift is the most important internal interaction in NMR since it is sensitive to the chemical enviroment. This has led to NMR becoming one of the most important, if not the most important structure elucidation techniques available to mankind today. The chemical shift is caused by the electrons surrounding nuclei shielding them from the external magnetic field B_0. Thus the nuclei experience an effective magnetic field;

$$B_{eff} = B_0 - \left(\underline{\sigma} \cdot B_0 \right) \tag{2.53}$$

The electron density around a particular nucleus not only depends on the nuclei involved in bonding, but also the type and geometry of bonding. Thus the chemical shift is highly sensitive to the chemical environment. Due to the sensitivity towards geometry, the chemical shielding is generally anisotropic in nature and is best described by the chemical shielding tensor $\underline{\sigma}$ such that:

$$\mathcal{H}_{CS} = \gamma \hat{I} \cdot \underline{\sigma} \cdot B_0 \tag{2.54}$$

Under the secular approximation of the chemical shift Hamiltonian reduces to:

$$\mathcal{H}_{CS}^0 = \gamma \left(\hat{I}_x \sigma_{xz}^{\mathsf{LAB}} + \hat{I}_y \sigma_{yz}^{\mathsf{LAB}} + \hat{I}_z \sigma_{zz}^{\mathsf{LAB}} \right) B_0 \tag{2.55}$$

The chemical shielding tensor $\underline{\sigma}$ can be decomposed into isotropic, symmetric and anti-symmetric parts according to Equation 2.8:

$$\underline{\sigma} = \sigma_{iso} + \boldsymbol{\sigma}_{sym} + \boldsymbol{\sigma}_{asym} \tag{2.56}$$

The anti-symmetric part $\boldsymbol{\sigma}_{asym}$ of the chemical shielding tensor can however be neglected within the secular approximation and will not be further discussed.

Isotropic chemical shift

The isotropic part σ_{iso} is orientation independent and provides information regarding the magnitude of the interaction. In an isotropic liquid the motionally averaged chemical shift Hamiltonian is purely dependent on this part, such that:

$$\mathcal{H}_{CS}^{iso} = -\gamma \hat{I}_z \cdot \sigma_{iso} \cdot B_0 \tag{2.57}$$

where σ_{iso} is the average of σ_{zz} over all possible molecular orientations:

$$\sigma_{iso} = N^{-1} \int \sigma_{zz}(\Theta) \, d\Theta \tag{2.58}$$

The isotropic chemical shift σ_{iso} is equal to one third the trace of the chemical shielding tensor and related to the diagonal spatial Cartesian matrix elements:

$$\sigma_{iso} = \frac{1}{3} \text{Tr}\{\underline{\sigma}\} = \frac{1}{3}\left(\sigma_{xx} + \sigma_{yy} + \sigma_{zz}\right) \tag{2.59}$$

Although the individual elements σ_{xx}, σ_{yy} and σ_{zz} are dependent on molecular orientation, their sum is not.

Chemical shift anisotropy

When diagonalised, the symmetric part of the chemical shift Hamiltonian $\boldsymbol{\sigma}_{sym}$ provides information regarding the anisotropy of the shielding. This is because the placing of all elements onto the diagonal is equivalent to a transformation into the principal axis system. In the principal axis system $\underline{\sigma}$ has the following form:

$$\underline{\sigma} = \sigma_{iso} + \delta_{CS} \begin{pmatrix} -\frac{1}{2} + \frac{\eta_{CS}}{2} & 0 & 0 \\ 0 & -\frac{1}{2} - \frac{\eta_{CS}}{2} & 0 \\ 0 & 0 & 1 \end{pmatrix} \tag{2.60}$$

where δ_{CS} is the so-called anisotropy parameter:

$$\delta_{CS} = \omega_L(\sigma_{zz}^{\text{PAS}} - \sigma_{iso}) \tag{2.61}$$

and η_{CS} is the so-called asymmetry parameter

$$\eta_{CS} = \frac{\sigma_{yy}^{\text{PAS}} - \sigma_{xx}^{\text{PAS}}}{\sigma_{zz}^{\text{PAS}} - \sigma_{iso}} \tag{2.62}$$

The symmetric part of the chemical shielding tensor $\boldsymbol{\sigma}_{sym}$ is commonly referred to as chemical shift anisotropy (CSA). In gases, liquids and solutions where fast isotropic motion readily occurs, the CSA is averaged to zero leaving only the isotropic chemical shift (Equation 2.57). However, in solids where isotropic motion is not normally present, the orientation dependence of the CSA leads to significantly broader line shapes. If θ and ϕ are the polar orientation of the B_0-field in the principal axis system of the chemical shielding tensor, the anisotropic frequency (in analogy to Equation 2.52) is given by:

$$\omega_{CS} = \frac{\delta_{CS}}{2}\left(3\cos^2\theta - 1 - \eta_{CS}\sin^2\theta\cos 2\phi\right) \tag{2.63}$$

The theoretical powder line shape has been calculated in general [Bloembergen 53] and can be found in most solid-state NMR textbooks [Mehring 83, Schmidt-Rohr 94]. For an isotropic distribution of orientations, i.e. a powder average, characteristic powder pattern spectra for different η_{CS} are seen (Figure 2.5).
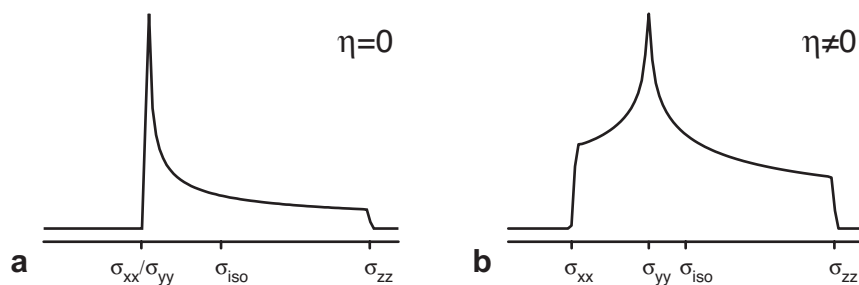
Figure 2.5: *Theoretical line shapes for (a) symmetric and (b) asymmetric CSA tensors.*

The principal values of the CSA tensor can be identified from spectra as the points of discontinuity and are assigned using the Spiess convention [Spiess 78]:

$$|\sigma_{11}| \quad \geq \quad |\sigma_{22}| \quad \geq \quad |\sigma_{33}| \tag{2.64}$$

where:

$$
\begin{aligned}
|\sigma_{11}| &= |\sigma_{xx}^{\text{PAS}} - \sigma_{iso}| \\
|\sigma_{22}| &= |\sigma_{yy}^{\text{PAS}} - \sigma_{iso}| \\
|\sigma_{33}| &= |\sigma_{zz}^{\text{PAS}} - \sigma_{iso}|
\end{aligned}
\tag{2.65}
$$

The advantage of using the Spiess convention is that $0 \leq \eta_{CS} \leq 1$, and $\eta_{CS} = 0$ for a uniaxial tensor.

Chemically shifted Larmor frequency

The chemical shift is not directly measured, with only the effect on the Larmor frequency detected. It is thus convenient to combine the Zeeman and chemical shift interactions:

$$\hat{\mathcal{H}}_Z + \hat{\mathcal{H}}_{CS} = \hat{\mathcal{H}}_{Z+CS} = \delta \hat{I}_z \tag{2.66}$$

where δ is the chemically shifted Larmor frequency, and is related to the chemical shift by:

$$\delta = -\gamma B_0 \cdot (1 + \sigma) \tag{2.67}$$

As these formulae neglect susceptibility effects the origin of the δ-scale must be calibrated via a reference compound of known chemical shift. The unit of measure for the δ-scale is parts-per-million of the corresponding Larmor frequency (ppm). The use of this unit thus allows comparison of spectra taken using the same nuclei under different external magnetic fields to be easily compared.

Influences on chemical shift

The presence of low-lying electronic excited states strongly influences the chemical shift. With more such states present for heavier atoms larger chemical shift ranges are seen for such heavier isotopes. The chemical shift range for ^{1}H is only around 10 ppm, while for ^{13}C it is around 200 ppm.

The chemical shift also correlates strongly with the electronegativity of neighbouring groups, such as O, Cl, and F. These tend to withdraw electron density, increasing the field experienced by the neighbouring nuclei resulting in an increased δ value. This is of particular interest for N··H-O and O··H-O hydrogen bonds, where the ^{1}H chemical shift is influenced by the presence of two electronegative neighbouring sites. The degree to which this increases δ is approximately proportional to the hydrogen bond length N··H/O··H. This leads to relatively high proton chemical shifts of between 6–13 ppm and are thus an important handle on hydrogen bonding in the solid-state.
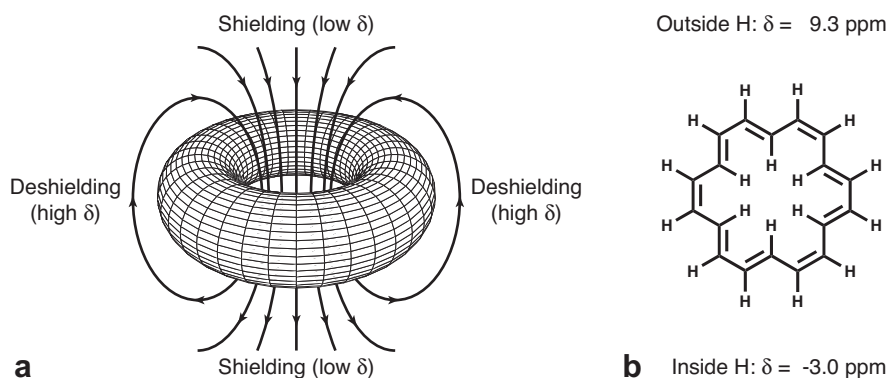
Figure 2.6: *(a) The induced electron currents in aromatic systems lead to shielding and deshielding regions. (b) The shielded (inside) and deshielded (outside) protons of [18]annulene, with their corresponding chemical shifts.*

The chemical shift is highly influenced by molecular units with strong magnetic susceptibilities, such as π-systems, which can readily support induced electron currents. In molecules with well-defined three-dimensional structure, such ring-currents can strongly affect the chemical shift, even if there is no direct chemical link. If nuclei are close to the axis of symmetry of an aromatic ring, the local fields are decreased resulting in a lower δ than expected (Figure 2.6). However, if nuclei are close to the plane of the aromatic ring, the local fields are increased resulting in a higher δ than expected. Information about the secondary structure of a molecule can thus be provide due to the through-space nature of this interaction.

If fast molecular motion occurs with respect to the NMR timescale the observed chemical shift is an average value. This can be misleading, as at no point does any chemical species exist with this actual chemical shift value. A special case of chemical shift occurs in metals due to the presence of delocalised electrons. This so-called Knight shift is dependent on the crystallographic environment of the metal nuclei and can be up to three orders of magnitude greater than the typical chemical shift.

Ab-initio chemical shift calculation

After calculation of the optimum geometry of a system by ab-initio methods the electronic structure is known. With the chemical-shift highly dependent on the electronic environment, ab-initio electronic structure methods can also be used to calculate NMR properties. Technically this is undertaken by calculation of the electronic current density after a perturbing field is applied. In practice, the components of the induced field in the x, y and z directions are each calculated for separate perturbations along x, y and z. From the electronic current density the chemical shielding tensor of a given nucleus can be calculated. By limiting chemical-shift calculation to protons problems associated with the core electrons are negated.

A more general approach are nucleus independent chemical shift (NICS) maps; a generalisation of the atom specific chemical shift calculated at every point in space [Schleyer 96]. When no explicit probe atom is defined only the quantitative degree of shielding and deshielding is shown. Calculation of the NICS map for an aromatic ring shows how the chemical shift is strongly affected by both distance and orientation (Figures 2.7, 2.8 and 2.9) [Sebastiani 04a].
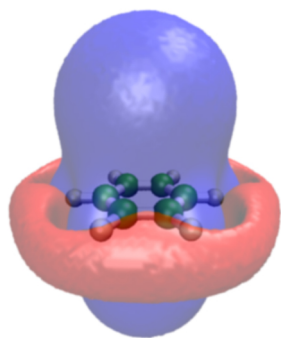
Figure 2.7: *The $\Delta\delta_H$ = 0.3 (blue) and −0.3 (red) isosurfaces of the NICS map of benzene.*
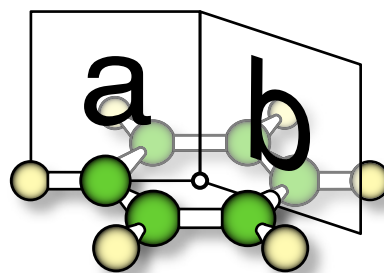
Figure 2.8: *The planes through the NICS map of benzene illustrated in Figure 2.9.*
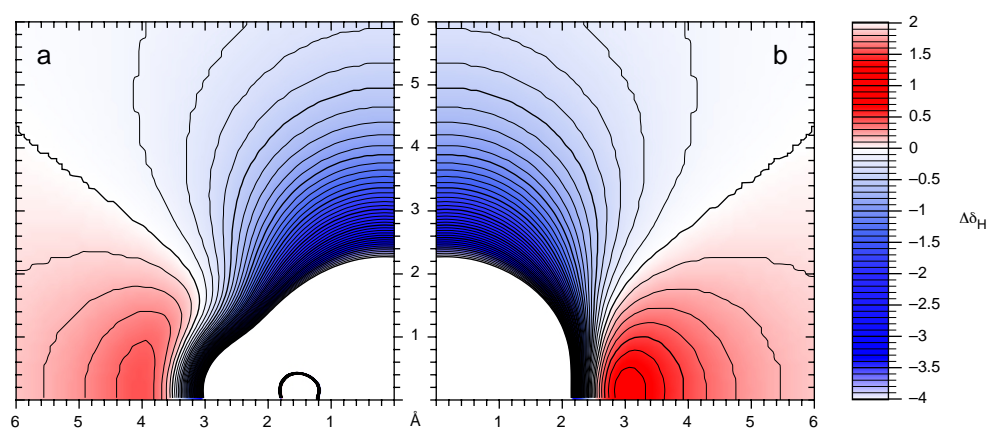
Figure 2.9: *The NICS map of benzene illustrating the shielding (blue) and deshielding (red) regions. Planes through the NICS map are aligned (a) with and (b) between the C–H bonds (Figure 2.8).*

2.1.5 Dipole-dipole coupling

The dipole-dipole interaction involves the interaction of a spin $\hat{I}_j$ with the local magnetic field generated by another spin $\hat{I}_k$. The interaction is mutual, with spin $\hat{I}_k$ also interacting with the magnetic field generated by spin $\hat{I}_j$. Thus, spin-coupling occurs. This interaction propagates through the intervening space between nuclei without the involvement of electrons. Thus the full title for the interaction is the direct through-space dipole-dipole interaction, or more concisely the dipolar coupling.

The full form of the spin Hamiltonian for dipole-dipole interaction between spins $\hat{I}_j$ and $\hat{I}_k$ is given by:

$$\mathcal{H}^{jk}_{D,full} = D_{jk}\left(3(\hat{I}_j \cdot e_{jk})(\hat{I}_k \cdot e_{jk}) - \hat{I}_j \cdot \hat{I}_k\right) \tag{2.68}$$

where e_{jk} is a unit vector parallel to the internuclear vector, such that $e_{kj} \cdot e_{jk} = 1$. The magnitude of the interaction is given by the dipolar coupling constant D_{jk}:

$$D_{jk} = -\frac{\mu_0}{4\pi}\frac{\gamma_j\gamma_k\hbar}{r_{jk}^3} \tag{2.69}$$

where γ_j and γ_k are the gyromagnetic ratios of the two spins and r_{jk} the distance between the spins.[†] The interaction also scales linearly with the gyromagnetic ratio of each spin, thus for the same internuclear distance and $\gamma_I > \gamma_S$: $D_{II} > D_{IS} > D_{SS}$. For example, for two spins with $r_{jk} = 1$ Å : $D_{HH} = 120.1$ kHz, $D_{CH} = 30.2$ kHz and $D_{CC} = 7.6$ kHz. With such large proton homonuclear dipolar coupling seen one would expect the ^{1}H spectrum to be dominated by the dipolar coupling, and this is true in the solid state. In liquids and gases however the rapid molecular motion present averages the dipolar coupling to its isotropic value of zero. Due to the dependence of D_{jk} on only known physical constants and the inverse cube of the internuclear distance (r_{jk}^{-3}) the dipolar coupling is very useful for structure elucidation. Quantification of the dipolar coupling constant allows direct spectroscopic access to the distance between nuclei, and hence the geometrical form of the molecule. This is of particular interest for distance measurements in non-crystalline solids or other systems where techniques such as X-ray scattering cannot readily be used.

Although the dipolar coupling constant D_{jk} is not orientation dependent the dipolar Hamiltonian $\mathcal{H}_D$ is, due to the internuclear vector term e_{jk} (Equation 2.68). The nature of this orientation dependence is clearly seen when the secular approximation is applied to the dipolar interaction.

[†]The dipolar coupling constant in Equation 2.69 is defined in radians-per-second, however, its magnitude is more commonly expressed in Hertz, i.e. $2\pi \cdot D_{jk}[rad \cdot s^{-1}] = D_{jk}[Hz]$. For simplicity the conversion factor of 2π is omitted when the unit of D_{jk} is explicitly given.

Secular dipole-dipole coupling

In a sample containing many spins, each pair of spins has a dipolar coupling, leading to the overall dipolar Hamiltonian being given by:

$$\mathcal{H}_{D,full}^0 = \sum_k \sum_j^{k-1} \mathcal{H}_{D,full}^{jk} = \sum_{j<k} \mathcal{H}_{D,full}^{jk} \tag{2.70}$$

For homonuclear dipolar coupling the secular part of the dipolar spin Hamiltonian is given by:

$$\hat{\mathcal{H}}_D^{jk} = d_{jk}\left(3\hat{I}_z^j\hat{I}_z^k - \hat{\boldsymbol{I}}_j \cdot \hat{\boldsymbol{I}}_k\right) \tag{2.71}$$

For heteronuclear dipolar coupling the secular part of the dipolar Hamiltonian simplifies to:

$$\hat{\mathcal{H}}_D^{jk} = d_{jk}\left(2\hat{I}_z^j\hat{I}_z^k\right) \tag{2.72}$$

Both the homonuclear (Equation 2.71) and heteronuclear (Equation 2.72) dipolar coupling Hamiltonians contain the secular dipolar coupling constant d_{jk}. The full dipolar coupling constant D_{jk} is only dependent on the distance between the spins, and not orientation. The secular dipolar coupling constant d_{jk} however depends on both the distance and the orientation. The secular dipolar coupling constant d_{jk} is related to the full dipolar coupling constant D_{jk} in the following way:

$$d_{jk} = D_{jk} \cdot \frac{1}{2}\left(3\cos^2\theta_{jk} - 1\right) \tag{2.73}$$

where θ_{jk} is the angle between the internuclear vector and the external magnetic field such that $\cos\theta_{jk} = \boldsymbol{e}_{jk} \cdot \boldsymbol{e}_z$. There are two important points to note about Equation 2.73; firstly d_{jk} has opposite signs for spin pairs aligned with the field ($\theta_{jk} = 0$) as compared to spin pairs oriented perpendicular to the field ($\theta_{jk} = \pi/2$). Secondly, d_{jk} is equal to zero when $\theta_{jk} = 54.74°$ ($\arctan\sqrt{2}$) satisfying the equation:[†]

$$3\cos^2\theta_{jk} - 1 = 0 \tag{2.74}$$

These two observations have important repercussions as they allow the dipolar interaction to be averaged by physical manipulation of the sample with respect to the field. This angle where $d_{jk} = 0$ is known as the *magic-angle* θ_M. Due to the dependence on the second Legendre polynomial, a Pake pattern is observed for an isolated dipolar coupled spin pair. Practically however the observation of such fully isolated spin pairs is rare and homogeneous broadening from multiple coupling interactions is much more common.

[†] there is also a solution to Equation 2.74 at $\theta_{jk} = \pi - \theta_M \approx 125.26°$

Dipolar coupling in isotropic liquids

As previously mentioned, in an isotropic liquid the secular part of the intramolecular dipolar coupling averages to zero. This can be shown by integrating Equation 2.74 weighted by $\sin\theta_{jk}$.

$$\int_0^\pi \sin\theta_{jk} \left(3\cos^2\theta_{jk} - 1\right) \, \mathrm{d}\theta_{jk} = 0 \tag{2.75}$$

The $\sin\theta_{jk}$ term gives all orientations equal probability, as more states are possible when the internuclear vector is perpendicular to the field ($\theta_{jk} = \pi/2$) than parallel ($\theta_{jk} = 0$ and π). Although the secular dipolar couplings essentially vanish in isotropic liquids, it is still possible to exploit the non-secular dipolar couplings as these affect the relaxation behaviour of the spin system (Equation 2.5). Such non-secular dipolar couplings are responsible for the cross-relaxation between spin-pairs resulting in the nuclear Overhauser enhancement (NOE) [Solomon 55, Ernst 87].

Spherical tensor representation

In the bilinear product representation the dipolar interaction is given by:

$$\mathcal{H}_D^{jk} = \hat{I}_j \cdot \underline{D} \cdot \hat{I}_k \tag{2.76}$$

The dipolar coupling tensor $\underline{D}$ is traceless and symmetric:

$$\underline{D}_{jk}^{\mathsf{PAS}} = -2D_{jk} \begin{pmatrix} -\frac{1}{2} & 0 & 0 \\ 0 & -\frac{1}{2} & 0 \\ 0 & 0 & 1 \end{pmatrix} \tag{2.77}$$

where D_{jk} is the full dipolar coupling constant (Equation 2.69). By assigning a dipolar asymmetry parameter δ_D, similar to that of the quadrupolar and chemical shift interactions, such that:

$$D_{jk} = -\frac{1}{2}\delta_D \tag{2.78}$$

we can derive the only non-vanishing spherical tensor element:

$$\mathcal{A}_{20} = -\sqrt{6}\,D_{jk} \tag{2.79}$$

By expanding Equation 2.76 and sorting the various products of spin operators, one arrives at the famous 'dipolar alphabet' [Abragam 61]. In the secular approximation, several terms again average to zero, and one is left with the dipolar Hamiltonian:

$$\mathcal{H}_D = \mathcal{A}_{20}\hat{\mathcal{T}}_{20} \tag{2.80}$$

2.2 Magic-angle spinning (MAS)

Irradiation by RF-pulses is not the only method by which spin interactions can be manipulated, as such pulses only influence the spin part $\hat{\mathcal{T}}_{kq}$ of an interaction Hamiltonian. The space part $\mathcal{A}_{kq}$ of an interaction Hamiltonian can thus also be used to manipulate the spin interactions. In practice this is achieved by mechanically rotating the sample about an axis inclined at an angle θ to the external magnetic field B_0. With the anisotropic parts of the spin interactions dependent on the second Legendre polynomial $P_2(\theta) = \frac{1}{2}(3\cos^2\theta - 1)$, and represented by second rank tensors, the anisotropic parts can be averaged if $\theta = 54.7°$ such that $P_2(\theta) = 0$. With this being the magic-angle θ_M the overall technique is known as *magic-angle spinning* (MAS) [Andrew 58, Lowe 59]. As the anisotropic interactions cause severe line broadening the application of MAS significantly narrows the lines and leads to only isotropic interactions being seen. However, complete averaging of an anisotropic interaction to zero is only achieved when the sample is spun with a rotational frequency much greater than the characteristic frequency of the interaction, i.e. $\omega_r \gg \omega_\lambda$. For this reason considerable effort has been taken to achieve the highest possible MAS frequency. Currently, commercially available MAS hardware is capable of spinning at 35 kHz [Bruker 97] utilising 2.5 mm outer diameter zirconia sample containers, or *rotors*. However, with specialised custom-built probeheads spinning speeds of up to 70 kHz are achievable with slightly smaller rotors [Samoson 03].
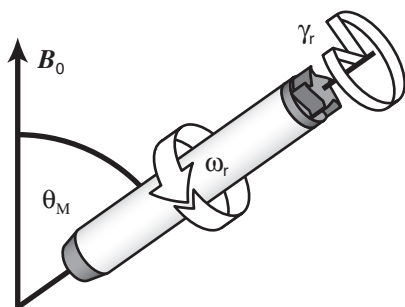
Figure 2.10: *Magic-angle spinning.*

A theoretical description of MAS is most conveniently carried out in the irreducible tensor representation (Section 2.1). As previously described for the static case the *secular* part of a second rank tensor interaction is given by Equation 2.10. For dipolar coupling, chemical shift anisotropy and quadrupolar coupling $\mathcal{A}_{10}\hat{\mathcal{T}}_{10} = 0$ and thus Equation 2.11 simplifies to:

$$\mathcal{H}_\lambda = \mathcal{A}_{00}\hat{\mathcal{T}}_{00} + \mathcal{A}_{20}\hat{\mathcal{T}}_{20} \qquad (2.81)$$

Magic-angle spinning introduces a time-dependence of the space part $\mathcal{A}_{kq}$ of the interaction Hamiltonian. Since $\mathcal{H}$ is now time-dependent, $\mathcal{H}(t)$, Equation 2.29 is no longer a solution of the Liouville-von-Neumann equation (Equation 2.26). However, as long as $\mathcal{H}(t)$ does not contain non-commuting contributions at any given time, the problem can be solved by average Hamiltonian theory (AHT). Average Hamiltonian theory states that if the problem is cyclic an average time-independent Hamiltonian can be calculated for one cycle.

With MAS inherently a cyclic problem, with the cycle-time t_c equal to the rotor period τ_r, only the average Hamiltonian $\hat{\bar{\mathcal{H}}}$ for a single rotor period needs to be calculated:

$$\hat{U}(t_c) = e^{-i\mathcal{H}_n\tau_n}\ldots e^{-i\mathcal{H}_2\tau_2}e^{-i\mathcal{H}_1\tau_1} = e^{-i\hat{\bar{\mathcal{H}}}\tau_r} \tag{2.82}$$

Since the average Hamiltonian $\hat{\bar{\mathcal{H}}}$ is time-independent, it commutes with itself at arbitrary times, $[\hat{\bar{\mathcal{H}}}(t_1), \hat{\bar{\mathcal{H}}}(t_2)] = 0$, and hence the propagator for N rotor periods can be written as:

$$\hat{U}(N\tau_r) = \exp(-i\hat{\bar{\mathcal{H}}}N\tau_r) \tag{2.83}$$

Unfortunately, $\hat{\bar{\mathcal{H}}}$ cannot simply be calculated as the sum $\sum \mathcal{H}_i\tau_i/\tau_r$ because generally $[\mathcal{H}_i, \mathcal{H}_j] \neq 0$. For MAS it is advantageous to expand the propagators with two non-commuting Hamiltonians according to the Baker-Campbell-Hausdorff relationship:

$$e^{\hat{B}}e^{\hat{A}} = \exp\left(\hat{B} + \hat{A} + \frac{1}{2}[\hat{A}, \hat{B}] + \frac{1}{12}\left([\hat{B}, [\hat{B}, \hat{A}]] + [[\hat{B}, \hat{A}], \hat{A}]\right) + \ldots\right) \tag{2.84}$$

The resulting average Hamiltonian is most clearly written as the sum of different orders, where the order i indicates the overall power of τ_r and the number of nested commutators involved:

$$\hat{\bar{\mathcal{H}}} = \hat{\bar{\mathcal{H}}}^{(0)} + \hat{\bar{\mathcal{H}}}^{(1)} + \hat{\bar{\mathcal{H}}}^{(2)} + \ldots + \hat{\bar{\mathcal{H}}}^{(i)} \tag{2.85}$$

The zeroth-order average Hamiltonian now reads:

$$\hat{\bar{\mathcal{H}}}^{(0)} = \frac{1}{\tau_r}\sum_{i=1}^{n}\mathcal{H}_i\tau_i \tag{2.86}$$

With $\mathcal{H}_i$ not being constant during the time-interval τ_i, the problem can only be treated at the limit of $\tau_i \to 0$ and $n \to \infty$. By doing so Equation 2.82 can be used to calculate the zeroth-order average Hamiltonian because the commutators $[\mathcal{H}(t), \mathcal{H}(t + \Delta t)]$ vanish for infinitely small time steps. Thus, in the limit $\Delta t \to 0$ the full average Hamiltonian can be written as a sum of integrals or Magnus expansion. The first three terms of which are:

$$\hat{\bar{\mathcal{H}}}^{(0)} = \frac{1}{\tau_r}\int_0^{\tau_r}dt\,\mathcal{H}(t) \tag{2.87}$$

$$\hat{\bar{\mathcal{H}}}^{(1)} = -\frac{i}{2\tau_r}\int_0^{\tau_r}dt_1\int_0^{t_1}dt_2\,[\mathcal{H}(t_1), \mathcal{H}(t_2)], \tag{2.88}$$

$$\hat{\bar{\mathcal{H}}}^{(2)} = -\frac{1}{6\tau_r}\int_0^{\tau_r}dt_1\int_0^{t_1}dt_2\int_0^{t_2}dt_3\left([\mathcal{H}(t_1), [\mathcal{H}(t_2), \mathcal{H}(t_3)]] + \right.$$
$$\left. [\mathcal{H}(t_3), [\mathcal{H}(t_2), \mathcal{H}(t_1)]]\right) \tag{2.89}$$

Interactions for which the commutator $[\hat{\mathcal{H}}(t_1), \hat{\mathcal{H}}(t_2)]$ vanishes may specifically be termed *inhomogeneous* [Maricq 79]. The dipole-dipole coupling of an isolated spin pair, chemical-shift anisotropy and quadrupolar coupling are all inhomogeneous interactions. For these interactions the higher-order terms in the Magnus expansion vanish leaving only the zeroth-order average Hamiltonian to describing the evolution under a given interaction λ and MAS at an arbitrary time:

$$\hat{\bar{\mathcal{H}}}_\lambda^{(0)} = \frac{1}{t}\int_0^t \hat{\mathcal{H}}_\lambda(t)\,\mathrm{d}t = \hat{\mathcal{T}}_{00}\mathcal{A}_{00}^{\mathsf{LAB}} + \hat{\mathcal{T}}_{20}\frac{1}{t}\int_0^t \mathcal{A}_{20}^{\mathsf{LAB}}(\omega_r t)\,\mathrm{d}t \tag{2.90}$$

The explicit calculation of the average Hamiltonian according to Equation 2.90 requires the knowledge of the space part of the interaction in the laboratory frame, $\mathcal{A}_{20}^{\mathsf{LAB}}$. However, with the interaction tensor defined in the principal axis system (PAS), transformation from this frame of reference to the laboratory frame (LAB) is necessary. This involves three Euler angle transformations; first from the PAS to the molecular frame (MOL), second from the molecular frame to the rotor frame (ROT) and finally from the rotor frame to the laboratory frame:

$$\begin{array}{ccccccc}
 & \alpha_{\mathsf{PM}}, \beta_{\mathsf{PM}}, \gamma_{\mathsf{PM}} & & \alpha_{\mathsf{MR}}, \beta_{\mathsf{MR}}, \gamma_{\mathsf{MR}} & & \omega_r t, \beta_{\mathsf{M}}, 0 & \\
\mathsf{PAS} & \Longrightarrow & \mathsf{MOL} & \Longrightarrow & \mathsf{ROT} & \Longrightarrow & \mathsf{LAB} \\
 & \textit{tensor orientation} & & \textit{powder average} & & \textit{MAS} &
\end{array}$$

The time dependence is only seen in the last transformation, where the Euler angle $\alpha_{RL} = \omega_r t$ is the angular position of the rotor, or rotor phase, which varies with time. Such rotational transformations can be handled with relative ease by the irreducible tensor representation, with the transformed tensor given by a linear combination of components with the same rank L:

$$A_{Lm}^Y = \sum_{m'=-L}^{L} A_{Lm'}^X \, \mathcal{D}_{m'm}^{(L)}(\Omega) \tag{2.91}$$

where $\mathcal{D}_{m'm}^{(L)}(\Omega)$ are elements of the Wigner rotation matrices:

$$\mathcal{D}_{m'm}^{(L)}(\alpha, \beta, \gamma) = d_{m'm}^{(L)}(\beta)\, e^{-im'\alpha}\, e^{-im\gamma} \tag{2.92}$$

with $d_{m'm}^{(L)}(\beta)$ being the reduced matrix elements (Appendix A). For the three subsequent rotations:

$$\begin{aligned}
\mathcal{A}_{20}^{\lambda,\mathsf{LAB}}(t) &= \sum_{m=-2}^{2} \mathcal{A}_{2-m}^{\lambda,\mathsf{ROT}} \times e^{im\omega_r t}\, d_{-m0}^{(2)}(\beta_{\mathsf{M}}) \tag{2.93} \\[2mm]
&= \sum_{m=-2}^{2} \left[\sum_{m'=-2}^{2} \mathcal{A}_{2-m'}^{\lambda,\mathsf{MOL}}\, \mathcal{D}_{-m'-m}^{(2)}(\Omega_{\mathsf{MR}}) \right] \times e^{im\omega_r t}\, d_{-m0}^{(2)}(\beta_{\mathsf{M}}) \tag{2.94} \\[2mm]
&= \sum_{m=-2}^{2} \left[\sum_{m'=-2}^{2} \left[\sum_{m''=-2}^{2} \mathcal{A}_{2-m''}^{\lambda,\mathsf{PAS}}\, \mathcal{D}_{-m''-m'}^{(2)}(\Omega_{\mathsf{PM}}) \right] \mathcal{D}_{-m'-m}^{(2)}(\Omega_{MR}) \right] \\
&\quad \times e^{im\omega_r t}\, d_{-m0}^{(2)}(\beta_{\mathsf{M}}) \tag{2.95}
\end{aligned}$$

Only if more than one interaction is to be considered does the full treatment of all three transformations become necessary, otherwise direct transformation from PAS $\Rightarrow$ ROT and then to LAB is sufficient. By doing so $\mathcal{A}_{20}^{\text{LAB}}(t)$ can be obtained from Equation 2.95 by setting $\mathcal{A}_{20}^{\lambda,\text{MOL}} = \mathcal{A}_{20}^{\lambda,\text{PAS}}$. Inserting the expression obtained for $\mathcal{A}_{20}^{\lambda,\text{LAB}}(t)$ into Equation 2.90 and integrating yields a general expression for the complete averaged interaction Hamiltonian for the interaction λ under MAS:

$$\hat{\bar{\mathcal{H}}}_{MAS}^{\lambda} = \hat{\mathfrak{T}}_{00}\mathcal{A}_{00}^{\lambda,\text{LAB}} + \hat{\mathfrak{T}}_{20} \cdot \frac{1}{t} \cdot \int_0^t \mathcal{A}_{20}^{\text{LAB}}(\omega_r t)\, \mathrm{d}t \tag{2.96}$$

$$= \hat{\mathfrak{T}}_{00}\mathcal{A}_{00}^{\lambda,\text{LAB}} + \hat{\mathfrak{T}}_{20} \cdot \frac{1}{t} \cdot \sqrt{\frac{3}{2}} \cdot \Phi_\lambda \tag{2.97}$$

For the dipole-dipole and quadrupolar interactions the first term is zero since $\mathcal{A}_{00}^{Q,\text{LAB}} = \mathcal{A}_{00}^{D,\text{LAB}} = 0$. The term Φ_λ in Equation 2.97 is known as the integrated phase and is given by:

$$\Phi_\lambda(t) = \frac{C_1}{\omega_r}\Big\{ \sin(\gamma + \omega_r t) - \sin\gamma \Big\} + \frac{C_2}{2\omega_r}\Big\{ \sin(2\gamma + 2\omega_r t) - \sin 2\gamma \Big\} \tag{2.98}$$
$$-\frac{S_1}{\omega_r}\Big\{ \cos(\gamma + \omega_r t) - \cos\gamma \Big\} - \frac{S_2}{2\omega_r}\Big\{ \cos(2\gamma + 2\omega_r t) - \cos 2\gamma \Big\}$$

where:

$$C_1 = -\frac{\delta_\lambda}{\sqrt{2}} \sin 2\beta (1 + \frac{\eta_\lambda}{3}\cos 2\alpha) \tag{2.99}$$

$$C_2 = \frac{\delta_\lambda}{2}\sin^2\beta \frac{\delta_\lambda \eta_\lambda}{6}(1 + \cos^2\beta)\cos 2\alpha \tag{2.100}$$

$$S_1 = \frac{\sqrt{2}\delta_\lambda \eta_\lambda}{3}\sin\beta \sin 2\alpha \tag{2.101}$$

$$S_2 = \frac{\delta_\lambda \eta_\lambda}{3}\cos\beta \sin 2\alpha \tag{2.102}$$

For dipolar coupling, and for most ^{2}H quadrupolar couplings, the expression for $\Phi_\lambda(t)$ is greatly simplified due to $\eta_\lambda = 0$, leading to:

$$C_1 = -\frac{\delta_\lambda}{\sqrt{2}}\sin 2\beta \tag{2.103}$$

$$C_2 = \frac{\delta_\lambda}{2}\sin^2\beta \tag{2.104}$$

$$S_1 = 0 \tag{2.105}$$

$$S_2 = 0 \tag{2.106}$$

For the calculation of pulse sequence Hamiltonians the lower limit of the integral in Equation 2.97, i.e the initial rotor phase, often needs to be not equal to zero.

For an arbitrary initial rotor phase the acquired MAS phase for an interaction λ can be defined as:

$$[\Phi_\lambda]_{t_1}^{t_2} = \Phi_\lambda(t_2) - \Phi_\lambda(t_1) \tag{2.107}$$

From this two useful relationships can be derived:

$$[\Phi_\lambda]_t^{t+\tau_r} = 0 \qquad\qquad [\Phi_\lambda]_0^{\frac{\tau_r}{2}} = -[\Phi_\lambda]_{\frac{\tau_r}{2}}^{\tau_r} \tag{2.108}$$

The first relationship shows that no phase integral is acquired after a single full rotor period, this being responsible for the averaging effect of MAS. After each full rotor period, the initial signal is fully refocused resulting in the theoretical time-domain signal not decaying with time. After Fourier transformation the isotropic resonance in the frequency-domain spectrum shows infinitely narrow spinning sidebands separated by $\frac{2\pi}{\tau_r} = \omega_r$.

With the expression for the averaged Hamiltonian under MAS (Equation 2.97) the evolution of an initial state $\hat{\rho}(0) = \hat{I}_x$ under an interaction under MAS is given by

$$\hat{I}_x \xrightarrow{\overline{\hat{\mathcal{H}}}_{MAS}^\lambda(t)} \hat{I}_x \cos\Phi_\Lambda + \hat{W}\sin\Phi_\Lambda \tag{2.109}$$

where:

$$
\begin{array}{llll}
\Phi_{CSA} & = & \omega_{iso}t + \Phi_{CS} & \hat{W} = \hat{I}_y \\[4pt]
\Phi_{Quad} & = & \sqrt{\frac{3}{2}}\Phi_Q & \hat{W} = i(\hat{\mathcal{J}}_{21} + \hat{\mathcal{J}}_{2-1}) \\[4pt]
\Phi_D^{homo} & = & \sqrt{\frac{3}{2}}\Phi_D & \hat{W} = 2\left(\hat{I}_y^i\hat{I}_z^j + \hat{I}_y^j\hat{I}_z^i\right) \quad \hat{I}_x = \hat{I}_x^i + \hat{I}_x^j \\[4pt]
\Phi_D^{hetero} & = & \frac{1}{2}\Phi_D & \hat{W} = 2\hat{I}_y\hat{S}_z
\end{array}
$$

It should be noted that the acquired phase angles Φ_Λ differ from the integrated phases Φ_λ because they include the additional pre-factors from the corresponding spin part $\hat{T}_{20}^\lambda$ of the Hamiltonian. The acquired phase angles are functions of time and depend on the Euler-angles transforming the interaction from PAS $\Rightarrow$ ROT. The Euler-angles α and β are identical to the polar angles of the rotor axis in the PAS. A dependence on α is only seen for asymmetric tensors with $\eta \neq 0$. The final angle γ denotes the initial rotor phase, with the time-dependence $\omega_r t$ always relative to this angle (Equation 2.98).

An important point not yet discussed is the way time dependence enters the Hamiltonian. This can be seen by representing the MAS Hamiltonian as five Fourier components as suggested by Equation 2.93:

$$\omega_\lambda^{(m)} = \mathcal{A}_{2-m}^{\lambda,\text{ROT}} d_{-m0}^{(2)}(\beta_\text{M}) \tag{2.110}$$

The time-dependent Hamiltonian thus becomes:

$$\hat{\bar{\mathcal{H}}}_\lambda^{MAS}(t) = \hat{\mathfrak{T}}_{20} \sum_{m=-2}^{2} \omega_\lambda^{(m)} e^{im\omega_r t} \tag{2.111}$$

This representation introduces time dependence as trigonometric functions of $\omega_r t$ and $2\omega_r t$, and is a consequence of the interactions being represented by a second-rank tensors. Thus elements of the Wigner rotation matrices up to second order (L=2) are involved (Equations 2.93–2.95). The time-dependence is a mere rotor modulation of the Hamiltonian, and does not effect the spin part. However, if the spin part is manipulated by suitably placed rotor-synchronised RF-pulses, components of the Hamiltonian with a certain symmetry with respect to time are modulated by MAS in different ways. This is the basis of the *recoupling* methods introduced in Chapter 3.

2.3   Basic solid-state NMR techniques

In the following section, the basic solid-state NMR experiments and two-dimensional NMR will be introduced. The single-pulse excitation experiment and the fundamentals of signal detection will be presented first (Section 2.3.1). This will be followed by common heteronuclear techniques such as dipolar decoupling (Section 2.3.2) and cross-polarisation (Section 2.3.3). A brief overview of echo techniques (Section 2.3.4) and two-dimensional NMR (Section 2.3.5) will then be given.

The general experimental procedures used for all solid-state NMR experiments are given in Appendix B with the Bruker implementation of each pulse sequences given in Appendix C.

2.3.1   Single-pulse excitation (SPE)

The application of a single RF pulse to nuclei with $I \geq \frac{1}{2}$ and monitoring their return to equilibrium is the epitome of FT-NMR spectroscopy (Figure 2.11).
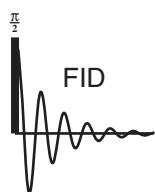
Figure 2.11: *Single-pulse excitation.*

The pulse in question is described as being a 90° or $\frac{\pi}{2}$ pulse as it results in the bulk magnetisation being flipped from along the z-axis, to being aligned in the xy-plane. The exact orientation of the magnetisation in the xy-plane depends on the phase of the RF during the pulse. Such a pulse can be achieved in two ways; by a long pulse of low power, resulting in a weak $\boldsymbol{B}_1$ field, or a short pulse of high power, resulting in a strong $\boldsymbol{B}_1$ field. These two classes of pulse are generally described as being 'soft' or 'hard' pulses respectively, and differ in the time taken to achieve their desired effect and excitation bandwidth.

After the $\frac{\pi}{2}$ pulse, the Larmor precession of the transverse magnetisation induces a weak voltage in the RF-coil, which is subsequently detected at the NMR signal $S(t)$. Technically, the signal is mixed-down with a reference carrier frequency ω_{ref} to aid digitisation, and is equivalent to observing the response in the rotating frame. With modern spectrometers capable of separately detecting both the x- and y-components of the precessing magnetisation a complex signal is measured. Such phase-sensitive, or quadrature, detection allows distinction between signals of opposite sign differing from the carrier by the same frequency, i.e. $\omega_{ref} \pm \omega$, thus doubling the effective spectral window.

The spin system in a perturbed state, with observable transverse magnetisation, is free to relax back to the equilibrium state, with no observable transverse magnetisation. This *free induction decay* (FID) signal from the observable magnetisation is characterised by a time constant T_2, the transverse or spin-spin relaxation time

(Figure 2.11). Similarly, the return of magnetisation, along the *z*-axis, to the initial $\hat{I}_z$ state is characterised by the time constant T_1, the longitudinal or spin-lattice relaxation time. The former dictates how long coherent signal lasts for and the latter the time taken to return to equilibrium.

Using the density matrix formalism introduced in Section 2.18 the signal is given as the expectation value of the transverse magnetisation. In order to obtain the full complex signal, the expectation value of the shift-operator $\hat{I}_+$ must be calculated:

$$\langle \hat{I}_+ \rangle = \mathsf{Tr}\{\boldsymbol{\hat{\rho}} \cdot \hat{I}_+\} = \frac{1}{\sqrt{2}}\Big(\mathsf{Tr}\{\boldsymbol{\hat{\rho}} \cdot \hat{I}_x\} + i\mathsf{Tr}\{\boldsymbol{\hat{\rho}} \cdot \hat{I}_y\}\Big) = \frac{1}{\sqrt{2}}\Big(\langle \hat{I}_x \rangle + i\langle \hat{I}_y \rangle\Big) \quad (2.112)$$

The spectrum containing full phase information may then be obtained by Fourier transformation of $\langle \hat{I}_+ \rangle(t)$

2.3.2 Heteronuclear dipolar-decoupling (DD)

When dealing with low natural abundance nuclei *S*, such as 1.1% ^{13}C, homonuclear couplings can safely be neglected due to the low probability of two *S* nuclei occurring in close proximity. However heteronuclear couplings between low abundance and high abundance nuclei *I*, such as ^{1}H , still cause significant line broadening even under MAS of $\omega_r/2\pi > 30$ kHz. To overcome these line broadening interactions a number of *decoupling* schemes have been developed, and continue to be an important field of research [De Paëpe 03, Ernst 03, Khitrin 03]. All these methods typically involve continuously irradiating the *I* nuclei with high-power RF-fields whilst simultaneously acquiring the FID of the *S* nuclei. To do this a double-resonance probehead is required. This design allows a single RF-coil to be addressed by two separate resonance circuits, operating at the Larmor frequencies of the *S* and *I* nuclei, at the same time.

In solid-state NMR under MAS, high-power continuous-wave (CW) decoupling was initially used to achieve heteronuclear decoupling (Figure 2.12a). In order to obtain sufficient decoupling efficiency, and avoid interference between the physical rotation of MAS (ω_r) and spin rotation of RF decoupling (ω_1), high-power decoupling with strong RF-fields of 50–150 kHz is necessary. The most important interference effects arise when either the $n \cdot \omega_r = \omega_1$ or $\omega_r = 2 \cdot \omega_1$ rotary-resonance conditions are met [Dusold 00]. The former condition resulting in the recoupling of heteronuclear dipolar couplings [Oas 88], and the latter in the recoupling of homonuclear dipolar couplings [Nielsen 94]. These conditions are easily avoided by choosing decoupling frequencies at least two times that of the spinning frequency. It should be noted that under MAS of $\omega_r > 40kHz$ low-power CW-decoupling, with the RF-frequency much less than that of the spinning frequency, can be advantageous [Ernst 01].

At present, high-power multiple-pulse decoupling schemes are considered the most efficient methods for solids under MAS, and in the worst case equal in efficiency
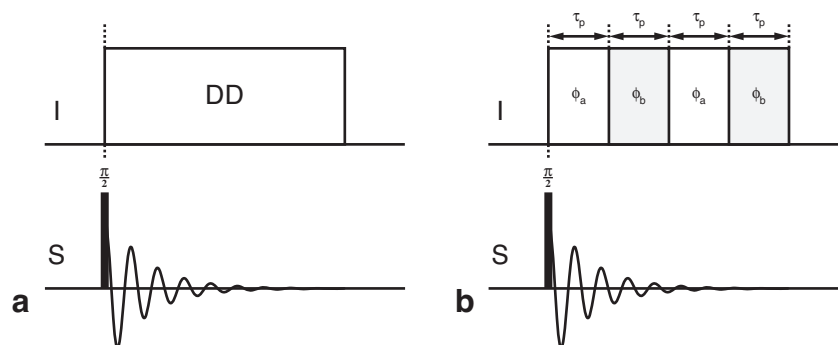
Figure 2.12: *Heteronuclear decoupling sequences. An RF-field is applied during the whole data acquisition time. For CW decoupling a single pulse of continuous phase is used (a). For TPPM and XiX the irradiation is divided into pulses of differing length and phase (b).*

to CW decoupling. The most widely adopted scheme is the two-pulse phase-modulated (TPPM) decoupling sequence [Bennett 95], and provides significant improvement in both linewidth and intensity under a wide range of experimental conditions. This consists of two pulses of length τ_p equivalent to $\approx 170°$ tip angle, alternating in phase by $\Delta\phi = 10$–$50°$, i.e. $\phi_a = \phi_b + \Delta\phi$ (Figure 2.12b). The optimum decoupling efficiency being found by empirically optimising both the tip angle and phase difference. The improved decoupling efficiency is ascribed to a second averaging of the coupling interaction [Gan 97, Carravetta 00]. Provided the RF-field is much greater than the MAS frequency, the spin Hamiltonian is first truncated by the RF irradiation and then averaged by MAS over a longer time-scale. Only at the zeroth-order approximation does CW decoupling lead to full decoupling in a heteronuclear spin system under MAS for such a Hamiltonian. When a higher order of approximation is considered, a cross-term between the heteronuclear dipole-dipole coupling tensor and the chemical shielding tensor of the irradiated spins is reintroduced. It is the influence of TPPM on this cross-term which results in the reduced line widths. Several variants of TPPM have been proposed offering improvements in TPPM decoupling efficiency for a number of specific experimental conditions [Gan 97, Yu 98, Fung 00, Takegoshi 01].

An alternative multi-pulse decoupling scheme is the X inverse-X (XiX) sequence [Detken 02]. This consists of two pulses of length τ_p alternating in phase by 180°, e.g. $\phi_a = 0$ and $\phi_b = 2\pi$ (Figure 2.12b). The decoupling efficiency is now only dependent on a single parameter, τ_p/τ_r, where τ_r is the rotor period. This simplification allows an initial value for the pulse length to be chosen based solely on the MAS frequency. Typically, $\tau_p = 1.85 \cdot \tau_r$ or $\tau_p = 2.85 \cdot \tau_r$, with optimum decoupling efficiency achieved by experimental fine-tuning. When compared to TPPM, an increase in peak height of up to 29% has been seen [Detken 02, Ernst 03]. The gain is primarily attributed to the reduction of the broad base of the peak in TPPM spectra, and is reflected in similar line-widths seen for both methods. The XiX scheme only performs well at high spinning frequencies (> 20 kHz) and decoupling RF-Fields (> 100 kHz). When these criteria cannot be met TPPM is often the better choice.

2.3.3 Cross-polarisation (CP)

With the maximum polarisation achievable by single pulse excitation governed by the gyro-magnetic ratio of the nucleus under investigation, signal intensity for low-γ nuclei (S) such as ^{13}C and ^{15}N can be problematic. One common method to circumvent this is to transfer polarisation from the more abundant high-γ nuclei (I) such as protons, which are typically also present. This technique was first applied by A. Pines, M. Gibby and J. S. Waugh [Pines 72, Pines 73] and originally referred to as *proton enhanced nuclear induction spectroscopy*. Since then, however, the more general term *cross-polarisation*[†] has become commonplace.

Practically, after an initial $\frac{\pi}{2}$ pulse on the I nuclei generates transverse magnetisation, polarisation is transferred to the S nuclei by simultaneous irradiation for 50 μs to 5 ms on both I and S channels. After this so-called *contact-time* (τ_{CP}) the enhanced signal from the S nuclei is detected, usually in the presence of heteronuclear dipolar decoupling (Figure 2.13a).
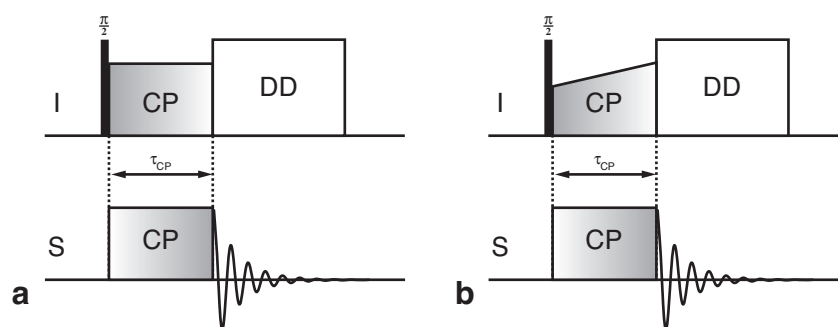
***Figure 2.13**: The cross-polarization experiment: (a) Hartmann-Hahn-CP and (b) Ramp-CP.*

The maximum polarisation transfer occurs when the Hartmann-Hahn match condition is satisfied:

$$-\gamma_S B_1(S) = -\gamma_I B_1(I) \qquad \text{or} \qquad \omega_1(S) = \omega_1(I) \tag{2.113}$$

The match condition represents the Zeeman levels of both S and I becoming degenerate when the two lock-fields are applied. Under these conditions, both spin species precess with the same frequency $\nu_1 = -\gamma B_1/2\pi$, about the axis of the lock-field, in their respective rotating frames. With both rotating frames sharing a common z-axis, and both z components of the I and S magnetisation oscillating at the same frequency (ν_1), energy transfer and thus polarisation transfer is permitted. To allow such a transfer to occur a mediating interaction is also required, this typically being the heteronuclear dipolar coupling. Formally, satisfying the match condition reintroduces flip-flop terms (e.g. $2\hat{I}_z\hat{S}_z$) from the heteronuclear dipolar coupling into the effective dipolar Hamiltonian responsible for polarisation transfer. Hence, the effi-

---

[†]Resulting in the less dubious acronym CP.

ciency of the cross-polarisation process is governed by the magnitude of the dipolar interaction between I and S spins. Thus, the maximum signal enhancement is given by the factor γ_I/γ_S.

With increasing contact time, S magnetisation M_S builds-up with a time constant T_{SI} characteristic of the dipolar coupling strength. As the I and S nuclei are still subject to relaxation phenomena during their respective spin-locks the S magnetisation passes through a maximum before decaying. The characteristic time constants for such longitudinal relaxation in the rotating frame are termed $T_{1\rho}^I$ and $T_{1\rho}^S$ for the I and S spins respectively. For dilute S spins in a large system of I spins the contact time dependence of the S magnitisation $M_S(\tau_{CP})$ is given by Equation 2.114 [Mehring 83, Slichter 96]:

$$M_S(\tau_{CP}) = \frac{M_0}{\lambda} \cdot \left[1 - \exp\left(-\frac{\lambda \cdot \tau_{CP}}{T_{SI}} \right) \right] \cdot \exp\left(-\frac{\tau_{CP}}{T_{1\rho}^I} \right) \tag{2.114}$$

where:

$$\lambda = 1 + \frac{T_{SI}}{T_{1\rho}^S} - \frac{T_{SI}}{T_{1\rho}^I} \tag{2.115}$$

The relationship described in Equation 2.114 can be derived using thermodynamic principles when considering a large system of coupled I spins, e.g. protons in organic solids. However, for an isolated two-spin system an oscillatory dependence on contact time for M_S is observed. Strongly coupled nuclei exhibit a small T_{IS} and thus S magnetisation is built-up quickly, with the opposite trend seen for weakly coupled nuclei. With molecular motion reducing dipolar couplings, the site specific buildup behaviour can provide qualitative insight into site mobility. For more quantitative analysis knowledge of the individual relaxation time constants is required [Voelkel 88]. Another important advantage of the CP experiment is the dependence of the recycle-delay on T_1^I, and not T_1^S, which is typically the larger. Thus, in contrast to the SPE experiment where T_1^S governs the recycle-delay, shorter recycle-delays are possible for CP experiements facilitating shorter measurement time.

Under MAS the Hartmann-Hahn match condition (Equation 2.113) changes to:

$$\omega_1(S) = \omega_1(I) \pm n \cdot \omega_r \tag{2.116}$$

Under such condition the Hartmann-Hahn match condition also shows strong mismatch dependence if the MAS frequency and dipolar couplings are of the same order of magnitude. At higher MAS frequencies the maximum signal intensity is observed for $n = \pm 1$, leading to difficulties in both establishing and maintaining an efficient match condition. A flat matching profile, over a wide range of match conditions, can be produced by linearly increasing the amplitude of either the I or S lock pulse during the contact time (Figure 2.13b). This is commonly known ramp-CP [Metz 94].[†]

[†]For pulse sequences see Section C.3.2 and Section C.3.3.

2.3.4   Echo techniques

In the solid-state problems can occur due to the FID decaying rapidly. In such cases the signal cannot be adequately detected because of the coil not having enough time to fully recover from the initial RF pulse. An elegant way to overcome this so-called 'dead-time' problem is to form an echo of the original signal and detect that instead. This is achieved by allowing the spins to evolve for a given amount of time τ after the initial $\frac{\pi}{2}$ excitation pulse, and then applying a suitable echo pulse. The FID is then only acquired after the same time τ after the echo pulse.

The tip angle of the echo pulse, and relative phase to the excitation pulse, depend on the type of interaction the echo should refocus. For interactions linear in $\hat{I}_z$, e.g. chemical shift, resonance offset and heteronuclear dipolar coupling, a π pulse of the same phase as the excitation pulse generates an echo (Figure 2.14a). This type of echo is generally know as the Hahn spin echo [Hahn 50].[†] For bilinear interactions of the same spin species, e.g. homonuclear dipolar coupling [Powles 63] and quadrupolar coupling, a $\frac{\pi}{2}$ echo pulse 90° out of phase from the initial excitation pulse generates an echo [Davis 76]. This being known as the solid echo (Figure 2.14b).[‡] It can be shown by calculating the propagator $2 \cdot \tau$ after the initial excitation pulse that, for a given interaction and echo type, full recovery of the initial state may be achieved [Schmidt-Rohr 94].
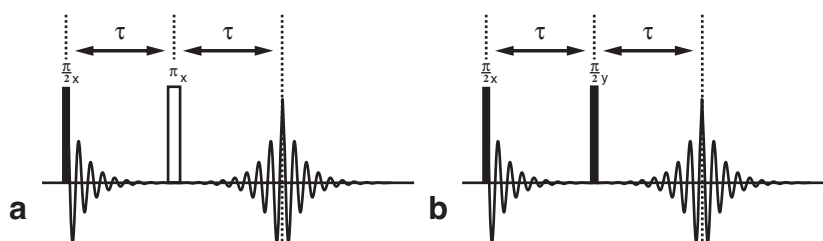
***Figure 2.14**: Echo Techniques: (a) the Hahn spin echo and (b) solid echo.*

The solid echo is routinely used for deuteron NMR spectroscopy, in particular the study of molecular dynamics. Molecular reorientation during the echo cause changes of the quadrupolar evolution leading to characteristic line shapes [Spiess 81, Macho 01].

[†]For pulse sequences see Section C.1.2.
[‡]For pulse sequences see Section C.1.3.

2.3.5 Two-dimensional (2D) NMR

One of the major advances in NMR has been the introduction [Jeener 71] and development [Ernst 87] of two-dimensional NMR spectroscopy. This involves the placement of an incremented evolution time t_1 into a pulse sequence and correlating the effect this has on the FID measured during t_2. Implementing this as an arrayed experiment, results in a two dimensional FID, with a direct dimension t_2 and an indirect dimension t_1. Fourier transformation with respect to both t_1 *and* t_2 thus yields a two dimensional spectrum correlating ω_1 and ω_2 respectively (Figure 2.15).
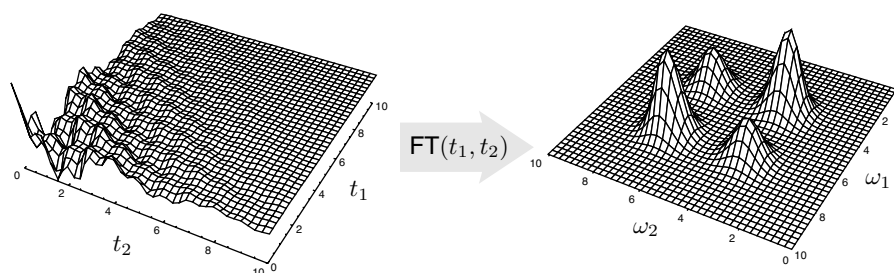
Figure 2.15: *Two dimensional free induction decay* (t_1, t_2) *and corresponding spectrum* (ω_1, ω_2)

Two dimensional experiments consist of four stages: excitation, evolution, mixing and detection. The excitation stage generates the spin state which is desired to be monitored during the evolution time t_1, and thus in the indirect dimension of the resulting 2D spectrum. This is followed by a mixing period which generates detectable magnetisation for the detection period, t_2 (Figure 2.16)
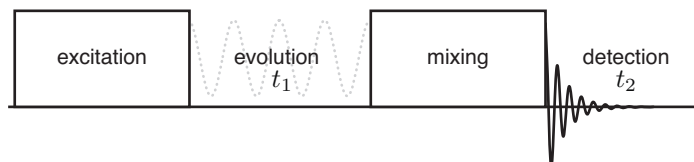
Figure 2.16: *The four stages of a 2D NMR experiment.*

The ability to follow an interaction in an indirect dimension is particularly important for multiple-quantum (MQ) coherences as these are not able to be directly excited or detected during t_2. Two-dimensional techniques enable such phenomena to be probed in the indirect dimension of a two-dimensional spectrum by following the evolution of MQ coherence during t_1.

2.3.6 NOESY/EXSY/Dipolar-exchange

The three pulse 2D ^{1}H–^{1}H correlation experiment (Figure 2.17a) provides information about connectivity in the form of an SQ-SQ correlation spectrum (Figure 2.17b).[†] The effect of polarisation transfer is seen as symmetric off-diagonal *cross-peaks* between the respective on-diagonal *auto-peaks* of the sites involved. The sign of the cross-peaks (ω_1, ω_2) and (ω_2, ω_1) relative to the auto-peaks (ω_1, ω_1) and (ω_2, ω_2) depends on the cross-relaxation mechanism and time-scale of the interactions.
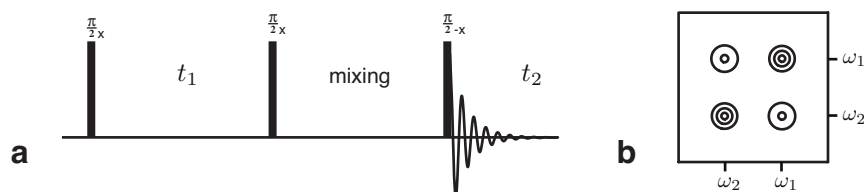
Figure 2.17: The (a) three pulse experiment and (b) illustrative SQ-SQ correlation spectrum.

In the solution-state the major mechanism of communication between sites is the nuclear Overhauser enhancement (NOE), a cross-relaxation interaction based on transient dipolar couplings, and is thus called NOE spectroscopy (NOESY) accordingly [Jeener 79]. A sign inversion is seen between the auto-peaks and cross-peaks due to the dominant DQ cross-relaxation mechanism that takes place during the mixing time if molecular motion is fast with respect to the Larmor frequency. However, if chemical rearrangement occurs during the mixing time the physical exchange of excited spins will also generate cross peaks. Under these conditions no sign inversion is seen between auto and cross-peaks as polarisation transfer step has taken place. Thus, although exactly the same pulse sequence is used, when probing chemical exchange phenomena the experiment is called exchange spectroscopy (EXSY),.

The application of this three pulse experiment to samples in the solid-state leads to a third incarnation, rotor-synchronised dipolar-exchange[‡] spectroscopy. With a complex network of dipolar couplings present in a dense rigid spin systems it is possible for polarisation to move between sites by multiple energy-conserving ZQ steps, mediated by the dipolar interaction. This process is called spin diffusion[§]. Due to the dominant ZQ cross-relaxation mechanism during the mixing time if molecular motion are slow with respect to the Larmor frequency, no sign inversion is seen between the auto-peaks and cross-peaks. With MAS based homonuclear dipolar-decoupling a prerequisite for proton resolution in the solid state, inevitably dipolar mediated spin-diffusion is partially suppressed. This results in only the residual stronger dipolar couplings being seen. The monitoring of cross-peak intensity as a function of mixing time may also provide information on the rate of polarisation transfer between sites by spin-diffusion, and hence also on the degree of dipolar coupling.

[†]For pulse sequence see Section C.2.1.
[‡]Sometimes called spin-diffusion spectroscopy.
[§]Unlike EXSY at no point does the actual spin move through the matrix.

Chapter 3

Multiple-Quantum Coherence & Dipolar Recoupling under MAS

In Chapter 2 the fundamental interactions, and basic techniques of NMR on materials in the solid-state were introduced. In this chapter the specific techniques used will be presented. All the techniques described involve the recoupling of the anisotropic part of an NMR interaction under MAS and can consequently be viewed as recoupling experiments. The general principle of recoupling will be introduced before turning to each particular technique in detail.

3.1   Recoupling

As mentioned in the previous chapter, magic-angle spinning (MAS) provides a powerful tool to obtain spectral resolution in solid state NMR, with resolution a prerequisite for the elucidation of structure and dynamic properties in solid materials [Brown 01b]. However, the line narrowing achieved by fast MAS comes at the price of a loss in information about the anisotropic parts of the interaction tensors. This including all orientation dependent phenomena, as well as distance information from the dipolar coupling, which is of high value for structure determination in solids. Methods which allow such information to be selectively reintroduced, whilst retaining the spectral resolution provided by MAS, are therefore of great value.

The first approach to partly regain anisotropic information usually involved sacrificing part of the spectral resolution gained by MAS. Examples of which are slow magic-angle spinning and off-magic-angle spinning (OMAS). For slow MAS, where $\omega_r < \omega_{CSA}$, the isotropic signal is flanked on either side by rotational sidebands at multiples of the spinning frequency ω_r. The intensities of the MAS sidebands provide information about the chemical shift tensor [Herzfeld 80]. Alternatively, spinning the

sample at a known angle slightly offset from the magic-angle, allows the anisotropic interaction to be retained in a scaled down manner. By doing so the overlap of the broad anisotropic line shapes is decreased [Stejskal 77, Blümich 90].

The aim of regaining anisotropic tensor information while simultaneously keeping the full spectral resolution gained from MAS was finally achieved by a 'recoupling' approach [Gullion 89b, Carravetta 00]. Recoupling takes advantage of the fact that MAS, as a rotation in real space, affects only the space part of an interaction Hamiltonian. Conversely, the RF pulses affect only the spin part of an interaction Hamiltonian. Thus by the application of a suitably designed pulse sequence it is possible to counter act, and compensate for the averaging effects of MAS. By doing so an interaction of interest can be recoupled. A great variety of pulse sequences are currently available for recoupling of various NMR interactions [Gullion 97, Lee 95, deAzevedo 99, Dusold 00, Schnell 01b, Saalwächter 02].

3.1.1   Types of recoupling

The field of NMR recoupling can be categorised into two main classes: the first class utilises short/high-power (hard), rotor-synchronised RF-pulses to achieve recoupling. The other class uses continuously applied, relatively long, rotor-synchronised RF-pulses to achieve recoupling. Hereafter these two basic recoupling strategies are referred to as *laboratory-frame* and *tilted-frame* methods respectively.

In laboratory frame methods, the pulses are usually assumed to be δ-pulses[†] to aid the calculation of the average Hamiltonian for the sequence. The average Hamiltonian is calculated in the laboratory frame, thus leading to laboratory frame recoupling pulse sequences. In order to have confidence in the use of the δ-pulse approximation, the pulse lengths of the recoupling pulses in the pulse-train must be significantly shorter than the MAS rotor period, i.e. $\tau_{Pulse} \ll \tau_r$. At the increased MAS spinning speeds used to remove homonuclear proton dipolar coupling ($\omega_r/2\pi > 20$ kHz) this becomes technically demanding in terms of pulse performance and spectrometer timing.

In tilted frame methods, the nutation frequency ω_{nut} of the relatively long pulses are matched to multiples of the MAS rotation frequency ω_r. The synchronisation of the tilted rotating frame and the MAS rotor frame forms the basis of the recoupling effect for these pulse sequences. The selection of the interaction to be recoupled is achieved based on symmetry arguments related to the symmetry properties of the individual NMR interactions [Brinkmann 00, Zhao 01a]. For this reason these methods are also known as symmetry based pulse sequences. Due to the long pulses employed, these experiments are sensitive to pulse stability, and require fast power and phase switching to be applied successfully.

[†]Pulses taking an infinitely short time to achieve their desired manipulation of the spins.

All recoupling sequences presented in the following sections belong to the laboratory frame class of pulse sequences, with no tilted-frame or symmetry-based pulse sequences having been investigated. More specifically, all the pulse sequences discussed utilise the application of rotor-synchronised pulse-trains with pulses spaced by exactly half a rotor period $\tau = \tau_r/2$.[†]

3.1.2 Rotor synchronised pulse-trains

Before the individual experiments, and their associated pulse sequences, are described the general effects of rotor-synchronised pulse-trains will be introduced, as these pulse-sequence 'building-blocks' play a key role in all the recoupling methods used.

As previously mentioned, anisotropic interactions, which would otherwise be averaged to zero by MAS, can be recoupled by the application of suitable rotor synchronised pulse-trains. The approach is clearly demonstrated in the rotational-echo double-resonance (REDOR) experiment by Schaefer and Gullion [Gullion 89b, Gullion 89a]. In the initial REDOR experiment the heteronuclear dipolar coupling between two different low-γ nuclei species S_j and S_k was recoupled. The recoupling was achieved by the application of a π pulse-train timed such that the pulses were spaced by exactly half a rotor period. These so called REDOR-type π pulse-trains can also serve to recouple the anisotropic part of any interaction which is linear with respect to the irradiated spin. Hence, they are not limited to the dipolar interaction alone, but can also be used for CSA-recoupling [deAzevedo 99, Hong 00] and *IS* heteronuclear dipolar recoupling [Hing 92, Saalwächter 01b].

In order to gain an understanding of the recoupling effect of such a π pulse-train, it is instructive to regard the effect of MAS on an interaction Hamiltonian first. According to Equation 2.97 the averaged Hamiltonian of an interaction λ under MAS is given by the sum of an isotropic (first term) and an anisotropic (second term) contribution:

$$\bar{\hat{\mathcal{H}}}_\lambda^{MAS} = \hat{\mathcal{T}}_{00} \mathcal{A}_{00}^{\lambda,\text{LAB}} + \hat{\mathcal{T}}_{20} \cdot \frac{1}{t} \cdot \sqrt{\frac{3}{2}} \cdot \Phi_\lambda \tag{3.1}$$

The application of MAS imposes a sine ω_r modulation on the anisotropic part of $\bar{\hat{\mathcal{H}}}_\lambda^{MAS}$, which manifests itself as the acquired phase angle $\Phi_\lambda(t)$, the time-dependence of which is given by Equation 2.98. By setting $t = \tau_r$ in Equation 2.98, it directly follows that the acquired phase over a full rotor period is zero, i.e. $\Phi_\lambda(\tau_r) = 0$. Thus, the anisotropic part of $\bar{\hat{\mathcal{H}}}_\lambda^{MAS}$ also becomes zero over a full rotor period. This is the origin of interaction averaging by MAS. This may be more intuitively understood when the sine ω_r modulation is schematically depicted, with the mathematical sign of the sine-oscillation labelled $\oplus$ and $\ominus$ respectively (Figure 3.1a).

[†]Pulses spaced by $\tau_r/2$ recouple the ω_r modulated part of the spin Hamiltonian under MAS, however the $2 \cdot \omega_r$ modulated part can also be recoupled using pulses spaced by $\tau_r/4$.
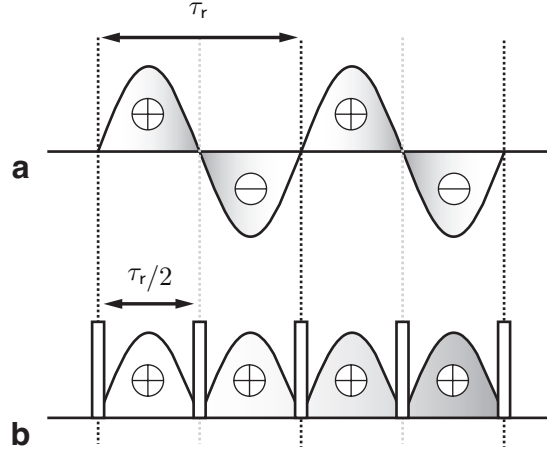
Figure 3.1: *(a) The sine modulation of the anisotropic part of an interaction Hamiltonian by MAS ($\mathfrak{H}^{MAS}_{\lambda,aniso}$) with associated time period τ_r. The average interaction after $n \cdot \tau_r$ is zero. (b) The application of a pulse which changes the sign of the interaction every $\tau_r/2$ results in the interaction building up with time, and not averaging to zero. (Shading indicates average interaction intensity)*

Under MAS the contribution from the first half ($\oplus$) and the second half ($\ominus$) of the rotor period cancel, hence after an integer number of rotor periods the anisotropic part of the interaction Hamaltonian modulated by MAS $\mathfrak{H}^{MAS}_{\lambda,aniso}$ is averaged to zero[†] or *refocused*:

$$\int_{t}^{t+n\cdot\tau_r} \mathfrak{H}^{MAS}_{\lambda,aniso}(t)\,\mathrm{d}t = 0 \tag{3.2}$$

If the sign of $\mathfrak{H}^{MAS}_{\lambda,aniso}$ is inverted every $\tau_r/2$, only lobes of the same sign are present. By doing so the anisotropic contributions from each $\tau_r/2$ interval accumulate over time (Figure 3.1b), thus the interaction is described as being *recoupled*:

$$\int_{t}^{t+n\cdot\tau_r} \mathfrak{H}^{MAS+RF}_{\lambda,aniso}(t)\,\mathrm{d}t \neq 0 \tag{3.3}$$

Such sign-inversion is achieved by the application of a suitable RF pulse every $\tau_r/2$ and inverting the sign of the spin-part $\hat{\mathfrak{T}}_{20}$. The application of such rotor synchronised pulses can be considered as a counter-rotation of the MAS modulated space-part by use of the spin-part of the Hamiltonian. The nature of the pulse applied to recouple an interaction depends on the nature of the spin part $\hat{\mathfrak{T}}_{20}$ of the respective interaction. For interactions linear in $\hat{I}$, e.g. heteronuclear dipolar coupling and CSA, the sign inversion of $\hat{\mathfrak{T}}_{20}$ is accomplished by rotor synchronised π pulses. However, for interactions bilinear in $\hat{I}$, e.g. homonuclear dipolar coupling, $\frac{\pi}{2}$ pulses are needed. This is analogous to the refocusing of linear and bilinear interactions by the Hahn and solid-echo techniques respectively. The particular method of homonuclear dipolar recoupling used for this work does not use a single $\frac{\pi}{2}$ pulse. Instead of a single pulse, a pair of $\frac{\pi}{2}$ pulses with orthogonal phases, e.g $\frac{\pi}{2}_x$, $\frac{\pi}{2}_{y'}$ are used. Due to the form

---

[†]Such *rotor-echoes* every $n \cdot \tau_r$ in the FID lead to MAS artifacts called *spinning-sidebands* in the associated spectrum. Due to the reciprocal nature of the Fourier-transform these occur at: $\delta_{iso} \pm n \cdot \frac{2\pi}{\tau_r} = \delta_{iso} \pm n \cdot \omega_r$

of the homonuclear dipolar coupling Hamiltonian the application of two such pulses leads to a time-reversal of the homonuclear dipolar coupling during the second half of each rotor period, and thus to recoupling [Feike 96a]. This approach leads to a higher recoupling efficiency as compared to that achieved with a single $\frac{\pi}{2}$ pulse.

3.2 Multiple-quantum techniques

With the selective reintroduction of anisotropic interactions, by rotor-synchronised pulses under MAS, the spectroscopist gains greater control over other interactions due to the possibility of further modification of the pulse sequence. This allows for the selective excitation of multiple-quantum coherence. With the multiple-quantum (MQ) aspect crucial for the method used, the general area of multiple-quantum NMR spectroscopy will be briefly introduced.

Since the first multiple-quantum NMR experiments in the solid-state [Weitekamp 82, Munowitz 87], many further methods have been developed. Of particular interest are those involving the homonuclear and heteronuclear dipolar coupling, allowing quantification of the dipolar coupling constant D_{jk} and thus internuclear distance determination.

As their name implies, multiple-quantum experiments involve the probing of multiple-quantum coherence between spins. An m-quantum coherence is defined as a change in the overall magnetic spin quantum number M by m. In the spherical tensor notation, a MQ coherence of order m, involving L spin $I = \frac{1}{2}$ nuclei, can be written as a single tensor operator of rank L and order m, i.e. $\hat{\mathcal{T}}_{L\pm m}$. Although formally, the selection rules state that transitions of $\Delta M > 1$ are forbidden, under the influence of perturbing interactions, such as dipolar coupling, these become weakly allowed. In contrast to single-quantum (SQ) coherence, MQ coherence does not induce a current in the detection coil and thus cannot be directly observed. This has lead to many elegant methods of *indirect detection*. These mostly consist of converting the undetectable MQ coherences into SQ coherence prior to detection.

Two-dimensional methods for multiple-quantum NMR

To gain access to MQ information the evolution of MQ coherence is most conveniently monitored in the indirect dimension (ω_1) of a two-dimensional NMR experiment. Such MQ experiments typically occur in four stages: excitation, evolution, reconversion and detection (Figure 3.2).

During the excitation period, a suitable pulse sequence for the excitation of the desired MQ coherence is applied. Usually an average Hamiltonian, $\hat{\overline{\mathcal{H}}}_{exc}$, can be used to describe this whole period. The resulting MQ coherence is then allowed to evolve during the t_1 period. After the evolution the MQ coherence is reconverted into ob-
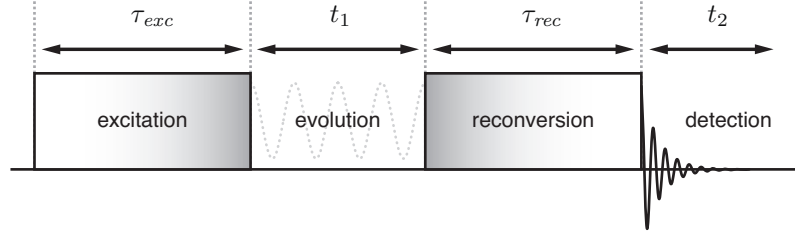
Figure 3.2: The four states of a 2D multiple-quantum experiment.

servable SQ magnetisation, this period being described by $\hat{\bar{\mathcal{H}}}_{rec}$. The resulting SQ magnetisation is then detected as a FID during the t_2 period. This results in the MQ coherence being indirectly monitored as an amplitude modulation of the FID as a function of t_1. The particular order of coherence monitored in the indirect dimension of the 2D spectrum is selected by phase cycling the excitation-block with respect to the reconversion block. By doing so, only the desired coherence is constructively added when the FIDs for each t_1 increment are combined.

If sign discrimination in the indirect dimension is desired, a further layer of phase cycling is applied on top of that used to select the order of coherence. This shifts both excitation and reconversion blocks in subsequent t_1 increments[†] such that the evolution period is both cosine *and* sine modulated. This is sometimes known as quadrature detection in the indirect dimension and is analogous to the detection of both the real and imaginary components of the FID by phase-sensitive quadrature detection in the direct dimension. For SQ magnetisation a phase shift of the sine modulated signal by $\Delta\Phi_{SQ} = \frac{\pi}{2}$ leads to the cosine modulated signal. However, more generally the phase shift is related to the order of coherence m, such that $\Delta\Phi_{mQ} = \frac{1}{m} \cdot \frac{\pi}{2}$. This is because of the multiple quantum coherence precessing at multiples of the Larmor frequency, i.e. $\omega_L^{mQ} = m \cdot \omega_L$. Thus for double quantum experiments phase shifts of $\frac{\pi}{4}$ are employed. Common implementations for achieving quadrature in the indirect dimension include time-proportional phase incrementation (TPPI) [Marion 83] and States-TPPI [Marion 89]. For TPPI the phase and t_1 increment are incremented concurrently, whereas for States-TPPI for each t_1 increment both phases are detected. This leads to TPPI having an effective t_1 increment ($\Delta t_1'$) twice that of the actual increment (Δt_1), resulting in an effective spectral width half of that expected for Δt_1:

$$\omega_{max}^{TPPI}(F1) = \frac{2\pi}{\Delta t_1'} = \frac{1}{2} \cdot \frac{2\pi}{\Delta t_1} \tag{3.4}$$

Thus sign discrimination only occurs with no increase in indirect spectral width. However, for States-TPPI $\Delta t_1' = \Delta t_1$ and thus both sign discrimination and increased indirect spectral width occur. For MQ NMR due to the higher MQ Larmor frequencies and their associated larger chemical shift ranges, e.g. 0–20 ppm for $\delta_H{}^{DQ}$, the States-TPPI method is usually preferred.

[†]Lousily termed *slices* of a 2D experiment.

MQ NMR of dipolar coupled systems

Homonuclear MQ experiments allow the determination of the homonuclear dipolar coupling constant D_{jk} by monitoring the build-up behaviour of the MQ coherence [Graf 96], or by analysing spinning-sideband patterns in the MQ dimension of 2D experiments [Geen 95, Gottwald 95, Friedrich 98]. Heteronuclear MQ experiments allow access to the heteronuclear dipolar coupling constants, with the added advantage of possible increased spectral resolution for one of the coupled species, e.g. resolution in the carbon dimension when probing $^{13}C-^{1}H$ dipolar couplings.

By probing double quantum coherence (DQC) only the complexity of a dipolar coupled systems is greatly reduced, as such DQCs only contain information about coupled spin-pairs. This facilitates the pair-wise analysis of a dipolar coupled network with respect to the DQ and SQ chemical shift of the nuclei involved, via 2D DQ-SQ correlation spectroscopy (Figure 3.3).
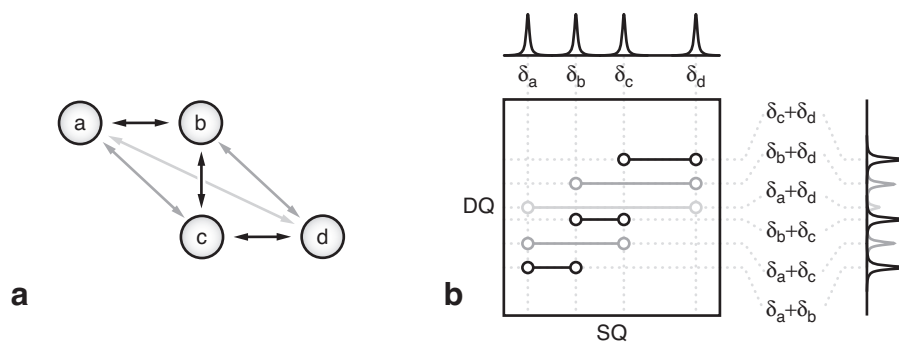
Figure 3.3: *(a) A four membered spin system showing the six dipolar couplings detected by DQ NMR. (Shading indicates magnitude of coupling) (b) Associated 2D SQ-DQ correlation spectrum with projections of the SQ and DQ dimensions. (shading indicates magnitude of cross peaks). The magnitudes of the DQCs suggest the geometry shown in (a).*

3.3   The 'back-to-back' pulse sequence

The *Back-to-back* or BABA pulse sequence recouples the homonuclear dipolar coupling under MAS [Feike 96a], and was used for all homonuclear MQ NMR presented in Chapters 4–6. This method has been routinely used for the determination of proximity relationships and quantification of ^{1}H–^{1}H internuclear distances in a range of materials [Schnell 01b, Schnell 04a]. The discussion here will be limited to the use of this method for double-quantum NMR generation, although with slight modification triple-quantum (TQ) NMR is possible with the same basic method.[†]

The BABA pulse sequence (Figure 3.4) consists of a repeated block of:

$$\left[90_x - \frac{\tau_r}{2} - 90_{-x}90_y - \frac{\tau_r}{2} - 90_{-y}\right]_n$$

For convenience this is often abbreviated to $x - \bar{x}y - \bar{y}$. For longer excitation and reconversion periods $\tau_{exc/rec}$ such as those over two, four and eight rotor periods the signs of the phases are set such that offset effects and pulse imperfections are compensated.[‡] As previously mentioned, the relative phase of the excitation and reconversion block is phase cycled to select the desired DQ coherence pathway.
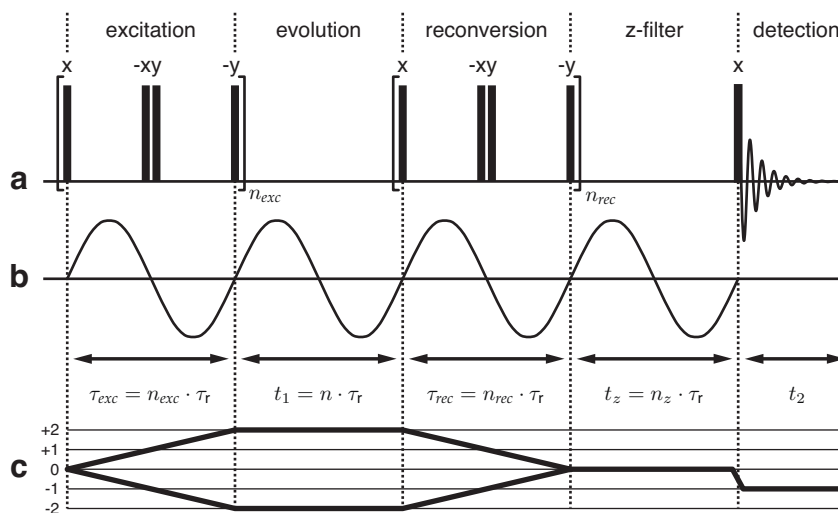
Figure 3.4: *(a) The BABA pulse sequence showing the (b) rotor synchronised stages of a 2D MQ MAS experiment, and corresponding (c) coherence transfer pathway diagram for the selection of DQ coherence.*

The BABA sequence recouples the homonuclear dipolar coupling described in a zeroth-order average Hamiltonian approach as:

$$\hat{\bar{\mathcal{H}}}_D^{homo} = \hat{\mathfrak{T}}_{20}^{jk} \cdot \frac{1}{t} \cdot \int_0^t \mathcal{A}_{20}^{\mathsf{LAB}} = \hat{\mathfrak{T}}_{20}^{jk} \cdot \frac{1}{t} \cdot \sqrt{\frac{3}{2}} \Phi_D^{homo} \tag{3.5}$$

[†]For TQ BABA pulse sequence see Section C.2.3.
[‡]For pulse sequence implementation of rotor synchronisation and phase cycle see Section C.2.2.

where according to Equation 2.98:

$$\Phi_D^{homo} = -\sqrt{2} \cdot \frac{D_{jk}}{\omega_r} \cdot \sin 2\beta \cdot \Big(\sin(\omega_r t + \gamma) - \sin\gamma \Big) \tag{3.6}$$

$$+ \frac{1}{2} \cdot \frac{D_{jk}}{\omega_r} \cdot \sin^2\beta \cdot \Big(\sin(2\omega_r t + 2\gamma) - \sin 2\gamma \Big) \tag{3.7}$$

The term δ_D^{homo} has been replaced by the more familiar dipolar coupling constant, where $D_{jk} = \frac{1}{2}\delta_D^{homo}$, which was defined in Equation 2.69. The average Hamiltonian for a BABA segment $x - \bar{x}y - \bar{y}$ of one rotor period length can be calculated as [Schnell 01c]:

$$\bar{\hat{\mathcal{H}}}_{BABA} = \frac{1}{\tau_r} \cdot 3[\Phi_D^{homo}]_0^{\frac{\tau_r}{2}} \cdot \Big(\hat{\mathfrak{T}}_{2,+2}^{jk} + \hat{\mathfrak{T}}_{2,-2}^{jk} \Big) \tag{3.8}$$

$$= \frac{1}{\tau_r} \cdot [\Omega^{jk}]_0^{\frac{\tau_r}{2}} \cdot \Big(\hat{\mathfrak{T}}_{2,+2}^{jk} + \hat{\mathfrak{T}}_{2,-2}^{jk} \Big) \tag{3.9}$$

where the term $[\Omega^{jk}]_0^{\frac{\tau_r}{2}} = 3[\Phi_D^{homo}]_0^{\frac{\tau_r}{2}}$ was introduced to use the common notation found in the literature. As reflected by the order of the tensor components $m = \pm 2$, the BABA sequence, as presented, generates DQ coherence. Calculating $[\Omega^{jk}]_0^{\frac{\tau_r}{2}}$ explicitly yields:

$$[\Omega^{jk}]_0^{\frac{\tau_r}{2}} = 3\sqrt{2} \cdot \frac{D_{jk}}{\omega_r} \cdot \sin 2\beta_{jk} \sin\gamma_{jk} \tag{3.10}$$

Applying the BABA Hamiltonian to a two spin system in thermal equilibrium, i.e. $\rho_0^{jk} \propto \hat{I}_z^j + \hat{I}_z^k$, results in a DQ coherence, whose amplitude is modulated by $\sin(\Omega_{exc}^{jk})$. During reconversion, a corresponding amplitude modulation of $\sin(\Omega_{rec}^{jk})$ is introduced. For n rotor periods of excitation and reconversion, the relative intensity of the double-quantum signal can be described by a multiplication of the modulations from the excitation and reconversion periods:

$$S_{DQ}^{jk}(t_1) \propto \Big\langle \sin(n_{exc} \cdot \Omega_{exc}^{jk}) \cdot \sin(n_{rec} \cdot \Omega_{rec}^{jk}) \Big\rangle_{\beta,\gamma} \tag{3.11}$$

where the angled brackets indicate a powder average of the orientation dependent enclosed term by varying β and γ independently.[†] For all examples presented here $n_{exc} = n_{rec}$ and will collectively be termed $n_{exc/rec}$. Consequently, the length of the excitation and reconversion periods are also identical, i.e. $\tau_{exc} = \tau_{rec} = \tau_{exc/rec}$.

As can be seen from Equation 3.11, the DQ signal intensity depends on the t_1 evolution time and consequently the BABA experiment can be conducted in a number of ways, depending on the setting of t_1 and the t_1-increment Δt_1. As a one-dimensional experiment where $t_1 = \Delta t_1 = 0$ the BABA sequence serves as a double-quantum filter, with only the SQ signal from spins also capable of supporting DQ coherence appearing in the spectrum (Section 3.3.1). Wheras the two-dimensional version ($\Delta t_1 \neq 0$)

[†]Due to the symmetry of the dipolar interaction only the Euler angles β and γ need to be considered.

can be carried out in two ways with $\Delta t_1 = n \cdot \tau_r$ or $\Delta t_1 = \frac{1}{n} \cdot \tau_r$. These yielding either rotor-synchronised SQ-DQ correlation spectra (Section 3.3.2) or ^{1}H–^{1}H DQ MAS spinning-sideband patterns (Section 3.3.3) respectively.

3.3.1 DQ build-up curves

The simplest incarnation of BABA is as a one-dimensional experiment with no evolution period ($t_1 = 0$). In this form the BABA experiment serves as a double-quantum filter (DQF). Since $t_1 = 0$ the integrated phases in Equation 3.11 become identical, i.e. $\Omega_{exc}^{jk} = \Omega_{rec}^{jk} = \Omega_{exc/rec}^{jk}$. Hence, the DQ-filtered signal intensity is given by:

$$
\begin{aligned}
S_{DQ}^{jk} \quad &\propto \quad \left\{ \sin(n_{exc/rec} \cdot \Omega_{exc/rec}^{jk}) \right\}^2 & (3.12)\\
&\approx \quad \left\{ n_{exc/rec} \cdot \Omega_{exc/rec}^{jk} \right\}^2 & (3.13)\\
&\propto \quad \left\{ D_{jk} \cdot \tau_{exc/rec} \right\}^2 & (3.14)\\
&\propto \quad r_{jk}^{-6} \cdot \tau_{exc/rec}^2 & (3.15)
\end{aligned}
$$

At the limit of short excitation/reconversion times, limited to integer multiples of the rotor period $\tau_{exc/rec} = n \cdot \tau_r$, or for weak dipolar couplings Equation 3.12 can be approximated to Equation 3.13. Under these limiting conditions, weaker dipolar couplings $D_{jk} \cdot \tau_{exc/rec} \ll 1$ can be neglected (Equation 3.14). In other words, for short recoupling times only the stronger dipolar couplings contribute to the signal, whereas at longer recoupling times weaker couplings also contribute. Thus by monitoring the DQ signal intensity as a function of excitation time a double-quantum *build-up curve* is measured, from which the underlying dipolar coupling can be determined.

However in real, non-ideal systems a dense coupling network is present leading to inevitable multi-spin coherence, these being also partly excited by the BABA sequence. This effects the BABA sequence as technically Equation 3.11 was only the first term of a series expansion resulting from the evolution of a multi-spin system [Schnell 01b]. Thus the truncation is only fully valid for short recoupling times, where the double-quantum term dominates. In reality, with increasing recoupling time dense spin systems develop multi-spin character and deviate from the ideal build-up behaviour of an isolated dipolar coupled spin-pair. The onset of multi-spin effects at longer recoupling times can be illustrated by the DQ build-up curve of tribromoacetic acid, a ^{1}H–^{1}H spin-pair model compound with a dipolar coupling of $D_{jk} = 2\pi \cdot 6.5$ khz (Figure 3.5). The initial build-up is dominated by two-spin behaviour, whereas at longer recoupling times the destructive interference of several couplings leads to a lack of the characteristic oscillations expected for an ideal spin-pair. As well as the lack of oscillations, the signal also decays. This is due to the weaker interactions and higher orders of coherence relaxing faster and thus reducing the overall signal intensity at longer recoupling times. In some fortunate cases char-

acteristic oscillations in the build-up curve can be detected, and the dipolar coupling constant directly extracted, provided that only one dipolar coupling gives rise to the monitored DQ peak.
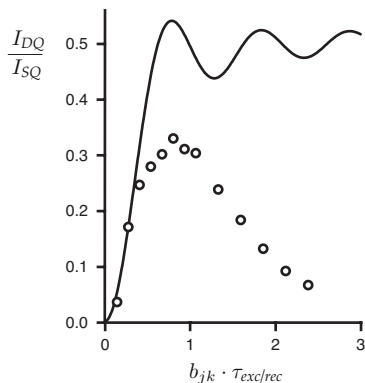
Figure 3.5: DQ buildup curves of an ideal two-spin system (solid) and two-spin model compound tribromoacetic acid. Initial slope dominated by two-spin behaviour. (adapted from [Schnell 01b])

If the oscillations are ill-defined, a more complicated procedure has to be applied, based on DQ intensity being expressed as a product:

$$S_{DQ}^{jk} = A \cdot (D_{jk} \cdot \tau_{exc/rec})^2 \cdot \exp\left\{ -\frac{\tau_{exc/rec}}{T_1^{DQ}} \right\} \quad (3.16)$$

where the term A contains several constants and is fixed for a series of experiments and the exponential term describes the decay of the DQ coherence with a time constant T_1^{DQ}. However, since A is usually unknown only relative strengths of dipolar couplings may be obtained using this method without more involved referencing procedures [Graf 98a].

For proton solid-state NMR, the strong dipolar couplings give rise to pronounced decay effects and hence require high MAS spinning frequencies to provide spectral resolution, this in turn puts high demands on the performance of the recoupling sequence. Consequently, DQ build-up measurements are usually only carried out on systems where the dipolar couplings are weaker than those found in dense proton spin systems. For example in mobile systems such as liquid crystals [Langer 01] and polymer melts [Graf 98b], or in non-protonated systems with weak homonuclear couplings such as ^{31}P–^{31}P in crystalline phosphates [Schnell 96].

Due to the described limitations, the build-up approach was not used for the dense protonated solid systems investigated in Chapters 4–6. Nonetheless, one-dimensional DQF experiments serve as qualitative sources of information about the dipolar couplings present in a system, and can have enhanced spectral resolution as compared to the SQ SPE spectra of the same compound.

3.3.2   Rotor-synchronised DQ correlation spectra

As previously mentioned, two-dimensional BABA spectra are obtained by increasing the t_1 evolution time over subsequent slices of the 2D experiment. Here the case where the t_1 increment Δt_1 is incremented by an integer number of rotor periods $\Delta t_1 = n \cdot \tau_r$ is described. By rotor-synchronising the increment of the evolution time no spinning-sidebands are observed in the indirect dimension of the 2D spectrum:

$$\omega_{max}(F1) = \frac{2\pi}{\Delta t_1} = \frac{2\pi}{\tau_r} = \omega_r \quad (3.17)$$

More formally, all spinning-sidebands in the indirect dimension are *folded* back onto their corresponding centerband, thus during the evolution period t_1 only evolution of DQ coherence occurs. During t_1 the DQ coherence evolves under the influence of the isotropic chemical shift and dipolar interactions. The evolution of DQ coherence between two spins j and k, with respective chemical shifts ω_j and ω_k, results in a modulation of:

$$\omega_{DQ}^{jk} \propto \exp\left\{ i(\omega_{SQ}^j + \omega_{SQ}^k)t_1 \right\} \tag{3.18}$$

If only the dipolar coupling between spins j and k forming the DQ coherence is present, no evolution due to the dipolar interaction occurs during t_1. However, the presence of spins other than j and k give rise to an evolution of the DQ coherence during t_1. This interaction usually manifests itself as a loss of DQ signal intensity, due to these contributions not being refocused by the subsequent reconversion period. Thus the peak position in the indirect dimension is purely governed by the isotropic chemical shift evolution of the DQ coherence. Where the resonance frequency of the DQ coherence is the sum of the resonance frequencies of the two spins involved. With the acquisition period t_2 detecting only evolution of SQ coherence, the rotor-synchronised experiment correlates DQ and SQ coherence in the indirect and direct dimension respectively. It is therefore convenient to display the 2D spectrum such that the ω_1 frequency axis is scaled by a factor of two compared to the ω_2 frequency axis.
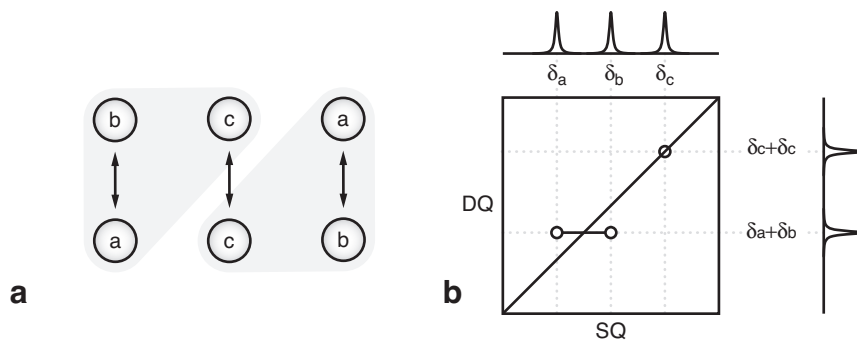
Figure 3.6: (a) A dimer of two, three membered spin systems showing two intramolecular (AB) and one intermolecular (CC) dipolar couplings. (b) Associated 2D DQ correlation spectrum showing the two types of peaks possible between unlike (AB) and like spins (CC). The presence of the CC DQC suggests the geometry shown in (a).

The peaks in the 2D spectra are denoted by (ω_2, ω_1), where ω_2 is the SQ frequency and ω_1 the DQ frequency. Two general types of peak patterns can be distinguished, those resulting from DQ coherence between like and unlike spins. A DQ coherence between like spins CC, of identical chemical shift gives rise to a single peak at $(\omega_C, 2 \cdot \omega_C)$, i.e. on the diagonal $\omega_1 = 2 \cdot \omega_2$. Although the peak lies on the diagonal of the spectrum it is not a true *auto-peak*, as two distinct spins are needed to form the DQC. A DQ coherence between unlike spins AB, of different chemical shift leads to a pair of cross-peaks at $(\omega_A, \omega_A + \omega_B)$ and $(\omega_B, \omega_A + \omega_B)$, i.e. symmetric about the

diagonal. The two DQ cross-peaks of an *AB* type coherence ideally have the same intensity, as this is related to the number of spins involved. However, in the presence of strong cross peaks, weaker peaks may be suppressed, or not be present at all. This is due to weaker dipolar coupling between one spin-pair being suppressed by the presence of a stronger dipolar coupling between another spin-pair. This process is generally known as *dipolar truncation* [Schmidt-Rohr 94].

Even though the dipolar coupling does not directly contribute to the DQ evolution during t_1 it is the mediating interaction, and thus the overall signal intensity is governed by the strength of coupling. This results in the choice of excitation/reconversion time $\tau_{exc/rec}$ needing to be adjusted for DQ coherence with different associated dipolar couplings. Under the fast MAS conditions employed for this work DQ coherence between spin-pairs with $r_{HH} \leq 350$ pm were observed.

3.3.3 DQ spinning-sideband patterns

In contrast to the rotor-synchronised experiments presented in the previous section, incrementing the t_1 evolution time in steps of $\Delta t_1 < \tau_r$ leads to spinning-sidebands in the indirect dimension [Geen 94, Geen 95]. The sideband intensities strongly depend on the excitation/reconversion time and the strength of the underlying dipolar coupling [Friedrich 98]. Hence, this type of experiment allows the quantitative determination of dipolar coupling strengths [Brown 01c].
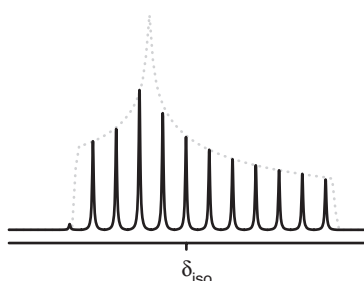
Figure 3.7: *The slow MAS sideband pattern produced by the evolution rotor modulation (ERM) mechanism of a nuclei with CSA. Sidebands are confined to the static CSA tensor (dotted line), with the centreband found at $\delta = \delta_{iso}$.*

Since an isolated spin-pair has no anisotropic evolution of the DQ coherence during t_1, the sidebands observed cannot arise from evolution rotor modulation (ERM), the *normal* sideband generation mechanism [Friedrich 98]. Sidebands generated by ERM are produced by the evolution of an anisotropic interaction under MAS and are thus governed by the anisotropy of the evolving spin interaction. For example, in slow MAS 1D SPE spectra the ERM sideband pattern of nuclei with chemical shift anisotropy will be confined to the underlying CSA tensor (Figure 3.7). Under fast MAS however, the contribution from ERM is almost entirely found in the centerband, thus the ^{1}H–^{1}H DQ MAS spinning sideband patterns result from the reconversion rotor encoding (RRE) mechanism. This mechanism arises from the rotor-phase dependence of the average Hamiltonian used for excitation and reconversion. Conversely, the average Hamiltonian must depend explicitly on the rotor phase in order to allow RRE, and is sometimes called *rotor-* or *γ-encoding* as it allows the interaction to be encoded by the rotor phase. The laboratory-frame recoupling sequences presented here meet

this condition but many tilted-frame sequences do not, as their average Hamiltonian does not depend on the initial rotor phase.

The RRE mechanism does not require an accompanying spin evolution during t_1. Thus terms arising from evolution during t_1, in particular the chemical shift evolution, will not be considered when describing the RRE mechanism.
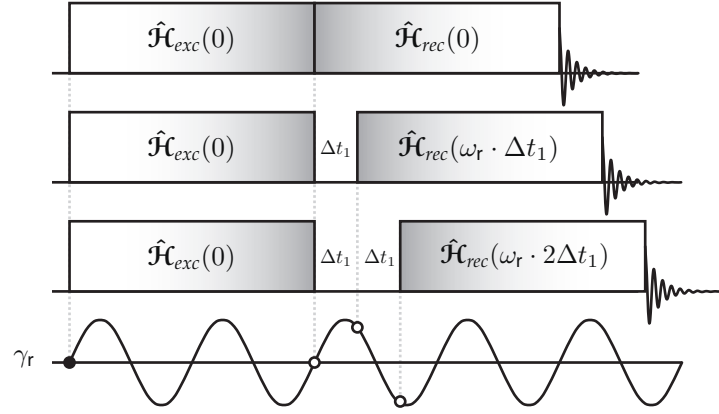
Figure 3.8: *Schematic representation of reconversion rotor encoding (RRE). The excitation Hamiltonian $\hat{\mathcal{H}}_{exc}$ is independent of Δt_1, as each period has the same initial rotor phase γ_r (filled points). However, the reconversion Hamaltonian $\hat{\mathcal{H}}_{rec}$ is proportional to Δt_1 as the initial rotor phase varies (open points).*

When $t_1 = 0$, both the excitation and reconversion periods have the same initial rotor phase, with this found in the integrated phase Ω^{jk} (Equation 3.10). However, as t_1 is incremented, the rotor phase dependence of the reconversion period changes relative to that of the excitation period. Thus, the integrated phases for excitation and reconversion differ with respect to their initial rotor phases:

$$[\Omega_{exc}^{jk}]_0^{\frac{\tau_r}{2}} = 3\sqrt{2} \cdot \frac{D_{jk}}{\omega_r} \cdot \sin 2\beta_{jk} \cdot \sin(\gamma_{jk}) \tag{3.19}$$

$$[\Omega_{rec}^{jk}]_{\frac{\tau_r}{2}+t_1}^{\tau_r+t_1} = -3\sqrt{2} \cdot \frac{D_{jk}}{\omega_r} \cdot \sin 2\beta_{jk} \cdot \sin(\gamma_{jk} + \omega_r \cdot t_1) \tag{3.20}$$

The integrated phase of the reconversion period Ω_{rec}^{jk} is thus shifted relative to the integrated phase of the excitation period Ω_{exc}^{jk}. This leads to an encoding on the DQ signal by a sine function of $\omega_r \cdot t_1$.

Thus, without any *real* evolution during t_1, MAS modulates the amplitudes of DQ coherence by means of phase encoding. It can clearly be seen from Equation 3.20 that no rotor modulations occur if $\Delta t_1 = n \cdot \tau_r$, this being the case for the rotor-synchronised experiment (Section 3.3.2). Reconversion rotor encoding consequently leads to rotor echoes occurring in the t_1-signal for evolution times of $t_1 = n \cdot \tau_r$, thus RRE generates sidebands spaced by multiples of the rotor period in the indirect dimension. It should be noted that this sideband generation mechanism inherently requires at least a two-dimensional experiment to occur.

In analogy to Equation 3.11 the DQ signal as a function of t_1 is now given by:

$$S_{DQ}^{jk}(t_1) \propto \sin\left(n_{exc} \cdot [\Omega^{jk}]_0^{\frac{\tau_r}{2}}\right) \cdot \sin\left(n_{rec} \cdot [\Omega^{jk}]_{\frac{\tau_r}{2}+t_1}^{\tau_r+t_1}\right) \tag{3.21}$$

By substituting Equation 3.20 into Equation 3.21 and separating the terms which do not depend on t_1 into the coefficient C_{ij}, Equation 3.21 becomes:

$$S_{DQ}^{jk}(t_1) \propto \sin\left[C_{jk} \cdot \sin(\omega_r \cdot t_1 + \gamma)\right]. \tag{3.22}$$

Using the relation [Abramowitz 72]:

$$\sin\left[x\sin(\omega_r \cdot t_1 + \gamma)\right] = 2\sum_{n=0}^{\infty} J_{2n+1}(x)\sin\left[(2n+1)(\omega_r \cdot t_1) + \gamma(2n+1)\right] \tag{3.23}$$

the DQ signal intensity can be rewritten as a Fourier series, whose terms contain Bessel functions $J_n(C_{jk})$ of nth order:

$$S_{DQ}^{jk}(t_1) \propto 2\sum_{n=1}^{\infty} J_{2n+1}(C_{jk})\sin\left[(2n-1)(\omega_r \cdot t_1) + \gamma(2n+1)\right] \tag{3.24}$$

From the Fourier series it can be seen that the DQ signal is modulated by only odd multiples of the spinning frequency. Thus, after Fourier transformation with respect to t_1, the sideband pattern consists solely of odd-order sidebands. The intensity distribution between the sidebands is determined by the Bessel functions and the coefficients C_{jk}, which depend on the orientation (β, γ) and on the ratio D_{jk}/ω_r. Hence, DQ sideband patterns contain information regarding sample orientation and dipolar coupling strength. In samples with a known orientation distribution, e.g. isotropic powder samples, the orientation distribution can be taken into account by powder averaging leading to the quantitative determination of the dipolar coupling constant. The essential parameter for determining the envelope of the DQ sideband patterns is the product of the dipolar coupling constant and the excitation/reconversion time, $D_{jk} \cdot \tau_{exc/rec}$. Due to this relationship, by choosing a suitable excitation time, the number of observed sidebands can be pumped to a desired level (Figure 3.9a). Experimentally, it has proven advantageous to choose $D_{jk} \cdot \tau_{exc/rec} \approx 1.2$, which is a compromise between enough sidebands to allow fitting and not so many as to distribute the intensity too thinly.

The analysis of the spinning sideband patterns is usually carried out by comparison to the relative sideband intensities of simulated sideband patterns.[†] Such simulations commonly assume the presence of an isolated spin-pair. In organic solids however, protons rarely exist as well isolated spin-pairs. An important question is thus raised regarding the validity of such a spin-pair approximation and the influence of remote protons. Under sufficiently fast MAS the weaker dipolar couplings are initially averaged first leaving only the stronger interactions, in an ideal case thus leaving isolated

---

[†]For BABA sideband simulations see Section D.1.
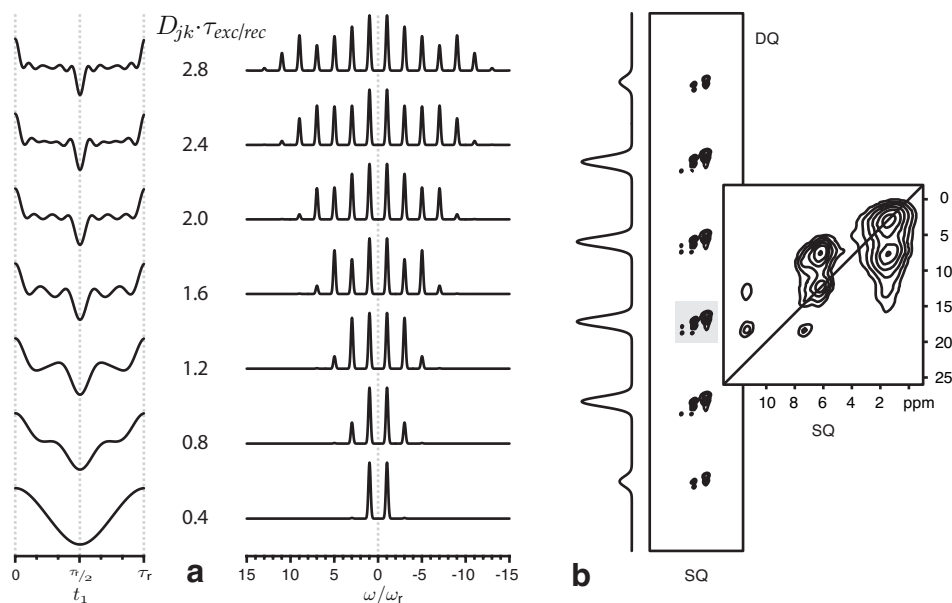
Figure 3.9: *(a) Calculated $I_{DQ}(t_1)$ variation over a rotor period and corresponding DQ spinning sideband patterns for various $D_{jk} \cdot \tau_{exc/rec}$. (b) Ideal full 2D DQ sideband spectrum also providing chemical shift resolution in the indirect dimension. Enlargement shows each odd-order sideband effectively consists of a full chemical shift resolved spectrum*

spin-pairs only. However, even if weak dipolar couplings are still present they have been found to contribute to the first-order sidebands only [Friedrich 98, Schnell 99, Schnell 01b]. Hence, restricting analysis to the higher order sidebands only still leads to reliable results for the stronger interactions [Brown 01c, Schnell 04a]. Another observation frequently made in multispin systems is the observation of even-order sidebands. These arise by the ERM mechanism due to evolution of DQ coherence during t_1. Such evolution can occur when one of the spins involved in a DQ coherence undergoes dipolar coupling to an external spin, i.e. not the spin with which it is forming the DQ coherence. With the ERM mechanism suppressed under fast MAS conditions, increasing the spinning rate generally suppresses unwanted centerband and even-order sideband intensity.

Experimentally, the Δt_1 is chosen such that $\Delta t_1 = \frac{\tau_r}{n}$ with n being 20-25, thus a rotor period is divided into n equal parts. However, other than the influence of the RRE mechanism, the chemical shift also undergoes evolution during the t_1 period. This results in multiple rotor periods of rotor-encoding needing to be measured in order to obtain the chemical shift information as well as the rotor encoded information. Practically, this requires the acquisition of many slices of a 2D experiment. By doing so the sideband patterns from spin-pairs with different DQ frequencies can be separated. Due to the retention of chemical shift information each group of sidebands contains an intensity weighted full DQ-SQ correlation spectrum equivalent to that produced if t_1 was incremented in a rotor-synchronised fashion (Figure 3.9b).

3.4 REDOR-based heteronuclear dipolar recoupling

In this section a variety of techniques based on recoupling the ^{1}H-S heteronuclear dipolar couplings will be presented. Compared to the homonuclear ^{1}H methods, described in the previous section, the heteronuclear approach benefits from the higher chemical shift range of most S nuclei, resulting in higher resolution spectra. All the experiments presented here rely on the high homonuclear dipolar decoupling efficiency of fast MAS ($\omega_r > 20$ kHz) and REDOR-type π pulse-trains to achieve heteronuclear dipolar recoupling [Jaroniec 00].

Before the individual experiments are described, the average Hamiltonian under REDOR-type π pulse-trains will be considered [Naito 96, Naito 98] as this is applicable for all the experiments. From initial proton transverse magnetisation[†] the evolution over one rotor period of π pulse-train based recoupling is:

$$\hat{I}_x \xrightarrow{\quad \Phi 2\hat{I}_z\hat{S}_z \quad} \hat{I}_x \cos\Phi + 2\hat{I}_y\hat{S}_z \sin\Phi \tag{3.25}$$

$$\xrightarrow{\quad \pi\hat{S}_x \quad} \hat{I}_x \cos\Phi - 2\hat{I}_y\hat{S}_z \sin\Phi \tag{3.26}$$

$$\xrightarrow{\quad \Phi'2\hat{I}_z\hat{S}_z \quad} \hat{I}_x \left(\cos\Phi\cos\Phi' + \sin\Phi\sin\Phi'\right) - 2\hat{I}_y\hat{S}_z \left(\sin\Phi\cos\Phi' - \cos\Phi\sin\Phi'\right)$$

$$= \hat{I}_x \cos 2\Phi - 2\hat{I}_y\hat{S}_z \sin 2\Phi \qquad \text{when} \qquad \Phi = -\Phi' \tag{3.27}$$

$$\xrightarrow{\quad \pi\hat{S}_y \quad} \hat{I}_x \cos 2\Phi + 2\hat{I}_y\hat{S}_z \sin 2\Phi \tag{3.28}$$

where:

$$\Phi = -[\Phi_D^{hetero}]_0^{\frac{\tau_r}{2}} \qquad \text{and} \qquad \Phi' = -[\Phi_D^{hetero}]_{\frac{\tau_r}{2}}^{\tau_r} \tag{3.29}$$

with $[\Phi_D^{hetero}]_{t_1}^{t_2}$ being defined in Equation 2.109. The equality $\Phi' = -\Phi$ used in the simplification of Equation 3.27 corresponds to the effective inversion of the space part of the Hamiltonian by MAS. The effect of a second π pulse, as described in Equation 3.28, needs to be included in order to describe a full cycle of the recoupling pulse-train, that being equal to one rotor period. Comparing Equation 3.25 with Equation 3.28 shows that the evolution over one rotor period of π pulse-train recoupling can conveniently be described by an average Hamiltonian:

$$\bar{\hat{\mathcal{H}}}_D^{hetero} = \bar{\Phi} 2\hat{I}_z\hat{S}_z \frac{1}{\tau_r} \tag{3.30}$$

where:

$$\bar{\Phi} = 2\Phi = -2[\Phi_D^{hetero}]_0^{\frac{\tau_r}{2}} = 2\sqrt{2} \cdot \frac{D_{jk}}{\omega_r} \cdot \sin 2\beta \sin\gamma \tag{3.31}$$

[†]Analogous treatment for initial transverse S magnetisation.

Consequently, over a pulse-train of n rotor periods in length the total evolution is given by:

$$\hat{I}_x \xrightarrow{\ \overline{\hat{\mathcal{H}}}_D^{hetero}\, n\cdot\tau_r\ } \hat{I}_x \cos\left(n\cdot\Phi\right) + 2\hat{I}_y\hat{S}_z \sin\left(n\cdot\Phi\right) \tag{3.32}$$

By applying π pulses of arbitrary phases in Equations 3.25–3.28, it can be shown that neither the phase, nor the channel on which the π pulses are applied, have an influence on the average Hamiltonian. This freedom over pulse phase and channel allows schemes of π pulse-trains to be implemented which are compensated for offsets, chemical-shift anisotropy, and pulse imperfections. The (xy-4) phase cycle [Gullion 90] has proved to be particular useful in these cases and was implemented for the π pulses in all the experiments used.

A number of different experiments are possible using such π pulse-train based heteronuclear dipolar recoupling experiments. As with the proton experiments, these experiments may also be divided into the typical four stages of a MQ experiment. The excitation and reconversion periods both consist of π pulse-train recoupling blocks. The first *excitation* π pulse-train block results in a cosine-modulation of the initial coherence and a sine-modulation of the antiphase coherence (Equation 3.32). After t_1 evolution, the antiphase coherence is converted back into a transverse coherence state by the *reconversion* π pulse-train block.

The differences between the various techniques arise from the different types of coherence created by the excitation block and thus the coherence probed during the t_1 evolution period. The various experiments are distinguished by the polarised nucleus before initial recoupling (^{1}H or S via CP), the coherence state probed during t_1 and the detected nucleus (S or ^{1}H[†]). The particular conditions for each experiment are listed in Table 3.1.

Table 3.1: Heteronuclear recoupling experiments based on REDOR-type π pulse-trains

experiment	initial	coherence	detect	literature
TEDOR	$\hat{I}_{x/y}$	$\hat{I}_{x/y}$	S	[Hing 92]
REPT-HMQC	$\hat{I}_{x/y}$	$2\hat{I}_x\hat{S}_x$	S	[Saalwächter 99, Saalwächter 01a]
REPT-HSQC	$\hat{I}_{x/y}$	$2\hat{I}_x\hat{S}_z$	S	[Saalwächter 01a]
REPT-HDOR	$\hat{I}_{x/y}$	$2\hat{I}_z\hat{S}_z$	S	[Saalwächter 01a]
DIP-HMQC	$\hat{S}_{x/y}$	$2\hat{S}_y\hat{I}_x$	S	[Saalwächter 01b]
DIP-HSQC	$\hat{S}_{x/y}$	$2\hat{S}_z\hat{I}_x$	S	[Saalwächter 01b]
DIP-HDOR	$\hat{S}_{x/y}$	$2\hat{S}_z\hat{I}_z$	S	[Saalwächter 01b]
REREDOR	$\hat{S}_{x/y}$	$\hat{S}_y + 2\hat{S}_x\hat{I}_z$	S	[Saalwächter 02]
RELM	$\hat{S}_{x/y}$	$\hat{S}_z$	S	[De Paul 00]
inv. HSQC	$\hat{I}_{x/y}$	$2\hat{I}_x\hat{S}_z$	I	[Schnell 01a]
inv. TEDOR	$\hat{S}_{x/y}$	$\hat{S}_x$	I	[Schnell 02]
inv. REPT	$\hat{S}_{x/y}$	$2\hat{S}_z\hat{I}_z$	I	[Schnell 02]

[†]by means of inverse detection.
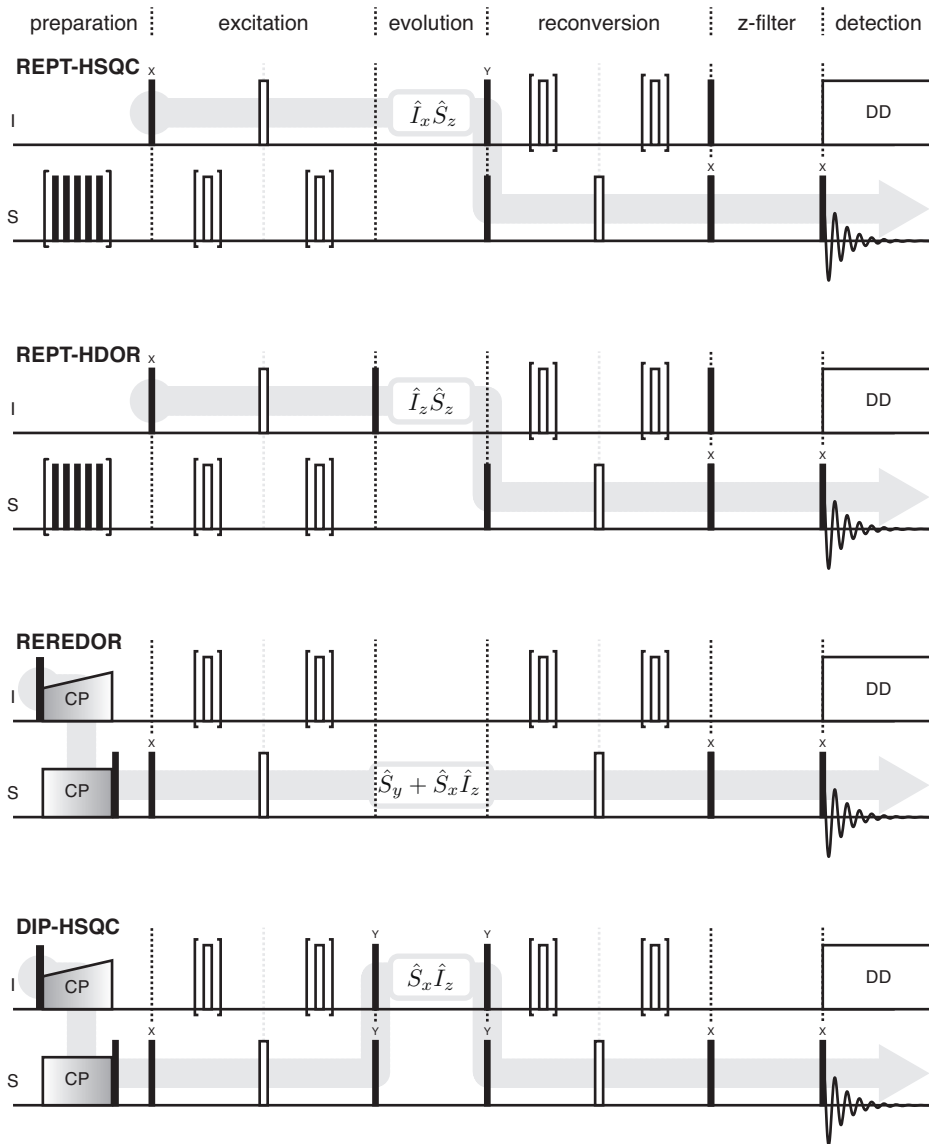
Figure 3.10: *Pulse sequences for heteronuclear dipolar recoupling based on REDOR π pulse-trains. Arrows indicate pathways for the transverse components of the coherence states probed during t_1.*

The TEDOR experiment [Hing 92] was the first such experiment of this type. However, with the t_1 evolution period being placed at the beginning of the experiment, it lacked the possibility to create sidebands by reconversion rotor encoding and will therefore not be further discussed. The other experiments may be further distinguished by the symmetry of the coherence pathway after initial polarisation preparation and by whether polarisation is transferred between nuclei (Figure 3.10). From these experiments only the DIP class of the experiments [Saalwächter 01b] is symmetric with respect to the recoupling procedure, i.e. $S \rightarrow I \rightarrow S$. The REREDOR experiment is also symmetric as no polarisation transfer step occurs, i.e. $S \rightarrow S \rightarrow S$. The remaining experiments are all asymmetric with the polarisation being transferred from $I \rightarrow S$ or vice-versa. The aspect of using initial

proton magnetisation for the generation of heteronuclear multiple quantum (HMQ) coherence, via a polarisation transfer to carbon, is reflected in the name of this class of experiments, i.e. recoupled polarisation transfer (REPT). This being analogous to the insensitive nuclei enhanced by polarisation transfer (INEPT) solution-state NMR method [Morris 79]. However, whereas INEPT employs the J-coupling for the generation of HMQ coherence REPT exploits the dipolar coupling. With no initial cross polarisation step being required, the REPT technique is of interest in cases where cross polarisation efficiency under fast MAS is low. Recently, inverse detected experiments have also been introduced [Schnell 01a]. Of specific relevance to the work presented in Chapters 4–6 are the REPT-HSQC, REPT-HDOR and REREDOR experiments. In the following sections these particular experiments will be further discussed.

3.4.1 REPT-HSQC

The REPT-HSQC experiment [Saalwächter 01a], can be thought of as the heteronuclear equivalent to the BABA experiment (Figure 3.10). Like BABA, it can be implemented in three different ways. As a 1D experiment, with $t_1 = 0$, HSQC build-up curves can be measured by varying the length of the recoupling period with the form of the curve sensitive to the strength of the heteronuclear dipolar coupling. As a 2D experiment, if t_1 is incremented in full rotor periods, a heteronuclear correlation (HETCOR) spectrum correlates S chemical shift in the direct dimension with I chemical shift in the indirect dimension. Alternatively, if t_1 is incremented in fractions of a rotor period RRE spinning-sidebands are produced in the indirect dimension. From the spinning-sideband pattern the heteronuclear dipolar coupling constant can be quantified. However, the REPT-HDOR (Section 3.4.2) and REREDOR (Section 3.4.3) experiments provide a more elegant method for heteronuclear dipolar coupling constant determination in less time. This results in the measurement of REPT-HSQC sideband patterns not being used in practice.

In order to understand the interactions probed during t_1, the dependence of the S spin detected signal with respect to t_1 for this experiment needs to be considered. During the t_1 period the antiphase coherence $\hat{I}_x\hat{S}_z$, created by the excitation π pulse-train, evolves under the influence of chemical shift and dipolar couplings. Considering the isotropic chemical shift evolution of the I spin only, the x and y-components of the signal are modulated by sine and cosine functions of $\omega_{CS}^I \cdot t_1$. With the CSA for protons usually being very small the influences of CSA can safely be neglected. After reconversion of the antiphase coherence to observable SQ coherence, the two components of the S-detected signal are:

$$S_x(t_1) = \left\langle \sin(n_{exc} \cdot \bar{\Phi}_0) \cdot \sin(n_{rec} \cdot \bar{\Phi}_{t_1}) \cdot \cos(\omega_{CS}^I \cdot t_1) \right\rangle \tag{3.33}$$

$$S_y(t_1) = \left\langle \sin(n_{exc} \cdot \bar{\Phi}_0) \cdot \sin(n_{rec} \cdot \bar{\Phi}_{t_1}) \cdot \sin(\omega_{CS}^I \cdot t_1) \right\rangle \tag{3.34}$$

It can be seen from Equation 3.34 that in order to obtain the full phase information for the indirect dimension both the cosine and sine modulated components need to be acquired. This is achieved using the TPPI procedure (Section 3.2). From Equation 3.34 it can be seen that if implemented in a rotor-synchronised manner (i.e. $\Delta t_1 = n \cdot \tau_r$) the t_1 dependent signal is only modulated by the isotropic chemical shift of the I spins. Hence, a heteronuclear correlation spectrum is recorded. The intensity of the correlation peaks is determined by the strength of the underlying dipolar coupling and the number of recoupling cycles $n_{exc/rec}$. Due to the mediating interaction being the through-space dipolar interaction, the correlation seen is not limited to directly bound ^{1}H-S spin-pairs only, as would be the case if the J-coupling mechanism was used. This leads to the possibility of probing strong dipolar interactions with short recoupling times, and weaker interactions with longer recoupling times. Typically at short recoupling times of $\tau_{exc/rec} = 1 \cdot \tau_r$ only directly bound spin-pairs are observed, the resulting spectra being useful for spectral assignment purposes. However, at extended recoupling times correlation between long range non-bound heteronuclear spin-pairs may be observed. This can provide valuable information regarding the supramolecular structure (Figure 3.11).
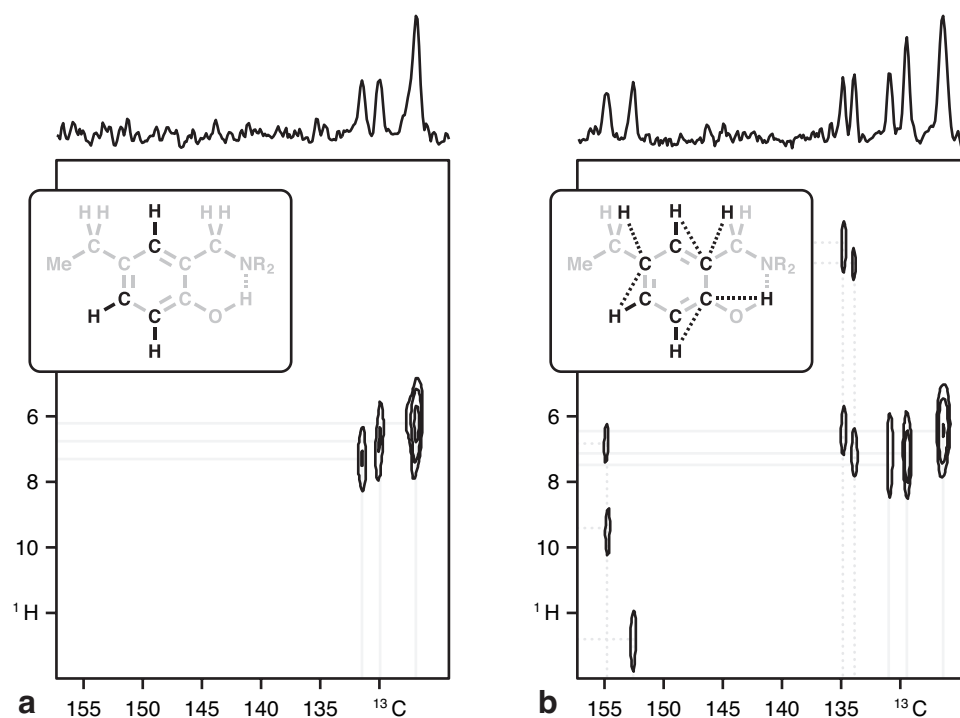
Figure 3.11: *Aromatic region of two REPT-HSQC Heteronuclear correlation spectra of H,Et–N–Pr obtained at 30 kHz MAS with different recoupling times. (a) Only directly bound heteronuclear spin-pairs with strong dipolar couplings (solid) observed at $\tau_{exc/rec} = 1 \cdot \tau_r$. (b) Long-range heteronuclear spin-pairs with weaker dipolar couplings (dashed), as well as directly bound spin-pairs, observed at $\tau_{exc/rec} = 2 \cdot \tau_r$.*
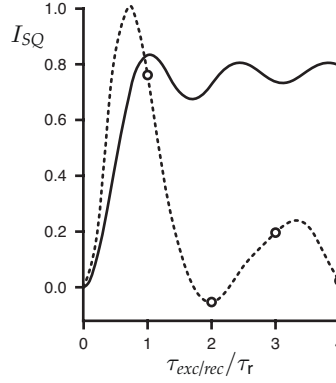
Figure 3.12: Theoretical HSQC build-up curves for CH (solid) and CH$_2$ groups (dashed) at 25 kHz MAS. A null in signal intensity occurs for the CH$_2$ group at recoupling times of two rotor periods. Experimentally accessible points are marked.

The build-up behaviour, as measured by monitoring 1D filtered intensity with increasing recoupling time, provides a quick method to estimate the strength of the underlying dipolar couplings.[†] Comparison of the calculated build-up curves of a rigid, directly bonded CH spin-pair and CH$_2$ group show the latter strongly deviates from the spin-pair approximation (Figure 3.12). For the simulation of CH$_2$ and CH$_3$ groups three and four spin models need to be considered [Saalwächter 01a]. It should also be noted that the theoretical build-up curve of a CH$_2$ group has a null in signal intensity at recoupling times of ≈ 80 μs, or $\tau_{exc/rec} = 2 \cdot \tau_r$ at 25 kHz MAS. This leads to problems when rigid CH$_2$ groups are to be detected. This problem may however be circumvented by the use of the REREDOR approach (Section 3.4.3), as no such null in signal intensity is seen with this method.

3.4.2 REPT-HDOR

The REPT-HDOR experiment (Figure 3.10) is based on creating a state of dipolar longitudinal order $\hat{I}_z\hat{S}_z$ during t_1. After the build-up of the $2\hat{I}_x\hat{S}_z$ antiphase coherence during the excitation time, the antiphase coherence is converted into the longitudinal dipolar ordered state $\hat{I}_z\hat{S}_z$ by a $\frac{\pi}{2}$ pulse on the I spins. After the evolution period this state is converted back into the antiphase coherence $\hat{I}_z\hat{S}_y$ by a $\frac{\pi}{2}$ pulse on the S spins. The subsequent recoupling period reconverts this antiphase coherence into observable S spin SQ coherence.[‡] The advantage of creating a state of heteronuclear dipolar order lies in the lack of evolution of this state during t_1. Hence, the detected signal of the S spins of the HDOR experiment simply reads as:

$$S_x(t_1) = \left\langle \sin(n_{exc} \cdot \bar{\Phi}_0) \cdot \sin(n_{rec} \cdot \bar{\Phi}_{t_1}) \right\rangle \qquad (3.35)$$

$$S_y(t_1) = \left\langle \sin(n_{exc} \cdot \bar{\Phi}_0) \cdot \sin(n_{rec} \cdot \bar{\Phi}_{t_1}) \right\rangle \qquad (3.36)$$

[†]For REPT-HSQC pulse sequence see Section C.4.1.
[‡]For REPT-HDOR pulse sequence see Section C.4.2.

From Equation 3.36 it can be seen that the amplitude modulation as a function of t_1 is solely due to the reconversion rotor encoding (RRE) mechanism. The sine dependence of the signal leads to only odd-order spinning-sidebands being produced in the indirect dimension.
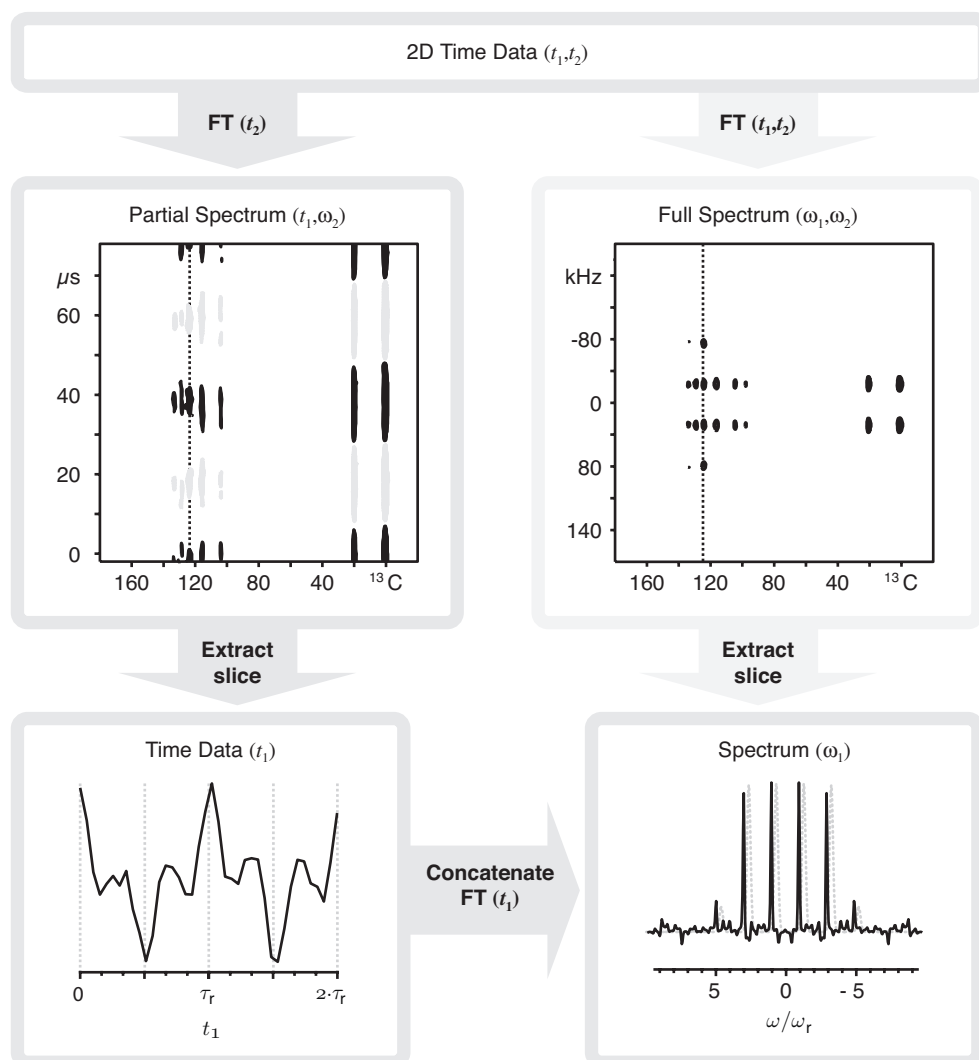
Figure 3.13: *REPT-HDOR processing method. The two-dimensional data (t_1, t_2) upon 2D Fourier transformation yields the sideband patterns as slices in the indirect dimension of the spectrum (ω_1, ω_2) (right). Alternatively, after FT along the direct dimension slices along t_1 can be extracted from the partial spectrum (t_1, ω_2), concatenated and then Fourier transformed to yield the same sideband pattern (left). Overall experimental time is saved using the latter method as less t_1 increments are needed.*

Due to the absence of any contributions from I spin chemical shift, c.f. REPT-HSQC Equation 3.34, phase sensitive detection in t_1 is not needed. Thus the acquisition of only the cosine data reduces the overall experimental time by a factor of two. Another advantage in terms of overall measuring time arises due to the signal in t_1 being periodic, other than the inevitable influence of relaxation. That is, the ideal signal obtained from recoupling the first rotor period is identical to that obtained from any subsequent rotor periods. The influence of relaxation is typically minimal, due to the

difference in time-scale of T_1 relaxation and MAS. However, if relaxation does occur during the t_1 period, the results can easily be corrected for by the application of a suitable linear or exponential function to the indirect time-domain data.

Although all desired information is rotor encoded in a single rotor period, Fourier-transformation with respect to t_1 on the raw data leads to large sinc artefacts being produced in the indirect dimension. These arise due to the uncertainty of the frequency contained within the signal from a single rotor period. However, as the signal contains only a limited number of harmonics, the sideband peak widths can be artificially narrowed by concatenating the signal and applying a window function prior to Fourier Transformation in the indirect dimension. The resulting sideband patterns can be fitted to yield the heteronuclear dipolar coupling constant. [†]

Practically two rotor periods of evolution are recorded and concatenated, this allows the degree of correlated noise, inherent in such a pseudo-time domain signal, to be estimated. With correlated-noise over two rotor periods appearing at half rotor period intervals, an estimation of one rotor period correlated noise in the sidebands is gained.

For multi-spin systems, such as CH_2 and CH_3, the spin-pair formula in Equation 3.36 needs to be replaced by the appropriate formula for the multi-spin systems in question [Saalwächter 01a]. As with REPT-HSQC, the REPT-HDOR experiment exhibits a null in CH_2 signal at $\approx 80\ \mu$s recoupling. Thus the generation of spinning sideband patterns for CH_2 groups with REPT-HDOR is problematic. Access to the CH_2 groups is usually gained by the REREDOR technique (Section 3.4.3). As with the other recoupling experiments generating spinning-sidebands by reconversion rotor encoding, the number of sidebands is influenced by the length of the recoupling time, due to their dependence on $D_{jk} \cdot \tau_{exc/rec}$. Experimentally, it has proven advantageous to choose $D_{jk} \cdot \tau_{exc/rec} \approx 1.6$. The REPT-HDOR experiment makes the determination of heteronuclear dipolar coupling constants in samples with ^{13}C in natural abundance possible within reasonable measuring times.

The sideband patterns generated for REPT-HDOR (Figure 3.14) deviate from those previously encountered for the BABA experiment (Figure 3.9) due to the difference between the homonuclear (Equation 2.71) and heteronuclear (Equation 2.72) dipolar coupling. This results in a factor of $\frac{3}{2}$ difference when comparing RRE sideband patterns produced by HDOR and BABA:

$$\text{SSB}_{BABA}\left(2 \cdot D_{jk} \cdot \tau_{exc/rec}\right) = \text{SSB}_{HDOR}\left(3 \cdot D_{jk} \cdot \tau_{exc/rec}\right) \tag{3.37}$$

[†]For REPT-HDOR sideband simulations see Section D.2.
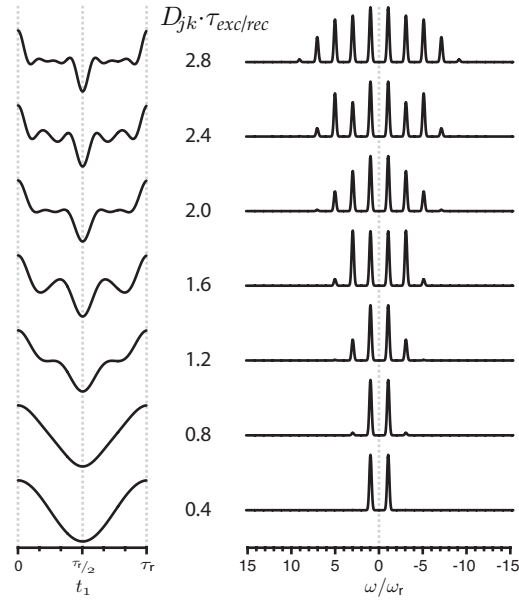
Figure 3.14: *Calculated $S_{SQ}(t_1)$ variation over a rotor period (left) and corresponding REPT-HDOR sideband patterns (right) for various $D_{jk} \cdot \tau_{exc/rec}$ (centre).*
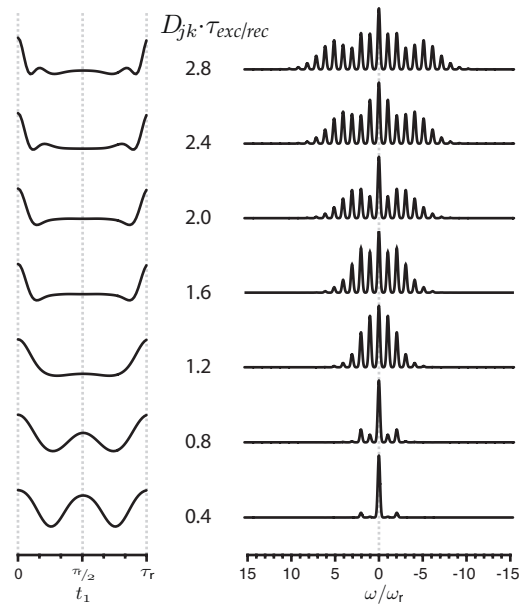
Figure 3.15: *Calculated $S_{SQ}(t_1)$ variation over a rotor period (left) and corresponding REREDOR sideband patterns (right) for various $D_{jk} \cdot \tau_{exc/rec}$ (centre).*

3.4.3 REREDOR

The rotor-encoded REDOR or REREDOR experiment [Saalwächter 02] is based on simply inserting a t_1 delay after *both* excitation *and* recoupling period (Figure 3.10c).[†] Like the REPT-HDOR experiment it can be used to generate spinning sideband patterns by reconversion rotor encoding. The REREDOR time evolution is calculated by summation of the phases acquired under the action of the whole sequence, i.e. $[\tau_{exc} - t_1 - \tau_{rec} - t_1]$:

$$S \propto \left\langle \prod_i \cos \left(n_{exc} \cdot \bar{\Phi}_0^i - [\Phi^i]_0^{t_1} - n_{rec} \cdot \bar{\Phi}_{t_1}^i + [\Phi^i]_{t_1}^{2t_1} \right) \right\rangle \tag{3.38}$$

The product of Equation 3.38 includes the possibility for dipolar couplings to more than one spin and is thus not limited to the spin-pair approximation.

The REREDOR experiment has two main advantages over REPT-HDOR. Firstly, the null in CH_2 group signal intensity at ≈ 80 μs recoupling time is no longer seen. Thus, sufficient higher order sidebands can be created for the precise determination of the dipolar coupling constant. This leads to REREDOR being of particular interest for the investigation of CH_2 groups. Secondly, the experiment produces both even *and* odd order sidebands (Figure 3.16).[‡] Under fast MAS conditions and/or weak dipolar couplings, the two $[\Phi]_t^{t'}$ terms in Equation 3.38 may be neglected as they describe the residual dipolar evolution during the two t_1 periods. By restriction to only the dominant recoupling terms $n_{exc/rec} \cdot \bar{\Phi}_t$ and a single spin-pair interaction, Equation 3.38 becomes:

$$
\begin{aligned}
S \quad &\propto \quad \left\langle \cos(n_{exc} \cdot \bar{\Phi}_0 - n_{rec} \cdot \bar{\Phi}_{t_1}) \right\rangle && \text{(3.39)} \\
&\propto \quad \left\langle \sin(n_{exc} \cdot \bar{\Phi}_0) \sin(n_{rec} \cdot \bar{\Phi}_{t_1}) \right\rangle + \left\langle \cos(n_{exc} \cdot \bar{\Phi}_0) \cos(n_{rec} \cdot \bar{\Phi}_{t_1}) \right\rangle && \text{(3.40)}
\end{aligned}
$$
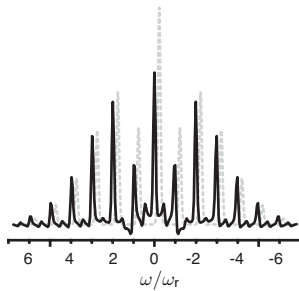
***Figure 3.16**: REREDOR sideband patterns of l-alanine (CH). (solid line) Simulation with $D_{jk} = 21$ kHz, $\omega_r/2\pi = 25$ kHz and $\tau_{exc/rec} = 2 \cdot \tau_r$. (dashed line)*

This clearly shows how both odd and even order sidebands are created from the sine-sine and cosine-cosine terms respectively.[§] Under this approximation, a REREDOR sideband pattern can formally be decomposed into the sum of REPT-HDOR (sine-sine) odd-order only and RELM (cosine-cosine) even-order only sidebands (Figure 3.15).

Since the REREDOR experiment generates more sidebands than the other heteronuclear recoupling methods presented, it is deemed more sensitive. However if the efficiency of the initial cross polarisation step is low then the overall outcome of the experiment may be limited.

[†]For REREDOR pulse sequence see Section C.4.3.
[‡]For REREDOR sideband simulations see Section D.3.
[§]Using: $\cos(A - B) \equiv \cos A \cos B + \sin A \sin B$

Chapter 4

Effects of Ring-Substitutents on Dimer Structure

Previous research showed that the supramolecular structure of model benzoxazine dimers was strongly influenced by the amine-substituent [Schnell 98a]. The dimeric hydrogen bonding structure was found to be most likely for the N-methyl system, while the continuous structure was predominantly seen for the larger N-ethyl, N-propyl and N-butyl systems. With the supramolecular structure closely related to the hydrogen bonding, further investigation into the effect of substituents on the hydrogen bonding was undertaken.
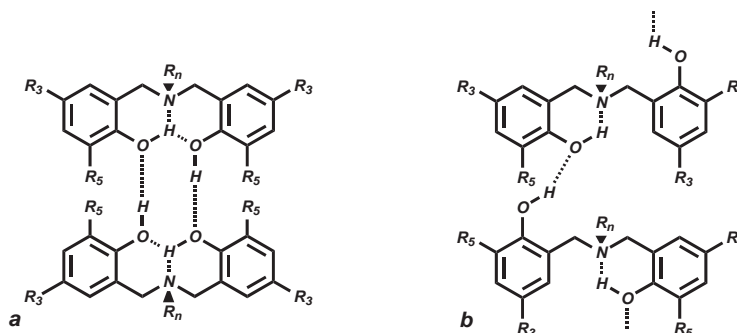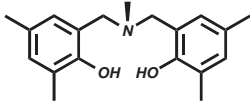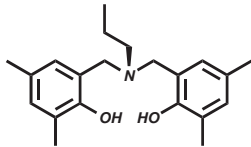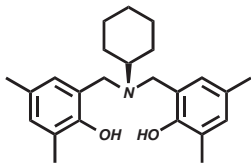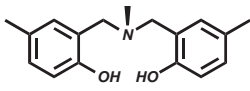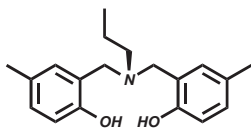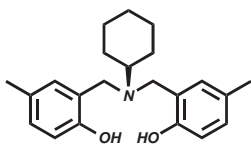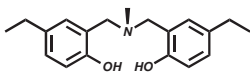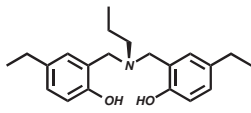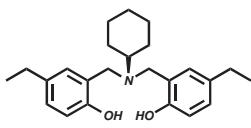
Figure 4.1: *The (a) dimeric and (b) continuous hydrogen bonding structure of the dimers [Schnell 98a].*

In all previous solid-state NMR studies the 3,5-dimethyl ring-substituents remained constant [Schnell 98a, Goward 01, Goward 03]. To investigate the role the ring-substituents on hydrogen bonding a number of compounds with varying amine and ring-substituents were examined. As well as the N-methyl (N-Me) and N-propyl (N-Pr) dimers previously studied, dimers containing a cyclohexyl amine substituent (N-Cy) were also studied. Each class of dimer was available with either 3,5-dimethyl (Me,Me), 3-methyl (H,Me) or 3-ethyl (H,Et) ring-substituents (Table 4.1).

***Table 4.1**: Structure and nomenclature of dimers investigated in Chapter 4.*

	N-methyl	N-propyl	N-cyclohexyl
3,5-dimethyl	Me,Me-N-Me	Me,Me-N-Pr	Me,Me-N-Cy
3-methyl	H,Me-N-Me	H,Me-N-Pr	H,Me-N-Cy
3-ethyl	H,Et-N-Me	H,Et-N-Pr	H,Et-N-Cy

The materials, H,Me-N-Pr, H,Me-N-Cy and H,Et-N-Cy had previously been studied by IR, solution-state NMR spectroscopy and X-ray diffraction, showing further evidence for the dimeric structure [Laobuthee 01]. The three-dimensional geometry of the heavy atoms was known for Me,Me-N-Me and H,Me-N-Cy by X-ray diffraction, both of which showed the dimeric hydrogen bonding structure (Figure 1.2). Crystal structures were also reported to have been measured for H,Me-N-Pr and H,Et-N-Cy by Laobuthee *et al.* [Laobuthee 01] but were to be discussed in a future paper [Chirachanchai 01]. Unfortunately these results were never published. Further attempts to retrieve the remaining two crystals structure failed [Chirachanchai 04].

The thermal degradation of some of these material had also been studied by Hemvichian *et al.* using thermogravimetric analysis (TGA), gas chromatography-mass spectrometry (GC-MS) and FT-IR. [Hemvichian 01, Hemvichian 02b, Hemvichian 02a, Hemvichian 05]. However, other than details regarding the preparation of the Me,Me and H,Me dimers [Hemvichian 02a] the findings of these articles were not found to be relevant to this work.

4.1 Physical properties of model dimers

With nine compounds of similar structure, the first tentative indications of inter-molecular interactions were seen from their respective melting points (Table 4.2). With only small differences in chemical structure found between dimers the strong assumption was made that only molecular weight (Table 4.3) and intermolecular interactions affect the melting point. It should be noted that the melting point can be influenced by many other interactions not considered here.

Table 4.2: Melting points of dimers.

T_m [°C]	N-Me	N-Pr	N-Cy
Me,Me	124.6	117.3	148.3
H,Me	159.3	149.6	175.2
H,Et	130.1	131.2	173.5

Table 4.3: Molecular weights of dimers.

MW [amu]	N-Me	N-Pr	N-Cy
Me,Me	299.2	327.5	367.5
H,Me	271.2	299.4	339.5
H,Et	299.2	327.5	367.5
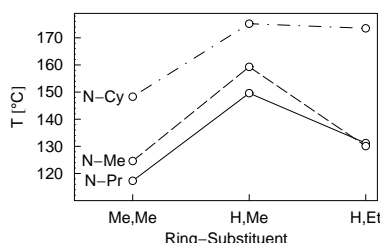
Figure 4.2: Correlation of melting point with amine and ring-substituents.
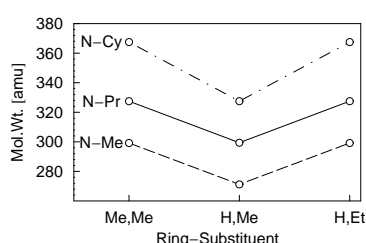
Figure 4.3: Correlation of molecular weight with amine and ring-substituents.

Comparison of the melting points of systems with the same amine substituent showed the influence of the ring-substituents (Table 4.4).

Table 4.4: Differences between melting points of studied dimers: ring-substituent effects.

ΔT_m [°C]	N-Me	N-Pr	N-Cy
Me,Me→H,Me	+34.4	+32.3	+27.0
Me,Me→H,Et	+5.4	+13.9	+25.2
H,Me→H,Et	-29.2	-18.4	-1.7

When comparing Me,Me→H,Me systems, the melting point was seen to increase as the molecular weight decreased, suggesting the strengthening of intermolecular interactions. The increase in melting point varied from $\approx$ 27–34°C, with ΔT_m N-Me > N-Pr > N-Cy. A similar increase in melting point for similar molecular weights was seen for Me,Me→H,Et. In contrast, the opposite effect was seen for H,Me→H,Et. With these systems the melting point decreased by 2–29°C as the molecular weight increased, suggesting a weakening of the intermolecular interactions. The small 1.7°C difference between H,Me-N-Cy and H,Et-N-Cy could imply that only small changes in intermolecular interaction occurred upon changing ring-substituents, and is anomalous. In general T_m H,Me > H,Et > Me,Me, with the same trend suggested for the strength of intermolecular interaction in the dimers.

Comparison of the melting points of dimers with the same ring-substituents showed the effect of the amine substituent (Table 4.5).

Table 4.5: *Differences between melting points of studied dimers: amine substituent effects.*

ΔT_m [°C]	N-Me→N-Pr	N-Me→N-Cy	N-Pr→N-Cy
Me,Me	-7.3	+23.7	+31.0
H,Me	-9.7	+15.9	+25.6
H,Et	+1.1	+43.4	+42.3

As expected, the general effect upon changing from N-Me→N-Pr was less pronounced then from N-Me→N-Cy, or from N-Pr→N-Cy. For N-Me→N-Pr even though the molecular weight increased, the melting point decreased or remained approximately constant with $\Delta T_m \approx 1.1$°C. This suggested less intermolecular interaction in the N-Pr systems than the N-Me systems. Comparison of both N-Me and N-Pr systems to N-Cy systems showed that both the molecular weight and melting point increased. The change of 16–44°C when comparing N-Me and N-Pr to N-Cy reflected a combination of molecular weight and intermolecular interaction differences. Both of which caused by the increased bulk of the cyclohexyl amine substituent. As was previously suggested the melting point of H,Et-N-Cy seems anomalous, and indicated a different structure to that of H,Et-N-Pr was present. In general, T_m N-Cy > N-Me > N-Pr, with the stronger intermolecular interactions suggested for the N-Me dimers due to their higher than expected melting points.

4.2 NMR spectroscopy of model dimers

With the form of the proton spectra strongly dependent on the amine substituent [Schnell 98a], analysis by NMR was divided into three sections. Firstly, the effect of different ring substituents on dimers with the same amine substituents (Section 4.2.1). Secondly, the effects of different amine substituents on dimers with the same ring substituents (Section 4.2.2), and finally general trends across all nine dimers will be discussed (Section 4.2.3).

In proton rich rigid spin systems ^{1}H–^{1}H dipolar coupling is the dominant line broadening interaction, thus homonuclear dipolar decoupling by MAS was a prerequisite for resolution in proton solid-state NMR. At present, commercially available MAS probeheads are limited to a maximum spinning frequency of $\omega_r/2\pi = 35$ kHz [Bruker 97]. Although the resulting proton spectra are much improved, the effects of remaining ^{1}H–^{1}H dipolar couplings, not averaged under these conditions, broaden the spectra. Despite this, much information can be gathered from these relatively low resolution spectra. Recently, custom built MAS probeheads capable of spinning samples at rotational frequencies of up to $\omega_r/2\pi = 70$ kHz have been developed by the group of Dr. Ago Samoson at the National Institute of Chemical Physics and Biophysics (NICP), Tallinn, Estonia [Samoson 03]. With the model polybenzoxazine dimers already showing promising resolution at 30 kHz MAS [Schnell 98a, Goward 01], measurements at higher MAS frequencies were made in collaboration with the group of Dr. Samoson. The gain in resolution achieved by this, herein termed, fast-MAS was clearly illustrated by comparison of spectra measured at incremental spinning speeds from 5–65 kHz (Figure 4.4).
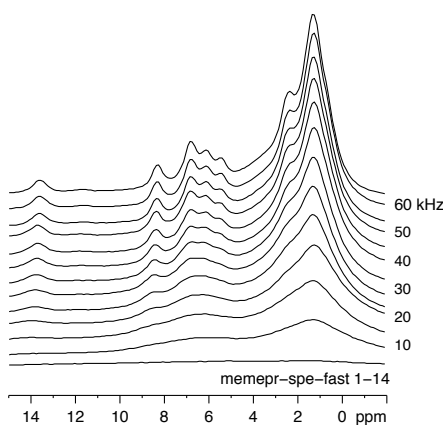
Figure 4.4: *^{1}H SPE spectra of Me,Me-N-Pr measured at different MAS spinning frequencies of $\omega_r/2\pi = 5$–65 kHz.*
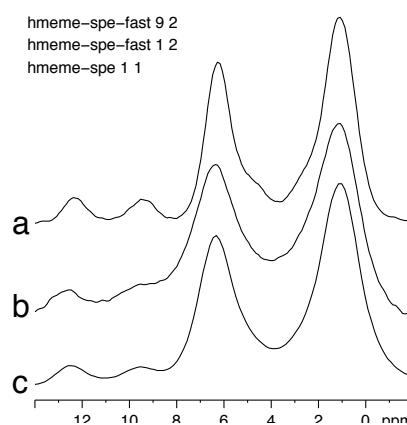
Figure 4.5: *^{1}H SPE spectra of H,Me-N-Me with different ν_{1H} (MHz) and $\omega_r/2\pi$ (kHz): (a) 600/70, (b) 600/30 and (c) 700/30.*

At 30 kHz MAS greater resolution was seen with ν_{1H} = 700 MHz at the MPIP (Figure 4.5c), as compared to ν_{1H} = 600 MHz at the NCIP (Figure 4.5d). However, the loss of resolution seen when going to a lower B_0 field was compensated for, and sometimes improved upon, by the increased spinning frequency (Figure 4.5a).

4.2.1 Proton spectroscopy: amine substituent trends

Comparison of N-methyl dimers

For the mono ring substituted systems, H,Me‑N‑Me and H,Et‑N‑Me, the SPE spectra showed clear evidence of both N··H‑O and O··H‑O hydrogen bonding (Figure 4.6e–f). Due to their high chemical shift of ≈ 9.4 ppm the O··H‑O hydrogen bonding protons were partially resolved in the 1D spectra. This was in contrast to Me,Me‑N‑Me where the O··H‑O protons at 6.5 ppm were obscured by the stronger aromatic protons at 6.3 ppm (Figure 4.6d). The chemical shifts of the N··H‑O protons in the mono ring substituted systems were also seen to be higher than for those of Me,Me‑N‑Me, both appearing at ≈ 12.3 ppm (Figure 4.6e–f) as compared to 11.7 ppm (Figure 4.6d). This higher chemical shift was indicative of stronger hydrogen bonding, with the shorter proton-heteroatom internuclear distance resulting in increased proton chemical shift [Jeffrey 86].
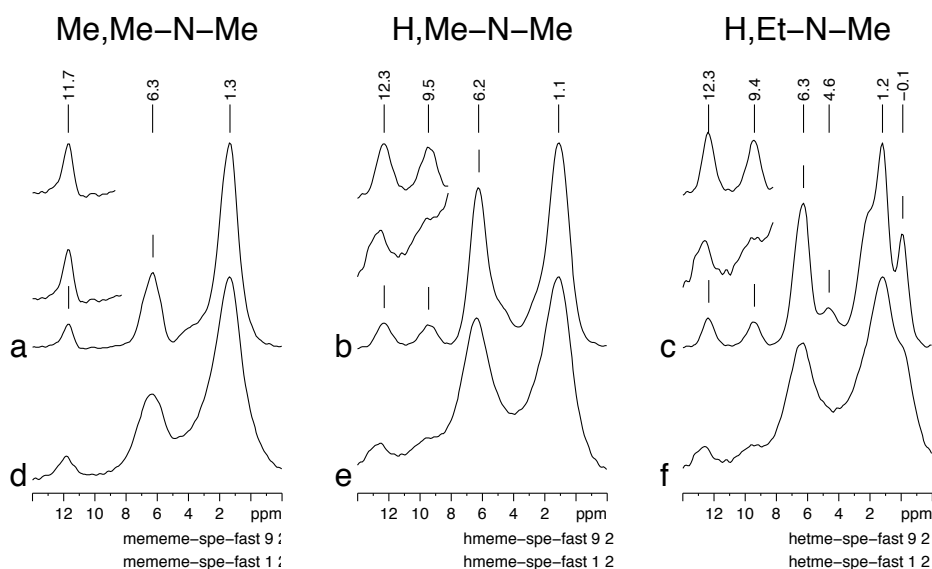
Figure 4.6: *SPE spectra of N-Me Dimers: (a–c) $\omega_r/2\pi = 70$ kHz and (d–f) $\omega_r/2\pi = 30$ kHz*

At 70 kHz MAS the hydrogen bonding peaks were further resolved (Figure 4.6a–c) allowing accurate determination of chemical shift values without the need for deconvolution. At higher spinning speed the H,Et‑N‑Me aliphatic peak clearly showed a shielding interaction with a lower than expected chemical shift of −0.1 ppm. This was only present as a shoulder in the 30 kHz MAS spectra (Figure 4.6f). The shielding suggested close proximity of this site to an aromatic system, with the decreased chemical shift indicating a facial interaction (Section 2.1.4 & Figure 2.9). In general the CH$_2$ protons also became more resolved at 4.6 ppm in all three spectra under the faster MAS conditions.

Dipolar exchange spectroscopy showed dense spin systems for all three N-Me dimers, with the aromatic protons readily exchanging magnetisation with the N··H-O and O··H-O protons (Figure 4.7a). Although the rate of spin-diffusion was further suppressed at 65 kHz MAS the same rapid communication between aromatic and the hydrogen bonding protons was still observed (Figure 4.7b). Unfortunately, at higher MAS frequencies a large negative spectral artefact was seen at the centre of all the dipolar exchange spectra, appearing as a negative auto peak at 7 ppm (Figures ring/hetme-noseyb–4.8). The origin of this artifact is currently unknown but, could be related to the relatively high degree of background signal seen with such small rotors.
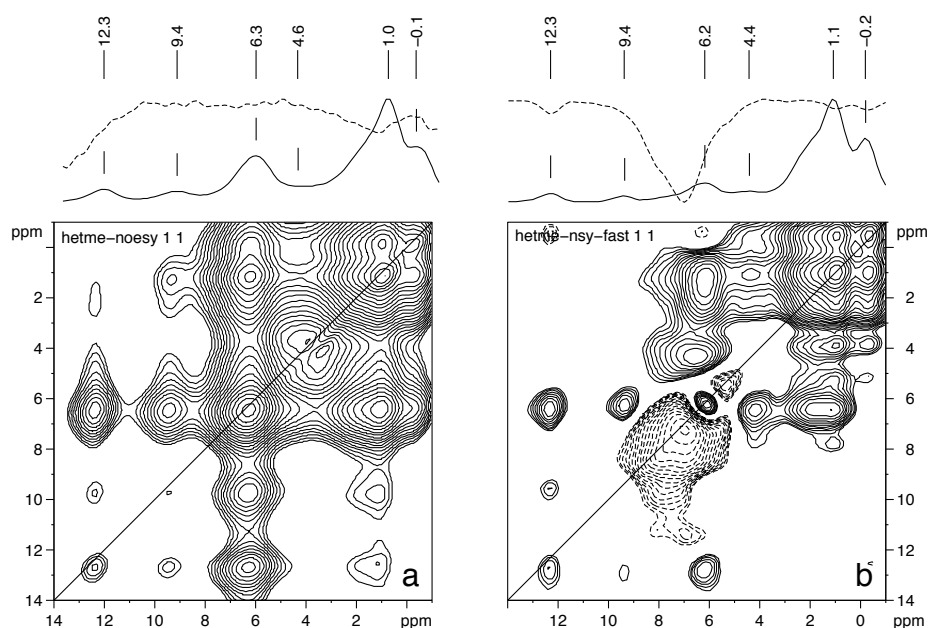
Figure 4.7: *Dipolar Exchange spectra of H,Et-N-Me with $\tau_{mix} = 50$ ms: (a) $\omega_r/2\pi = 30$ and (b) $\omega_r/2\pi = 65$ kHz. Positive (solid) and negative (dashed) projections shown illustrating negative artefact.*
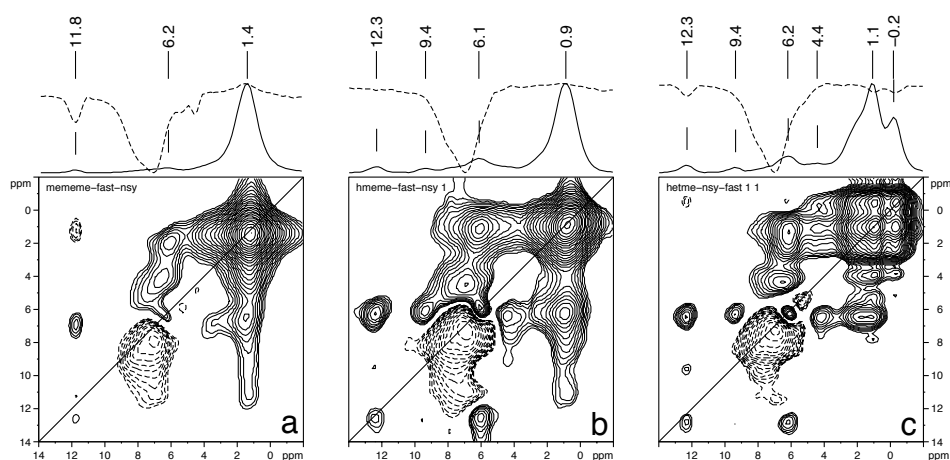
Figure 4.8: *Dipolar exchange spectra of N-Me dimers at $\omega_r/2\pi = 65$ kHz with $\tau_{mix} = 50$ ms: (a) Me,Me (b) H,Me and (c) H,Et. Positive (solid) and negative (dashed) projections shown illustrating negative artefacts*

For H,Et-N-Me a negative cross-peak was observed between the N··H-O and shielded aliphatic protons at 12.3 and −0.2 ppm respectively (Figure 4.8c). A similar negative cross-peak was observed for the N··H-O and aliphatic protons, at 11.8 and 1.4 ppm, of Me,Me-N-Me (Figure 4.8a). Similar negative cross-peaks were observed for some of the N-Pr dimers at 30 kHz and are thus thought to not be artefacts themselves, or be related to the large central negative artefact at 7 ppm. The origin of these negative cross-peaks will be discussed in full for the N-Pr systems later (Section 4.2.1).

As with Me,Me-N-Me the mono ring-substituted dimers also show relatively high resolution 2D DQ correlation spectra with improved resolution seen in the 65 kHz MAS spectra (Figure 4.10b). Under the fast-MAS conditions phase errors for the methyl protons were seen in the indirect dimension. This possibly indicated a problem with the recoupling of the mobile methyl groups under these conditions.
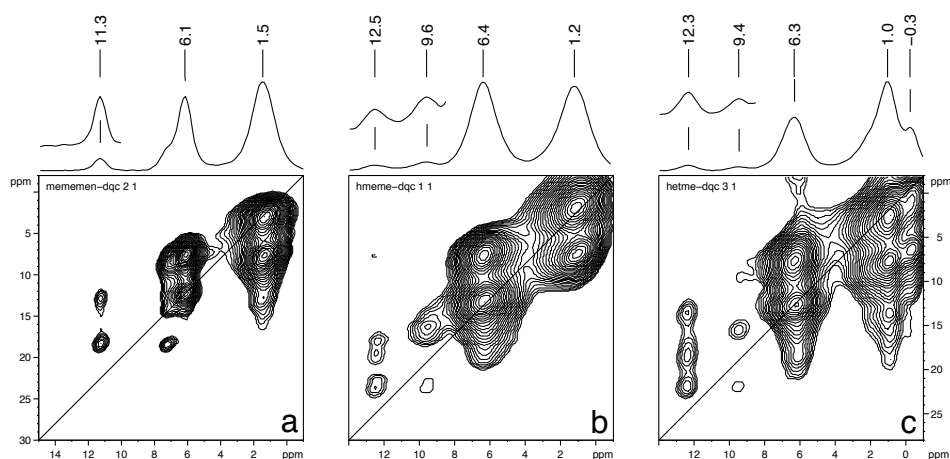
Figure 4.9: *DQ correlation spectra of the N-Me dimers at $\omega_r/2\pi = 30$ kHz*
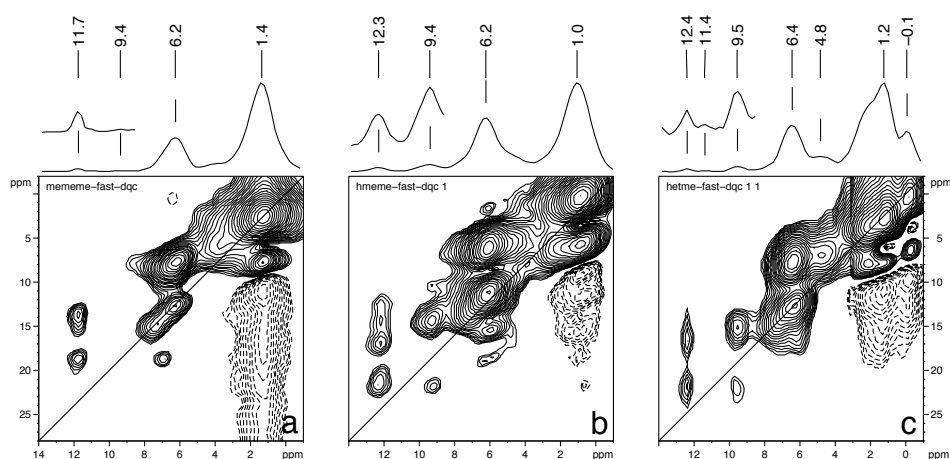
Figure 4.10: *DQ spectra of the N-Me dimers at $\omega_r/2\pi = 65$ kHz MAS: (a) Me,Me, (b) H,Me and (c) H,Et.*

All DQ spectra showed correlations between the N··H‑O and O··H‑O protons indicating their close proximity (Figures 4.9 &4.10). This suggested a supramolecular structure formed by co-operative hydrogen bonding. Correlation was also seen between the N··H‑O and methyl amine group in all three N‑Me dimers. In H,Me‑N‑Me and H,Et‑N‑Me the N··H‑O proton also correlated with the aromatic protons suggesting the presence of the continuous hydrogen bonding structure (Figure 4.10b–c). This DQ correlation (DQC) was relatively weak for H,Me‑N‑Me possibly indicating the presence of a combination of both dimeric and continuous supramolecular structure, as previously suggested for Me,Me‑N‑Me [Schnell 98a]. With the DQC being much stronger for H,Et‑N‑Me, a higher amount of the continuous states was suggested. The deshielded proton of H,Et‑N‑Me at −0.1 ppm was found to correlate with aromatic protons and implied that these protons belonged to the terminal methyl groups of the ethyl ring-substituents (Figure 4.10c). However, due to geometric constraints it is thought that such shielding interactions have a higher chance of being intermolecular as opposed to intramolecular in origin.

Summary

Proton SPE and DQ spectra, under both MAS conditions, bore close resemblance to that of Me,Me-N-Me. The increase of N··H-O and O··H-O chemical shift implied that the hydrogen bonding in the mono ring-substituted dimers were comparable to each other, and stronger than those found in Me,Me-N-Me. The resemblance of the DQ spectra also implied that H,Me-N-Me and H,Et-N-Me had similar supramolecular structures. Weak DQ coherence seen between the N··H-O and aromatic protons for H,Me-N-Me and H,Et-N-Me showed that to some degree the continuous hydrogen bonding structure was also present for these compounds. The strong intensity of this correlation in H,Et-N-Me, as compared to H,Me-N-Me, suggested that the continuous structure was more dominant as compared to H,Me-N-Me. Proton DQ spectroscopy of H,Et-N-Me also assigned the shielded protons at −0.1 ppm to the two terminal methyl groups of the ethyl ring-substituents.
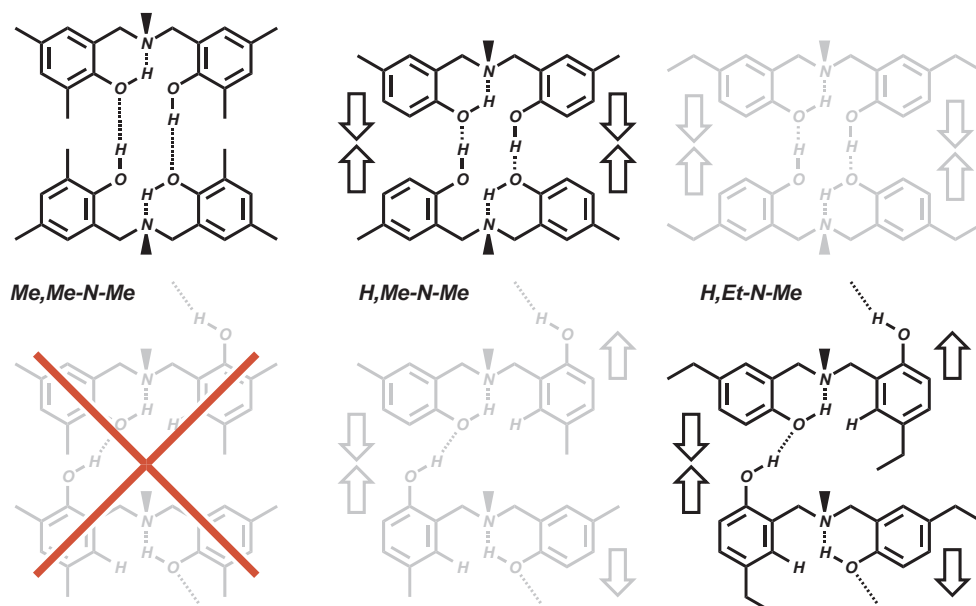
Figure 4.11: *Suspected structures of the N-Me dimers. Less dominant forms shown in grey.*

Comparison of N-propyl dimers

As with the N-Me dimers, both mono-ring substituted N-Pr dimers also showed evidence of N··H-O and O··H-O hydrogen bonding. The chemical shifts of the hydrogen bonding sites were similar for H,Me-N-Pr and H,Et-N-Pr (Figure 4.12).
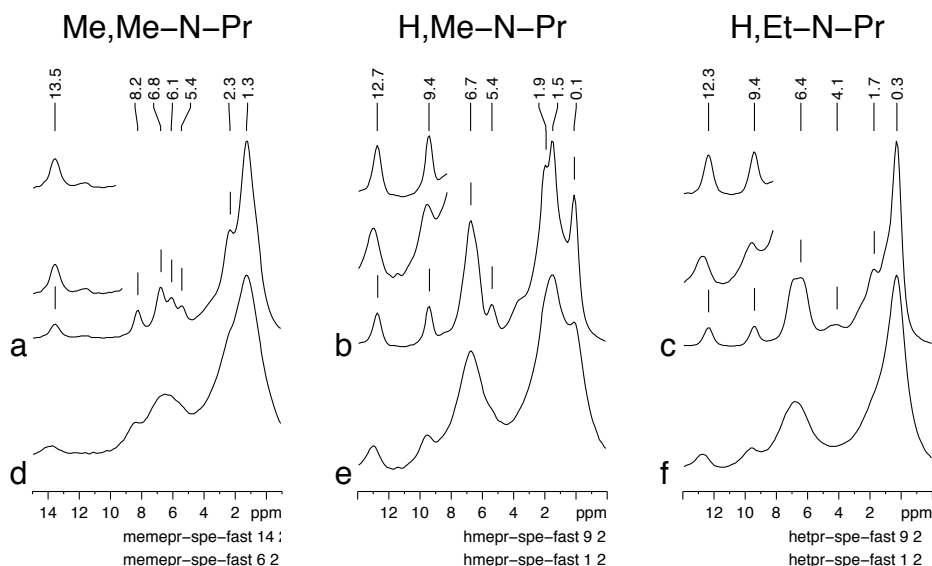
Figure 4.12: *SPE spectra of N-Pr dimers: (a–c) $\omega_r/2\pi = 70$ kHz MAS and (d–f) $\omega_r/2\pi = 30$ kHz MAS.*

As was seen for the N-Me dimers, both mono ring-substituted dimers have similar N··H-O and O··H-O proton chemical shifts, indicating similar bond lengths. However, unlike the N-Me dimers, Me,Me-N-Pr had the highest overall N··H-O chemical shift. Surprisingly, the O··H-O chemical shifts of Me,Me-N-Pr showed the opposite trend, being the lowest of all three N-Pr dimers. This indicated that possibly a different supramolecular structure was present for the mono and di ring-substituted systems. The O··H-O sites were more clearly seen under 70 kHz MAS (Figure 4.12a–c). Under such conditions further resolution in the aromatic region was seen for Me,Me-N-Pr, and serves as a good example of the resolution gains achievable by fast-MAS (Figure 4.4). In H,Et-N-Pr most of the methyl protons were found to experience shielding interactions, as seen for H,Et-N-Me, with a chemical shift of 0.3 ppm (Figure 4.12c). Further shielding was seen for H,Me-N-Pr. Although most methyl groups remained unaffected (1.5–1.9 ppm), one methyl group experienced a shielding interaction was seen at 0.1 ppm (Figure 4.12b). In Me,Me-N-Pr and H,Me-N-Pr further methyl sites were identified, other than those affected by shielding. These were attributed to the propyl amine-substituent and the associated effect of the nitrogen heteroatom on the chemical shift.
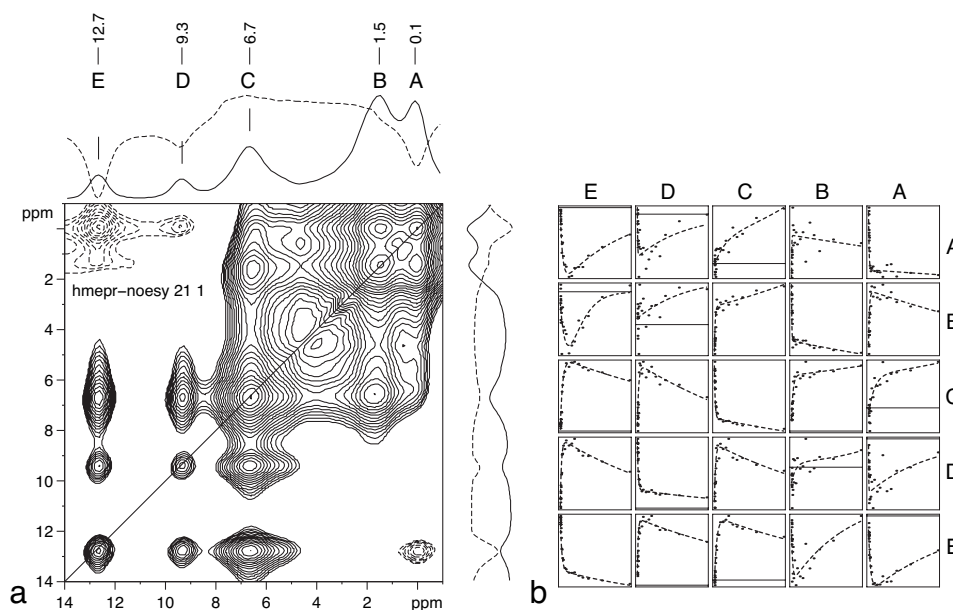
Figure 4.13: *Dipolar Exchange spectrum of H,Me-N-Pr under $\omega_r/2\pi = 30$ kHz MAS: (a) Spectrum with $\tau_{mix} = 50$ ms. Both positive (solid) and negative (dashed) projections are shown for both dimensions. (b) Cross-peak build-up behaviour from $\tau_{mix} = 50$ μs to 250 ms)*

As was previously seen for the dipolar exchange spectra of H,Et-N-Me, negative cross-peaks were observed for all N-Pr dimers. For H,Me-N-Pr, both the N··H-O and O··H-O sites formed negative cross-peaks with the shielded methyl protons at a mixing time of $\tau_{mix} = 50$ ms under 30 kHz MAS. These negative cross-peaks were more clearly seen when both the positive and negative projections were shown for the direct and indirect dimensions of a dipolar exchange spectrum (Figure 4.13a)

By varying τ_{mix} and integrating the peak intensity in defined regions, the rate of magnetisation transfer and decay was followed (Figure 4.13b). From these build-up curves time constants for the magnetisation buildup t_a (Table 4.6) and decay t_b (Table 4.7) processes were obtained by fitting the experimental data to the double exponential function:

$$I = I_a^0 \cdot \exp\left\{ -\frac{\tau_{mix}}{t_a} \right\} + I_b^0 \cdot \exp\left\{ -\frac{\tau_{mix}}{t_b} \right\} \tag{4.1}$$

Due to the problems associated with integrating two-dimensional spectra containing broad lines, the extracted time constants are considered to have relatively large error. For simplicity the integration regions have been replaced by the letters A–E, with E corresponding to the N··H-O protons and A to the shielded methyl protons. Even at long mixing times the cross peaks EA, DA and EB, and their diagonal opposites AE, AD and BE, remained negative and did not return to their equilibrium state via positive signal intensity (Figure 4.13b).

Magnetisation was also found to be transferred approximately seven times faster between the methyl and the N··H-O protons (AE,EA) than between the methyl and the O··H-O protons (AD,DA) (Table 4.6). These cross peaks also decay with time constants similar to that of the N··H-O and O··H-O protons, 178–324 ms (Table 4.7).

Table 4.6: Intensity buildup time constants, t_a

ms	E	D	C	B	A
A	8.7	1.2	39.6	0.8	2.0
B	25.5	396.6	2.8	1.3	3.2
C	8.3	5.0	2.8	6.0	21.1
D	4.4	3.0	4.3	15.3	0.8
E	5.4	3.0	8.3	4.2	7.3

Table 4.7: Intensity decay time constants, t_b

ms	E	D	C	B	A
A	235	178	-334	3342	2980
B	43	507	-879	1316	1226
C	651	627	749	-1615	-795
D	483	413	582	-199	225
E	419	587	574	209	324

The sign inversion of the cross-peak was not believed to be an artefact, being both reproducible and present for other systems. The origin of the sign inversion was thought to be related to the mobility of the sites involved. With nuclear cross-relaxation caused by mutual spin flips in pairs of dipolar-coupled spins the time-scale of the motional processes which induce these spin flips, relative to the Larmor frequency ω_L, becomes important [Ernst 87]. Thus, the distinction between the fast-motion and slow-motion limits is made based on the motional correlation time τ_c of the species. The fast-motion limit corresponds to species with short correlation times ($\tau_c \ll \omega_L^{-1}$) and the slow-motion limit to those with long correlation times ($\tau_c \gg \omega_L^{-1}$). When the probabilities of the ZQ, SQ and DQ transitions for a coupled AB spin system are considered, a clear difference in behaviour is observed between the two motional limits (Figure 4.14).
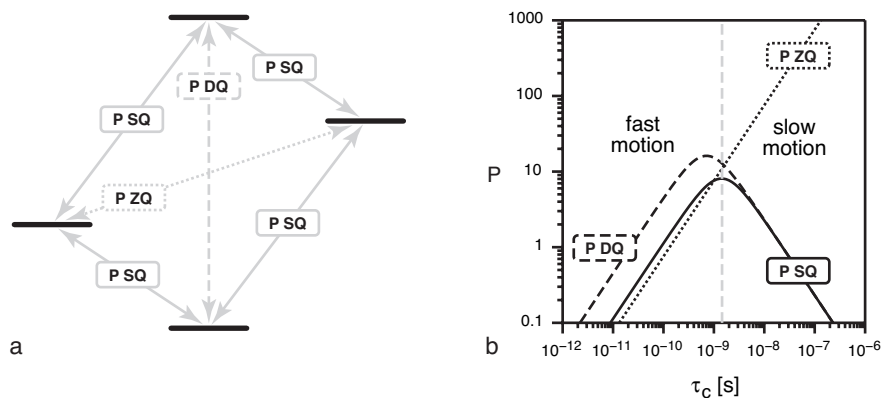
Figure 4.14: *The (a) transition probabilities P ZQ, P SQ and P DQ and (b) their dependence on correlation time τ_c for homonuclear ^1H–^1H cross-relaxation at $\omega_L/2\pi = 700$ MHz.*

For long correlation times, the ZQ transition probability dominates. With this process responsible for energy-conserving flip-flop transitions ($\alpha\beta \leftrightarrow \beta\alpha$), an exchange in energy occurs between the two coupled spins resulting in positive cross-peaks. However, for short correlation times the DQ transition probability dominates. This leads to flop-flop transitions ($\alpha\alpha \leftrightarrow \beta\beta$) dominating. The resulting negative cross-peaks are explained by the fact that a spin may lose a quanta of energy preferably

when a second spin also loses one. As a result a mutual enhancement of relaxation is observed, rather than an exchange of magnetisation.

In the context of H,Me-N-Pr, the majority of the sites were in the slow-motion regime, thus the ZQ spin-diffusion pathway dominated resulting in positive cross-peaks being observed. In contrast, the rapidly rotating methyl group of the propyl amine-substituent was in the fast-motion regime. The negative cross-peaks were therefore observed due to the DQ cross-relaxation pathway being dominant. Hence, only between the relatively isolated N··H-O proton and the rapidly rotating methyl groups were these effects observed. Such a distinction between these sites was most likely caused by the simplification of the dipolar-network under the MAS condition employed.

Although hampered by the strong negative central artefacts seen before with the N-Me dimers, negative cross peaks were also seen for all N-Pr dimers under fast-MAS (Figure 4.15). The origin of the these large central artefacts and as to why the spectra of H,Et-N-Pr seems not affected is at present unclear.
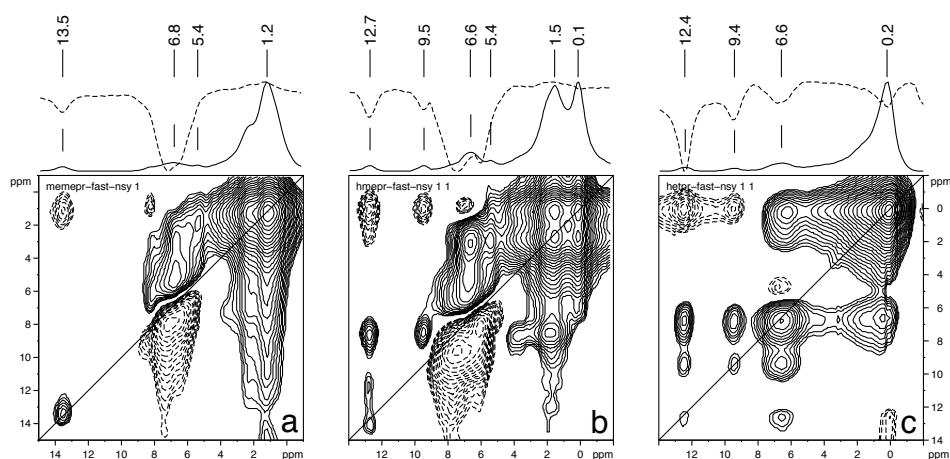
Figure 4.15: *Dipolar exchange spectra of the N-Pr dimers at $\omega_r/2\pi = 65$ kHz MAS. Positive (solid) and negative (dashed) projections shown illustrating negative cross-peaks and artefacts.*

The DQ correlation spectra of the N-Pr systems showed multiple correlation to the N··H-O and O··H-O hydrogen bonding protons (Figure 4.16). Strong similarities were seen between H,Me-N-Pr and H,Et-N-Pr with the only major difference found in aliphatic resolution. The increased resolution of H,Me-N-Pr was most probably caused by a combination of the relative intensities of the sites and the greater shielding. Compared to the DQ spectra of Me,Me-N-Pr with a broad methyl region and unresolved O··H-O site (Figure 4.16a), higher resolution was seen for the mono ring-substituted N-Pr dimers. As for H,Et-N-Me, the shielded protons were found to correlate strongly with the aromatic protons, again suggesting the shielded protons were associated with the ethyl ring-substituents. For the N-Pr dimers a second possibility also arises, that of the terminal methyl group of the propyl amine-substituent. Evidence for this alternative assignment was found in the

DQ spectrum of H,Me-N-Pr, where shielded methyl protons were observed despite no ethyl ring-substituents being present (Figure 4.16b). This assignment also applied to H,Et-N-Pr, with both propyl amine and ethyl ring-substituents contributing to the peak at 0.3 ppm (Figure 4.16c). In both mono ring-substuted dimers DQ correlation was seen between both N··H-O and O··H-O hydrogen bonding protons and aromatic protons, thus indicating the continuous hydrogen bonding structure. These correlations were however weak and as with H,Me-N-Me could indicate either a weak interaction or a mixture of dimeric and continuous structures.
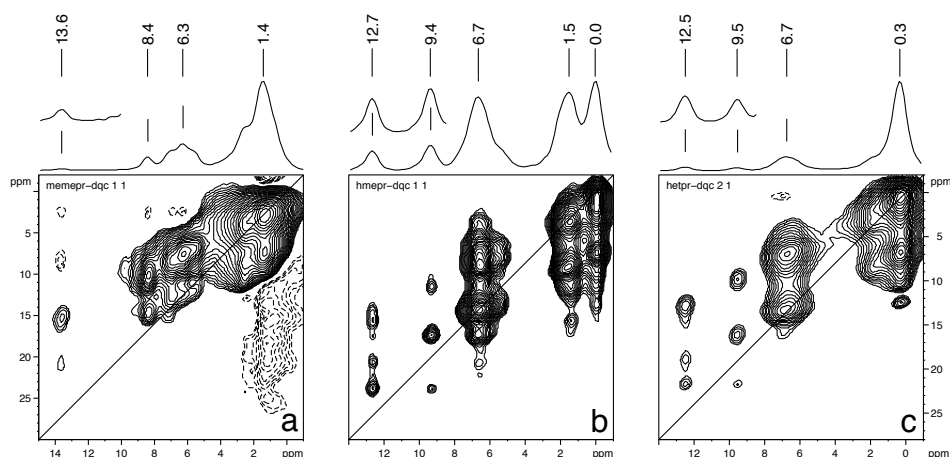
Figure 4.16: *DQ correlation spectra of the N-Pr dimers at $\omega_r/2\pi = 30$ kHz*

In the DQ spectra of Me,Me-N-Pr a number of negative cross-peaks were seen (Figure 4.16a). The position of these peaks did not correspond to the double-quantum coherence expected for this type of DQ spectroscopy. These cross-peak did however occur between the sites which previously had given rise to negative cross-peaks in dipolar-exchange spectra. It was thus thought that these peaks resulted from the 'break-through' of the DQ mediated SQ–SQ correlation (dipolar-exchange) signal, as both DQ pathways would have been allowed by the phase cycle. This provided credence to the double-quantum origin of the negative cross-peaks seen in the dipolar-exchange spectra.

With the shielded protons of H,Me-N-Pr occurring at the unusual chemical shift of 0.0 ppm triple quantum (TQ) spectroscopy was used to confirm the assignment. Comparison of DQ and TQ spectra allowed all four possible TQ coherences involving the shielded methyl protons and the aromatic protons to be assigned (Figure 4.17). Due to the higher number of artefacts seen in TQ spectroscopy no further assignments were made for fear of over-interpreting the spectrum. For example, the presence of three O··H-O protons in close proximity is suggested by the O··H-O auto peak at 9.4 ppm, although this physical situation is thought to be extremely unlikely.
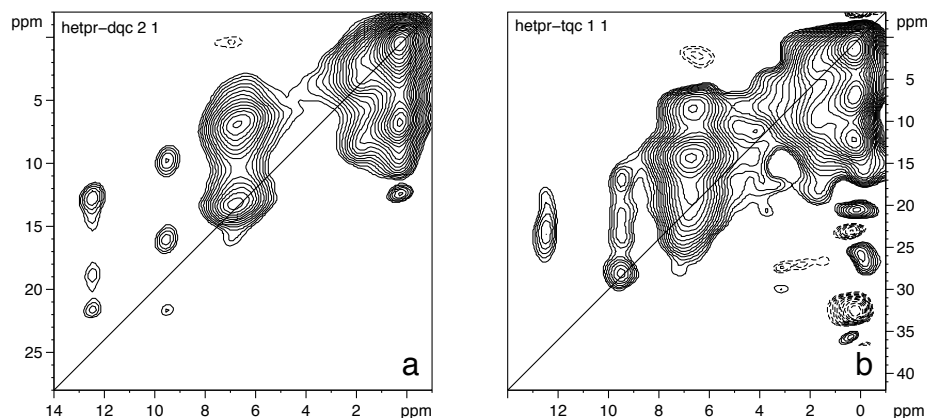
Figure 4.17: *(a) DQ and (b) TQ correlation spectra of H,Et-N-Pr $\omega_r/2\pi = 30$ kHz*

Under fast-MAS an improvement in DQ spectral resolution was not seen for the N-Pr dimers (Figure 4.18). This was thought to be due to the frictional heating caused by MAS as Me,Me-N-Pr, the dimer with the lowest melting point (Table 4.2), had the worst resolution. For MAS at $\omega_r/2\pi = 35$ kHz frictional heating of 30–40°C has been found using $Sm_2Sn_2O_7$ [Langer 99] and vanadocene [Köhler 97] as chemical shift thermometers. Under fast-MAS these effects are expected to lead to even higher discrepancies between ambient and sample temperatures. Unfortunately no temperature calibration was undertaken under for the fast-MAS conditions.
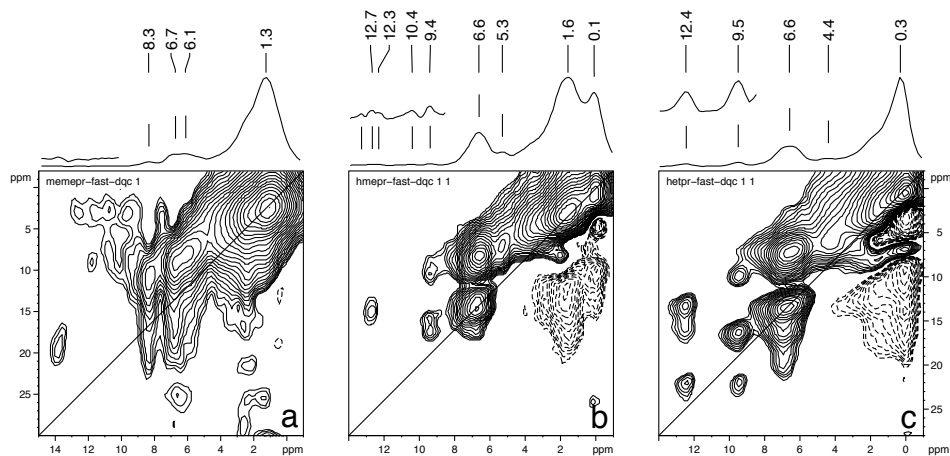
Figure 4.18: *DQ correlation spectra of N-Pr Dimers at $\omega_r/2\pi = 65$ kHz*

Summary

In general the proton SPE and DQ spectra bore close resemblance to that of Me,Me-N-Me. The decrease of N··H-O chemical shift implied that the hydrogen bonding in the dimethyl ring-substituted dimer Me,Me-N-Pr was stronger than that found in the two mono ring-substituted dimers. In contrast, the O··H-O hydrogen bonding showed the opposite trend with higher chemical shifts found for both H,Me-N-Pr and H,Et-N-Pr. As with the N-Me dimers the DQ spectra of the two mono ring-substituted dimers bore close resemblance, and suggested a similar supramolecular structure. For both systems weak DQ coherence were seen between the N··H-O and aromatic protons showing the continuous hydrogen bonding structure was present, to some degree, for these compounds as well. Surprisingly, no evidence of the continuous structure was seen for Me,Me-N-Pr in contrast to what has previously been reported by Schnell *et al.* [Schnell 98a]. However, when the previously published DQ spectrum of Me,Me-N-Pr was re-examined this seemed to be the only major difference. This suggested that in these two investigations different forms of Me,Me-N-Pr had been examined, again indicating the ability of the dimers to exist in both dimeric and continuous hydrogen bonding structures. Proton DQ spectroscopy of H,Et-N-Pr, as with H,Et-N-Me, also assigned the shielded protons at 0.3 ppm to the two terminal methyl groups of the ethyl ring-substituents. However, for the N-Pr dimers interaction via the terminal methyl group of the amine-substituent was also seen to be possible. These protons were found at 0.0 ppm for H,Me-N-Pr, with the assignment comfirmed by TQ NMR.
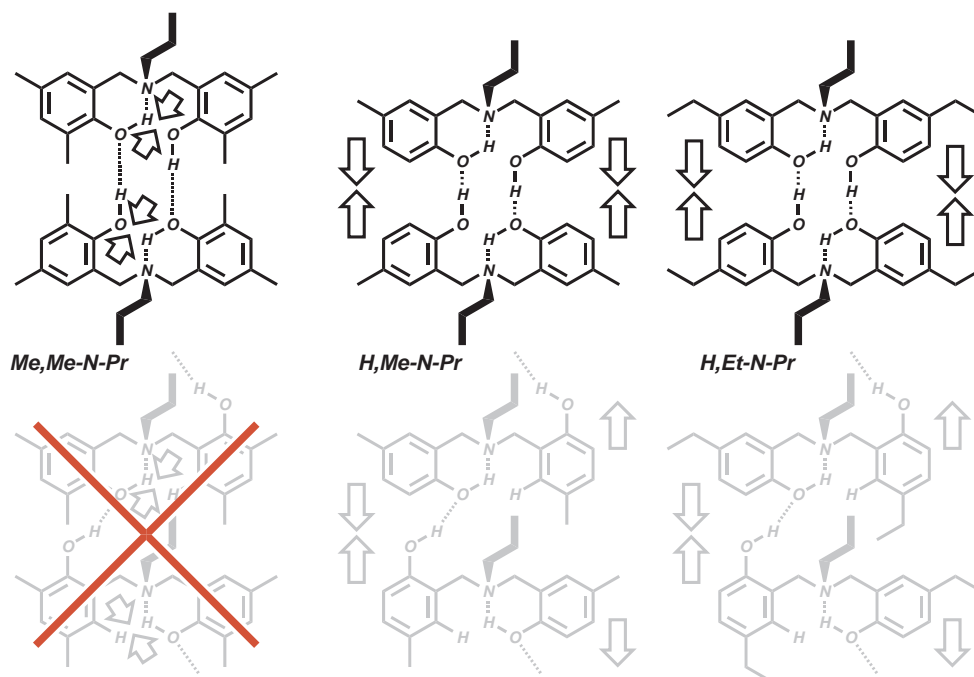
***Figure 4.19**: Suspected structures of the N-Pr dimers. Less dominant forms shown in grey.*

Comparison of N-cyclohexyl dimers

The N-Cy dimers showed a similar trend in chemical shift of the protons involved in hydrogen bonding as the N-Me dimers. The O··H-O proton of Me,Me-N-Cy had a similar chemical shift to aromatic protons, and thus were obscured in the SPE spectrum. For the mono ring-substituted systems both N··H-O and O··H-O proton chemical shifts were higher than those seen in Me,Me-N-Cy (Figure 4.20). Unlike the N-Me and N-Pr systems, evidence of shielding interactions were seen in the Me,Me dimer at 0.5 ppm (Figure 4.20a). Such shielding was also found in H,Et-N-Cy, with the main aliphatic peak found at 0.3 ppm (Figure 4.20c), as seen in H,Et-N-Pr. The influence of ring-currents was not seen for H,Me-N-Cy, however due to the wide base of the aliphatic peak shielded sites might be obscured (Figure 4.20b).
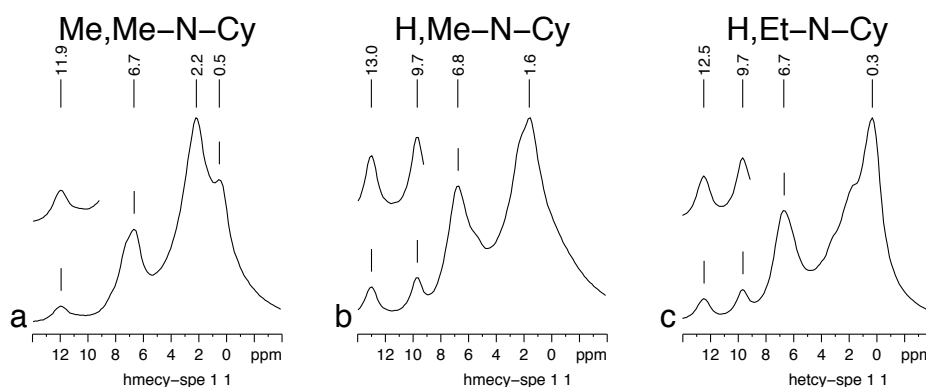
Figure 4.20: *SPE spectra of the N-Cy dimers at $\omega_r/2\pi = 30 ZkHz$*

Unfortunately fast-MAS spectra were only available for H,Et-N-Cy (Figure 4.21). This showed further resolution of the O··H-O and aliphatic regions. A slight shift to lower chemical shift values was seen for the N··H-O and O··H-O protons when comparing spectra, with this most likely being due to the MAS heating effects.
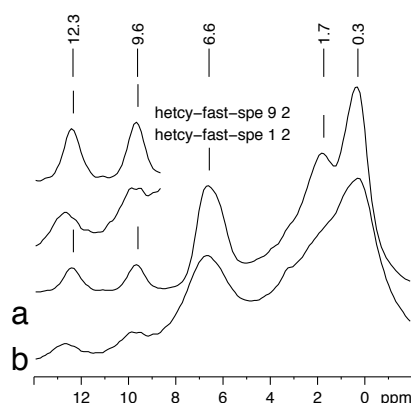
Figure 4.21: *SPE spectra of H,Et-N-Cy at (a) $\omega_r/2\pi = 70$ and (b) 30 kHz.*
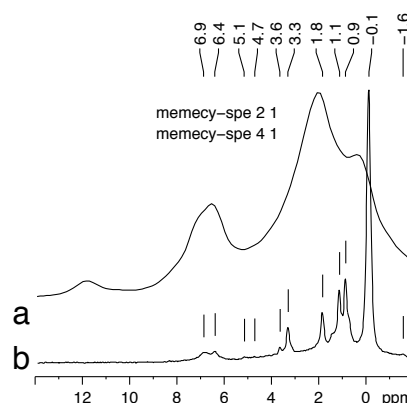
Figure 4.22: *(a) SPE and (b) Hahn echo ($\tau = 1.4$ ms) spectra of Me,Me-N-Cy.*

For these systems, depending on recycle delay, a superposition of broad and narrow peaks were on occasion observed. The more mobile part could be selectively refocused by a Hahn spin-echo [Hahn 50] (Figure 4.22b). The echo spectrum showed that the cyclohexyl peak could be clearly assigned on the basis of intensity. The cyclohexyl protons were also found to be significantly shielded with a chemical shift of −0.1 ppm, suggesting the amine-substituent was in a region above at least one of the aromatic rings. A number of other sites were also seen to pass through the spin-echo, of particular interest were the two aromatic sites at 6.4 and 6.9 ppm. These two sites were also partially seen in the SPE spectrum (Figure 4.22a). The form of the SPE spectrum suggested a rigid solid, heavily broadened by homonuclear dipolar coupling, much like all previous dimers encountered. In contrast, the echo spectrum revealed a chemically similar flexible system where motional averaging of the dipolar-coupling resulted in narrower spectral lines. The coexistence of both these states was not expected. A possible explanation could be a partial melting of the sample during the measurement, or a strong mobility gradient within the sample itself. However, it is unclear if such well defined N··H‑O and O··H‑O hydrogen bonding could take place with such a high degree of amine-substituent mobility.
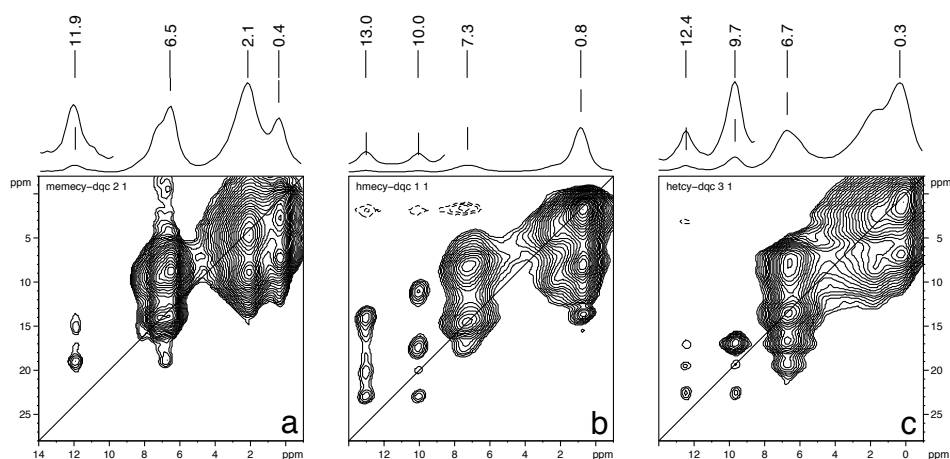
Figure 4.23: *DQ correlation spectra of N-Cy Dimers at $\omega_r/2\pi = 30\ kHz$*

As with the other dimers DQ correlation spectra again provided most insight into the structure of the N‑Cy dimers. For Me,Me‑N‑Cy both the cyclohexyl (2.1 ppm) and shielded methyl protons (0.4 ppm) can be seen to correlate with the aromatic protons at 6.5 ppm in Me,Me‑N‑Cy (Figure 4.23a). Upon closer inspection the two aromatic sites, suggested by the echo spectrum at 6.4 and 6.9 ppm, can be resolved. However, full assignment of this region was problematic due to the presence of the O··H‑O protons at 8.2 ppm. A clear DQC between the N··H‑O and aromatic protons at 6.4 ppm was observed suggesting the presence of the continuous structure. Unlike the mono ring-substituted systems, Me,Me‑N‑Cy did not show a DQC between N··H‑O and O··H‑O protons. This could however be due to the low intensity of both sites in this spectrum. Indeed, the only evidence for O··H‑O hydrogen bonding in Me,Me‑N‑Cy was the weak DQ auto peak on the diagonal at 8.2 ppm, and the asym-

metric aromatic aliphatic correlation above. This suggested that O··H‒O hydrogen bonding was rare within this system. The mono ring-substituted dimers bore close resemblance to their corresponding N‒Pr dimers in the hydrogen bonding region (Figure 4.23b–c). Both showed weak DQ coherence between N··H‒O and aromatic protons suggesting the continuous structure. Relatively strong correlation was also seen between the O··H‒O and aromatic protons for these two dimers. For all N‒Cy dimers DQ auto correlation peaks were seen for the O··H‒O protons (Figure 4.23). This implied that two equivalent O··H‒O sites were in relatively close proximity to each other. This type of interaction was not seen for any of the other dimers investigated as the inter-nuclear distance was too large.

As with the N‒Pr dimers, the DQ spectra of H,Et‒N‒Cy measured under fast-MAS did not show any gain in resolution (Figure 4.24). The weaker hydrogen bond proton intensities and lower than expected resolution were again attributed to the elevated sample temperatures found during fast-MAS.
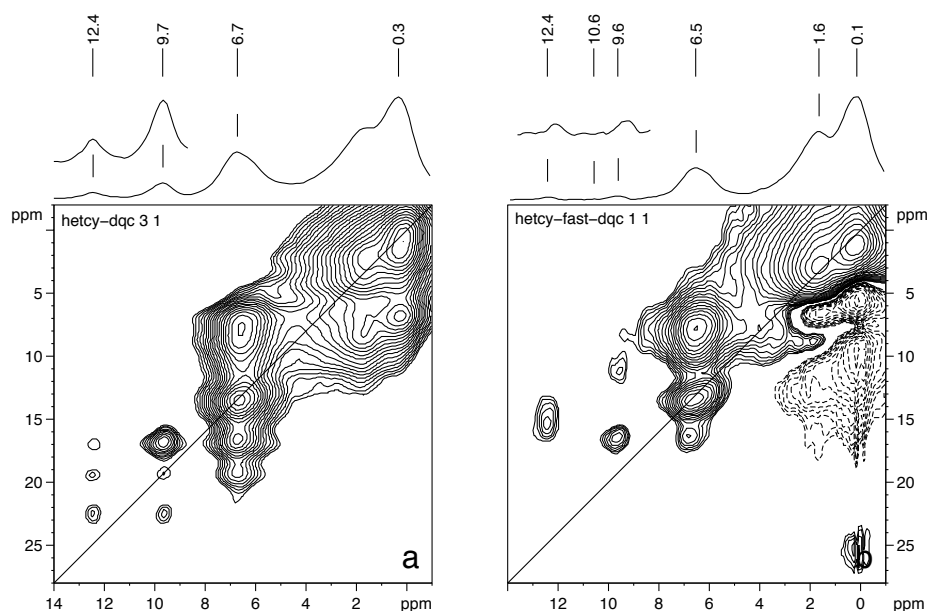
Figure 4.24: *DQ correlation spectra of H,Et‒N‒Cy at (a) $\omega_r/2\pi = 30$ and (b) 65 kHz*

Summary

In general proton DQ spectra bore close resemblance to those of the N-Me dimers. As with the N-Me dimers the Me,Me systems had weaker hydrogen bonding than both mono ring-substitued systems. As was seen in Me,Me-N-Me, the O··H-O hydrogen bond of Me,Me-N-Cy was also found to be relatively weak and the protons obscured by the aromatic protons. For all systems weak DQ coherences were seen between the N··H-O and aromatic protons again suggesting the continuous hydrogen bonding structure to some degree. It was thought that H,Me-N-Cy, as with Me,Me-N-Me, predominantly existed in the dimeric structure. Thus, as was seen by Schnell *et al.* [Schnell 98a], although the associated X-ray diffraction structure showed the dimeric structure only one form was selected (as a relatively large crystal) for X-ray analysis. The presence of shielded protons was detected for all N-Cy dimers. These sites were assigned to the cyclohexyl group, on the basis of intensity. The shielding interaction suggested close proximity of the cyclohexyl protons to the face of one of the aromatic systems present in the dimer, as suggested by the X-ray structure [Laobuthee 01].
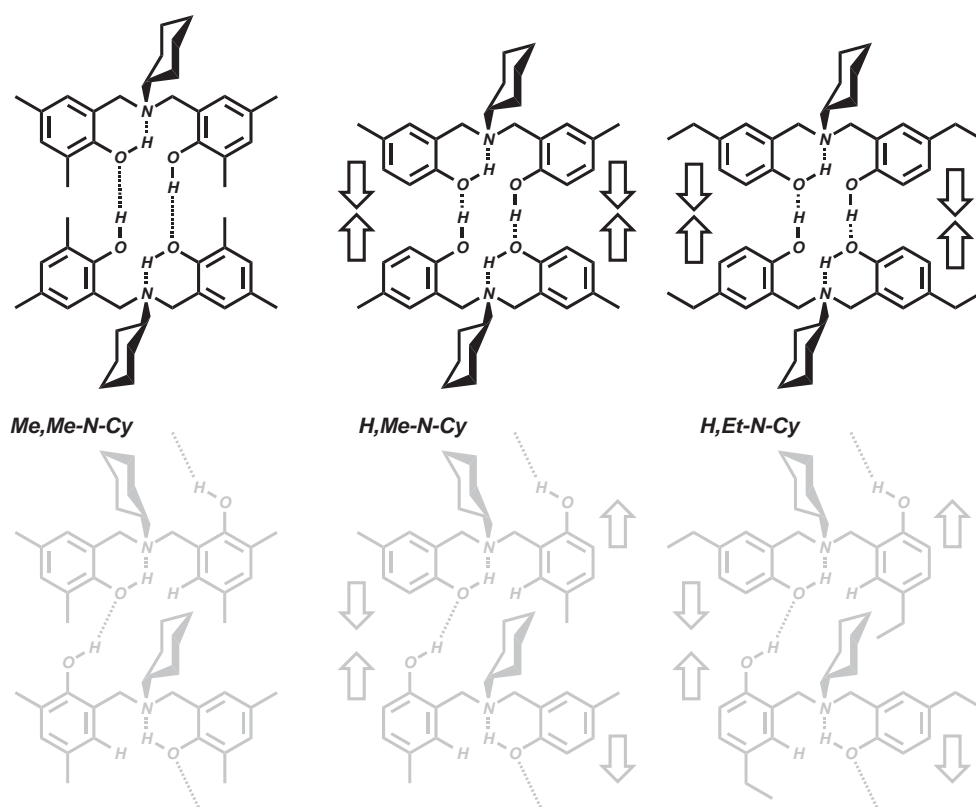
Figure 4.25: *Suspected structures of the N-Cy dimers. Less dominant forms shown in grey.*

4.2.2   Proton spectroscopy: ring-substituent trends

Me,Me dimers

The N··H‑O chemical shift showed most variation for the Me,Me dimers, occurring between 11.7–13.6 ppm. The large variation was mostly due to Me,Me‑N‑Pr having much higher chemical shift of 13.6 ppm, as compared to 11.3 and 11.9 ppm of the N‑Me and N‑Cy dimers respectively. Although the chemical shift of the N··H‑O proton was certainly directly influenced by the amine substituent, the anomalous behaviour of Me,Me‑N‑Pr was thought to be due to changes in supramolecular structure. With a difference of over 2 ppm seen between Me,Me‑N‑Me and Me,Me‑N‑Pr, significant differences in N··H‑O hydrogen bonding were suggested. The Me,Me‑N‑Pr dimer was also the only dimer investigated that did not clearly show a DQ coherence between N··H‑O and O··H‑O protons. Instead, a very weak, asymmetric correlation was seen (Figure 4.26b). This provided further evidence that the N··H‑O hydrogen bonding was different for Me,Me‑N‑Pr than the other dimers and placed the N··H‑O and O··H‑O protons further apart in space. The multiple aliphatic sites seen for Me,Me‑N‑Pr and Me,Me‑N‑Cy were directly attributed to the presence of chemically different aliphatic protons in the amine-substituents (Figure 4.26c).
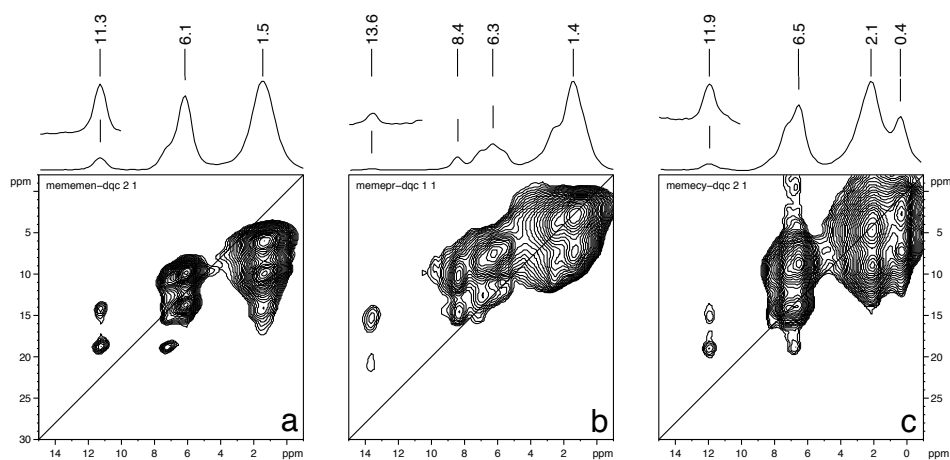
Figure 4.26: *DQ correlation spectra of the Me,Me dimers: (a) N‑Me, (b) N‑Pr and (c) N‑Cy.*

When the O··H‑O protons were considered the N‑Pr and N‑Cy systems showed similar chemical shift of 8.2 and 8.4 ppm respectively, but those of the N‑Me dimer were found at lower values of 7 ppm (Figure 4.26a). The chemical shifts of the O··H‑O protons were similar to those of the aromatic protons in all but the N‑Pr system. Such low chemical shift O··H‑O protons were not seen for any mono ring-substituted dimers and indicated that for the Me,Me dimers O··H‑O hydrogen bonding was relatively weak. This observation was rationalised by the intermolecular nature of the O··H‑O hydrogen bond. For both dimeric and continuous hydrogen bonding structures, the proximity of the dimer units strongly affects the O··H‑O hydrogen bond-

ing. Unlike the mono ring-substituted systems, the Me,Me dimers must accommodate the extra steric bulk of the 5-methyl group adjacent to the hydroxyl involved in the O··H‒O hydrogen bond. The increased steric hindrance between dimers promoting a longer O··H‒O hydrogen bond length, thus resulting in a lower chemical shift. With differences in N··H‒O and O··H‒O hydrogen bonding seen between Me,Me‒N‒Cy and the other Me,Me dimers the findings of Schnell *et al.* [Schnell 98a], regarding the importance of the amine-substituent, were confirmed.

H,Me dimers

For the H,Me dimers the N··H‒O and O··H‒O hydrogen bonding was more comparable for all systems. The N··H‒O chemical shifts were between 12.5–13.0 ppm and the O··H‒O chemical shift between 9.4–10 ppm. Both types of hydrogen bonding were stronger in the H,Me dimers, as compared to the Me,Me systems. As previously discussed, this was thought to be due to the reduced steric hindrance in the direction of the O··H‒O hydrogen bonding, allowing shorter hydrogen bonds to be formed.
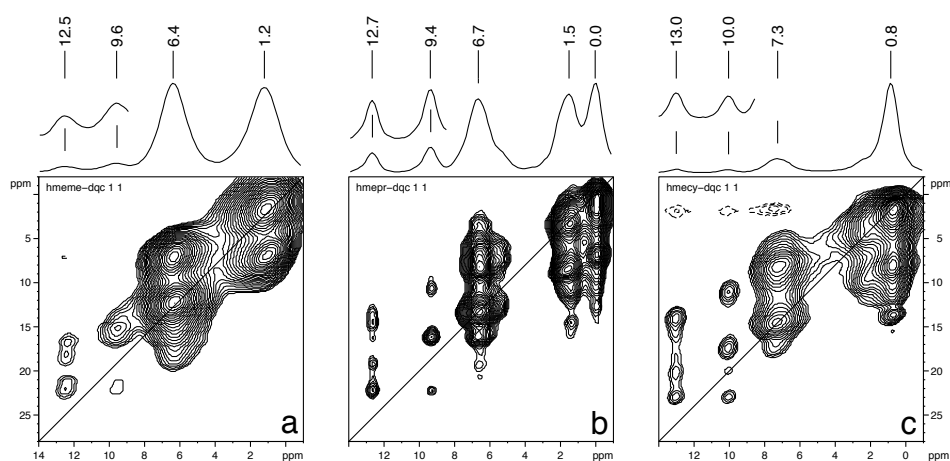
Figure 4.27: DQ correlation spectra of the H,Me dimers: (a) N‒Me, (b) N‒Pr and (c) N‒Cy.

Not only could DQ correlations between N··H‒O and O··H‒O sites be seen for all H,Me systems, but also those between N··H‒O and aromatic protons (Figure 4.27). Although weak, the latter correlations indicated that for all H,Me dimers the continuous structure was present. It is however unclear if this was the only structure present or if both dimeric and continuous structure were present in the same sample. All dimers showed correlation between the N··H‒O and aliphatic sites. For the N‒Pr and N‒Cy dimers correlations were also seen between the O··H‒O and aliphatic protons. With these aliphatic protons attributed to the amine-substituent this was further evidence for the continuous structure, as in that conformation the O··H‒O protons are also in close proximity to the amine substituents. It could be possible that the H,Me‒N‒Me dimer did not show this DQ correlation because the methyl group was too short, thus making the dipolar coupling too weak to be detected.

H,Et dimers

As with the H,Me dimers, the chemical shifts of the protons involved in hydrogen bonding showed little variation, as compared to the Me,Me dimers. The N··H-O protons ranged from 12.3–12.5 ppm and the O··H-O protons from 9.4–9.7 ppm.
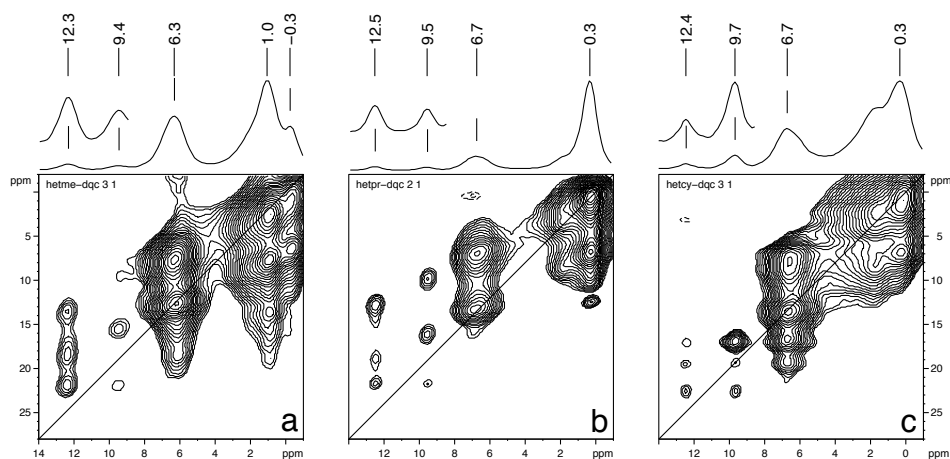
Figure 4.28: *DQ correlation spectra of the H,Et dimers: (a) N-Me, (b) N-Pr and (c) N-Cy.*

Also, as with the H,Me dimers, all H,Et dimers showed DQ correlation between the N··H-O and aromatic protons. However, although N-Pr and N-Cy showed a relatively weak interaction (Figure 4.28b–c), the N-Me interaction was the strongest seen for all dimers (Figure 4.28a). This suggested that out of all dimers studied H,Et-N-Me was the most likely to exist in the continuous hydrogen bonding structure.

4.2.3 Proton spectroscopy: general trends

The chemical shift of the N··H-O protons ranged from 11.7–13.5 ppm, with both extremes found amongst the Me,Me dimers (Table 4.8). The highest value of 13.5 ppm was found for Me,Me-N-Pr, but this seemed anomalous (Figure 4.29). When disregarding Me,Me-N-Pr, two general trends were seen: firstly, δ_H increased with increasing electron-donating ability of the amine substituent, i.e. δ_H Cy > Pr > Me. Secondly, H,Me and H,Et systems had higher chemical shifts as compared to the Me,Me systems, i.e. δ_H H,Me > H,Et > Me,Me. The O··H-O chemical shifts ranged from 7.0–9.7 ppm with the same trends shown (Table 4.9). When considering the O··H-O hydrogen bonding the anomalous behaviour of Me,Me-N-Pr was less pronounced (Figure 4.30). For all mono ring-substituted systems a general increase in O··H-O hydrogen bonding was observed. This confirmed that with the removal of the 5-methyl group, and its associated steric bulk, stronger O··H-O hydrogen bonds could be formed.

Table 4.8: N··H-O proton chemical shifts.			
δ_H [ppm]	N-Me	N-Pr	N-Cy
Me,Me	11.7	13.5	11.8
H,Me	12.3	12.7	13.0
H,Et	12.3	12.4	12.4

Table 4.9: O··H-O proton chemical shifts.			
δ_H [ppm]	N-Me	N-Pr	N-Cy
Me,Me	7.0	8.2	8.4
H,Me	9.3	9.4	9.7
H,Et	9.4	9.4	9.6
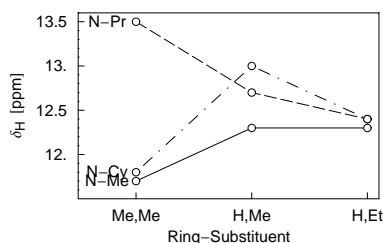
Figure 4.29: N··H-O proton chemical shifts.
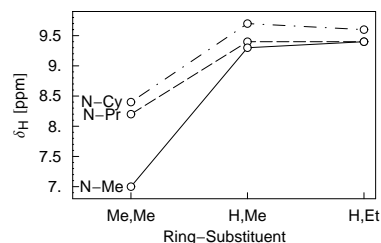
Figure 4.30: O··H-O proton chemical shifts.

The difference between the N··H-O and O··H-O chemical shifts was also found to be informative (Table 4.10). The chemical shift differences $\Delta\delta_H$ could be split into two groups. The majority of the dimers belonged to the first group, with $\Delta\delta_H <$ 3.5 ppm. The second group, with $\Delta\delta_H >$ 3.5 ppm, contained only Me,Me-N-Me and Me,Me-N-Pr with $\Delta\delta_H$ of 4.7 and 5.3 ppm respectively. These larger than average differences were attributed to the low O··H-O chemical shift in Me,Me-N-Me and the high N··H-O chemical shift in Me,Me-N-Pr. Considering these anomalies the same general trend observed for chemical shift was seen, i.e. $\Delta\delta_H$ Cy > Pr > Me. The similarity between H,Me and H,Et dimers with N-Pr and N-Cy amine-substituents was mostly due to the relatively high O··H-O chemical shifts seen in H,Me-N-Cy and H,Et-N-Cy.

Table 4.10: chemical shift difference.

$\Delta\delta_H$ [ppm]	N-Me	N-Pr	N-Cy
Me,Me	4.7	5.3	3.4
H,Me	3.0	3.3	3.3
H,Et	2.9	3.0	2.8
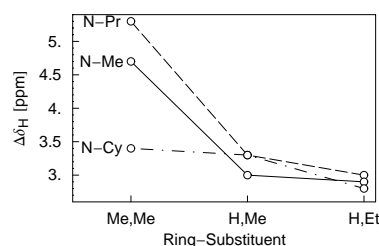
Figure 4.31: chemical shift difference.

From the intensity of the DQC between the N··H-O and aromatic protons the distribution of the continuous hydrogen bonding structure was seen (Table 4.11). For all mono ring-substituted dimers the characteristic DQC was found. However, for all but H,Et-N-Me the DQC was much weaker than previously reported [Schnell 98a]. This suggested that for all these systems the continuous hydrogen bonding structure was not the dominant supramolecular structure. This distribution between dimeric and continuous structures was thought to be reversed for H,Et-N-Me, with the continuous hydrogen bonding structure being dominant.

Table 4.11: Continuous structure DQ coherence.

	N-Me	N-Pr	N-Cy
Me,Me			+
H,Me	+	+	+
H,Et	++	+	+

Table 4.12: Shielded chemical shifts from DQ spectra.

δ_H [ppm]	N-Me	N-Pr	N-Cy
Me,Me			0.4
H,Me		0.0	0.3
H,Et	−0.1	0.3	0.3

From both SPE and DQ spectra shielded protons were found for a number of dimers. These were more common for systems with N-Pr and N-Cy amine-substituents, and H,Et ring-substituents. This suggested the systems with larger flexible aliphatic systems were most likely to experience shielding interactions. This was confirmed by DQ spectroscopy with correlation seen between these shielded sites and aromatic protons.

Summary

Proton spectroscopy provided evidence that most dimers examined could exist in the continuous structure. This form was more likely for mono ring-substituted systems, with the strongest signs seen for H,Et-N-Me. Only Me,Me-N-Me and Me,Me-N-Pr showed no signs of existing in the continuous hydrogen bonding structure. The discrepancy between this and the previous findings for Me,Me-N-Pr [Schnell 98a] was thought to be due to analysis of different batches of this material, each having a different forms. Such differences can also be seen in Chapter 5 when the Me,Me-N-Et dimer was reexamined.

4.2.4   Carbon spectroscopy

Comparison of N-methyl dimers

Surprisingly, given the highly crystalline nature suggested by the ¹H NMR, heteronu-clear dipolar recoupling methods were not found to be successful for Me,Me-N-Me, even though a REPT-HSQC spectrum of Me,Me-¹⁵N-Me had previously been reported [Goward 01] (Figure 4.32).
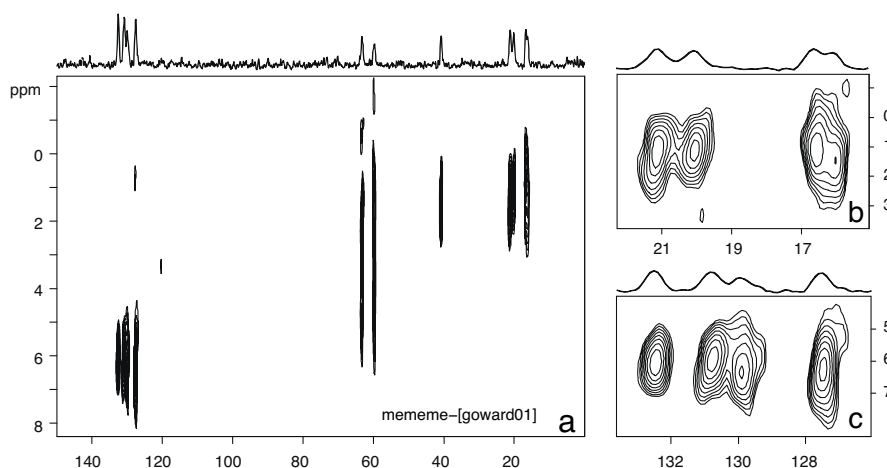
Figure 4.32: *¹³C–¹H HSQC spectrum of Me,Me-N-Me with $\tau_{exc/rec} = 1 \cdot \tau_r$: (a) full, (b) methyl and (c) aromatic regions. (adapted from [Goward 01])*

From the HSQC spectrum it was seen that both methyl ring-substituents showed two peaks at 16.1/16.6 and 20.1/21.2 ppm. No such splitting was seen for the methyl amine substituent found at 40.8 ppm indicating a symmetry about the amine site. The two CH_2 carbons were also found to have different chemical shifts of 59.7 and 63.2 ppm. The inequivalence of the two aromatic rings was also confirmed by the two CH aromatics ortho and para to the amine bridge at 127.5/129.9 and 130.9/132.3 ppm respectively (Figure 4.33).
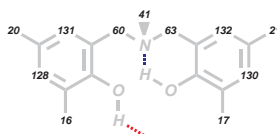
Figure 4.33: *Me,Me-N-Me ¹³C assignment.*

Although further measurements on Me,Me-N-Me was unsuccessful the mono ring substituted N-Me systems H,Me-N-Me and H,Et-N-Me proved more amenable. For H,Me-N-Me REPT based recoupling was not found to be possible, and thus no HSQC spectra are presented. However, ¹³C–¹H dipolar recoupling with the REREDOR method was relatively efficient (Figure 4.34). The REREDOR build-up behaviour of H,Me-N-Me was dominated by relaxation phenomena. After $\tau_{exc/rec} = 5 \cdot \tau_r$ almost no signal intensity remained on any of the sites. This inability to

recouple the dipolar interaction for longer periods of time was found to be common
for all dimers investigated.
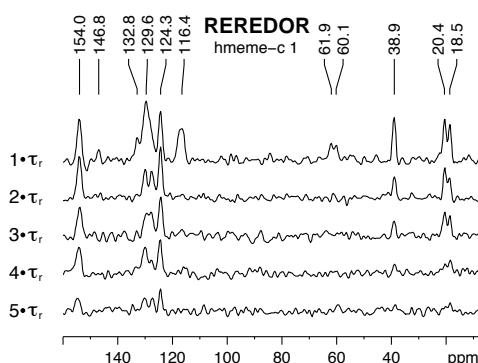
Figure 4.34: 1D REREDOR spectra of H,Me-N-Me.

Figure 4.35: H,Me-N-Me ^{13}C assignment.

From the 1D spectra all expected carbon sites were resolved. The methyl amine-
substituent was seen at 38.9 ppm with the two methyl ring-substituents found to
be inequivalent at 18.5 and 20.4 ppm. The CH$_2$ groups, either side of the amine,
were also found to be inequivalent having chemical shifts of 60.1 and 61.9 ppm. All
aromatic sites were able to be assigned, with the peak at 116.4 ppm also showing
signs of being comprised of two peaks resulting from inequivalence (Figure 4.35).
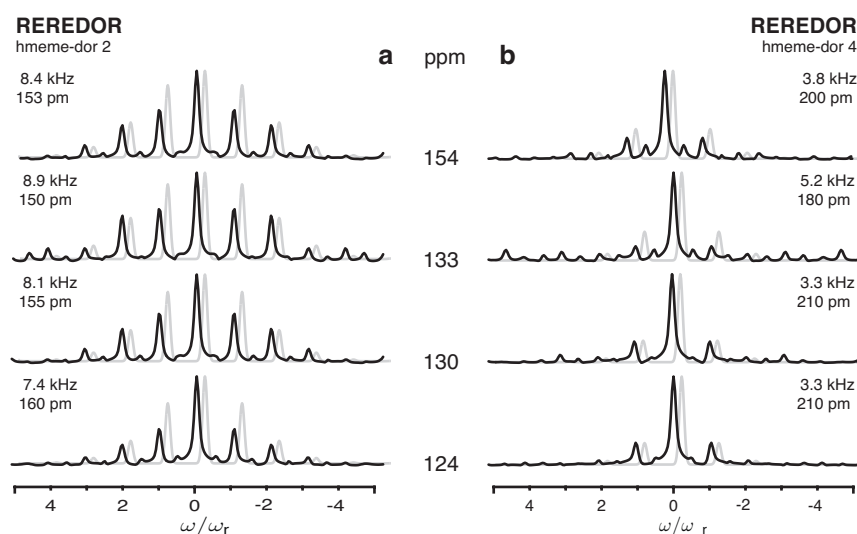
Figure 4.36: REREDOR sideband patterns of H,Me-N-Me with (a) $\tau_{exc/rec} = 3 \cdot \tau_r$ and (b) $4 \cdot \tau_r$. Simulated sideband patterns shown in grey with corresponding dipolar-coupling constant (kHz) and internuclear ^{13}C–^{1}H distance (pm).

The inability to pump high-order sidebands severely limited the quantitative analy-
sis of these systems, with high error seen for D_{jk} when fitting low-order sidebands
only. Thus, the extracted dipolar coupling constants from the sideband experiments
with $\tau_{exc/rec} = 3$ and $4 \cdot \tau_r$ gave little information (Figure 4.36). This was unfortu-
nately the case for most dimers where sidebands could be recorded. For the CH
aromatic site at 116.4 ppm neither length of recoupling gave the expected dipolar

coupling of $D_{jk} = 21$ kHz. The lower than expected dipolar coupling could have been a sign of mobility within the system but, considering the characteristically rigid proton spectra, this was thought unlikely. The apparently low heteronunclear dipolar coupling was thus deemed to result from interference from secondary couplings, these resulting in a breakdown of the spin-pair approximation used for simulation (Appendix D).

For H,Et-N-Me both REPT and REREDOR based recoupling was effecent and allowed dipolar HSQC spectra to be recorded. However as with H,Me-N-Me, recoupling was limited to $\tau_{exc/rec} = 5 \cdot \tau_r$ for both methods (Figure 4.37).
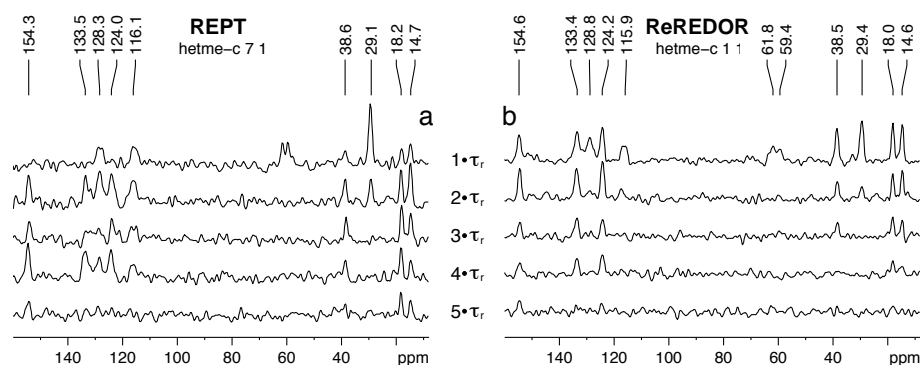
Figure 4.37: *1D ^{13}C (a) REPT and (b) REREDOR spectra of H,Et-N-Me with $\tau_{exc/rec} = 1$–5·τ_r.*
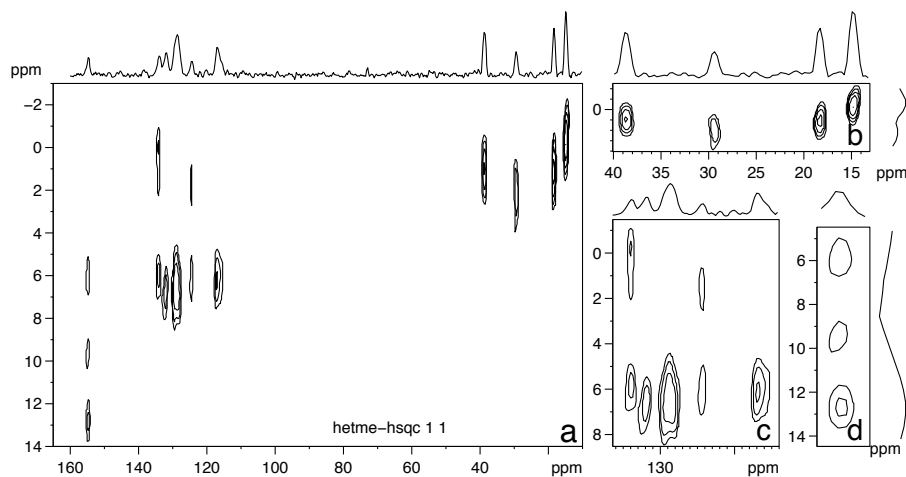
Figure 4.38: *^{13}C–^1H HSQC spectrum of H,Et-N-Me with $\tau_{exc/rec} = 2 \cdot \tau_r$: (a) full, (b) methyl, (c) aromatic and (d) hydrogen bonding region.*

The aliphatic region, showed the methyl amine carbon at 38.5 ppm, with the two adjacent CH_2 groups at 61.8 and 59.4 ppm, again suggesting the presence of inequivalent sites (Figure 4.37). The CH_2 carbons of the ethyl ring-substituents were found at 29.1 ppm and correlated to protons of higher chemical shift than the other CH_2 sites, at 2.2 and 1.0 ppm respectively (Figure 4.38b). The remaining two sites, at 14.7 and 18.2 ppm, thus belonged to the terminal methyl groups of the ethyl ring-substituents. These methyl groups showed strong inequivalence in both carbon and associated

proton chemical shifts. The low value of the 14.7 ppm group was explained when the proton chemical shift of -0.5 ppm was considered. Such a shielding interaction experienced by the protons would clearly also effect the carbon site, resulting in lower ^{13}C chemical shift than expected. In the aromatic region of the HSQC spectra a number of aromatic sites were seen. Those aromatic sites with higher intensity were assumed to be related to carbon sites with directly attached protons, i.e. 116.1, 128.5 and 129.5 ppm (Figure 4.38c). More specifically, these sites were assigned to the *meta*, *para* and *ortho*-CH sites, with respect to the aromatic carbon attached to the amine bridge. This assignment was based on the associated proton chemical shifts of 6.1, 6.8 and 6.8 ppm respectively and expected carbon chemical shifts. The 133.5 ppm site was identified as the *meta*-C-Et aromatic by correlation with the CH$_2$ protons at ≈ 2.2 ppm and the shielded methyl protons at -0.5 ppm (Figure 4.38c). Similarly, the second *meta*-C-Et site, whose ethyl group did not undergo shielding and contained the 18.2 ppm methyl group, was found at 132.1 ppm. As with H,Me-N-Me, the C-OH aromatic carbon of H,Et-N-Me was clearly separated from the other aromatic sites at 154 ppm. The HSQC spectra showed that this site not only experienced dipolar coupling with the adjacent aromatic protons at 6.1 ppm, but was also influenced by the O··H-O and N··H-O hydrogen bonding protons at 9.4 and 12.3 ppm respectively (Figure 4.38d). Such correlation indicated a close proximity between these sites. The remaining site at 124.3 ppm was seen to weakly correlate with the CH$_2$ protons adjacent to the amine, thus this peak was the single remaining unassigned aromatic site connecting the ring to the amine bridge (Figure 4.39).

Figure 4.39: H,Et-N-Me ^{13}C assignment.
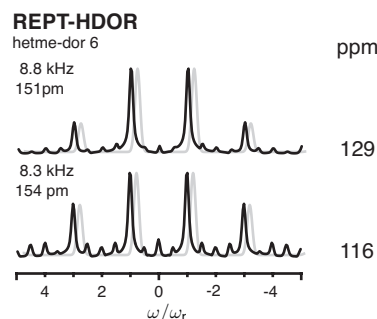
Figure 4.40: *REPT-HDOR sideband patterns of H,Et-N-Me with $\tau_{exc/rec} = 4 \cdot \tau_r$. Simulated sideband patterns shown in grey with corresponding dipolar-coupling constant (kHz) and internuclear ^{13}C–^{1}H distance (pm).*

Sideband patterns via REPT and REREDOR were possible, but were again limited by the accessible recoupling time. Using REPT-HDOR, with $\tau_{exc/rec} = 4 \cdot \tau_r$, only the aromatic CH sites showed third order sidebands and allowed fitting. The lack of high-order sidebands was seen for all other dimers examined. As was previously seen for H,Me-N-Me the dipolar coupling did not suggest rigid C-H aromatics (Figure 4.40).
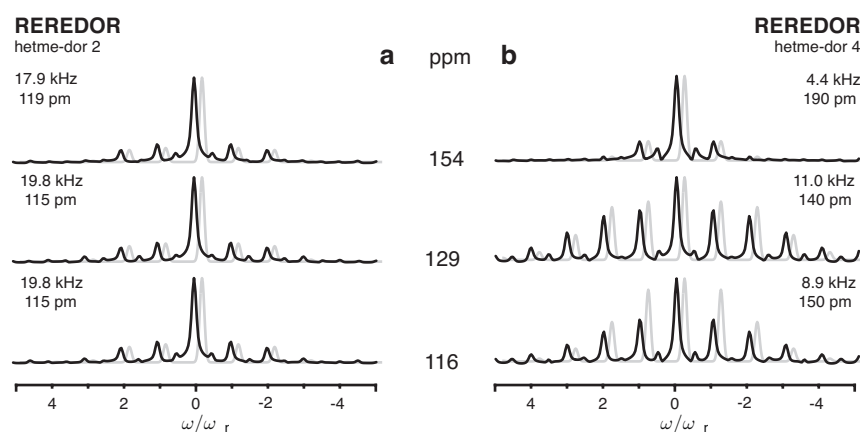
Figure 4.41: *REREDOR sideband patterns of H,Et⁻N⁻Me with (a) $\tau_{exc/rec} = 1 \cdot \tau_r$ and (b) $3 \cdot \tau_r$. Simulated sideband patterns shown in grey with corresponding dipolar-coupling constant (kHz) and internuclear ^{13}C–^{1}H distance (pm).*

Better results were obtained with REREDOR at $\tau_{exc/rec} = 1$ and $3 \cdot \tau_r$ (Figure 4.41). Assignments of the 116.1 and 128.5 ppm sites were confirmed with both sites found to have a $D_{jk} = 19.6$ kHz. Both experimentally determined values bore strong resemblance to the expected coupling of 21 kHz at $\tau_{exc/rec} = 1 \cdot \tau_r$. Although higher order sidebands were present at longer recoupling times, the associated dipolar coupling constants suggested a break down of the spin-pair approximation, with both sites showing weaker couplings of 8.9–11.0 kHz than expected. The 153.5 ppm C⁻OH aromatic, was seen to have a comparable distance of 190 pm to the 195 pm expected from its geometry. However, due to only first-order, and minor contributions from second-order, sidebands being fitted the accuracy of this value was doubtful.

Comparison of N-propyl dimers

As with the N-Me dimers, coherent recoupling techniques were found to be problematic for Me,Me-N-Pr and yielded results for the H,Me and H,Et systems only. For H,Me-N-Pr, recoupling beyond $\tau_{exc/rec} = 5 \cdot \tau_r$ was not viable, with 3k transients needing to be averaged to acquire an acceptable signal-to-noise.

Two main differences were seen between the carbon spectra of the N-Pr dimers as compared to the N-Me dimers: firstly, the peak at 38.5 ppm was no longer present confirming this was the methyl carbon of the amine-substituent. Secondly, two C-OH sites were seen at 155.4 and 153.3 ppm (Figure 4.42). For both H,Me-N-Pr and H,Et-N-Pr REPT based recoupling allowed access to HSQC heteronuclear correlation spectra.
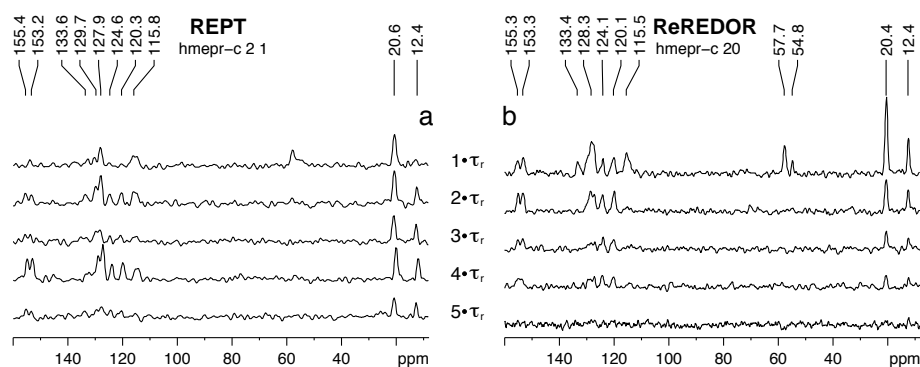
Figure 4.42: *1D ^{13}C (a) REPT and (b) REREDOR spectra of H,Me-N-Pr with $\tau_{exc/rec} = 1–5 \cdot \tau_r$.*

The HSQC spectra showed the two aromatic C-OH sites not only had different carbon chemical shifts, but that these correlated to protons of different chemical shifts, namely the hydrogen bonding protons (Figure 4.43d).
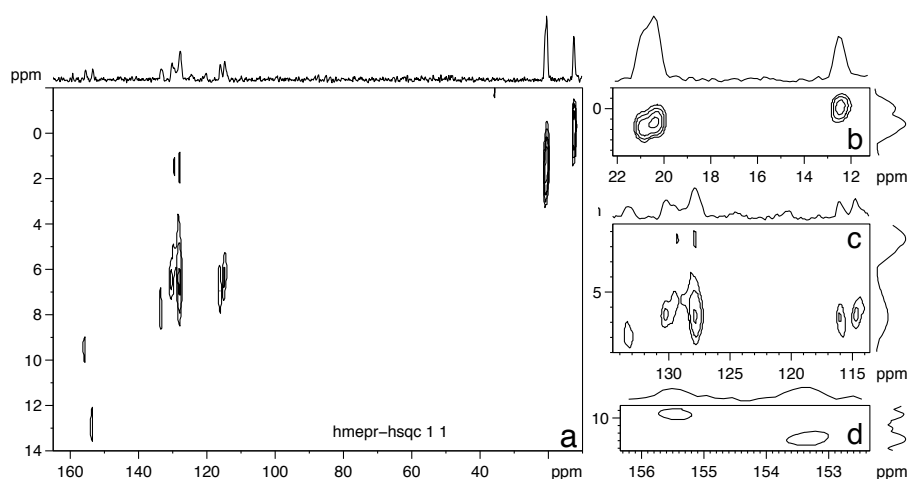
Figure 4.43: *^{13}C–^{1}H HSQC spectrum of H,Me-N-Pr with $\tau_{exc/rec} = 2 \cdot \tau_r$: (a) full, (b) methyl, (c) aromatic and (d) hydrogen bonding region.*

From the aliphatic region of the 1D spectra only two peaks were seen. The 12.5 ppm peak was assigned to the terminal methyl group of the propyl amine-substituent. This left the second 20.6 ppm peak to account for both the methyl ring-substituents and one of the CH_2 groups of the propyl amine-substituent. The HSQC spectra revealed that this peak contained two sites, at 20.4 and 20.8 ppm, each with different intensities and associated proton chemical shifts (Figure 4.43b). The 20.4 ppm site was thought to be that of the two methyl groups, whereas the 20.8 ppm site was associated to the CH_2 group due to the lower intensity and higher proton chemical shift. As with the N-Me dimers, multiple aromatic sites were resolved, and again suggested the aromatic rings were in different environments (Figure 4.43c). The stronger correlations were assigned to the CH aromatics with directly bound protons. The two peaks at 114.7 and 116.1 ppm were assigned to the *meta*-CH groups and the 127.9 ppm peak to both *para*-CH groups. The remaining *ortho*-CH aromatics were attributed to the peaks at 130.1 and 133.6 ppm. The aromatic carbons joining the rings to the amine were found at 120.3 and 124.6 ppm in the 1D spectra (Figure 4.42a). The two aromatic C-OH peaks at 153.2 and 155.4 ppm correlated with the N··H-O and O··H-O protons at 12.7 and 9.3 ppm respectively. The through space correlation between hydrogen bonding protons and carbon nuclei which lie in close proximity illustrated the possible strengths of such dipolar HSQC experiments. The remaining sites were assigned from those appearing in the 1D spectra but not the HSQC spectra (Figure 4.45).
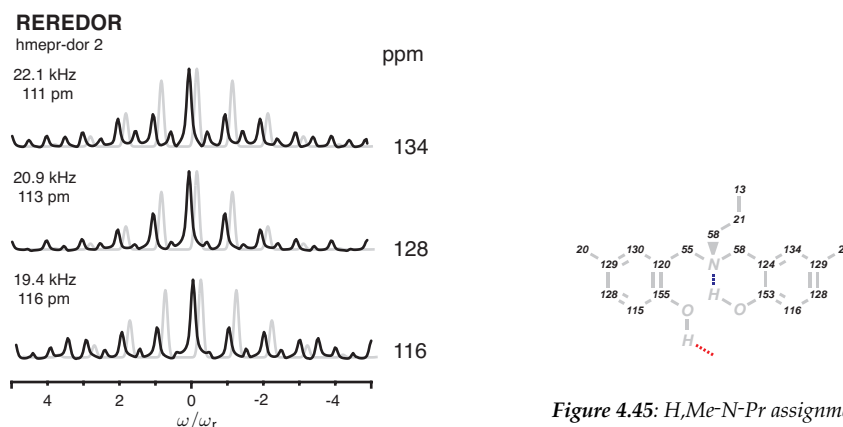
Figure 4.44: REREDOR sideband patterns of H,Me-N-Pr with $\tau_{exc/rec} = 3 \cdot \tau_r$. Simulated sideband patterns shown in grey with corresponding dipolar-coupling constant (kHz) and internuclear $^{13}C-^{1}H$ distance (pm).

Figure 4.45: H,Me-N-Pr assignment.

Assignment was confirmed by sideband analysis which showed the aromatic CH sites at 116.1, 127.9 and 134 ppm to have the expected dipolar coupling constants of D_{jk}=21 kHz (Figure 4.44). Due to low signal-to-noise and short recoupling time these values are not considered highly accurate and possibly reflect a breakdown in the two-spin approximation. Recoupling of the aromatic C-OH, N··H-O and O··H-O interactions did not yield meaningful results for the same reason.

The H,Et-N-Pr dimer showed similar ^{13}C spectra to H,Me-N-Pr, showing two C-OH carbon resonances at 153 and 155 ppm. Unfortunately, recoupling beyond $\tau_{exc/rec} = 5 \cdot \tau_r$ was also not found to be efficient for this system (Figure 4.46). The most obvious difference between H,Me-N-Pr and H,Et-N-Pr was seen in the aliphatic region, with the CH$_2$ sites of the ethyl ring-substituents separately resolved at 25.3 and 27.5 ppm. Both associated methyl groups had a chemical shift of 15.2 ppm and showed no inequivalence. The remaining sites at 19.1 and 11.6 ppm belonged to the CH$_2$ and CH$_3$ groups of the propyl amine substituent. The two CH$_2$ groups adjacent to the amine were again found to be inequivalent at 45.5 and 57.0 ppm.
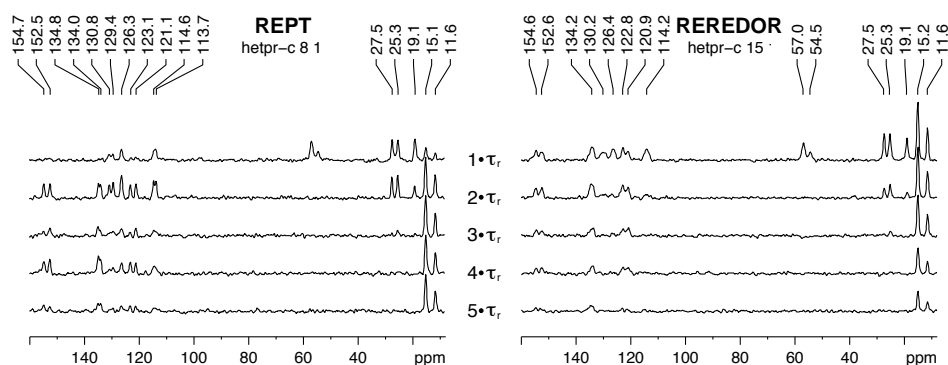
Figure 4.46: *(a) REPT and (b) REREDOR spectra of H,Et-N-Pr with $\tau_{exc/rec}$ =1–5·τ_r.*

The methyl group of the propyl amine-substituent (11.6 ppm) and the two ethyl ring-substituents (15.2 ppm) were both found to correlate with the shielded protons at 0 ppm in the $\tau_{exc/rec} = 1 \cdot \tau_r$ HSQC spectra (Figure 4.47b). This indicated a close proximity of both groups to the face of an aromatic system, due to the shielding of their associated protons. Further evidence of shielding was seen for the two inequivalent CH$_2$ sites of the ethyl ring-substituents at 25.3 and 27.5 ppm. These were associated with protons having chemical shifts of 0.6 and 1.6 ppm respectively. Although a strong correlation was seen for the CH$_2$ carbon at 57.0 ppm, only a much weaker interaction was seen for the 54.5 ppm site (Figure 4.47c). However, this could have been due to the known limitations of the REPT method with rigid CH$_2$ spin systems. Correlation of the CH$_2$ group of the propyl amine-substituent with its neighbouring methyl group was also suggested by the broad nature of the 19.1 ppm peak in the proton dimension (Figure 4.47b). The aromatic sites with directly bound protons were found between ≈114–131 ppm (Figure 4.47d). The weaker peaks at 113.7/114.6 and 129.4/130.8 ppm were again split and were associated to the aromatic CH sites meta and para to the amine bridge. The remaining aromatic ortho-CH group did not show inequivalence, with both sites found at 126.3 ppm.

With longer recoupling times of $\tau_{exc/rec} = 2 \cdot \tau_r$, correlation between carbon and proton sites mediated by weaker heteronuclear coupling were observed (Figure 4.48). In the aliphatic region the methyl group of the propyl amine-substituent can be seen to weakly correlate its adjacent CH$_2$ protons (Figure 4.48b). With longer recou-
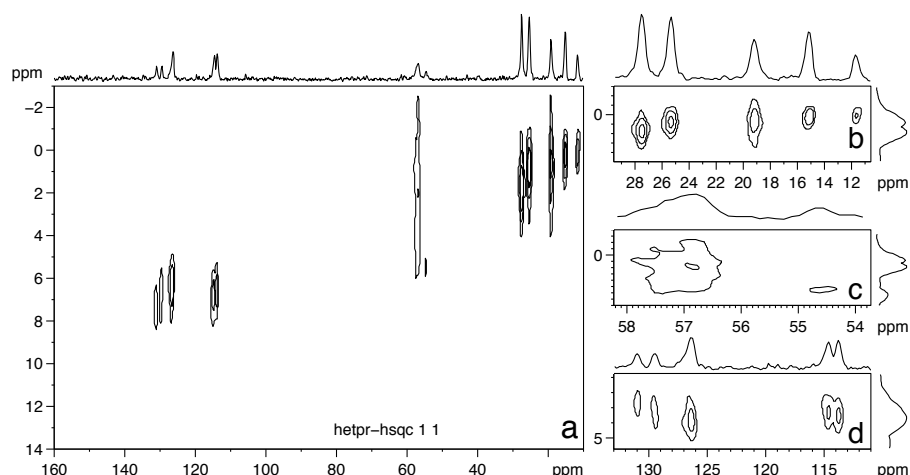
Figure 4.47: $^{13}C-^1H$ HSQC spectrum of H,Et-N-Pr with $\tau_{exc/rec} = 1 \cdot \tau_r$: (a) full, (b) methyl, (c) methelene and (d) aromatic region.

pling aromatic sites without directly bound protons were also seen. At 134.0 and 134.8 ppm the aromatic carbons to which the ethyl ring-substituents were attached were seen, again showing inequivalence of both carbon and associated proton sites (Figure 4.48c). These sites not only showed an interaction with their neighbouring aromatic protons, but also with the CH_2 protons of the ethyl ring-substituents. Similarly, weak correlation was seen for the 121.1 and 123.1 ppm aromatic sites joining the aromatic ring to the amine. The weak nature of this being due to the presence of only one neighbouring aromatic proton. This was partially confirmed by the weak correlation between the 121.1 ppm site and the CH_2 protons at 2 ppm. As with H,Me-N-Pr the C-OH aromatic carbon at 152.5 ppm was seen to correlate with the N··H-O protons at 12.4 ppm. However, unlike H,Me-N-Pr, the 154.7 ppm site not only correlated with the O··H-O protons at 9.4 ppm, but also with aromatic protons at 6.8 ppm, suggesting a change in structure (Figure 4.48d).
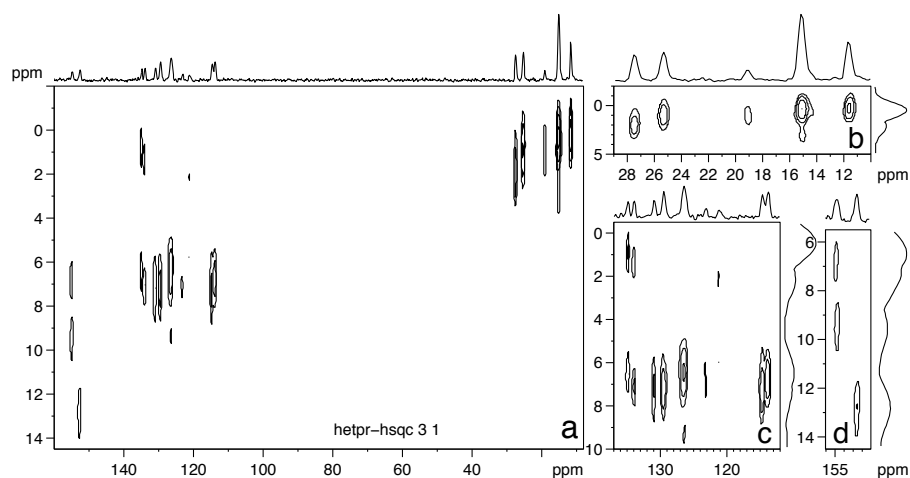
Figure 4.48: $^{13}C-^1H$ HSQC spectrum of H,Et-N-Pr with $\tau_{exc/rec} = 2 \cdot \tau_r$: (a) full, (b) methyl, (c) aromatic and (d) hydrogen bonding region.

REPT-HDOR

hetpr-dor 4
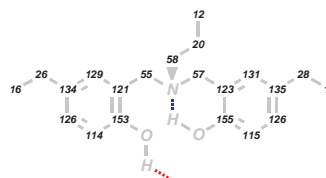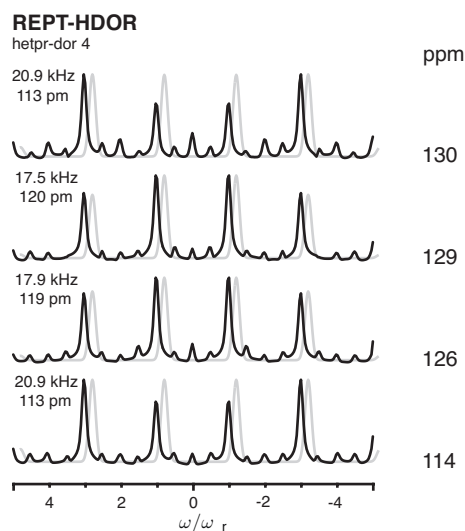
Figure 4.50: H,Et-N-Pr ^{13}C assignment.

Figure 4.49: REPT-HDOR sideband patterns of H,Et-N-Pr with $\tau_{exc/rec} = 2 \cdot \tau_r$. Simulated sideband patterns shown in grey with corresponding dipolar-coupling constant (kHz) and internuclear ^{13}C–^{1}H distance (pm).

Aromatics assignment was confirmed by REPT-HDOR and REREDOR sideband analysis, with 130.2, 129.4, 126.4 and 114.2 ppm sites all having $D_{jk} \approx 21$ kHz (Figure 4.51). The 152.6 and 154.6 ppm C-OH sites again showed a higher than expected dipolar coupling of 6.7 and 6.2 kHz respectively, corresponding to internuclear distances of 166 and 170 pm, comparable to those of H,Me-N-Pr.
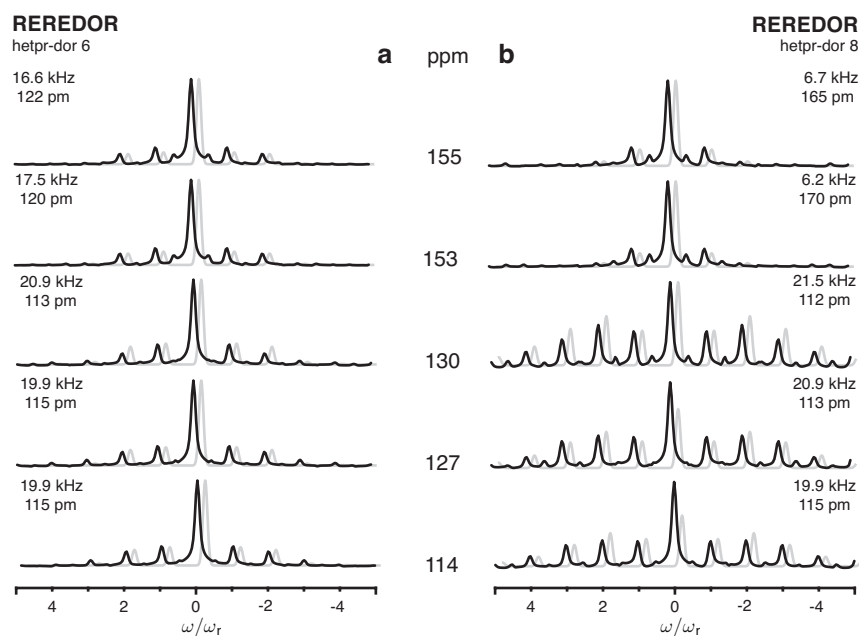
Figure 4.51: REREDOR sideband patterns of H,Et-N-Pr with (a) $\tau_{exc/rec} = 1 \cdot \tau_r$ and (b) $\tau_{exc/rec} = 2 \cdot \tau_r$. Simulated sideband patterns shown in grey with corresponding dipolar-coupling constant (kHz) and internuclear ^{13}C–^{1}H distance (pm).

Comparison of N-cyclohexyl dimers

Heteronuclear dipolar recoupling methods were not found to be efficient for all N-Cy dimers. Initially this was though to be caused by the mobile cyclohexyl group imparting increased mobility to the N-Cy dimers. Comparison of the cross-polarisation and heteronuclear Hahn-echo spectra of Me,Me-N-Cy showed that only the methyl groups at 22.7 and 17.6 ppm had significant mobility, with relatively long T_1 relaxation times. The CH_2 groups of the cyclohexyl amine substituent at 26.7 ppm were only partially mobile (Figure 4.52).
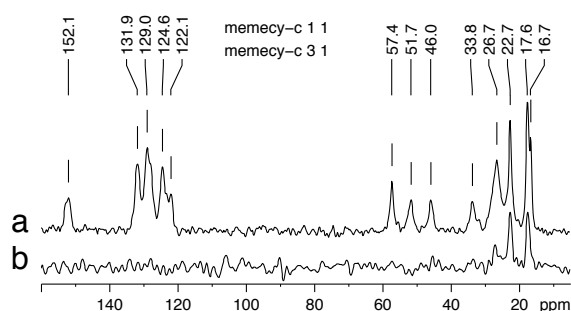
Figure 4.52: *(a) ^1H–^{13}C cross-polarisation spectrum of Me,Me-N-Cy obtained with 17k scans and (b) Hahn-echo spectrum obtained with 32 scans of the same material.*

For H,Me-N-Cy it was found that only cross-polarisation (CP) gave an acceptable signal-to-noise, with both REREDOR and REPT yielding very little signal, even after the accumulation of 4k transients (Figure 4.53).
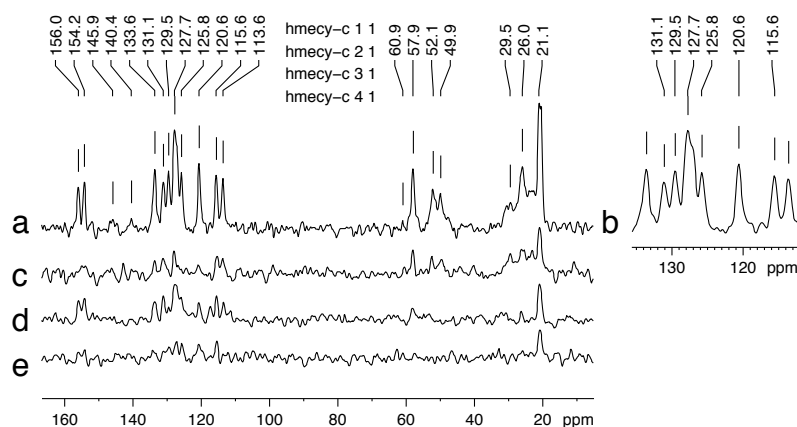
Figure 4.53: *Comparison of the (a,b) cross-polarisation and REPT spectra of H,Me-N-Cy obtained with (c) $\tau_{exc/rec} = 1 \cdot \tau_r$, (d) $2 \cdot \tau_r$ and (e) $3 \cdot \tau_r$.*

For H,Et-N-Cy polarisation transfer efficiency by CP, REPT or REREDOR was found to be significantly less than the already low levels for Me,Me-N-Cy and H,Me-N-Cy. Both carbon CP and SPE spectra of H,Et-N-Cy were found to be unobtainable with an acceptable signal-to-noise ratio within a reasonable period of time. With the acquisition of significantly more scans and the use of longer recycle delays (10 s) to counter any possible relaxation effects, no further gain in resolution was achieved.

Spectra of H,Et-N-Cy are not presented as no valid information could be extracted.

Although carbon spectroscopy of the N-Cy dimers proved problematic, some observation may be made from the spectra of Me,Me-N-Cy (Figure 4.52a) and H,Me-N-Cy (Figure 4.53a). As was seen in the carbon spectra of the N-Me and N-Pr dimers, evidence of crystallographic inequivalence was seen for the N-Cy dimers. Multiple C-OH aromatic sites were suggested in Me,Me-N-Cy, and clearly seen in H,Me-N-Cy at 154.2 and 156.0 ppm. As for all other dimers, the CH_2 sites adjacent to the amine were also found to be inequivalent at 46.0/51.7 and 49.9/52.1 ppm for Me,Me-N-Cy and H,Me-N-Cy respectively. In the aromatic region further evidence of inequivalence was seen for of H,Me-N-Cy, with two meta-CH sites found at 113.6 and 115.6 ppm. Considering these observations, H,Me-N-Cy bore close resemblance to the other mono ring-substituted dimers with N-Me and N-Pr amine-substituents. Combined with the known crystal structure the assignment of H,Me-N-Cy was made (Figure 4.55). In contrast, Me,Me-N-Cy showed only slight differences between the two aromatic rings, and suggested a more symmetric structure without site inequivalence (Figure 4.54).
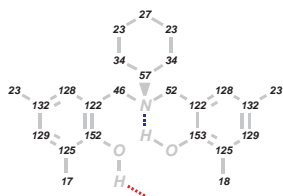
Figure 4.54: ^{13}C assignment of Me,Me-N-Cy.   *Figure 4.55: ^{13}C assignment of H,Me-N-Cy.*

4.2.5 Carbon spectroscopy: general trends

It was found that although relatively high quality proton DQ spectra could be obtained for Me,Me-N-Me and Me,Me-N-Pr, carbon spectroscopy proved problematic.[†] This situation was also encountered for all the N-Cy dimers, although similar problems were found with the proton spectra for these systems. With a HSQC spectrum of Me,Me-N-Me previously reported by Goward *et al.* information regarding this compound will be taken from the previous publication [Goward 01].

The mono ring-substituted dimers were found to be more amenable to the coherent methods. However, in order to achieve an adequate signal-to-noise level, desired for heteronuclear correlation and sideband analysis, extended measurement times were needed for relatively short recoupling times. This situation was in contrast to other materials previously studied using these techniques [Fischbach 02, Rapp 03].

In general, carbon spectroscopy echoed the results of the proton spectroscopy and showed the mono ring-substituted N-Me and N-Pr dimers existed in the more regular structures. It can also be concluded that, although Me,Me-N-Me and Me,Me-N-Pr showed signs of existing in regular forms, both systems showed anomalous behaviour when compared to other dimers with the same amine-substituent.
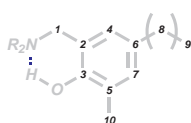
Figure 4.56: *Carbon site nomenclature used in Table* 4.13.

For all dimers which yielded carbon spectra, the two CH_2 groups either side of the amine were found to be inequivalent. Further examples of inequivalence were seen for the sites associated with the two aromatic rings (Table 4.13). The presence of two peaks-per-site has been attributed to a break in the symmetry about the amine [Goward 01]. This was confirmed with all peaks associated with the amine-substituents never found to exist in multiple environments. Even the relatively large cyclohexyl amine-substituent seemed to exist in a symmetric environment, with only slight differences possibly seen between the left and right hand-side of the ring.

Table 4.13: *Carbon chemical shifts (ppm) of chemically equivalent sites exhibiting crystallographic inequivalence. See Figure* 4.56 *for the carbon site nomenclature used in this table.*

δ_C	N-Me			N-Pr		N-Cy	
	Me,Me	H,Me	H,Et	H,Me	H,Et	Me,Me	H,Me
1	59.7 / 63.2	60.1 / 61.9	61.8 / 59.4	54.8 / 57.7	54.5 / 57.0	46.0 / 51.7	49.9 / 52.1
2	?	124.3	124.3	120.3/124.6	121.2/123.1	122.1	120.6
3	?	154.0	154.1	153.3/155.4	152.6/154.7	152.1/152.4	154.2/156.0
4	130.9/132.3	129.6	129.5	130.1/133.6	126.3	128.2	133.6
5		116.4/116.8	116.1/116.9	114.7/116.1	113.7/114.6		113.6/115.6
6	?	132.8	132.1/133.5	129.5	134.0/134.8	131.9	129.5/131.1
7	127.5/129.9	127.5	128.5	127.9	129.4/130.8	129.0	127.3/127.7
8			29.1		25.3 / 27.5		
9	21.1 / 21.2	18.5 / 20.4	14.7 / 18.2	20.4 / 20.8	15.2	22.7	20.9 / 21.1
10	16.1 / 16.6					16.7 / 17.6	

[†]i.e. acquisition of carbon spectra with acceptable quality in a reasonable amount of time proved difficult.

Although the presence of the two aromatic rings in slightly different orientations with respect to the amine would lead to the observation of such differences, evidence of π interactions were also observed. Such shielding interactions were most clearly seen in H,Et-N-Me where the terminal methyl groups of the ethyl ring-substituents were seen to exist at 14.7 and 18.2 ppm. The associated protons were also found to have chemical shifts of -0.5 and 1 ppm respectably, thus showing a shielding interaction caused by the close proximity of these groups to the face of an aromatic system (Figure 4.38b). The influence on chemical shift of the inequivalence was more clearly seen when only the difference between the two observed peaks was considered (Table 4.14).

Table 4.14: *Difference in carbon chemical shift of chemically equivalent sites exhibiting crystallographic inequivalence. See Figure 4.56 for the carbon site nomenclature used in this table.*

$\Delta\delta_C$	N-Me			N-Pr		N-Cy	
ppm	Me,Me	H,Me	H,Et	H,Me	H,Et	Me,Me	H,Me
1	3.5	1.8	2.4	2.9	2.5	5.7	2.2
2	?	-	-	4.3	1.9	-	-
3	?	-	-	2.1	2.1	0.3	1.8
4	1.4	-	-	3.5	-	-	-
5		0.4	0.8	1.4	0.9		2.0
6	?	-	1.4	-	0.8	-	1.6
7	2.4	-	-	-	1.4	-	0.5
8			-		2.2		
9	0.1	1.9	3.5	0.4	-	-	0.2
10	0.5					0.9	

When the CH_2 carbons directly attached to the amine are considered, a clear difference between the Me,Me and mono ring-substituted systems was seen. For both Me,Me-N-Me and Me,Me-N-Cy relatively high differences of 3.5 and 5.7 ppm were observed. For the mono ring-substituted systems $\Delta\delta_C$ varied by a lesser degree from 1.8–2.9 ppm. This suggested a more symmetric geometry was formed around the amine for the H,Me and H,Et dimers. The stronger influence of the cyclohexyl amine-substituent in Me,Me-N-Cy, as compared to the methyl amine-substituent of Me,Me-N-Me, further confirmed that steric factors associated with the amine-substituent play an important role in determining the final supramolecular structure.

The mono ring-substituted propyl dimers H,Me-N-Pr and H,Et-N-Pr were found to have the highest degree of asymmetry between the carbon sites associated with the aromatic rings. For H,Et-N-Pr almost every possible site showed two peaks. Although for H,Et-N-Pr the CH_2 group of the ethyl ring-substituents were split by 2.2 ppm, both accompanying methyl groups had the same chemical shift. The opposite trend was seen for H,Et-N-Me, where the two CH_2 groups had the same chemical shift and the methyl groups differed by 3.5 ppm. However, in the latter case these effects are thought to be more due to shielding interactions on these sites than crystallographic inequivalence. More importantly, for both systems two C-OH environments were seen, both with a $\Delta\delta_C = 2.1$ ppm. These inequivalent C-OH sites showed a closer proximity to either of the N··H-O or O··H-O hydrogen bonding pro-

tons, with the site with higher δ_C correlating to the O··H-O protons. This suggested that the inequivalent sites were indeed associated to the two aromatic rings of one molecule and not different crystallographic locations in the unit cell.

Using HSQC spectra, the protons undergoing shielding interactions found in H,Et-N-Me, H,Me-N-Pr and H,Et-N-Pr were assigned (Figure 4.57). As with the shielded sites seen by proton NMR, these interactions suggested close spatial proximity to the face of an aromatic system, however as to whether these interactions were intramolecular or intermolecular remained unknown. Both H,Et systems showed shielded ethyl ring-substituents. For H,Et-N-Me only the terminal methyl group showed the influence of shielding interactions, but for H,Et-N-Pr both CH$_2$ and CH$_3$ groups were shielded. As was suggested by the proton spectra, shielding interactions were also seen for the terminal methyl group of the propyl amine-substituents of the N-Pr dimers H,Me-N-Pr and H,Et-N-Pr.
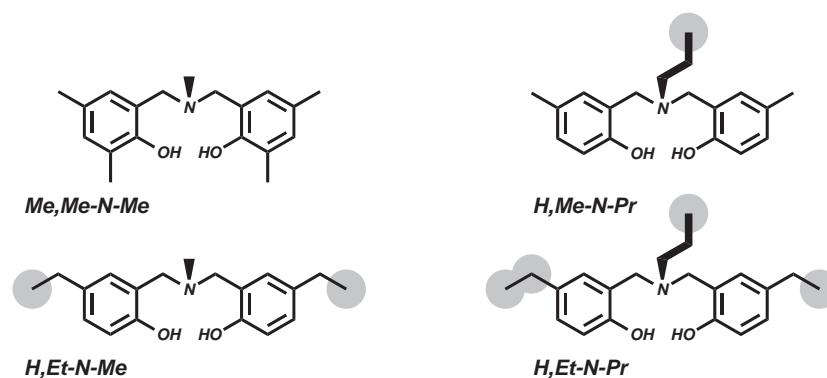
Figure 4.57: *Summary of the shielding interactions characterised by ^{13}C–^{1}H HSQC spectroscopy.*

It was expected that dimers with a higher degree of crystallinity would be both more amenable to the coherent techniques, and show higher resolution. In this respect H,Et-N-Pr and H,Me-N-Pr were considered to be the more structurally uniform systems followed by the Me,Me-N-Me system studied by Goward *et al.* [Goward 01]. Although carbon spectroscopy proved difficult, H,Me-N-Cy showed the next highest degree of crystallinity, as judged by the number of peaks alone, followed by H,Et-N-Me and H,Me-N-Me.

The crystal structure of H,Me-N-Cy clearly showed a different packing structure to that found in Me,Me-N-Me. It is suggested that all the mono ring-substituted dimers might exist in a similar structure, with the associated higher degree of asymmetry between the aromatic rings. The driving force for such a structural change being the stronger inter-molecular O··H-O hydrogen bonds formed.

As to why the carbon spectra of Me,Me-N-Pr and H,Me-N-Cy proved so problematic, and yet showed signs of high order in their corresponding proton DQ and carbon cross-polarisation spectra, is still unclear.

4.2.6   Nitrogen spectroscopy

With all nine dimers available in relatively large quantities, natural-abundance ^{15}N measurements were viable. The ^{15}N chemical shift was externally referenced to the tetrahedral ammonium ion of ammonium nitrate, i.e. δ_N (^{15}NH$_4^+$) = 0 ppm, thus giving small positive chemical shifts for all the tertiary amines found in the dimers. The absolute chemical shift varied from 13.9–27.3 ppm, with only a difference of 13.4 ppm between all systems. This was due to the strong similarity of the chemical environment of the nitrogen. This was comparable to the 15.9 ppm[†] determined by Goward *et al.* for an equivalent ^{15}N labelled methyl dimer [Goward 01]. As expected the directly attached amine substituent showed greatest influence over nitrogen chemical shift [Mason 87]. More electron donating amine-substituents were found to give higher chemical shifts, i.e. δ_N N-Cy > N-Pr > N-Me (Figure 4.58).
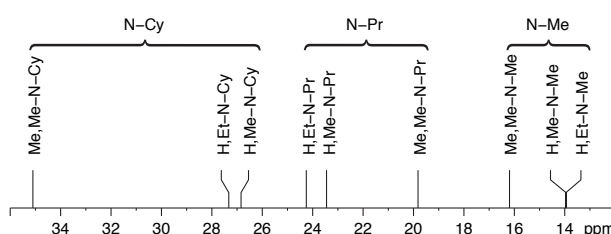
Figure 4.58: *Figurative representation of the ^{15}N chemical shifts of the N-Me, N-Pr and N-Cy dimers.*

More importantly, to a lesser extent the ring-substituents were also found to influence the chemical shift, with the largest differences seen between Me,Me and mono ring-substituted systems. This was more clearly seen when the spectra of dimers with the same amine-substituent were compared on the same chemical shift scale (Figure 4.59). The range of chemical shifts was largest for the N-Cy dimers, with least variation found for the N-Me dimers (Figure 4.59).
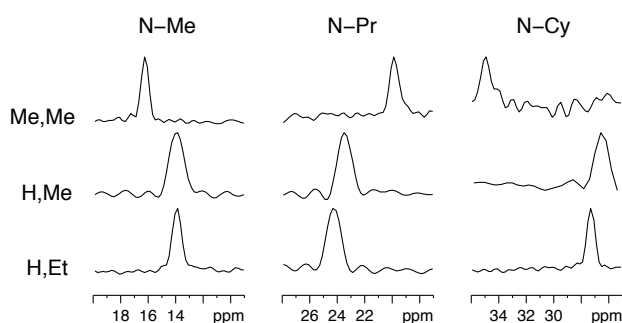
Figure 4.59: *Natural abundance ^{1}H–^{15}N CP MAS spectra of the N-Me, N-Pr and N-Cy dimers.*

[†]Goward *et al.* report a value of −342.5 ppm due to externally referencing the ^{15}N chemical shift scale to the nitrate ion of NH$_4$NO$_3$, i.e. δ_N (^{15}NO$_3^-$) = 0 ppm, thus resulting in δ_N (^{15}NH$_4^+$) = −358.4 ppm [Goward 01].

The influence of the ring-substituents on the nitrogen chemical shift was either due to a direct synergistic interaction through the covalent bonds, an indirect interaction through the N··H-O hydrogen bond or a combination of the two. The strongest differences were seen between the di-substituted and mono-substituted systems, with virtually no difference found between H,Me and H,Et forms for the same amine-substituent. Although this could have lent credence to the direct mechanism of influence, the resulting changes in ^{15}N chemical shift would be small. Furthermore, with the direct mechanism, stronger influences would be expected between H,Me and H,Et systems. With significant differences seen in both the proton and carbon spectra between the supramolecular structures of the Me,Me and mono ring-substituted dimers, the differences in hydrogen bonding were thought to be the more dominant interactions [Benedict 98].

Table 4.15: *^{15}N chemical shifts of the dimers.*

δ_N [ppm]	N-Me	N-Pr	N-Cy
Me,Me	16.2	19.8	34.9
H,Me	13.9	23.5	26.5
H,Et	13.9	24.2	27.3
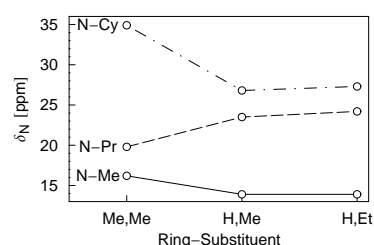
Figure 4.60: *Trends in dimer ^{15}N chemical shift.*

For the N-Me and N-Cy dimers, both H,Me and H,Et mono ring-substituted systems showed lower chemical shifts than their respective Me,Me forms. However, the opposite trend was seen for the N-Pr dimers, with the Me,Me system having the lowest chemical shift (Figure 4.60). The degree by which the chemical shift varied from Me,Me to mono ring-substituted forms was also dependent on amine-substituent, with $\Delta\delta_N$ N-Cy > N-Pr > N-Me. The anomalous behaviour of the N-Pr dimers was explained by the stronger N··H-O hydrogen bonding of Me,Me-N-Pr, and stronger O··H-O hydrogen bonding in H,Me-N-Pr and H,Et-N-Pr, as seen by proton NMR (Section 4.2.3). With stronger hydrogen bonding seen to affect the nitrogen chemical shift, evidence for the indirect mechanism of influence was found.

When nitrogen and N··H-O proton chemical shifts were correlated a weak trend was observed, with two strong residuals: Me,Me-N-Cy and Me,Me-N-Pr (Figure 4.61b). The deviation being due to higher and lower ^{15}N chemical shifts found in Me,Me-N-Cy and Me,Me-N-Pr respectively (Figure 4.60). Two weaker residuals of H,Me-N-Me and H,Et-N-Me were also seen. A stronger correlation was found between ^{15}N and O··H-O proton chemical shift. As previously seen Me,Me-N-Cy, H,Me-N-Me and H,Et-N-Me did not fit the general trend (Figure 4.61a). The deviation of the mono ring-substituted N-Me dimers was explained by the shortening of the O··H-O hydrogen bond upon removal of the methyl groups adjacent to the hydroxyls. The reduction of steric hindrance in the same direction as the O··H-O hydrogen bond could have influenced the N··H-O hydrogen bond, thus explaining the residual behaviour of the N··H-O protons in

these systems.
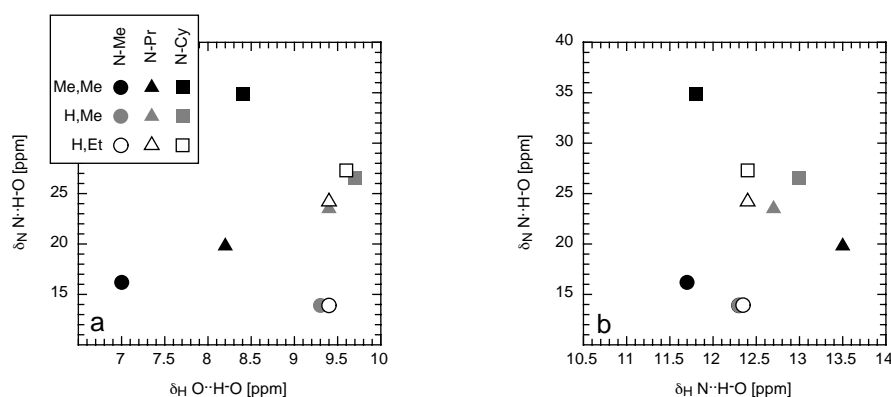
Figure 4.61: Correlation of nitrogen chemical shift with (a) O··H-O and (b) N··H-O proton chemical shift.

Generally, a clear distinction was again seen between the Me,Me and mono ring-substituted dimers. The mono ring-substituted systems with N-Me and N-Cy amine-substituents showing lower nitrogen chemical shifts. Even if the Me,Me-N-Pr system was considered anomalous, the spectra of the mono ring-substituted N-Pr systems clearly showed a different behaviour to that of Me,Me-N-Pr.
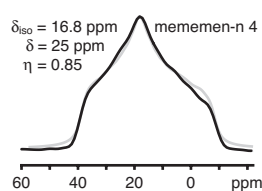
Figure 4.62: Symmetric Me,Me-^{15}N-Me CSA tensor.

It was hoped that information regarding the symmetry of the nitrogen site could have been gained by comparison of the η symmetry parameters, extracted from the static CSA tensors, of the dimers. Unfortunately natural abundance ^{15}N static NMR proved problematic, even with the use of custom built large volume detection coils, high B_0 field and polarisation enhancement techniques. For this reason CSA tensors of all dimers could not be measured in a realistic time frame. With Me,Me-N-Me also available in a ^{15}N enriched form, the CSA tensor of this compound was however recorded (Figure 4.62). The extracted isotropic chemical shift of 16.8 ppm was comparable to the value of 16.2 found for Me,Me-N-Me and the 15.9 ppm determined by Goward *et al.* for an equivalent ^{15}N labelled methyl dimer [Goward 01]. As suggested from the crystal structure the chemical shielding anisotropy was small ($\delta = 25$ ppm) and relatively symmetric ($\eta = 0.85$). This was characteristic of the near tetrahedral symmetry found at the nitrogen atom upon N··H-O hydrogen bond formation [Mason 87].

4.3 An-initio electronic structure calculations of model dimers

Striking agreement had previously been seen between experimental proton solid-state NMR spectra and ab-initio chemical shift calculations of N-methyl model polybenzoxazine oligomers [Goward 03]. With the crystal structures of Me,Me-N-Me [Dunkers 96] and H,Me-N-Cy [Laobuthee 01] known, further simulations were undertaken using similar methods in collaboration with Dr Daniel Sebastiani[†].

Evidence for both dimeric and continuous hydrogen bonding structures was provided by proton DQ spectroscopy. Unfortunately, simulation of the continuous hydrogen bonding structure proved extremely difficult. Although a number of possible geometries were constructed and tested, stable forms with comparable chemical shifts were not found. This was due to the multiple degrees of freedom present in such an ill-defined twisted geometry. These simulations were also computationally 'expensive' when compared to those of the dimeric structure, as more atoms were needed to fully describe the periodic nature of the continuous structure.

Due to the problems associated with simulating the continuous structure, an alternative approach was taken. This involved forcing the dimer to adopt the dimeric structure and monitoring the outcome, with the crystal structure of Me,Me-N-Me used as the starting geometry. From this initial geometry substituents were exchanged and the total energy minimised using density-functional theory (DFT) based ab-initio electronic structure methods (Appendices E & D). From the resulting optimised geometry the proton chemical shifts were calculated and the proton SPE spectrum simulated. This method has been shown to yield good agreement with experiment, in particular concerning the effects of hydrogen bonding [Goward 02, Sebastiani 02a, Sebastiani 02b].

[†]Co-author of previous investigation [Goward 03] (MPIP).

4.3.1 Ring-substituent effects

The effect of the ring-substituents on the N··H-O and O··H-O hydrogen bonding was studied by simulating the three N-Me dimers. Generally, the simulated spectra bore close resemblance to experiment (Figure 4.63), importantly the higher chemical shift of protons involved in hydrogen bonding was reproduced [Jeffrey 86]. Although the simulated chemical shifts were externally referenced[†] the absolute chemical shift values were generally higher than those from experiment. For this reason the relative chemical shifts were deemed more accurate, and thus the differences between simulated N··H-O and O··H-O proton chemical shift ($\Delta\delta_H$) were also calculated (Table 4.16).
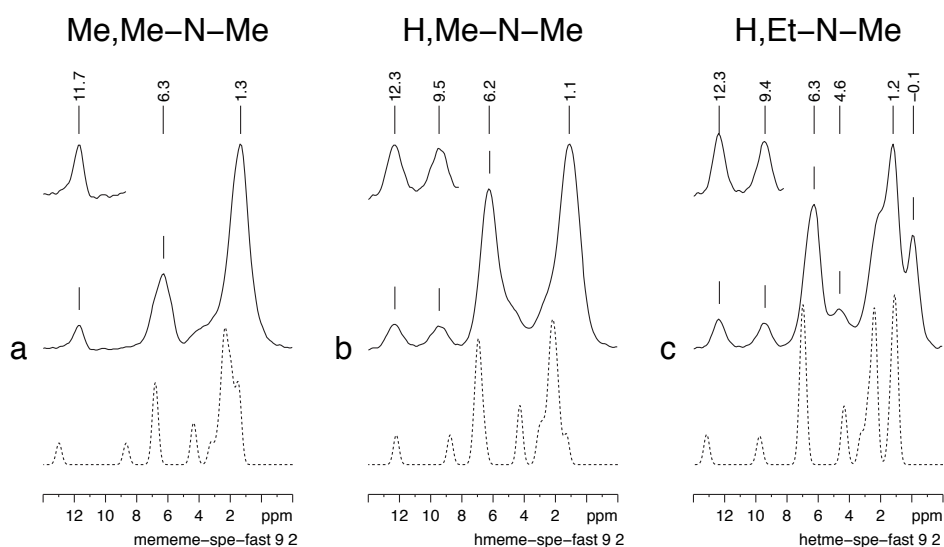
Figure 4.63: *Experimental (solid) and simulated (dashed)* ^1H *SPE spectra of the N-Me dimers.*

Table 4.16: *Comparison of experimental and simulated (in parentheses) chemical shifts of the N-Me dimers.*

δ_H [ppm]	Me,Me	H,Me	H,Et
N··H-O	11.2 (12.9)	12.3 (12.2)	12.3 (13.1)
O··H-O	7.4 (8.6)	9.5 (8.7)	9.4 (9.8)
$\Delta\delta_H$	3.8 (4.3)	2.8 (3.5)	2.9 (3.3)
$\Delta\Delta\delta_H$	0.5	0.7	0.4

Comparison of $\Delta\delta_H$ values showed that, as with the experimental data, the largest differences in N··H-O and O··H-O proton chemical shift was seen for Me,Me-N-Me. Similarly the two mono ring-substituted systems were found to have approximately the same difference. Unlike the experimental spectra, no clear increase in N··H-O and O··H-O hydrogen bonding was seen when going from Me,Me to mono ring-substituted systems. This was due to the simulated structure of Me,Me-N-Me showing stronger than expected N··H-O (Figure 4.64) and O··H-O (Figure 4.65) hydrogen

---

[†]A single molecule of trimethylsilane (TMS) is simulated and used to calibrate all other simulated spectra. (see Appendix E for further details).
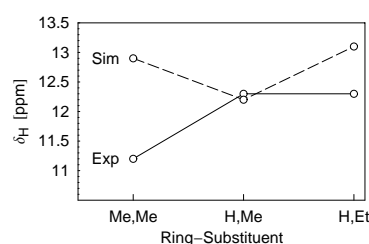
Figure 4.64: *Comparison of experimental (solid) and simulated (dashed) N··H-O proton chemical shifts of the N-Me dimers.*
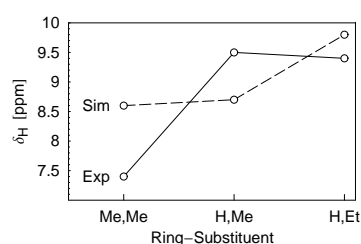
Figure 4.65: *Comparison of experimental (solid) and simulated (dashed) O··H-O proton chemical shifts of the N-Me dimers.*

bonding. When the two mono ring-substituted systems were compared, H,Me-N-Me showed stronger N··H-O and O··H-O hydrogen bonding than H,Me-N-Me, and suggested the simulated structure of H,Me-N-Me had weaker than expected hydrogen bonding. The combination of these interactions was thought to explain the deviations from experimental results. For all three systems the difference between experimental and simulated $\Delta\delta_H$ values ($\Delta\Delta\delta_H$) was small, and ranged between 0.4–0.7 ppm showing the accuracy of such simulations (Table 4.16). These differences in expected N··H-O and O··H-O hydrogen bonding were rationalised by considering the associated three-dimensional structures of the three systems.

The two aromatic rings of Me,Me-N-Me, associated with the O··H-O hydrogen bonds, were both bent out of plane and slightly overlapped with the neighbouring molecule (Figure 4.66). Such a geometry was not found to exist in the crystal structure (Figure 1.2) and most likely resulted from the lack of packing interaction from neighbouring molecules during the computational energy minimisation process. Without this steric hindrance the aromatic rings of both dimer units were able to form shorter N··H-O and O··H-O hydrogen bonds, resulting in the higher proton chemical shifts calculated.
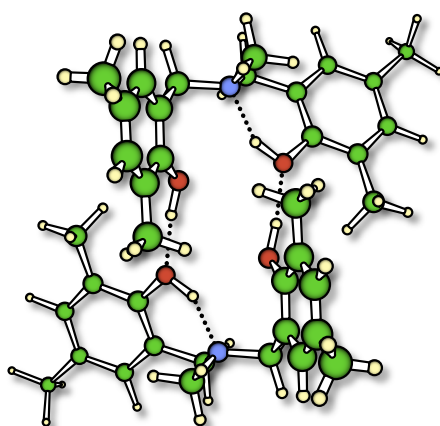
Figure 4.66: *Optimised geometry of Me,Me-N-Me, N··H-O and O··H-O protons at 12.9 and 8.6 ppm respectively.*
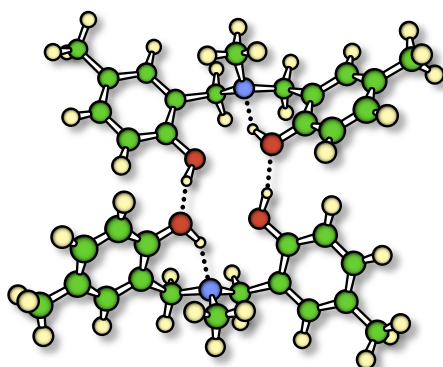
Figure 4.67: *Optimised geometry of H,Me-N-Me. N··H-O and O··H-O protons at 12.2 and 8.7 ppm.*
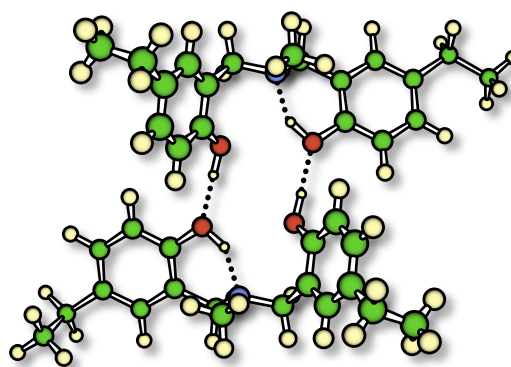
Figure 4.68: *Optimised geometry of H,Et-N-Me. N··H-O and O··H-O protons at 13.1 and 9.8 ppm*

This argument also applied to the three-dimensional structures of H,Me-N-Me and H,Et-N-Me (Figures 4.67 and 4.68). A more comparable structure to that of the X-ray structure was found for H,Me-N-Me, with the angle between aromatic rings belonging to the same molecule being relatively small. For H,Et-N-Me, as with Me,Me-N-Me, the aromatic rings were found to lie more out of plane than expected.

Table 4.17: *Comparison of N··H-O and O··H-O hydrogen bond lengths of the N-Me dimers.*

r_{jk} [pm]	Me,Me	H,Me	H,Et
N··H	171/171	176/176	171/171
O··H	182/183	178/179	175/174

From the three-dimensional structure the absolute bond lengths of the N··H-O and O··H-O hydrogen bonds were measured. As expected this showed the same trend as the simulated chemical shifts and ranged from 171–176 pm (Table 4.17). For comparison, the N··H distance experimentally determined by Goward *et al.* for Me,Me-N-Me was 195 pm [Goward 01]. The experimentally determined bond length was thought to be longer than that simulated due to packing constraints during geometry optimisation being neglected and possible anisotropic out-of-plane vibrations (librations) averaging the dipolar-coupling used to determine the bond length [Nakai 89].

4.3.2 Interaction of O··H‑O and N··H‑O hydrogen bonds.

Further investigation of the influence of steric hindrance on the N··H‑O and O··H‑O hydrogen bonding was undertaken. For H,Me‑N‑Me, a number of geometry optimisation and chemical shift calculation cycles were carried out with the inter-nuclear O··O distance constrained (Figure 4.69). This approach probed the influence of steric hindrance on the intermolecular O··H‑O hydrogen bonds, and also provided information regarding the synergy between O··H‑O and N··H‑O hydrogen bonds in the N··H‑O··H‑O configuration. Both the N··H‑O and O··H‑O hydrogen bonds were found to be influenced by changing the intermolecular O··O distance by only 90 pm (Figure 4.70 and Table 4.18).
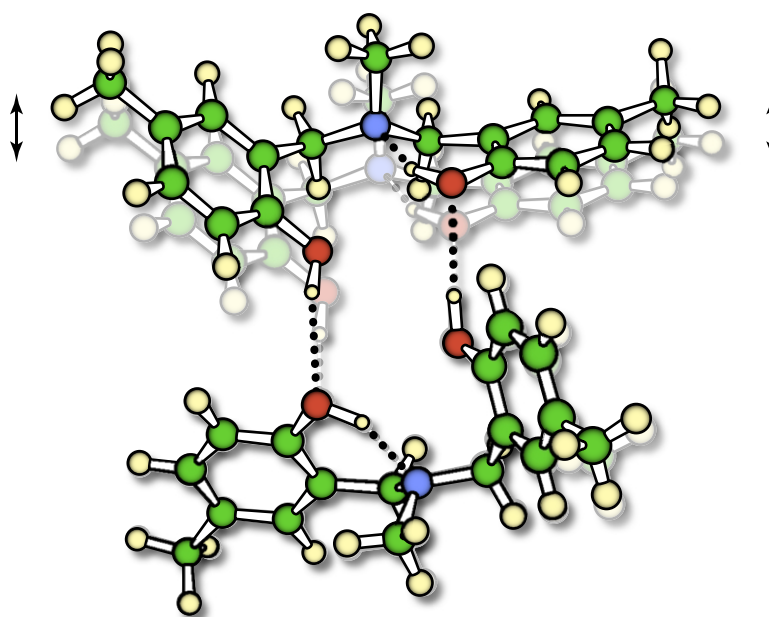
Figure 4.69: *Superposition of H,Me‑N‑Me geometries with $r_{O··O}$ distances of 250 and 340 pm. The different geometries resulted in differences in N··H‑O and O··H‑O proton chemical shift of 2.8 and 6.9 ppm respectively.*

Table 4.18: *chemical shifts of the N··H‑O and O··H‑O protons of H,Me‑N‑Me taken from simulated structures with constrained $r_{O··O}$ intermolecular distances.*

	N··H‑O		O··H‑O	
$r_{O··O}$	δ_H	$r_{N··H}$	δ_H	$r_{O··H}$
pm	ppm	pm	ppm	pm
250	15.08/14.48	169/165	13.63/13.48	151/150
260	14.43/13.81	172/169	12.35/12.21	160/160
271	14.70/14.39	168/166	11.64/11.28	171/171
278	14.25/14.03	170/168	10.53/10.47	177/176
287	13.32/12.94	176/173	9.58/9.51	188/187
306	12.55/12.53	178/177	8.32/8.04	208/207
320	12.55/12.50	178/176	7.67/7.47	223/221
330	12.38/12.34	197/177	7.26/7.11	231/230
340	12.35/12.31	178/177	6.94/6.79	244/241
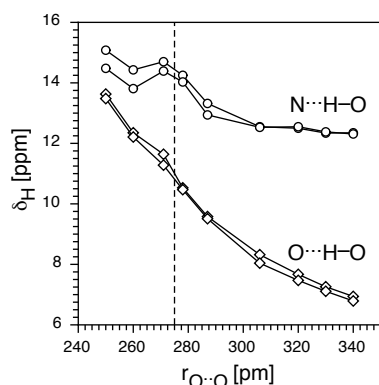
Figure 4.70: *Correlation of N··H-O and O··H-O proton chemical shift with constrained $r_{O··O}$ distances. Dashed line shows equilibrium separation of 275 pm.*
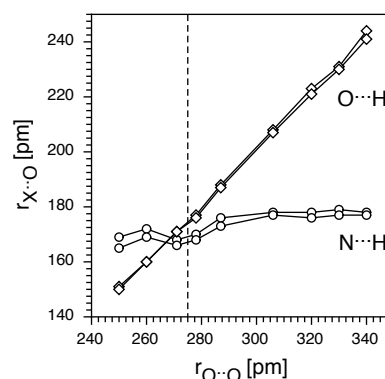
Figure 4.71: *Correlation of N··H and O··H bond lengths with constrained $r_{O··O}$ distances. Dashed line shows equilibrium separation of 275 pm.*

The O··H-O chemical shift varied between 6.9–13.6 ppm ($\Delta\delta_H$ = 6.9 ppm), whereas the N··H-O chemical shift only varied from 12.3–15.1 ppm ($\Delta\delta_H$ = 2.8 ppm) (Table 4.18). The chemical shift of the O··H-O proton showed a steady increase with decreased dimer separation (Figure 4.70). This confirmed the known experimental observation that O··H-O hydrogen bond strength is directly related to the O··O internuclear distance distance [Berglund 80, Jeffrey 86, Harris 88]. Thus, the O··H distance, from the O··H-O hydrogen bond, showed a strong linear correlation with the O··O distance (Figure 4.71).

Although slight differences in chemical shift were seen between the two N··H-O sites for all $r_{O··O}$ lengths, as with the O··H-O hydrogen bonds, below 271 pm N··H-O symmetry was more strongly distorted. This resulted in two distinct N··H-O resonances separated by $\approx$ 0.6 ppm. With multiple N··H-O sites not seen in any experimental spectra, this was thought to only occur because the system was forced below its equilibrium separation of 275 pm. Prior to the breakdown of symmetry, the N··H-O proton chemical shift were were also shown to increase slightly in strength with intermolecular separation (Figure 4.70). This suggested that the N··H-O hydrogen bond was weakly influenced by intermolecular separation, and thus O··H-O hydrogen bonding. However, the chemical shift and N··H distance only varied upon approaching the equilibrium separation. At larger separations ($r_{O··O} \geq$ 306 pm) both chemical shift and N··H distance remained approximately constant.

The behaviour of O··H-O hydrogen bonding with dimer separation provided corroborative evidence for the increased hydrogen bond strength, and thus proton chemical shift, seen for the mono ring-substitued dimers as compared to their equivalent Me,Me systems. Similar arguments may also apply for the N··H-O hydrogen bonds in the N-Me and N-Cy dimers.

4.3.3 Simulation of H,Me‑N‑Cy.

With the crystal structure of H,Me‑N‑Cy known the position of the protons and subsequent calculation of their chemical shifts was undertaken. However, before the results of these simulations are presented a brief description of the H,Me‑N‑Cy crystal structure [Laobuthee 01] will be given.

The crystal structure of H,Me‑N‑Cy.

Although a detailed X-ray diffraction study of the continuous hydrogen bonded structure has not been published[†] the crystal structures of H,Me‑N‑Cy, H,Et‑N‑Cy and H,Me‑N‑Pr were recently reported [Laobuthee 01]. However, only the crystal structure of H,Me‑N‑Cy was explicitly discussed. The crystallographic data for H,Et‑N‑Cy and H,Me‑N‑Pr were cited as being reported in an article under preparation by Chirachanchai *et al.* [Chirachanchai 01]. This was was suspected to be the same article referred to by Schnell in [Schnell 04a] as [Chiranchckai 02][†], and to date remains unpublished. Further attempts to obtain the data concerning the other materials only resulted in further information regarding H,Me‑N‑Cy [Chirachanchai 04]. Despite only the two X-ray diffraction crystal structures of Me,Me‑N‑Me [Dunkers 96] and H,Me‑N‑Cy [Laobuthee 01, Chirachanchai 04] being available, important structural differences were seen. The dimeric hydrogen bonding structure of H,Me‑N‑Cy showed a higher degree of symmetry than that of Me,Me‑N‑Me. More specifically, the dimeric supramolecular structure of H,Me‑N‑Cy contained a centre-of-symmetry *i* resulting in both 'T'-shaped dimers forming an anti-parallel arrangement. Thus, unlike the crystal structure of Me,Me‑N‑Me, where both methyl amine-substituents pointed in roughly the same direction (parallel arrangement), for H,Me‑N‑Cy the cyclohexyl amine-substituents pointed in opposite directions. Similarly, the two sets of aromatic rings, i.e. those carrying proton donating and proton accepting OH groups, also showed an anti-parallel configuration (Figure 4.72).
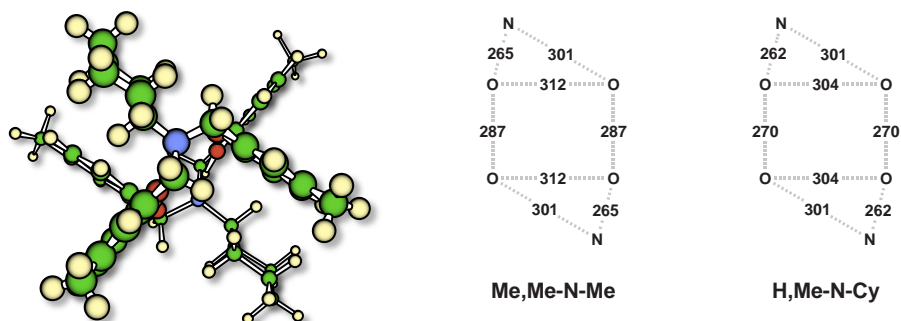
Figure 4.72: The anti-parallel configuration of the three groups attached to the amine in H,Me‑N‑Cy.

Figure 4.73: Internuclear distances related to hydrogen bonding measured from the crystal structures of Me,Me‑N‑Me and H,Me‑N‑Cy.

[†]For a more detailed summary see Appendix F.

This geometry resulted in a shortening of both intermolecular and intramolecular O··O internuclear distances (Figure 4.73). The intermolecular O··O distance decreased from 287 to 270 pm from Me,Me‑N‑Me to H,Me‑N‑Cy, with such a change possibly explaining the higher O··H‑O proton chemical shift of H,Me‑N‑Cy as compared to Me,Me‑N‑Cy (Section 4.2.1). Similarly, the intramolecular O··O distance decreased from 312 to 304 pm. Although only a minor difference, this could explain the observation of O··H‑O proton auto-correlation peaks in the proton DQ spectra of H,Me‑N‑Cy, and not Me,Me‑N‑Me (Section 4.2.1).

Whereas only hydrogen bonding supramolecular interactions were seen in the crystal structure of Me,Me‑N‑Me, π–π stacking was also present in H,Me‑N‑Cy. From the X-ray structure it can be seen that the aromatic rings of two distinct dimeric supramolecular units of H,Me‑N‑Cy stack 3.8 Å above each other (Figure 4.74).
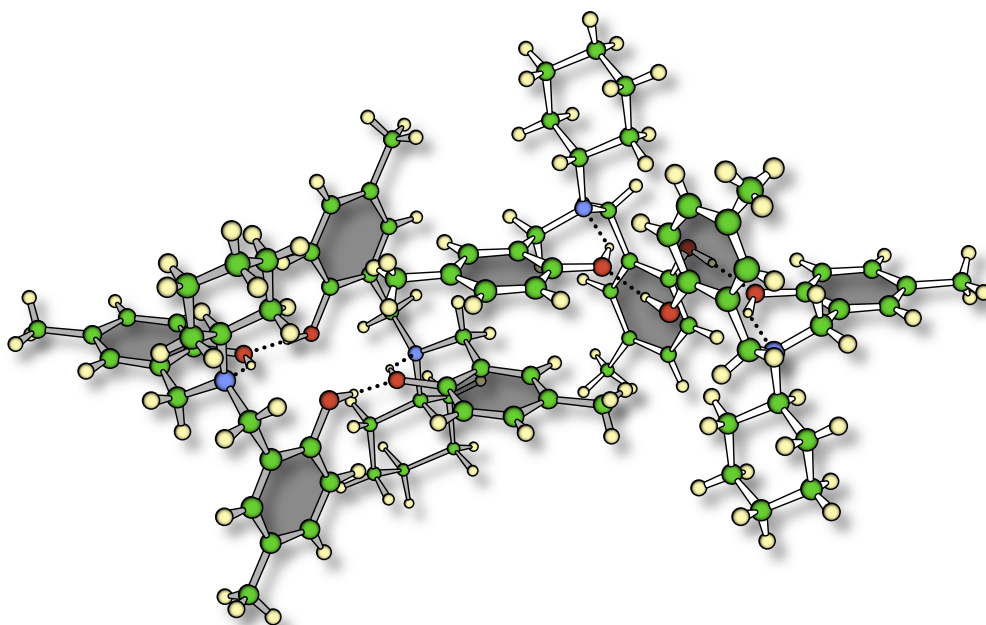
Figure 4.74: *The formation of π–π stacking in H,Me‑N‑Cy. Two distinct dimeric units are shown with the aromatic rings shaded to aid visualisation. The unit containing the lower ring of the π-stack is shown to the left (grey bonds), with that containing the upper ring shown on the right (white bonds).*

No further continuation of the π stack occurs, with the cyclohexyl groups of adjacent dimeric units found both above the supramolecular structure (Figure 4.75). From the crystal structure of H,Me‑N‑Cy the origin of the shielding interactions can also be seen, with multiple protons found within the shielding regions of various aromatic rings.
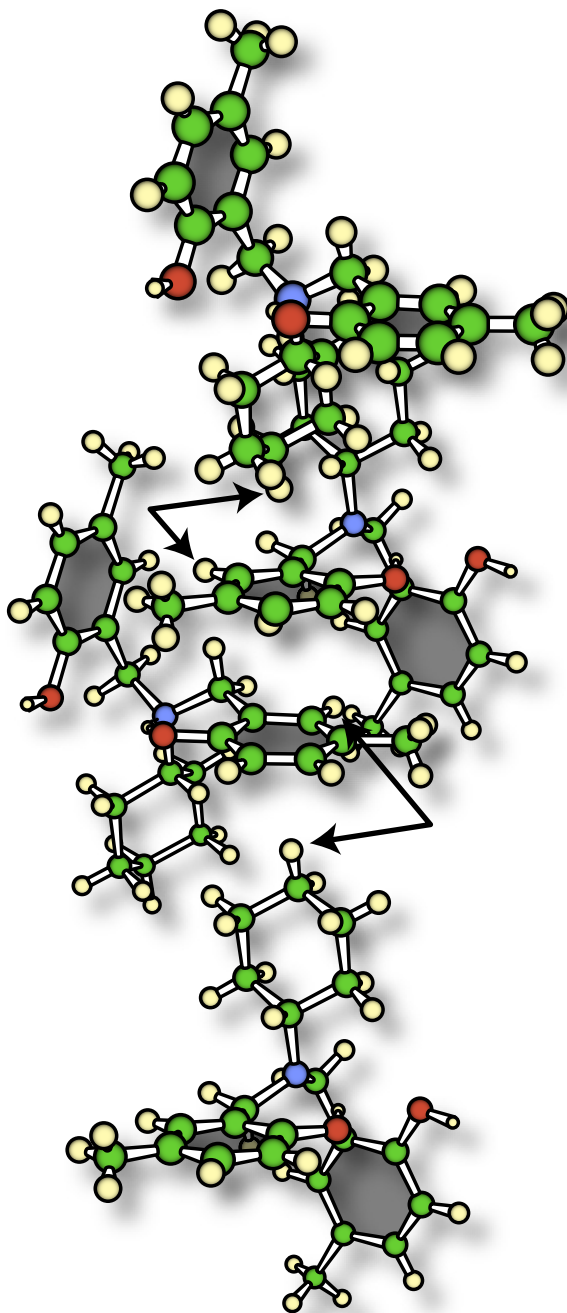
Figure 4.75: *The π stack only contained two aromatic ring with cyclohexyl groups found both above and below the supramolecular structure. Protons possibly experiencing shielding effects are indicated.*

Simulation of H,Me-N-Cy.

The H,Me-N-Cy dimer was modelled in the dimeric hydrogen bonding structure using the known positions of the heavy atoms taken from the crystal structure [Laobuthee 01]. From this geometry, the positions of the protons were optimised using ab-initio electronic structure methods. From the resulting geometry the proton chemical shifts were calculated (Figure 4.76). Very good agreement was seen between simulated and experimental SPE spectra (Figure 4.77).
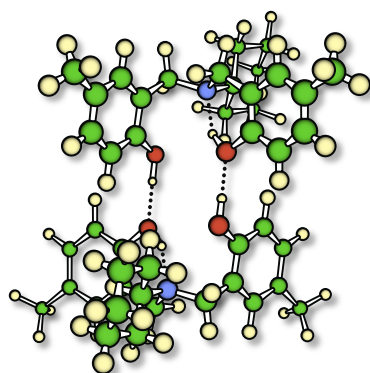
Figure 4.76: *Optimised geometry of the H,Me-N-Cy dimer based on a dimeric unit extracted from the known crystal structure.*
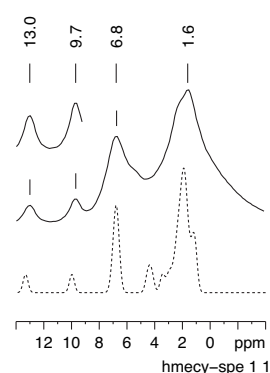
Figure 4.77: *Comparison of experimental (solid) and simulated (dashed) proton SPE spectra of the H,Me-N-Cy dimer.*

Unlike the simulations of the N-Me dimers (Section 4.3.1) good absolute agreement was seen between experimental and simulated spectra. Not only did the protons involved in hydrogen bonding show good agreement, but also those of the aromatic and aliphatic sites. This was strong evidence that the physical form of H,Me-N-Cy examined by solid-state proton NMR was the same as that described by the crystal structure.

Table 4.19: *Comparison of experimental and simulated (in parenthesis) chemical shifts of H,Me-N-Cy.*

	δ_H [ppm]	
N··H-O	13.0	(13.4)
O··H-O	9.7	(10.0)
$\Delta\delta_H$	3.3	(3.4)
$\Delta\Delta\delta_H$	0.1	

With full crystallographic information available, simulation of the whole unit cell with periodic boundary conditions also becomes possible. A comparison of Me,Me-N-Me and H,Me-N-Cy using this principle is currently under investigation [Parkinson 06]. However, simulations are problematic due to the larger unit cell of H,Me-N-Cy. For Me,Me-N-Me only 188 atoms (including protons) resided within the unit cell, whereas 432 are found for H,Me-N-Cy. The number of atoms is a known limiting factor when considering the non-linear scaling of computation time for current electronic structural methods. Despite this, the higher degree of symmetry found in H,Me-N-Cy might reduce the computational expense [Sebastiani 05].
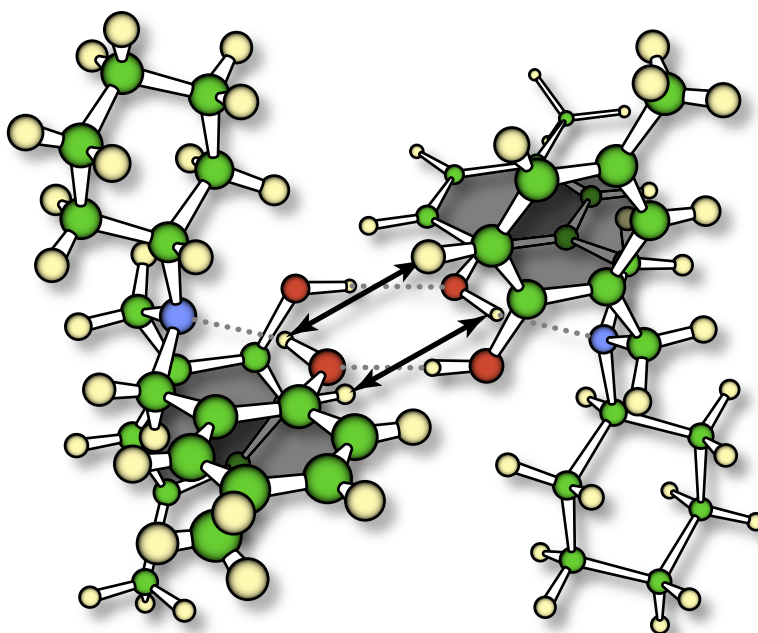
Figure 4.78: *The close proximity of aromatic and N··H-O protons in H,Me-N-Cy. $r_{HH} = 3.08$ Å.*

With the positions of the protons accurately determined on the framework of the X-ray structure, an important observation was made. Due to the perpendicular ring conformation, upon formation of the dimeric hydrogen bonding structure, aromatic protons came to lie within 308 pm of N··H-O protons (Figure 4.78). The aromatic protons which are in close proximity to the N··H-O protons are those which were only present for the mono ring-substituted dimers, i.e those at the 5-positions on the aromatic rings. With such a ^{1}H–^{1}H internuclear distance on the borderline of detection by DQ correlation spectroscopy [Schnell 01b], this observation had ramifications regarding the assignment of the continuous hydrogen bonding structure. In the previous section it was shown that in the absence of 5-methyl ring-substituents the dimers could come into closer proximity (Section 4.3.2), with the effects of this seen for both mono ring-substituted N-Me dimers (Section 4.3.1). It is thus suggested that upon exchange of the 5-methyl ring-substituents with protons, due to the lack of steric hindrance, these protons come into close proximity with the N··H-O protons. This could confirm the observations made in Section 4.2.3 that all H,Me and H,Et dimers exhibit at least a weak DQ correlation between N··H-O and aromatic protons. When the optimised geometries of H,Me-N-Me and H,Et-N-Me are reconsidered from this perspective, it was seen that H,Et-N-Me exhibited a r_{HH} distance of 325 pm as compared 384 pm for H,Me-N-Me. The shorter r_{HH} distance most likely due to the more perpendicular arrangement of the aromatic rings in H,Et-N-Me allowing stronger intermolecular hydrogen-bonding. With this highly efficient dimeric packing arrangement observed it is thus suggested that supramolecular structure more similar to that of H,Me-N-Cy were more common for all dimers in general, as opposed to those based on Me,Me-N-Me as previously thought.

4.4   Conclusions

It has been shown that, as well as the Me,Me-N-Me and Me,Me-N-Pr dimers examined by Schnell *et al.* [Schnell 98a], both mono ring-substituted and N-Cy dimers also possessed co-operative hydrogen bonding. The ^{1}H–^{1}H DQ correlation spectra all showed a similar general form to those previously reported, suggesting the presence of both intramolecular N··H-O and intermolecular O··H-O hydrogen bonds.

For all mono ring-substituted H,Me and H,Et dimers, a DQ correlation between the aromatic and N··H-O protons was observed, and subsequently suggested the presence of the continuous hydrogen bonding structure. Such a DQC was also seen for Me,Me-N-Cy. With the majority of these characteristic DQCs weak in nature polymorphism was suggested, with the dimeric hydrogen bonding structure being the more prevalent structure. An exception was found with H,Et-N-Me, which showed the strongest DQC of all dimers, thus indicating a higher proportion of the continuous hydrogen bonding structure for this system.

It was later shown by ab-initio calculations that, even in the dimeric hydrogen bonding structure, aromatic protons could come into close proximity with the N··H-O protons of H,Me-N-Cy. Due to the intermolecular nature of this interaction the perpendicular conformation of aromatic rings and reduction of steric hindrance between dimer units was thought to be of key importance. Furthermore, the aromatic protons in question were those in the 5-positions of the aromatic rings, these only being found in the mono ring-substitued dimers. With very good agreement seen between experimental and calculated proton spectra for H,Me-N-Cy, it is thus suggested that the supramolecular structure of H,Me-N-Cy was similar to that present in the crystal structure. This placed doubt over the assignment of the continuous hydrogen bonding structure based solely on the DQC between aromatic and N··H-O protons.

Less agreement was seen between the simulations of the mono ring-substituted N-Me dimers, based on the crystal structure of Me,Me-N-Me. This suggested that all mono ring-substituted dimers could possibly exist in supramolecular structures more similar to that of H,Me-N-Cy than Me,Me-N-Me.

Unlike the dimers previously investigated, a number of systems exhibited shielding interactions, which suggested close proximity to the 'face' of an aromatic system. These interactions were seen for all N-Cy dimers, both mono ring-substituted N-Pr dimers and for H,Et-N-Me. The shielded sites were assigned to the flexible terminal methyl groups of the ethyl ring-substituents (H,Et systems) and propyl amine-substituents (N-Pr systems) by ^{13}C–^{1}H heteronuclear correlation spectroscopy. Indications of the intermolecular origin of these interactions were seen in the crystal structure of H,Me-N-Cy.

Chapter 5

Effects of Amine-Substituents on Trimer Structure

As well as the model dimers studied in Chapter 4, higher oligomers were also synthesed as models for polybenzoxazines [Kim 03c]. These oligomers were extensions of the Me,Me-N-Me dimer by one or two further benzoxazine units, and thus resulted in an N-Me trimer and an N-Me tetramer respectively. The supramolecular structure of both oligomers was investigated by FT-IR, solid-state NMR and ab-initio electronic structure methods combined with chemical shift calculations. The trimer was found to adopt a cyclic supramolecular structure, whereas a helical geometry was suggested for the tetramer [Goward 03, Kim 03c]. However, in Chapter 4 the supramolecular structure of the dimers was found to be influenced by both the ring-substituents as well as the amine substituent. Thus the question arises: to what extent does the supramolecular structure of the higher oligomers depend on their chemical substituents? To help answer this question a comparison of N-Me and N-Et trimers was undertaken (Figure 5.1b). With no N-Et dimers studied in Chapter 4 it was also deemed prudent to confirm the supramolecular differences seen by Schnell *et al.* [Schnell 98a] between the Me,Me-N-Me and Me,Me-N-Et dimers (Figure 5.1a).
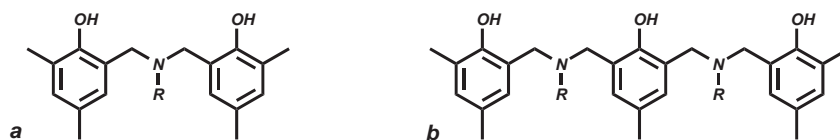
Figure 5.1: *General structure of N-methyl (R=Me) and N-ethyl (R=Et) model (a) dimers and (b) trimers. Note the hydroxyl groups of the N-methyl dimer drawn on the upper edge of the aromatic rings for comparison with trimer.*

5.1 Comparison of N-methyl & N-ethyl dimers

The chemical structures of the methyl and ethyl dimers differed only in the extension of the aliphatic amine-substituent by a single CH_2 unit (Figure 5.1a). Despite this small difference in chemical structure, previous investigation had shown evidence for relatively large differences in supramolecular structure [Schnell 98a]. The N-Me dimer was found to adopt the dimeric hydrogen bonding structure (Figure 5.2a) and the N-Et dimer the continuous hydrogen bonding structure (Figure 5.2b).
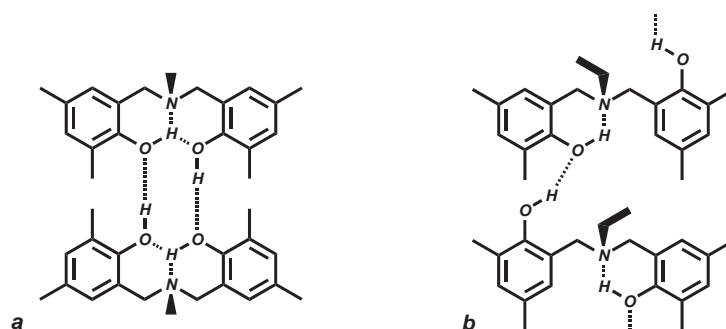
Figure 5.2: *The (a) dimeric structure of Me,Me-N-Me and (b) continuous structure of Me,Me-N-Et.*

In this study two forms of each dimer were studied, distinguished by their method of synthesis. The methyl dimer was available as either ^{15}N enriched or with ^{15}N in natural-abundance, referred to as Me,Me-^{15}N-Me and Me,Me-N-Me respectively. The Me,Me-^{15}N-Me form having previously been shown to have the same supramolecular structure as Me,Me-N-Me, but with a higher degree of order [Goward 01]. The extra degree of synthetic care taken during synthesis of a labelled compound, and resulting higher purity, was suggested to account for this increase in structural order. Both forms of the ethyl dimer had ^{15}N in natural-abundance. One form was synthesised by the same method as Me,Me-N-Me and the other by the more rigourous method used for Me,Me-^{15}N-Me, in the hope of once again creating a more uniform supramoleclar structure [Ishida 02]. These two ethyl dimers were thus designated Me,Me-N-Et and Me,Me-*N-Et. The quantity of material available for investigation was dependent on the method of synthesis, with Me,Me-N-Me and Me,Me-N-Et available in gram quantities but Me,Me-^{15}N-Me and Me,Me-*N-Et only available in milligram quantities (Table 5.1).
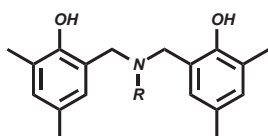
Figure 5.3: *General structure of methyl (R=Me) and ethyl (R=Et) dimers.*

Table 5.1: *Methyl and ethyl dimers studied*

R	name	mass	T_m [°C]
Me	Me,Me-N-Me	g	124.6
Et	Me,Me-N-Et	g	111.4
Me	Me,Me-^{15}N-Me	mg	–
Et	Me,Me-*N-Et	mg	–

5.1.1 NMR spectroscopy

Proton spectroscopy

Comparison of the methyl and ethyl dimer proton SPE spectra showed both large and small differences, caused by chemical and supramolecular structural changes (Figure 5.4).
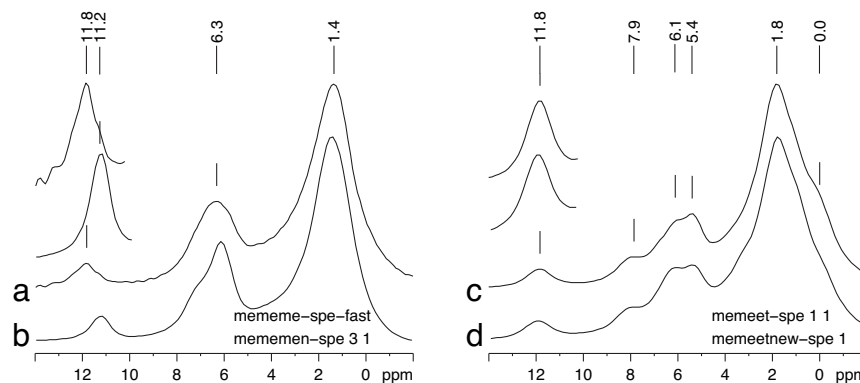
Figure 5.4: SPE spectra of (a) Me,Me-N-Me, (b) Me,Me-^{15}N-Me, (c) Me,Me-N-Et and (d) Me,Me-*N-Et.

The N··H-O hydrogen bonding protons of Me,Me-^{15}N-Me (11.2 ppm) were seen at lower chemical shift than those of Me,Me-N-Me (11.8 ppm) (Figure 5.4a–b). In contrast, the O··H-O protons of Me,Me-^{15}N-Me were observed at slightly higher chemical shift, as a more resolved shoulder to the left of the aromatic peak at 6.3 ppm. The difference between O··H-O peaks was more clearly seen in 2D ^{1}H spectra (shown later), from these the chemical shifts were seen to vary between 6.9 and 7.4 ppm for Me,Me-N-Me and Me,Me-^{15}N-Me respectively.

This implied that the N··H-O hydrogen bonds were stronger in Me,Me-^{15}N-Me than Me,Me-N-Me, with the reverse trend seen for the O··H-O hydrogen bonds. With the form of the 2D spectra (presented later) remaining similar, these differences were thought to be caused by slight conformational changes, which for Me,Me-^{15}N-Me favoured the intermolecular O··H-O hydrogen bond. Such differences could be rationalised with the chemical shift of the protons involved in hydrogen bonding not only sensitive to the bond length but also to bond angle. Ab-initio chemical shift calculations have shown that changes of ≈ 0.5 ppm, for N··H-O proton chemical shift in the dimeric hydrogen bonding structure, are not unreasonable for small conformational changes (Section 4.3.2). For Me,Me-^{15}N-Me the aromatic protons were also found to appear at a slightly higher chemical shift, and again suggested a slight change in conformation.

Only a very small difference in N··H-O proton chemical shift was seen for Me,Me-N-Et and Me,Me-*N-Et, and implied less structural change than that seen for the methyl dimers. Other differences between Me,Me-N-Et and Me,Me-*N-Et were more subtle. In the spectrum of Me,Me-N-Et a weak shoulder was seen at

≈ 0 ppm (Figure 5.4c), and indicated a shielding interaction from an aromatic system. This was less defined in the spectrum of Me,Me-*N-Et (Figure 5.4d). As well as this, the aromatic protons at 6.1 ppm were found to be slightly higher in intensity for Me,Me-*N-Et (Figure 5.4d). Such small spectral differences could be accounted for by slight changes in experimental conditions of the NMR experiments. However, with further differences seen between Me,Me-N-Et and Me,Me-*N-Et using 2D DQ spectroscopy (shown later) these small differences were thought to originate from the materials themselves.

When compared to SPE spectra, DQ filtered spectra showed slightly higher resolution. For both N-Me dimers the O··H-O shoulder became more pronounced and for Me,Me-*N-Et was resolved to a maximum at 7.7 ppm (Figure 5.5).
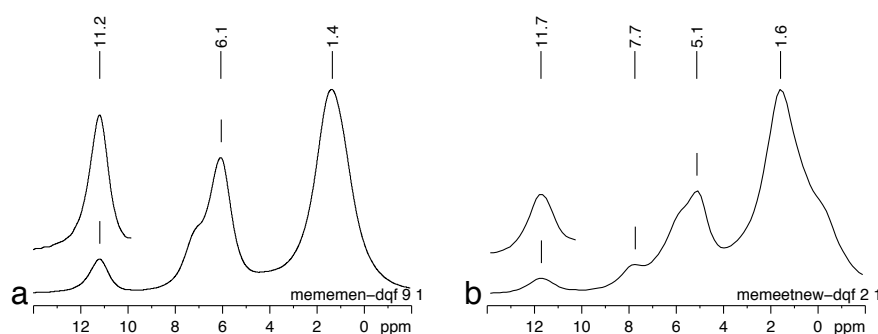
Figure 5.5: *DQ filtered spectra of (a) Me,Me-^{15}N-Me and (b) Me,Me-*N-Et with $\tau_{exc/rec} = 2 \cdot \tau_r$*

When comparing the methyl and ethyl dimers both N··H-O and O··H-O hydrogen bonds were shown to be influenced by a change in amine substituent (Table 5.2). Although the N··H-O protons were found at the same chemical shifts for Me,Me-N-Me and Me,Me-N-Et, both Me,Me-^{15}N-Me and Me,Me-*N-Et showed lower values. However, the ethyl dimers showed stronger O··H-O hydrogen bonding, with up to 1.0 ppm higher chemical shifts. Two aromatic sites were observed in the ethyl dimer systems with these possibly indicating different packing orientations of the two aromatic rings, each resulting in a different chemical shift. This was confirmed by the combined size of the two aromatic peaks being approximately equal to that of the single aromatic peak found for the methyl dimers. The increased intensity of the aliphatic peak for the ethyl dimers showed the incorporation of the CH$_2$ protons of the ethyl amine-substituent. This suggested that the shoulder at ≈ 0 ppm resulted from the terminal methyl protons of the ethyl amine-substituent.

Table 5.2: *Proton assignment of the N-Me and N-Et dimers. Parenthesis indicate chemical shifts from 2D spectra.*

δ_H [ppm]	Me,Me-N-Me	Me,Me-^{15}N-Me	Me,Me-N-Et	Me,Me-*N-Et
N··H-O	11.8	11.2	11.8	11.7
O··H-O	(6.9)	(7.4)	7.9	7.7
Ar #1	6.2	6.1	(6.1)	(6.0)
Ar #2	6.2	6.1	5.4	5.1
Ar CH$_3$	1.4	1.5	1.8	1.6
N CH$_2$	–	–	1.8	1.6
N CH$_3$	1.4	1.5	(0.0)	(−0.1)

The 2D DQ correlation spectra of Me,Me-^{15}N-Me and Me,Me-*N-Et had similar overall forms (Figure 5.6), as expected from their almost identical chemical structure and indicated O··H-O and N··H-O hydrogen bonding. However, more double quantum coherences were seen for Me,Me-*N-Et, due to the higher chemical shift of the O··H-O protons and two resolved aromatic sites.
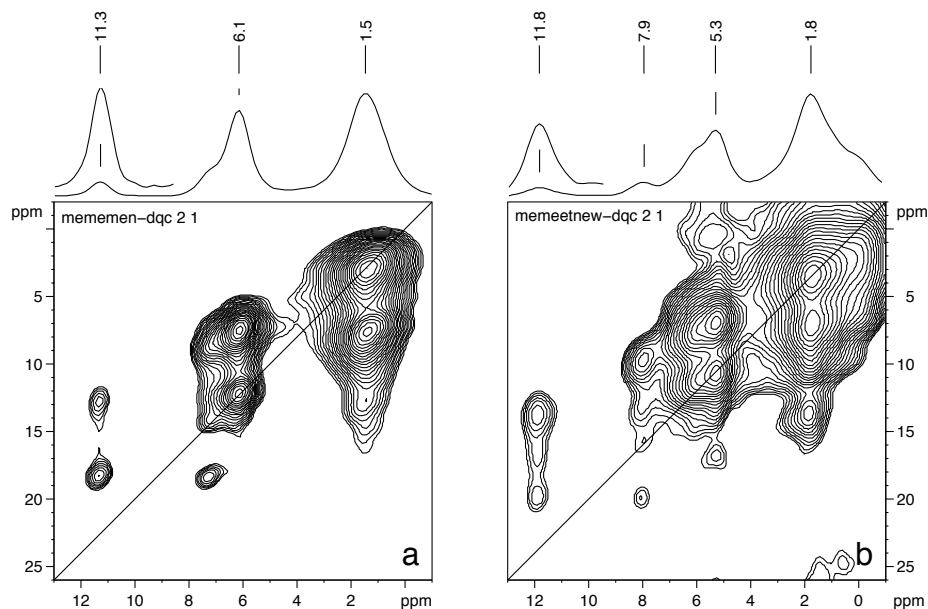
Figure 5.6: *DQ spectra of (a) Me,Me-^{15}N-Me and (b) Me,Me-*N-Et with $\tau_{exc/rec} = 2 \cdot \tau_r$*
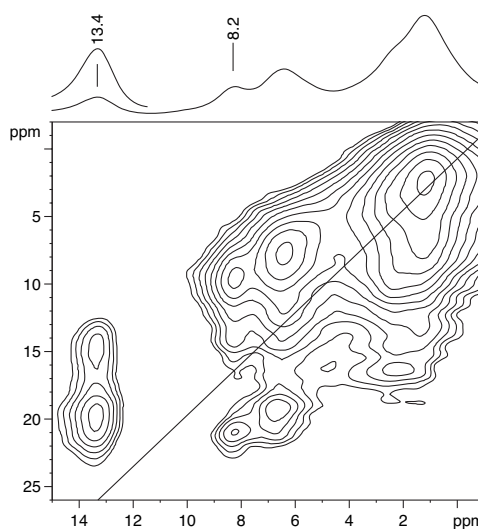
Figure 5.7: *DQ spectra of the ethyl dimer reported by Schnell et al. (reproduced from [Schnell 98a])*

A DQ coherence between N··H-O and aromatic protons was only present for the ethyl dimers (Figure 5.6b). The presence of such a DQ coherence had previously been suggested as an indication of the continuous hydrogen bonding structure [Schnell 98a]. However, the weak nature of the DQC suggested this form was

only present in low concentration. This was in contrast to the DQ spectra published by Schnell *et al.*, which showed a much stronger DQC for the ethyl dimer (Figure 5.7). From the DQ spectra of Schnell *et al.* the N··H‑O proton chemical shift was also higher, at 13.4 ppm as compared to 11.7‑11.8 ppm. Considering these significant differences it was concluded that a different supramolecular structure of the ethyl dimer was investigated by Schnell *et al.* during their investigation [Schnell 98a]. The high N··H‑O proton chemical shift was comparable to the anomalously high value seen for Me,Me‑N‑Pr (13.5 ppm) in Chapter 4 (Section 4.2.3).

In the hope of creating a more uniform supramolecular structure, recrystallisation of Me,Me‑N‑Et from n-hexane was undertaken. Unfortunately, no improvement in resolution, nor change in form of the DQ spectra was observed. Complete removal of residual solvent was also found to be difficult, with the best spectra recorded for a recrystallised sample showing little overall gain in resolution (Figure 5.8). With the lower N··H‑O chemical shift observed for both Me,Me‑N‑Et and Me,Me‑*N‑Et samples before, as well as after recrystallisation, it was concluded that this state was more representative of the ethyl dimer in general.
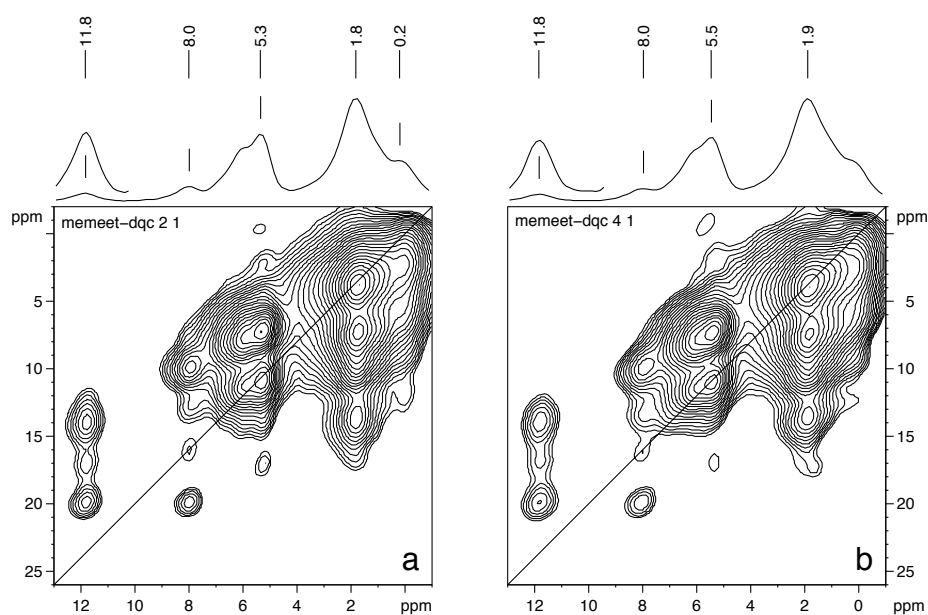
Figure 5.8: DQ spectra of Me,Me‑N‑Et (a) before and (b) after recrystallisation.

Surprisingly, direct comparison of the two ethyl dimers showed Me,Me‑N‑Et (Figure 5.8a) to have slightly better resolution, than Me,Me‑*N‑Et (Figure 5.6b). However, in general there was little difference between Me,Me‑N‑Et and Me,Me‑*N‑Et.

Fast-MAS proton spectroscopy

Due to small quantity restrictions only Me,Me-N-Me and Me,Me-N-Et were investigated using fast-MAS proton spectroscopy. However, the disadvantage of using Me,Me-N-Me as opposed to Me,Me-^{15}N-Me was found to be minimal. The resolution gain possible was illustrated by comparison of SPE spectra taken with $\omega_r/2\pi = 30$ and 70 kHz MAS (Figure 5.9).
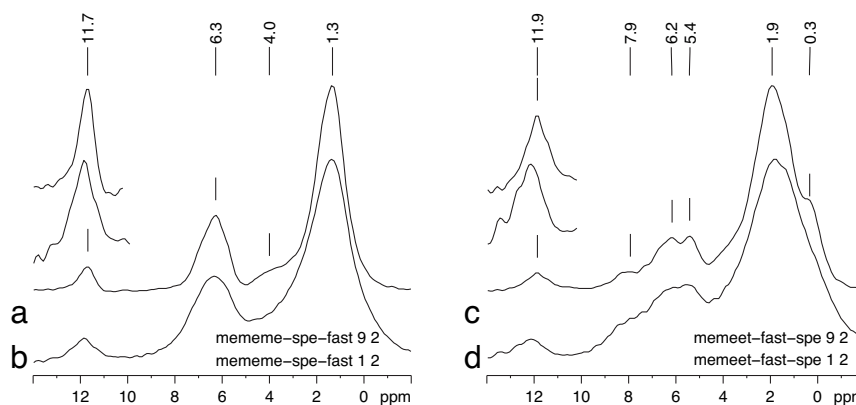
Figure 5.9: *SPE spectra of (a,b) Me,Me-N-Me and (c,d) Me,Me-N-Et at $\omega_r/2\pi = 70$ kHz (upper) and 30 kHz (lower). Note: $\nu_{1H} = 600$ MHz for all spectra.*

Under the different MAS conditions slight differences were observed for both methyl and ethyl dimers. For Me,Me-N-Me the CH$_2$ protons at 4 ppm were resolved, and for Me,Me-N-Et the aromatic and aliphatic shoulders became more pronounced (Figure 5.9). When considering these spectra the reduced external magnetic field strength should also be considered, with all fast-MAS spectra measured at ν_{1H} = 600 MHz. This accounted for the lower resolution in 30 kHz spectra as compared to those presented in the previous section acquired at ν_{1H} = 700 MHz (Figure 5.4). The lower signal-to-noise ratio of both 30 and 70 kHz spectra was attributed to the reduced sample volume available in the MAS rotors capable of spinning at such high rotational frequencies.

As with the fast-MAS dipolar exchange spectra presented in Chapter 4, large negative artefacts at the centre of the spectral window resulted in the dipolar exchange spectra providing little information. However, as with other dipolar exchange spectra, the presence of the negative cross-peaks between the isolated N··H-O proton and the mobile methyl protons were seen for Me,Me-N-Me (Figure 5.10a). No such negative cross-peaks were seen for Me,Me-N-Et under fast-MAS (Figure 5.10b), nor at $\omega_r/2\pi = 30$ kHz. As previously discussed, such negative cross peaks could indicate the DQ cross-relaxation was preferred under these MAS conditions.
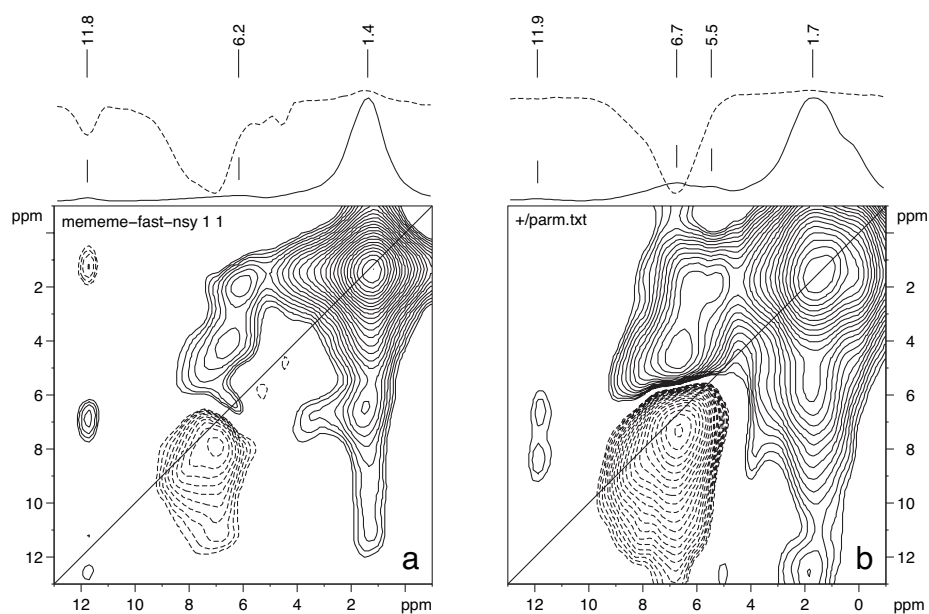
Figure 5.10: *Dipolar-exchange spectra of (a) Me,Me-N-Me and (b) Me,Me-N-Et at $\omega_r/2\pi = 65$ kHz. Positive (solid) and negative (dashed) projections shown illustrating negative cross-peaks and artefacts. Note: $\nu_{1H} = 600$ MHz.*
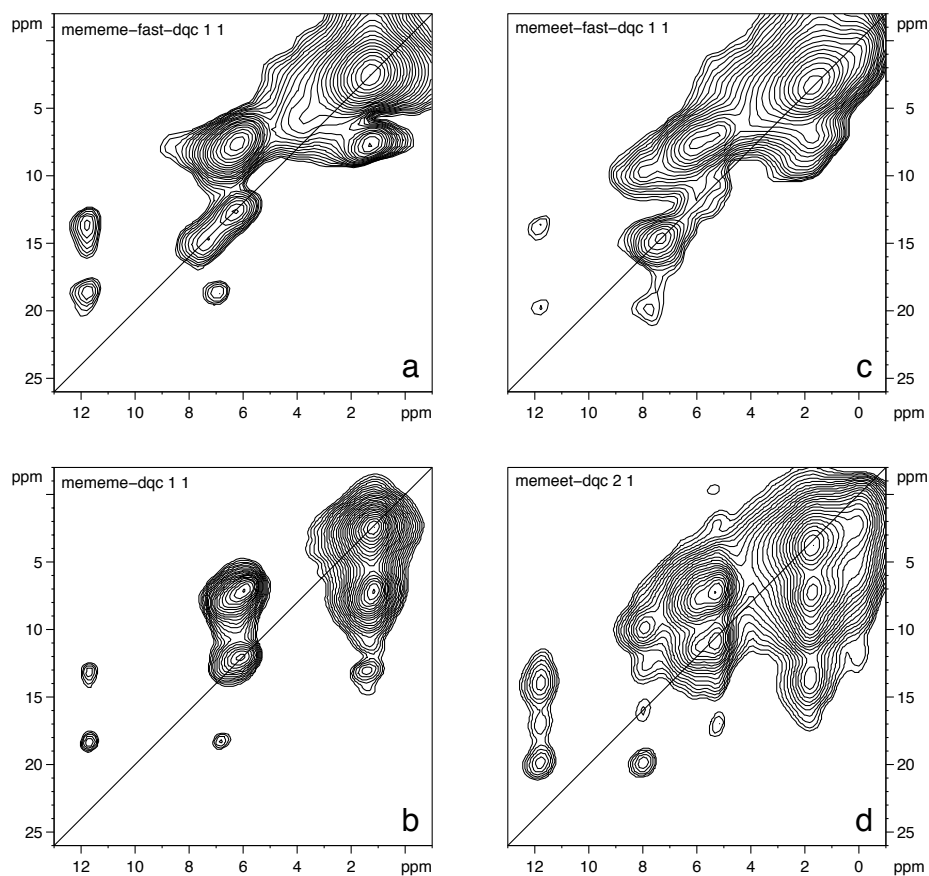
Figure 5.11: *DQ spectra of (a,b) Me,Me-N-Me and (c,d) Me,Me-N-Et at $\omega_r/2\pi = 65$ kHz (upper) and 30 kHz (lower). Note: $\nu_{1H} = 600$ MHz (upper) and 700 MHz (lower).*

Although acquired with different external magnetic field strenths, comparison of DQ correlation spectra measured at $\omega_r/2\pi = 30$ kHz ($\nu_{1H} = 700$ Mhz) and $\omega_r/2\pi = 65$ kHz MAS ($\nu_{1H} = 600$ Mhz) showed similar results (Figure 5.11). When comparing these spectra it should be noted that the samples would not have been at the same temperature, due to different degree of frictional heating under MAS. Unfortunately, no temperature calibration had been carried out for the fast-MAS probehead. However, it had previously been shown that the hydrogen bonding in the dimers persisted until the onset of melting, with only the intensity of proton resonance decreasing due to increased motional averaging [Schnell 98a].

Approximately the same DQ coherences were observed for Me,Me-N-Me at 65 (Figure 5.11a) and 30 kHz MAS (Figure 5.11b). As with the other fast-MAS DQ spectra presented in Chapter 4 a strong positive artefact was seen for both Me,Me-N-Me and Me,Me-N-Et, similar to an auto-peak at 7.5 ppm. This unfortunately totally obscured the weak O··H-O proton auto-correlation seen for Me,Me-N-Et in the same position (Figure 5.11d). For Me,Me-N-Me, the CH_2 protons were again seen at 4 ppm, and showed a possible interaction with the methyl protons. The DQ corelation between the N··H-O and methyl protons was found to be asymmetric in intensity distribution. As with previous DQ spectra measured under these conditions, phase errors were common for the more mobile methyl protons and could thus obscure the accompanying DQ cross peak. Similar asymmetry of this DQC and positive artefact at 7.5 ppm was seen for Me,Me-N-Et (Figure 5.11c). However, all DQ correlation involving N··H-O and O··H-O protons were weaker in intensity for the fast-MAS DQ spectrum. This was thought to be caused by the elevated temperature of the sample, and the resulting hydrogen bond vibrations hindering the recoupling mechanism. In general, a dramatic increase in resolution was not seen for fast-MAS, with arguably better resolution seen with 30 kHz MAS and $\nu_{1H} = 700$ MHz.

Heteronuclear spectroscopy

As previously discussed in Chapter 4 (Section 4.2.4), heteronuclear spectroscopy of Me,Me-N-Me proved problematic. Similar problems were found for Me,Me-N-Et. No ^{13}C spectra will be presented for either system for this reason. However, with Me,Me-^{15}N-Me being nitrogen enriched, and relatively large quantities of Me,Me-N-Me and Me,Me-N-Et available, the influence of hydrogen bonding on the ^{15}N chemical shift was investigated. Proton spectroscopy provided evidence for slight differences in N··H-O hydrogen bonding not only between the N-Me and N-Et dimers, but also between the two forms of the methyl dimer Me,Me-N-Me and Me,Me-^{15}N-Me (Figure 5.4).

For both Me,Me-N-Me and Me,Me-^{15}N-Me dimers a single resonance was seen at 16.2 and 17.0 ppm respectively (Figure 5.12). These were comparable to the value of 15.9 ppm[†] determined by Goward *et al.* for an equivalent ^{15}N labelled methyl dimer [Goward 01], and those determined in Section 4.2.6 for various N-Me, N-Pr and N-Cy dimers. The higher chemical shift of Me,Me-^{15}N-Me agreed with proton spectroscopy where weaker N··H-O hydrogen bonding was observed. With weaker N··H-O hydrogen bonding imparting less R_3N^+H character to the nitrogen site [Mason 87].
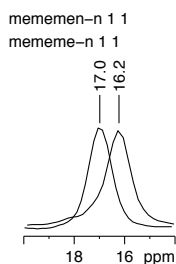
Figure 5.12: *^1H–^{15}N CP spectra of Me,Me-^{15}N-Me (17.0 ppm) and Me,Me-N-Me (16.2 ppm).*
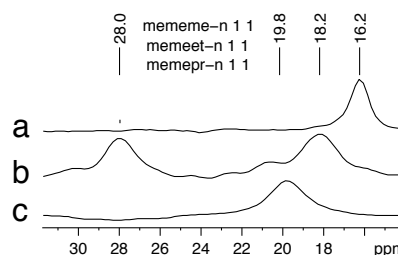
Figure 5.13: *^1H–^{15}N CP spectra of (a) Me,Me-N-Me, (b) Me,Me-N-Et and (c) Me,Me-N-Pr.*

Due to the small quantity of Me,Me-*N-Et available, natural abundance measurements were only carried out on Me,Me-N-Et. In contrast to the two forms of the methyl dimer, and all other dimers investigated in Chapter 4, the nitrogen spectrum of Me,Me-N-Et showed two peaks at 18.2 and 28 ppm (Figure 5.13b). Additionally, it had also been necessary to re-optimise the experimental conditions for Me,Me-N-Et, whereas for all other nitrogen cross-polarisation spectra the same general conditions had proven adequate. Comparison of the spectrum of Me,Me-N-Et with that of Me,Me-N-Me and an analogous propyl dimer Me,Me-N-Pr showed that the peak at 16.2 ppm followed the trend of increasing chemical shift with amine length, i.e. δ_N Me < Et < Pr (Figure 5.13). The observed chemical shifts of Me,Me-^{15}N-Me did not deviate from this trend. Thus showing the stronger influence of the amine-substituent, and weaker role of N··H-O hydrogen bonding,

---

[†]Goward *et al.* report a value of -342.5 ppm due to externally referencing the ^{15}N chemical shift scale to the nitrate ion of NH_4NO_3, i.e. $\delta_N\ (^{15}NO_3^-) = 0$ ppm, thus resulting in $\delta_N\ (^{15}NH_4^+) = -358.4$ ppm [Goward 01].

on ^{15}N chemical shift. The peak at 28.0 ppm was more comparable to the dimers with cyclohexyl amine-substituents of Chapter 4. The presence of two peaks in the spectrum, and the different optimum experimental conditions needed, possibly indicate polymorphism in Me,Me-N-Et. With the possibility of both the continuous and dimeric hydrogen bonding supramolecuar structures seen by proton DQ spectroscopy, the peak at 28 ppm could correspond to a chemically equivalent amine in the different supramolecular structures. However, further investigation needs to be carried out to confirm this.

5.1.2   Ab-initio electronic structure calculations

Evidence for both the continuous and dimeric hydrogen bonding structure was seen for Me,Me-N-Et by proton DQ spectroscopy, and polymorphism suggested by nitrogen spectroscopy. However, as previously described simulation of the continuous hydrogen bonding structure was impractical (Section 4.3). Thus, in order to compare the differences between the N-methyl and N-ethyl dimers, Me,Me-N-Et was simulated adopting the dimeric hydrogen bonding structure. The geometry of both systems was optimised using the crystal structure of Me,Me-N-Me as the starting geometry. From the resulting optimised geometries it was seen that, compared to Me,Me-N-Me (Figure 5.14), the symmetry of the Me,Me-N-Et dimeric unit was broken (Figure 5.15). The most likely cause for such a break in symmetry being the increased steric bulk of the ethyl amine-substituent.
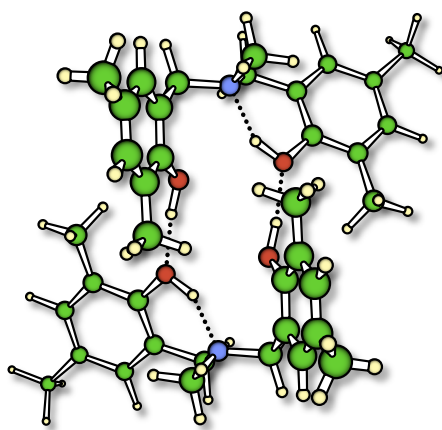
Figure 5.14: *Optimised geometry of Me,Me-N-Me with the two amines having similar local geometry.*
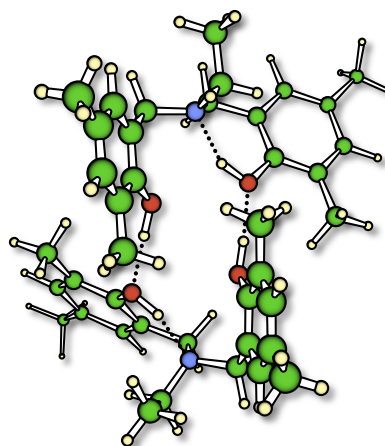
Figure 5.15: *Optimised geometry of Me,Me-N-Et, with the two amines having different local geometry.*

From the optimised geometries the chemical shift of the protons were calculated and compared to experimental data spectra of Me,Me-^{15}N-Me and Me,Me-N-Et (Figure 5.16)
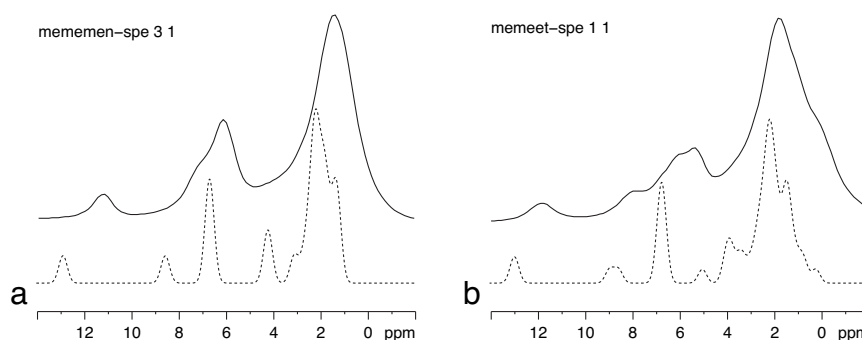
***Figure 5.16**: Experimental (solid) and simulated (dashed) proton SPE spectra of (a) Me,Me-N-Me and (b) Me,Me-N-Et.*

The simulated spectrum of Me,Me-N-Me was previously discussed in Section 4.3.1. Simulation of Me,Me-N-Et showed similar results to Me,Me-N-Me, with all chemical shifts slightly overestimated (Figure 5.16b). However, when the differences in chemical shift between the N··H-O and O··H-O protons ($\Delta\delta_H$) were considered good agreement was seen between simulated and experimental spectra (Table 5.3). The asymmetry in amine environment for the ethyl dimer was reflected in the two O··H-O sites seen in the simulated spectra of Me,Me-N-Et (Figure 5.16b). These having chemical shifts of 8.6 and 9.0 ppm. A similar, but weaker, effect was seen for the N··H-O protons at 13.0 and 13.1 ppm.

***Table 5.3**: Comparison of experimental and simulated (in parenthesis) chemical shifts.*

δ_H [ppm]	N··H-O	O··H-O	$\Delta\delta_H$	$\Delta\Delta\delta_H$
Me,Me-N-Me	11.2 (12.92/12.93)	7.4 (8.65/8.61)	3.8 (4.27/4.32)	0.47/0.52
Me,Me-N-Et	11.8 (12.95/13.05)	7.9 (8.60/8.97)	3.9 (4.35/4.08)	0.45/0.18

It was however unclear as to why such a change in amine geometry influenced the O··H-O hydrogen bond by 0.4 ppm and the N··H-O by only 0.1 ppm. Unlike the mono ring-substituted N-Me dimers (Section 4.3.1), the lengths of the respective O··H and N··H distances of Me,Me-N-Et did not vary by a large amount (Table 5.4). Both N··H distances were also comparable to that determined by Goward et al. for Me,Me-^{15}N-Me (195 pm) when accounting for vibrational effects [Goward 01]. This could indicate a possible asymmetry in shielding or bond angles between the different sets of O··H-O and N··H-O hydrogen bonds in Me,Me-N-Et.

***Table 5.4**: Comparison of hydrogen bond lengths and H··O-H··N torsion angles of the optimised geometries of Me,Me-N-Me and Me,Me-N-Et.*

	$r_{N··H}$ [pm]	$r_{O··H}$ [pm]	$\phi_{H··O-H··N}$ [°]
Me,Me-N-Me	171/171	182/183	−3.2/−3.5
Me,Me-N-Et	170/171	181/182	−1.4/ 13.6
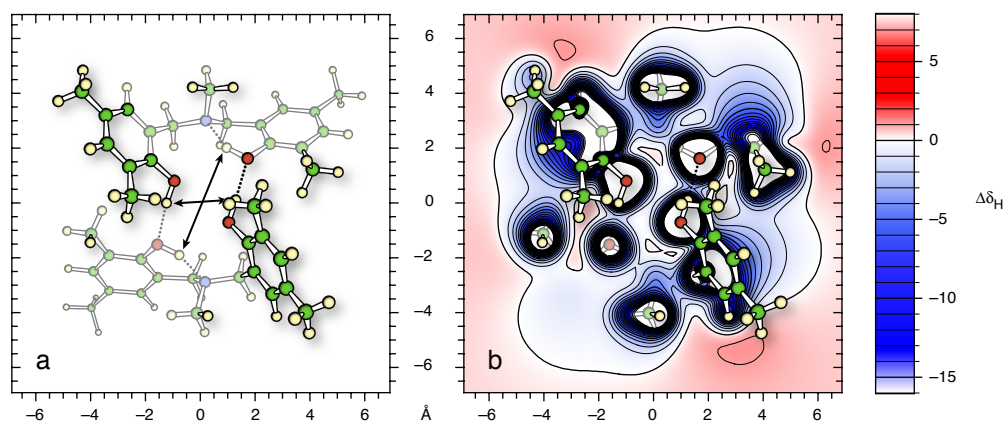
***Figure 5.17**: Slice through the the nucleus-independent chemical shift (NICS) map of Me,Me-N-Me. Slice aligned with the plane of N··H-O and O··H-O hydrogen bonds (a) showed no shielding/deshielding influences (b), with the low $\Delta\delta_H$ values solely due to their proximity to heteroatoms.*

From the nucleus independent chemical shift map of Me,Me-N-Me the likelihood of shielding interactions was discounted, with neither N··H-O nor O··H-O protons found within shielding or deshielding regions of any of the four aromatic rings (Figure 5.17b). With a difference of 15° found between the two H··O-H··N torsion angles in Me,Me-N-Et, and only 0.3° difference seen for Me,Me-N-Me, it was thought that bond-angle influences could explain these observations.

With good agreement seen between simulated and experimental proton spectra of Me,Me-N-Et, it was suggested that if this system were to adopt the dimeric hydrogen bonding structure a spectrum similar to that observed would be found. Combined with the proton DQ spectra of the previous section, this indicated that the dimeric hydrogen bonded structure was more prevalent in Me,Me-N-Et than the continuous structure.

5.1.3 Summary

The sensitivity of both proton and nitrogen chemical shift to slight changes in supramolecular structure has been shown by comparison of the two forms of the methyl dimer. A difference of ≈ 0.5 ppm in δ_H and 0.8 ppm in δ_N was seen between Me,Me-N-Me and Me,Me-^{15}N-Me indicating stronger N··H-O hydrogen bonding in Me,Me-N-Me. This having previously been attributed to the more ordered supramolecular structure formed from a sample of higher purity [Goward 01]. Little difference was seen between the two forms of the ethyl dimer Me,Me-N-Et and Me,Me-*N-Et, with arguably better results obtained for Me,Me-N-Et.

Unlike the spectra presented by Schnell *et al.* of the ethyl dimer [Schnell 98a], a strong DQ coherence between N··H-O and aromatic protons was not observed, with only a weak correlation present. The chemical shift of the N··H-O protons was also found to be lower (11.8 ppm c.f. 13.4 ppm), and a second aromatic site observed. Considering these observations it was concluded that a different supramolecular structure of Me,Me-N-Et was investigated by Schnell *et al.* during the previous investigation [Schnell 98a]. However, with the two separately synthesised samples Me,Me-N-Et and Me,Me-*N-Et showing similar spectra, both before and after recrystallisation, it was thought that the ethyl dimer investigated here was more representative. As with the majority of mono ring-substituted dimers of Chapter 4, the characteristic DQ coherence of the continuous structure was weak for Me,Me-N-Et. Thus suggesting that if such a supramolecular structure was present it was in low concentration. With the corresponding DQC for both methyl dimers being extremely weak, the continuous hydrogen bonding structure was thought to be unlikely for these systems. Unfortunately, DQ spectroscopy under fast-MAS supplied little further information, although slightly greater resolution was seen in the SPE spectra at $\omega_r/2\pi = 65$ kHz.

Evidence of polymorphism in the ethyl dimer was most clearly shown by ^{15}N spectroscopy, with two distinct peaks observed. The need to reoptimise experimental conditions also indicated that the ethyl dimer was dissimilar to all other dimers investigated. When compared to the chemical shifts of analogous methyl and propyl dimers a trend was seen for the peak with lower chemical shift. The origin of the second peak is still unknown.

Modelling of both methyl and ethyl dimers in the dimeric hydrogen bonding structure showed good agreement with experimental data, and provided further evidence that both systems predominantly existed in the dimeric structure.

5.2 Comparison of N-methyl & N-ethyl trimers

As with the methyl and ethyl dimers studied in the previous section, the chemical structure of the two trimers only differed in amine substituent, again N-methyl or N-ethyl (Figure 5.18). With small differences in amine-substituent playing an important role in determining the supramolecular structure of the dimers [Schnell 98a], similar effects for the trimers were expected.
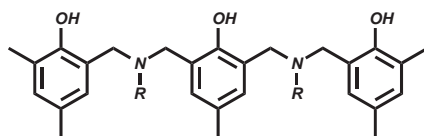
Figure 5.18: *General structure of the model methyl (R = Me) and ethyl (R = Et) trimers.*
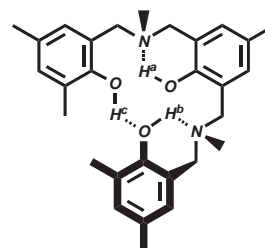
Figure 5.19: *Cyclic structure of the methyl-trimer. hydrogen bonding protons:* $\delta_{H_a} > \delta_{H_b} > \delta_{H_c}$

The supramolecular structure of the methyl trimer was first suggested by Dunkers *et al.* on the basis of molecular modelling [Dunkers 96]. These molecular-mechanics calculations built upon the X-ray structure of the Me,Me-N-Me dimer and extended the hydrogen bonding motif. Synthesis of the methyl trimer, as well as a related methyl tetramer, was undertaken by Ishida *et al.* and characterised by UV/VIS spectroscopy [Ishida 98], however for both the trimer and tetramer synthetic yields were low and purification found to be difficult. The existence of the cyclic conformation, containing three intramolecular hydrogen bonds (Figure 5.19), for the methyl trimer was shown by Goward *et al.* using a combination of ^{1}H solid-state NMR and ab-initio electronic structure methods [Goward 03]. An alternate method of trimer preparation and further evidence for the cyclic structure was shown by Kim *et al.* using FT-IR spectroscopy [Kim 03c]. Recently, the thermal degradation of the methyl trimer has provided insight into the thermal degradation pathways of polybenzoxazines in general [Hemvichian 05].

With the trimers more problematic to synthesise in a pure form, as compared to the dimers, only small quantities were available for analysis. The methyl trimer studied was partially ^{15}N enriched, and had the same ring-substituents as the systems previously studied by Goward and Kim *et al.* [Goward 03, Kim 03c]. The ethyl trimer had ^{15}N in natural-abundance and was synthesised by the method of Kim *et al.* [Kim 03c]. As with the enriched methyl dimer Me,Me-^{15}N-Me the extra synthetic care taken to produce an enriched system was expected to yield greater supramolecular order. As with the dimers discussed in the previous section both trimers had the equivalent of Me,Me ring-substituents (Figure 5.18). The trimers will be referred to as Me,Me-(N-Me)$_2$ and Me,Me-(N-Et)$_2$, emphasising the similarity between the dimers Me,Me-N-Me and Me,Me-N-Et and the presence of two substituted amines per model polybenzoxazine trimer.

5.2.1 NMR spectroscopy

Proton spectroscopy

As with the dimers, the general form of the SPE spectra of methyl and ethyl amine-substituted trimers was similar. Both methyl and ethyl trimers showed two distinct forms of N··H-O hydrogen bonding to be present (Figure 5.20). For both systems the N··H_b-O protons, those of the weaker N··H-O hydrogen bonds, had approximately the same chemical shift of ≈ 10.7–10.8 ppm. In contrast, almost a whole ppm difference was seen between the N··H_a-O protons, those of the stronger N··H-O hydrogen bonds. These were observed at 12.3 and 13.2 ppm for Me,Me-(N-Me)$_2$ and Me,Me-(N-Et)$_2$ respectively. The 13.2 ppm peak was also much less intense, with the ≈ 1:1 intensity ratio of the two N··H-O peaks as seen in the methyl trimers not found for the ethyl trimer. These observations implied the presence of stronger, albeit less abundant, N··H-O hydrogen bonding in Me,Me-(N-Et)$_2$. With such differences in N··H-O hydrogen bonding found between the trimers it was suggested that both systems did not exist in the same supramolecular structure.

The O··H-O protons of both trimers were obscured by the aromatic protons, and were only clearly seen in 2D spectroscopy (Figure 5.22). As with the N··H_b-O hydrogen bonds, the O··H-O hydrogen bonds showed little difference between the methyl and ethyl trimers, both being found between 7.4–7.6 ppm. Both trimers exhibited two aromatic sites at ≈ 5.6 and 6.8 ppm, the difference in chemical shift attributed to the central and terminal aromatic rings. The aliphatic peak of Me,Me-(N-Me)$_2$ showed a shoulder at 1.2 ppm to the right of the main peak at 1.9 ppm, this was attributed to a shielded methyl ring-substituent by HSQC spectroscopy (shown later). A similar interaction, although much weaker was also seen for Me,Me-(N-Et)$_2$ (Table 5.5).

Figure 5.20: *Proton SPE spectra of the trimers: (a) Me,Me-(N-Me)$_2$ and (b) Me,Me-(N-Et)$_2$.*
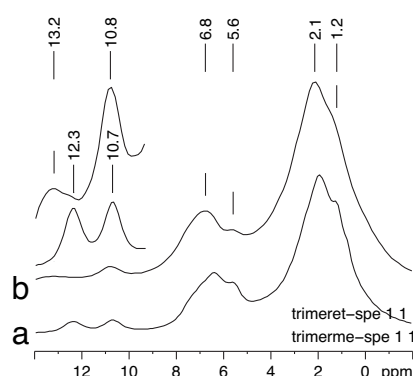
Table 5.5: *Assignment of trimer proton SPE spectra. Brackets indicate values obtained from 2D spectra*

δ_H [ppm]	Me,Me-(N-Me)$_2$	Me,Me-(N-Et)$_2$
N··H_a-O	12.3	13.2
N··H_b-O	10.7	10.8
O··H-O	(7.4)	(7.6)
H-Ar	6.4	6.8
H-Ar	5.6	5.6
CH$_3$	1.9	2.1
CH$_3$	1.2	1.2

The hydrogen bonding and aromatic sites were further resolved by DQ filtered spectroscopy (Figure 5.21). An increase in relative intensity of the N··H-O protons was also observed, this was thought to be due to the hydrogen bonding predominantly occurring in the structurally well defined regions favoured by dipolar recoupling [Goward 03].
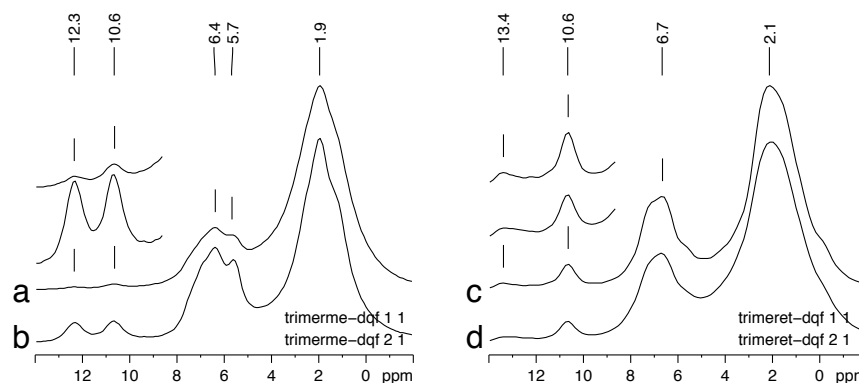
Figure 5.21: *DQ filtered spectra of (a–b) Me,Me-(N-Me)$_2$ and (c–d) Me,Me-(N-Et)$_2$ with $\tau_{exc/rec} = 1$ (upper) and $2 \cdot \tau_r$ (lower).*

For the methyl trimer further increase in intensity of the N··H-O peaks was seen when the recoupling time $\tau_{exc/rec}$ was extended from $1 \cdot \tau_r$ to $2 \cdot \tau_r$. Similarly, the two aromatic sites, as well as the aliphatic shoulder, became more resolved. No such increase in N··H-O intensity nor resolution enhancement was seen for the ethyl trimer, with relaxation effects dominating the DQ intensity buildup. This suggested the ethyl trimer was less ordered than the methyl trimer. The strongest evidence for different supramolecular structures was seen with 2D DQ correlation spectroscopy (Figure 5.22).

For the methyl trimer all three hydrogen bonding protons are clearly resolved (Figure 5.22a). A strong DQC was seen between the N··H$_a$-O and O··H-O protons. A weaker DQC was also observed between the N··H$_a$-O and N··H$_b$-O protons, with no interaction between either N··H-O and aromatic protons suggested.

As with the SPE spectra of the ethyl trimer, the DQ correlation spectra clearly showed the two N··H-O protons were present in different concentrations (Figure 5.22b). A weak DQC was seen between the N··H$_a$-O and O··H-O protons at ≈ 7.6 ppm, with a second weak DQC found between the N··H$_a$-O and aromatic protons of higher chemical shift (≈ 7.1 ppm). Unlike the methyl trimer, a strong DQC was observed between the N··H$_b$-O and aromatic protons of lower chemical shift (≈ 6.7 ppm). Both the N··H$_a$-O and O··H-O protons were not found to be present in high concentrations. The N··H$_b$-O protons were not only more abundant in Me,Me-(N-Et)$_2$, but were also suggested to exist in close proximity to aromatic protons. These observations could possibly be explained by the existence of other structural conformations of the ethyl trimer, similar to that found in the continuous hydrogen bonding structure of the dimers.
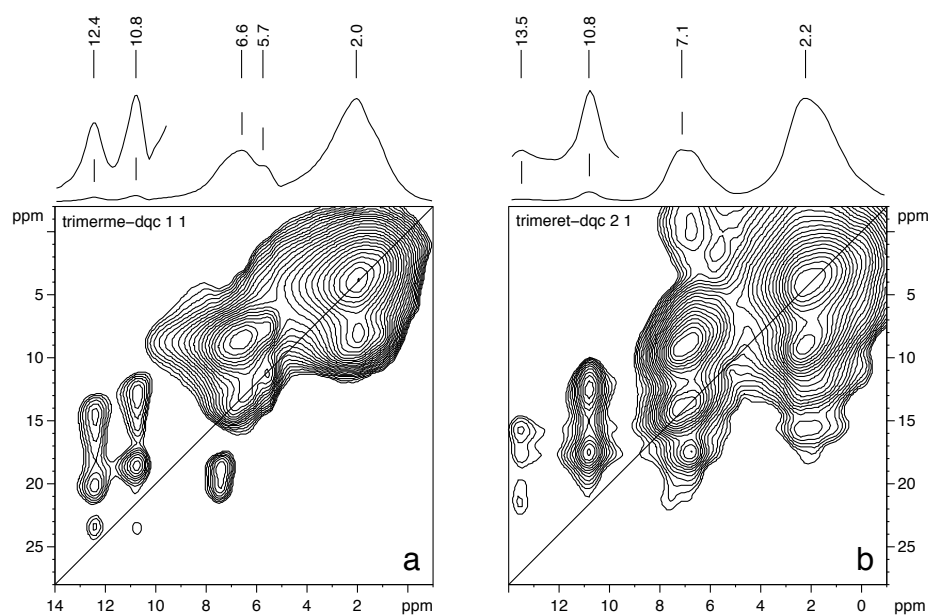
Figure 5.22: *DQ spectra of (a) Me,Me-(N-Me)$_2$ ($\tau_{exc/rec} = 2 \cdot \tau_r$) and (b) Me,Me-(N-Et)$_2$ ($\tau_{exc/rec} = 1 \cdot \tau_r$).*

As with the continuous hydrogen bonding structure, the conformations of the ethyl trimer are thought to involve the flexible CH$_2$-N(Et)-CH$_2$ 'bridge' units between aromatic rings. If the cyclic structure of the trimer were to be described as containing two *dimeric-structure-like* units then other conformations are possible by 180° aromatic ring-flips. Such rotation would result in so-called *continuous-structure-like* units. The four possible combinations of such structural units lead to three general conformations: dimeric-dimeric, dimeric-continuous/continuous-dimeric and continuous-continuous (Figure 5.23).
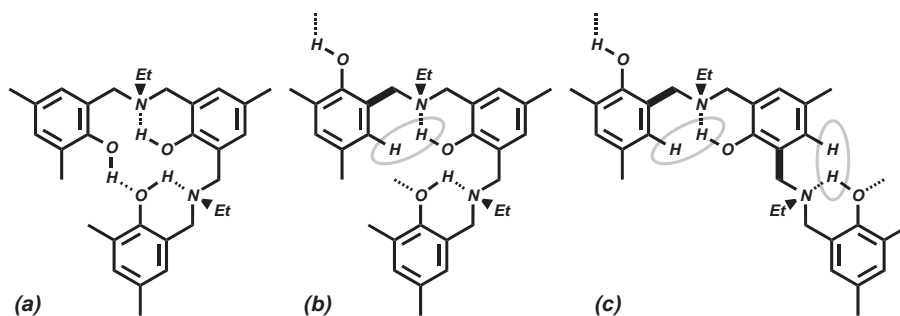
Figure 5.23: *Three possible general conformations for Me,Me-(N-Et)$_2$: (a) dimeric-dimeric, (b) continuous-dimeric and (c) continuous-continuous. (dimeric-continuous conformation not shown)*

The strong DQC between N··H-O and aromatic protons, seen for Me,Me-(N-Et)$_2$ only, was strong evidence for a conformation involving at least one continuous-structure-like unit. However, the presence of such a continuous structure-like unit results in numerous possible three-dimensional geometries. To describe such a structure in further detail from the experimental data currently available was thus considered conjecture.

One possible explanation for the weak O··H-O and stronger N··H-O peaks would be a mixture of supramolecular forms. The dominant form containing the N··H$_b$-O hydrogen bonds and continuous-structure-like units, responsible for the strong DQC between the N··H-O and aromatic protons. The lesser form containing the O··H-O and N··H$_a$-O hydrogen bonds, responsible for the weak DQC between N··H-O and O··H-O protons. The DQ spectra for such a mixture would be similar to that observed for the ethyl trimer, with the 1:5 ratio of the two N··H-O sites reflecting the ratio of the two forms.

In general, it was shown that Me,Me-(N-Et)$_2$ did not have as regular a supramolecular structure as Me,Me-(N-Me)$_2$.

Hetronuclear spectroscopy

Heteronuclear dipolar recoupling methods were relatively efficient for the methyl trimer, but quantitative measurement of the dipolar couplings by sideband analysis proved unsuccessful. As with the dimers examined in Section 4.2.4, carbon sites with directly bound protons were seen with short recoupling times, with longer recoupling allowing access to more weakly coupled sites (Figure 5.24).
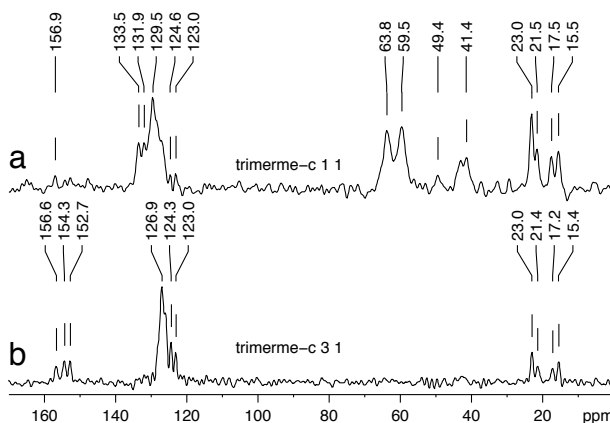
Figure 5.24: *REPT spectra of Me,Me-(N-Me)$_2$ with (a) $\tau_{exc/rec} = 1 \cdot \tau_r$ and (b) $6 \cdot \tau_r$.*

The two methyl amine-substituents were found to have different chemical shifts of 41.4 and 42.2 ppm (Figure 5.24a). The peak at 49.4 ppm was thought to be an artefact, as this was not seen in the equivalent $\tau_{exc/rec} = 1 \cdot \tau_r$ HSQC spectrum (Figure 5.25). As expected three aromatic C-OH sites were seen at 156.6, 154.3 and 152.7 ppm (Figure 5.24b). The observation of three C-OH sites combined with the two N-methyl groups confirmed the presence of the methyl trimer. The five methyl ring substituents were found to exist in four different environments, with two sites having the same chemical shift of 23.0 ppm, suggested by the approximate 2:1:1:1 intensity distribution.

Assignment of the carbon spectra of the methyl trimer was aided by HSQC spectroscopy, with the strong heteronuclear dipolar couplings probing the short range interactions (Figure 5.25) and the weaker couplings the long range interactions (Figure 5.26).
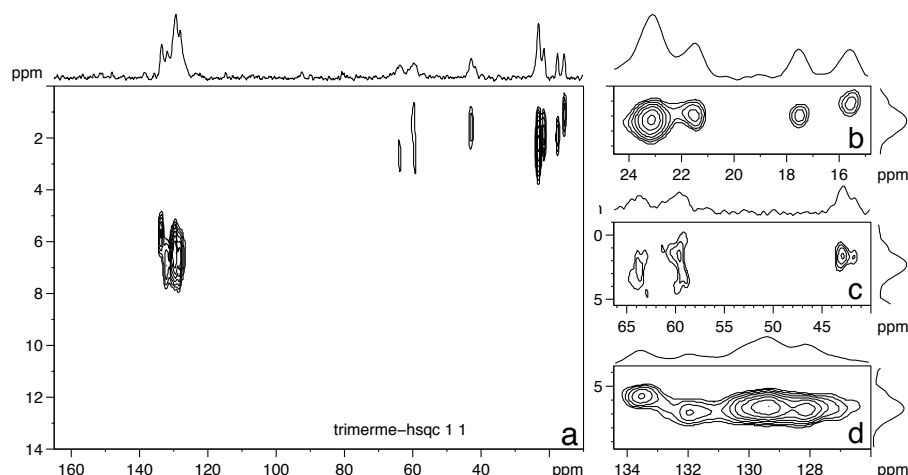
Figure 5.25: *HSQC spctra of Me,Me-(N-Me)$_2$ with $\tau_{exc/rec} = 1 \cdot \tau_r$: (a) full and (b–d) regions of interest.*

The $\tau_{exc/rec} = 1 \cdot \tau_r$ HSQC spectrum showed that both methyl amine-substituents correlated with protons at 1.8 ppm (Figure 5.25c). The methyl ring-substituents correlating with protons which ranged between 1.0–2.5 ppm (Figure 5.25b). The three methyl ring-substituents para to the hydroxyl groups had the lower chemical shift of 15–22 ppm, with the two ortho ring-substituents both found at 23 ppm (Figure 5.25b). The different chemical shifts seen for the three para methyl groups were most likely due to their crystallographic inequivalence in the cyclic structure. The methyl carbon at 15.5 ppm was shown to be associated with shielded protons with a chemical shift of 1.0 ppm, with these shielded protons having previously been observed as a shoulder in the ^{1}H SPE spectrum at 1.2 ppm (Figure 5.20). Such a shielding interaction suggested close proximity of this methyl group to the face of an aromatic system.

The CH$_2$ carbons at 59 and 63 ppm show correlation to their attached protons at ≈ 3 ppm (Figure 5.25c). A possible correlation with the protons of the methyl amine-substituent was also seen for the CH$_2$ group at 59 ppm. Caution should however be taken regarding this correlation due to the low signal-to-noise ratio of this peak.

The aromatic carbons with directly bound protons, or those adjacent to such sites, were found between 129–132 ppm with strong correlations to aromatic protons between 6.4–6.9 ppm (Figure 5.25d). In contrast to the majority of aromatic carbons, a single aromatic at 133.5 ppm showed correlation to an aromatic proton at 5.7 ppm. As with the shielded methyl substituent, this proton was previously resolved in the proton SPE spectra (Figure 5.20a). On the basis of the carbon and proton chemical shifts this was thought to be one of the unsubstituted aromatic sites meta to the hydroxyl group on one the terminal aromatic rings. As with the shielded methyl group, the associated proton chemical shift of this carbon implied close proximity to the face of an aromatic system.
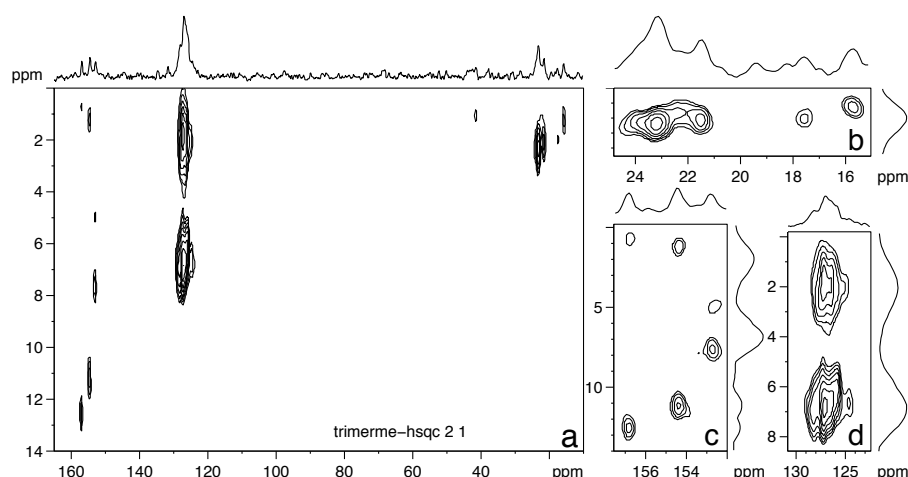
Figure 5.26: *HSQC spctra of Me,Me-(N-Me)$_2$ with $\tau_{exc/rec} = 6 \cdot \tau_r$: (a) full and (b–d) regions of interest.*

As expected, the HSQC spectrum of Me,Me-(N-Me)$_2$ with $\tau_{exc/rec} = 6 \cdot \tau_r$ showed longer range interactions and revealed carbon-proton correlations to all three hydrogen bonding protons (Figure 5.26a). The 156 and 154 ppm C-OH aromatic carbons were clearly seen to correlate with the 10.8 and 12.4 ppm N··H-O hydrogen bonding protons respectively (Figure 5.26c). If cyclic hydrogen bonding was assumed assignment of these carbons was able to be made on the basis of the N··H-O proton chemical shifts. The 156 ppm carbon assigned to the central aromatic ring, and the 154 ppm carbon to one of the terminal aromatic rings. By deduction, the third C-OH aromatic carbon at 153 ppm was assigned to the remaining terminal aromatic ring. This was confirmed by correlation between this site and protons involved in O··H-O hydrogen bonding at 7.4 ppm.

Both C-OH sites, shown to interact with the N··H-O hydrogen bonding protons, also showed weak interactions with methyl protons. The strongest of which was seen for the C-OH of the terminal ring, this was most likely due to the adjacent methyl ring substituent present. However, such an adjacent methyl ring substituent was not present for the central ring and implied a long range interaction, reflected in the weak nature of the correlation. The carbon found to correlate with the O··H-O hydrogen bond protons was also seen to interact weakly with the shielded aromatic proton at ≈ 5 ppm. As to whether this interaction was intramolecular or intermolecular in origin was however unclear. The methyl substituted aromatic carbons between 126–127 ppm were distinguished from the unsubstituted sites by their correlation to methyl protons (Figure 5.26d).

Carbon spectroscopy of the methyl trimer confirmed that Me,Me-(N-Me)$_2$ was indeed an N-methyl substituted benzoxazine trimer. It also provided further evidence for the presence of the cyclic hydrogen bonding supramolecular structure and suggested the origin for the two aromatic and aliphatic sites seen in the proton spectra. The assignment of the carbon spectra (Table 5.6) was more clearly shown when combined with the cyclic hydrogen bonding structure (Figure 5.27).

Table 5.6: ^{13}C assignment of Me,Me-(N-Me)$_2$.

Assignment	Ring	δ_C [ppm]	^1H Interaction
C-OH	2	156.6	N··H$_a$-O + Me
C-OH	3	154.3	N··H$_b$-O + Me
C-OH	1	152.7	O··H-O + Ar-H
Ar-H	3	133.5	Ar-H
Ar-H		131.9	
Ar-Me		129.5	Ar-Me
Ar-Me		126.9	Ar-Me
Ar		124.6	
Ar		124.3	
Ar		123.0	
CH$_2$	1–2	63.8	CH$_2$
CH$_2$	2–3	59.5	CH$_2$ + Me
N-CH$_3$	1–2	42.9	N-Me
N-CH$_3$	2–3	41.4	N-Me
o-CH$_3$	1,3	23.0	Ar-Me
o-CH$_3$	2	21.5	Ar-Me
p-CH$_3$	1	17.5	Ar-Me
p-CH$_3$	3	15.5	Ar-Me

Figure 5.27: ^{13}C assignment of Me,Me-(N-Me)$_2$ when in the cyclic conformation.

In contrast to the methyl trimer, heteronuclear recoupling experiments on the ethyl trimer proved more difficult and, as with the proton DQ spectra, indicated a more disordered structure. This was borne out in carbon spectra of generally lower quality than those previously encountered (Figure 5.28).

Figure 5.28: REPT spectra of the Me,Me-(N-Et)$_2$ with (a) $\tau_{exc/rec} = 1 \cdot \tau_r$ and (b) $2 \cdot \tau_r$.

To aid assignment a 14k scan CP MAS spectra was recorded. From the CP MAS spectrum two C-OH aromatics and five methyl sites were clearly resolved as well as a large number of other aromatic sites (Figure 5.29).

Although three C-OH aromatic sites were expected, only two were seen between 150–154 ppm. Despite this, two CH$_2$ carbons belonging to the ethyl amine substituents were seen between 46–49 ppm, confirming the presence of the trimer. Incidentally, the terminal methyl groups of the ethyl amine-substituents were both

Figure 5.29: CPMAS spectrum of the Me,Me-(N-Et)$_2$: (a) full spectrum and (b) enlargement of aromatic region.

found to have the same chemical shift of 12 ppm. The observation of only two aromatic C-OH sites suggested that either two sites had the same chemical shift, or that the CP efficiency of one of the sites was very low.

Heteronuclear correlation spectra were only recorded with $\tau_{exc/rec} = 1 \cdot \tau_r$. Although technically possible, HSQC spectra with longer recoupling times would have required significantly more scans to be averaged (5k), because of this and the 2D nature of the experiment such measurements were deemed impractical.

As with the $\tau_{exc/rec} = 1 \cdot \tau_r$ HSQC spectra of the methyl trimer (Figure 5.25a), only directly bonded ^{13}C–^{1}H spin-pairs were observed for Me,Me-(N-Et)$_2$ (Figure 5.30a). Thus, no correlations to any of the hydrogen bonding protons were observed.
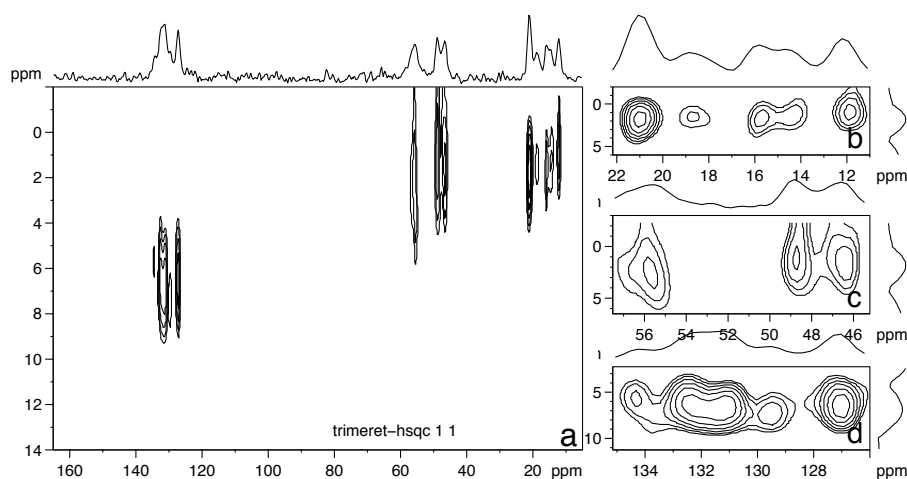
Figure 5.30: HSQC spectra of Me,Me-(N-Et)$_2$ with $\tau_{exc/rec} = 1 \cdot \tau_r$: (a) full and (b–d) regions of interest.

The methyl region showed five peaks, in contrast to the four seen for Me,Me-(N-Me)$_2$, the extra peak attributed to both the methyl carbons of the ethyl amine-substituents (Figure 5.30b). The peak at 12 ppm was assigned to these methyl groups on the basis of the higher intensity and lower chemical shift. The protons associated to these methyl groups had a chemical shift of ≈ 1 ppm, suggesting that they were shielded. Considering the extra flexibility of the ethyl amine-substituent the methyl protons

of these amine-substituents could easily be located in close proximity to the face of one of the three aromatic rings present.

As with the methyl trimer, the two methyl carbons ortho to the hydroxyl group on the terminal rings were assigned to the peak with highest intensity and highest chemical shift, found at 21 ppm for Me,Me-(N-Et)$_2$. The ortho methyl of the central ring was assigned to the 19 ppm peak. The two remaining methyl carbons, those para to the hydroxyl groups, were separately observed between 14–16 ppm. The para methyl of lowest chemical shift was also found to correlate with protons of slightly lower chemical shift, as seen for Me,Me-(N-Me)$_2$, again indicating a slight shielding interaction.

The CH$_2$ groups of the ethyl amine-substituent were identified by their distinctive chemical shifts between 45–49 ppm, and weak correlation to the methyl protons of the amine-substituents (Figure 5.30c). The CH$_2$ groups between the amine and aromatic rings were observed at a lower chemical shift of $\approx$ 55–57 ppm, as compared to 59–65 ppm for Me,Me-(N-Me)$_2$. The broad nature of these peaks suggested a distribution of chemical shifts. Further evidence for this was seen with the two shoulders either side of the 55.3 ppm peak in the CP MAS spectrum (Figure 5.29a).

Although eleven peaks were resolved in the aromatic region of the CP MAS spectrum (Figure 5.29b), only five were seen in the HSQC spectrum (Figure 5.30d). The carbon at 134 ppm correlated with the slightly shielded aromatic protons at 5.6 ppm. As with the methyl trimer this was assigned to the unsubstituted aromatic carbons on the terminal aromatic rings. These protons were also seen as a weak shoulder in the SPE spectra, to the right of the other aromatic protons at 6.8 ppm (Figure 5.20b). The protons associated to the other aromatic sites ranged between 6.5–7.5 ppm, in contrast those of Me,Me-(N-Me)$_2$ were only found from 6.5–7.0 ppm (Figure 5.25d). The stronger intensity of the 132, 131 and 127 ppm peaks suggested sites with directly bound to protons.

Carbon spectroscopy of the ethyl trimer confirmed that Me,Me-(N-Et)$_2$ was an N-ethyl amine-substituted benzoxazine trimer. A number of differences were observed between the methyl and ethyl trimers. Some differences were directly related to the amine substituent, but others were more subtle. As to whether the ethyl trimer does or does not exists in the cyclic hydrogen bonding structure, can not be determined from the $1 \cdot \tau_r$ HSQC spectra. However, considering the differences in proton DQ spectra it was thought highly unlikely that Me,Me-(N-Et)$_2$ existed in a similar cyclic strucutre. However, there was much similarity between the carbon spectra of Me,Me-(N-Me)$_2$ and Me,Me-(N-Et)$_2$, this being most clearly seen when the trimer carbon assignments of Me,Me-(N-Et)$_2$ (Table 5.7) are compared to that of Me,Me-(N-Me)$_2$. For comparison the carbon assignments are shown on Me,Me-(N-Et)$_2$ in the cyclic structure (Figure 5.31).

Table 5.7: ^{13}C *assignment of Me,Me-(N-Et)$_2$.*

Assignment	Ring	δ_C [ppm]	^{1}H Interaction
C-OH	3?	153.7	
C-OH	1?	152.1	
Ar	3	133.7	Ar-H (5.7)
Ar		132.1	Ar-H
Ar		129.8	Ar-H
Ar		128.8	
Ar		127.1	Ar-H
Ar		126.8	
Ar		125.9	
Ar		124.5	
Ar		123.0	
Ar		119.8	
CH$_2$	1–2	56.9	CH$_2$
CH$_2$	2–3	55.3	CH$_2$
CH$_2$ N-Et	1–2	48.2	CH$_2$
CH$_2$ N-Et	2–3	46.4	CH$_2$
o-CH$_3$	1,3	20.9	Me
o-CH$_3$	2	18.6	Me
p-CH$_3$	1	15.8	Me
CH$_3$	3	14.3	Me
CH$_3$ N-Et		12.0	Me N-Et

Figure 5.31: ^{13}C *assignment of Me,Me-(N-Et)$_2$ when in the cyclic conformation.*

5.2.2   An-initio electronic structure calculations

Two different supramolecular structures were investigated using ab-initio electronic structure methods for both methyl and ethyl trimers. With the hope of explaining the differences seen between the experimental spectra of the methyl and ethyl amine-substituted trimers, as well as the cyclic geometry, a semi-helical geometry was also investigated (Figure 5.32).
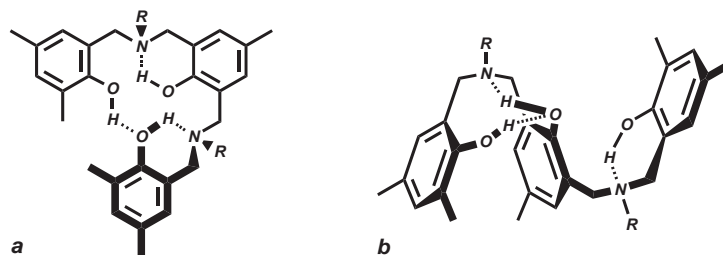
Figure 5.32: *The (a) cyclic and (b) semi-helical supramolecular structures modelled for both trimers.*

Trimers modelled in the cyclic geometry

Evidence for the methyl trimer adopting the cyclic structure was found by both Goward *et al.* [Goward 03] and Kim *et al.* [Kim 03c]. However, with significant differences seen between experimental proton spectra of the methyl and ethyl trimers, the likelihood of the ethyl trimer also existing in such a cyclic form was considered low. To confirm the assumption that the proton spectra should be similar if both systems had the same geometry, both methyl and ethyl trimers were modelled in the cyclic form. From the resulting optimised cyclic geometries the proton chemical shifts were calculated and compared to experimental spectra (Figure 5.33).
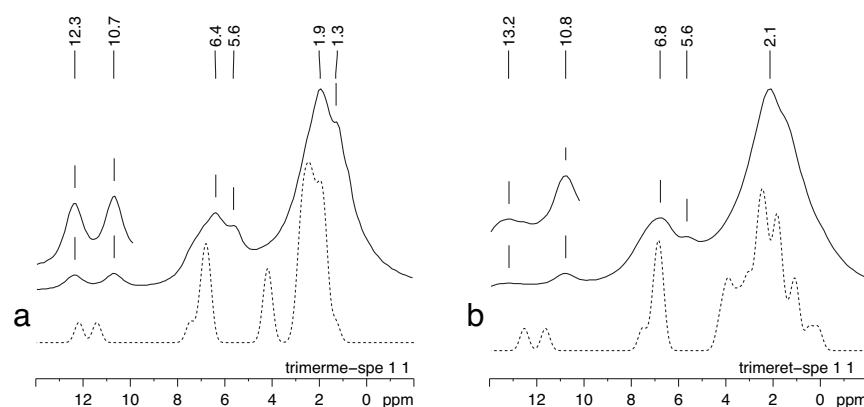
Figure 5.33: *Experimental (solid) and simulated (dashed) proton SPE spectra of the (a) methyl and (b) ethyl trimers modelled in the cyclic conformation.*

With structure optimisation carried out in-vacuo the effects of neighbouring trimer interactions were neglected. This, when combined with the orientation of the amine-substituents away from both aromatic rings and hydrogen bonds, resulted in only small differences in optimum geometry between systems. The similarity between geometries was clearly seen when superimposed and explained the strong resemblance between simulated spectra in the cyclic conformation (Figure 5.34). Considering these effects larger amine-substituents, such as N-Cy or N-^{t}Bu, might have more influence on the final structure for the trimers but this hypothesis was not investigated further.
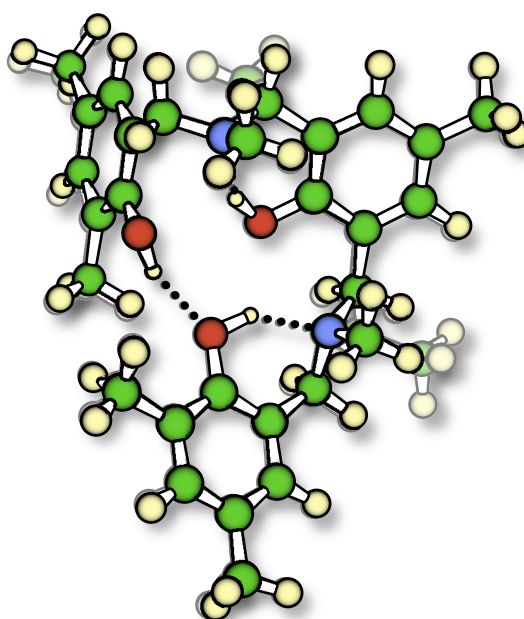
Figure 5.34: *Comparison of the optimised cyclic geometeries of the methyl (dark) and ethyl (light) trimer.*

With such small structural difference occurring upon changing from a methyl to an ethyl amine-substituent, only minor differences in N··H-O and O··H-O hydrogen bonding were expected. This was confirmed when the bond-lengths of the N··H-O and O··H-O hydrogen bonds were compared (Table 5.8).

Table 5.8: *Comparison of hydrogen bond lengths from the optimised geometries of the cyclic methyl and ethyl trimers.*

r_{jk} [pm]	N··H$_a$	N··H$_b$	O··H$_c$
N-Me I	173	185	192
N-Et I	171	183	191
Δr_{jk}	2	2	1

Table 5.9: *Comparison of hydrogen bond proton chemical shifts for cyclic trimers. (Calculated values shown in parenthesis).*

δ_H [ppm]	N··H$_a$-O	N··H$_b$-O	O··H$_c$-O
N-Me I	12.3 (12.17)	10.7 (11.42)	7.4 (7.47)
N-Et I	13.2 (12.45)	10.8 (11.56)	7.6 (7.49)
$\Delta \delta_H$	0.9 (0.28)	0.1 (0.14)	0.2 (0.02)

The calculated N··H‑O proton chemical shifts were found to deviate from experiment (Table 5.9), this was in contrast to the extremely good agreement seen between experiment and simulation by Goward *et al.* [Goward 03]. chemical shift calculations showed N··H_a‑O protons to be weaker, and N··H_b‑O protons to be stronger, than those seen in experimental spectra of both methyl and ethyl systems (Figure 5.33). Despite the inaccuracy seen for N··H‑O hydrogen bond proton chemical shift calculation, good agreement was seen for the O··H‑O hydrogen bond protons with only an absolute difference of ≈ 0.1 ppm found for both systems. With both N··H_a‑O and N··H_b‑O unreliably calculated, relatively large variation was seen when comparing the difference in chemical shift ($\Delta\delta_H$) between hydrogen bonding sites (Table 5.10). The variation of $\Delta\delta_H$ between simulated and experimental spectra was more prominent for the ethyl trimer than for the methyl trimer with differences of 0.7–1.5 and 0.2–0.9 ppm respectively.

Despite the lack of absolute agreement between experimental and simulated spectra, it was seen that neither the asymmetric distribution of N··H‑O proton intensity, nor the high chemical shift of 13.2 ppm, of the ethyl trimer was reproduced. This suggested that the ethyl trimer did not exist in the cyclic conformation. However, considering the differences seen between simulated and experimental spectra caution should be taken with this deduction. Considering the differences seen between experimental spectra, the N··H_a‑O protons of the ethyl simulation would only need to exceed that of the simulated spectra of the methyl trimer by 0.9 ppm to suggest the cyclic conformation for the ethyl trimer.

Table 5.10: Difference in chemical shift of hydrogen bond proton in cyclic trimers. (Calculated values in parenthesis)

$\Delta\delta_H$ [ppm]	$H_a - H_b$	$H_a - H_c$	$H_b - H_c$
N‑Me I	1.6 (0.75)	3.3 (3.95)	4.9 (4.70)
Δ	0.9	0.7	0.2
N‑Et I	2.4 (0.89)	3.2 (4.07)	5.6 (4.96)
Δ	1.5	0.9	0.7

Table 5.11: Individual and average calculated chemical shifts of the methyl protons belonging to the ethyl amine-substituent.

δ_H [ppm]	#1	#2	#3	$\overline{\delta_H}$
Et‑(N··H_a)	0.51	1.10	1.37	0.99
Et‑(N··H_b)	0.12	1.04	1.10	0.75

Although further aliphatic sites were expected for the ethyl system the observation of a peak at ≈ 0.3 ppm was unexpected (Figure 5.33). This peak resulted from two of the six methyl protons belonging to the ethyl amine-substitutnets. Thus, these predicted chemical shifts were unrealistic due to the static nature of the methyl group when the chemical shifts were calculated. When the average chemical shift of all protons in each methyl group was calculated the chemical shifts were more realistic (Table 5.11). The lower chemical shift of 0.75 ppm, associated with the Et‑(N··H_b) ethyl amine-substituent, could be the origin for the slight shoulder seen in the SPE spectrum of the ethyl trimer (Figure 5.33). However, the shoulder was more likely caused by intermolecular shielding interactions, as a similar shielded aliphatic site was being found for the methyl trimer at 1.3 ppm.

The cyclic geometry of Goward *et al.*

The cyclic methyl trimer geometry, which resulted in such good agreement between experimental and simulated data by Goward *et al.*, was investigated in more detail. Further optimisation of this initial geometry, using the same methods used by Goward *et al.*, gave insight into why similar simulated spectra were not seen in the previous section. When the initial (N-Me II) and further optimised (N-Me III) geometries were compared relatively large differences in structure were seen, as compared to the small differences previously observed between methyl and ethyl cyclic trimers. Both N··H-O and O··H-O hydrogen bonds were found to be affected. The orientation of the aromatic ring carrying the O··H-O proton donor also changed (Figure 5.35).
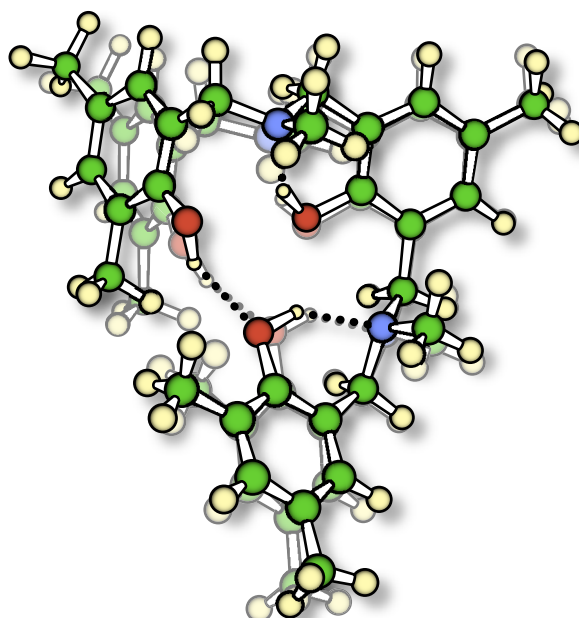
Figure 5.35*: Comparison of the initial N-Me II (dark) and further optimised N-Me III (light) cyclic geometries of the methyl trimer.*

The hydrogen bond lengths measured from the respective geometries varied by 7 and 16 pm for the N··H-O hydrogen bonds and 26 pm for the O··H-O hydrogen bonds (Table 5.12). As seen by the simulation of the dimers (Section 4.3.2), such a difference in bond length would easily result in detectable changes in calculated chemical shift. Indeed, upon calculation the hydrogen bond proton chemical shifts were found to vary by 0.58–1.27 ppm (Table 5.13).

Table 5.12: *Comparison of hydrogen bond lengths from the initial and further optimised geometry.*

r_{jk} [pm]	N··H_a	N··H_b	O··H
N-Me II	176	200	213
N-Me III	169	184	187
Δr_{jk}	7	16	26

Table 5.13: *Comparison of chemical shifts calculated from the initial and further reoptimised geometry.*

δ_H [ppm]	N··H_a-O	N··H_b-O	O··H-O
N-Me II	12.02	10.48	7.25
N-Me III	12.60	11.75	8.19
$\Delta\delta_H$	0.58	1.27	0.94

However, of most importance was the form of the simulated spectra from the initial and further optimised geometries (Figure 5.36). These showed that the small changes in hydrogen bonding resulted in a simulated spectrum which bore a much closer resemblance to that of the experimental spectrum. In contrast, the further optimised geometry resulted in a spectrum which was similar to that of the methyl and ethyl trimers previously discussed (Section 5.2.2). This was most obvious when the differences between hydrogen bonding proton chemical shifts were compared (Table 5.14). The difference in chemical shift between the N··H_a-O and N··H_b-O protons of the further optimised N-Me III (0.75 ppm) and previously discussed geometries N-Me I (0.85 ppm) was almost half that of the experimental (1.54 ppm) and initial geometry N-Me II (1.6 ppm).
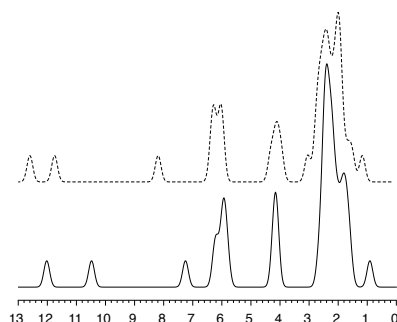
Figure 5.36: *The simulated spectra from the initial (solid) and reoptimised (dashed) geometry of Goward et al.*

Table 5.14: *Difference in chemical shifts for hydrogen bond protons in all simulated cyclic methyl trimers.*

$\Delta\delta_H$ [ppm]	H_a-H_b	H_a-H_c	H_b-H_c
experiment	1.6	4.9	3.3
N-Me II	1.54	5.23	3.23
N-Me III	0.85	4.41	3.56
N-Me I	0.75	4.70	3.95

Trimers modelled in the semi-helical geometry

With the differences in experimental spectra seen between the methyl and ethyl trimers, and relatively small differences found between the cyclic structures of these systems, an alternative geometry was investigated. In the cyclic geometry the O··H‑O hydrogen bond was formed between a proton donor and proton acceptor on the two terminal aromatic rings. In contrast, in the alternative geometry the O··H‑O hydrogen bond was formed between a proton donor and proton acceptor on neighbouring aromatic rings (Figure 5.32). Thus, such a semi-helical geometry was hoped to provide information regarding the formation of stronger N··H_a‑O and weaker N··H_b‑O hydrogen bonds, as seen for the ethyl trimer.
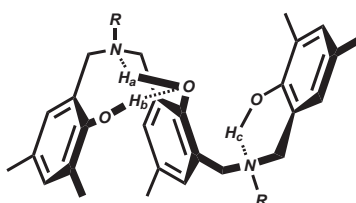
Figure 5.37: The semi-helical supramolecular structures modelled for both trimers.

As with the optimised geometries of the methyl and ethyl cyclic trimers, little structural difference was seen between systems with methyl and ethyl amine-substituents (Figure 5.38). This was again primarily due to the lack of packing interactions and the orientation of the amine-substituent.
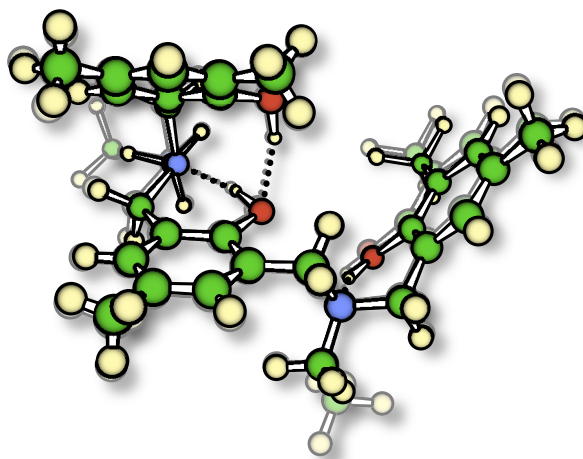
Figure 5.38: Comparison of the optimised semi-helical geometries of the methyl (dark) and ethyl (light) trimer.

Although the hydrogen bond lengths did not vary significantly (Table 5.15) the calculated chemical shifts of the hydrogen bonded protons varied slightly between methyl and ethyl systems (Table 5.16). Two important observations were made from the simulated spectra (Figure 5.39). Firstly, the two N··H‑O hydrogen bonds had been influenced with respect to the cyclic geometry, the N··H_a‑O becoming stronger

and N··H_b-O weaker. With this variation of N··H-O hydrogen bonding observed in the experimental spectrum of the ethyl trimer, it was shown that such variation of chemical shift was easily possible with different hydrogen bond configurations. Secondly, the O··H-O protons were found at much lower chemical shifts of ≈ 5.9 ppm, as compared to 7.5 ppm in the cyclic form (Table 5.9). This could suggest that either an O··H-O hydrogen bond had not fully formed, or that the chemical shift of the O··H-O proton was also influenced by the presence of the two semi-stacked aromatic rings. It should be noted that although peaks at ≈ 5.6 ppm were observed for both methyl and ethyl trimers experimentally, these were assigned to shielded aromatics via ^{13}C–^{1}H HSQC spectroscopy (Section 5.2.1).

Table 5.15: *Comparison of hydrogen bond lengths for semi-helical trimers.*

r_{jk} [pm]	N··H_a	N··H_b	O··H_c
N-Me	161	187	186
N-Et	159	186	185
Δr_{jk}	2	1	1

Table 5.16: *Comparison of chemical shifts of semi-helical trimers. (Calculated values in parenthesis)*

δ_H [ppm]	N··H_a-O	N··H_b-O	O··H_c-O
N-Me	12.3 (14.77)	10.7 (10.05)	7.4 (5.87)
N-Et	13.2 (15.08)	10.8 (10.16)	7.6 (5.90)
$\Delta\delta_H$	0.9 (0.31)	0.1 (0.11)	0.2 (0.03)
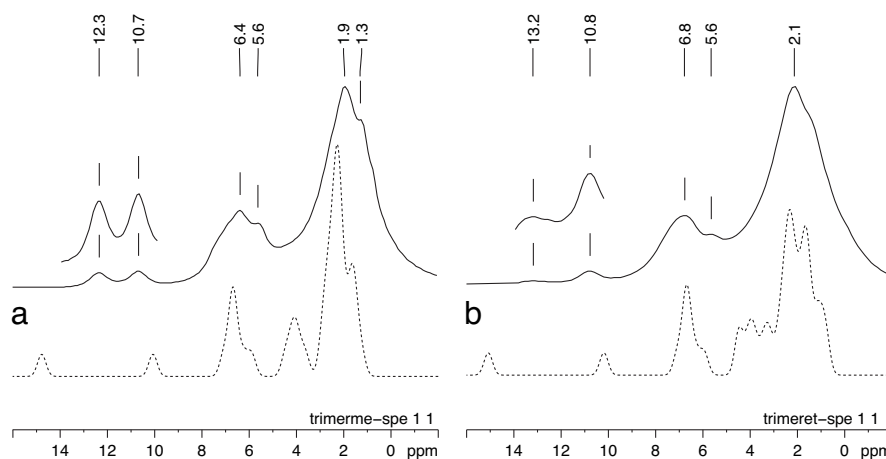
Figure 5.39: *Experimental (solid) and simulated (dotted) proton spectra of the semi-helical (a) methyl and (b) ethyl trimers.*

Table 5.17: *Difference in hydrogen bond proton chemical shift for semi-helical trimers. (Calculated values in parenthesis)*

$\Delta\delta_H$ [ppm]	H_a−H_b	H_a−H_c	H_b−H_c
N-Me	1.6 (4.72)	3.3 (8.9)	4.9 (4.18)
$\Delta\Delta\delta_H$	3.1	5.6	0.7
N-Et	2.4 (4.92)	3.2 (9.18)	5.6 (4.26)
$\Delta\Delta\delta_H$	2.5	6.0	1.3

In general, large differences were seen between the simulated spectra of the semi-helical geometries and the experimental spectra of the trimers (Table 5.17). Thus, it was concluded that neither system existed in this form. Despite the lack of agreement with experiment, the semi-helical structure showed how changes in hydrogen bond geometry can strongly alter the observed chemical shifts of such systems.

5.2.3   Summary

Proton SPE spectroscopy showed differences in hydrogen bonding between the two trimers. Although both systems showed two forms of N··H-O hydrogen bonds, the concentration and strength of the stronger N··H_a-O hydrogen bond varied between systems. Whereas equal amounts of N··H_a-O and N··H_b-O hydrogen bonding was found for the methyl system, N··H_a-O hydrogen bonding was both stronger and less abundant for the ethyl trimer. From these observations alone it was deemed highly unlikely that both trimers had the same supramolecular hydrogen bonding structure.

The differences became more apparent with ^{1}H DQ correlation spectroscopy. A strong DQC between N··H-O and aromatic protons was only observed for the ethyl trimer. It was thus suggested that in the ethyl trimer at least one of the aromatic rings was flipped, as with the continuous hydrogen bonding structure of the dimers. With further geometric constraints unavailable, suggestion of a possible three dimensional structure was considered only speculation. With all methyl trimer spectra able to be rationalised by the adoption of the cyclic structure the chances of the ethyl system adopting the same structure were low.

The differences in N··H-O proton intensities in Me,Me-(N-Et)$_2$ could be explained by polymorphism. The N··H_b-O sites and at least one continuous-structure-like unit from the more abundant form and the O··H-O and N··H_a-O sites from a less abundant form.

Carbon spectroscopy confirmed the chemical structures of both methyl and ethyl trimers. For the methyl trimer three separate aromatic C-OH sites were observed and, as with the dimers, were found to be in close proximity to the hydrogen bonding protons. For both trimers aromatic carbons were found to correlate with protons experiencing shielding interactions suggesting close proximity to the face of an aromatic ring. Similarly, the terminal methyl protons of the ethyl amine-substituent were also found to be slightly shielded. As to whether these shielding interactions were intramolecular or intermolecular in origin is however still unknown.

Chemical shift calculations showed that if the ethyl trimer were to adopt the cyclic structure a similar spectrum to that of the methyl trimer would be expected. Combined with the experimental spectra, the simulated spectra provided further evidence that the ethyl trimer did not exist in the cyclic structure. Simulation of a semi-helical trimer geometry showed similar changes in N··H-O hydrogen bonding to that seen for the ethyl trimer. This confirmed that changes in supramolecular structure were most likely responsible for the differences in observed hydrogen bonding in the methyl and ethyl trimers. Generally, little difference was observed between simulated spectra of the methyl and ethyl systems, with only minor differences in geometry and chemical shift found. It is thus thought that hydrogen bond configuration and packing play an important role in determination of the final trimer geometry.

5.3 Conclusions

The comparison of the methyl and ethyl dimers showed that a small change in amine-substituent played an important role in determining the supramolecular structure adopted. Both methyl and ethyl dimers were found to mostly adopt the dimeric hydrogen bonding structure. The presence of a weak DQC between N··H-O and aromatic protons showed that the continuous hydrogen bonding structure was also present for the ethyl dimer, albeit in low concentration. Stronger evidence for polymorphism of the ethyl dimer was seen by ^{15}N spectroscopy, with two sites observed. Modelling of both methyl and ethyl dimers showed good agreement with experiment and further confirmed the dimeric hydrogen bonding structure for these two systems.

Similar results were seen for the trimers, with the methyl system being much more well defined. The methyl trimer was confirmed to adopt the cyclic hydrogen bonding structure. From initial investigations, the ethyl trimer was seen to not adopt a similar cyclic structure. Significant differences in both strength, and concentration, of the stronger of the two N··H-O hydrogen bonds were seen. A strong DQC between N··H_b-O and aromatic protons, also suggested that the majority of the molecules in the ethyl trimer contained continuous-structure-like units (Figure 5.40b). In contrast, no evidence for such structure units was seen for the methyl trimer (Figure 5.40a). Polymorphism could explain why both the N··H_a-O and O··H-O protons were only present in low concentrations, with a second stable form containing no continuous-structure-like units and thus possibly similar in form to the cyclic geometry (Figure 5.40c).

In general, strong differences in supramolecular structure were observed between dimers and trimers with similar chemical structures.
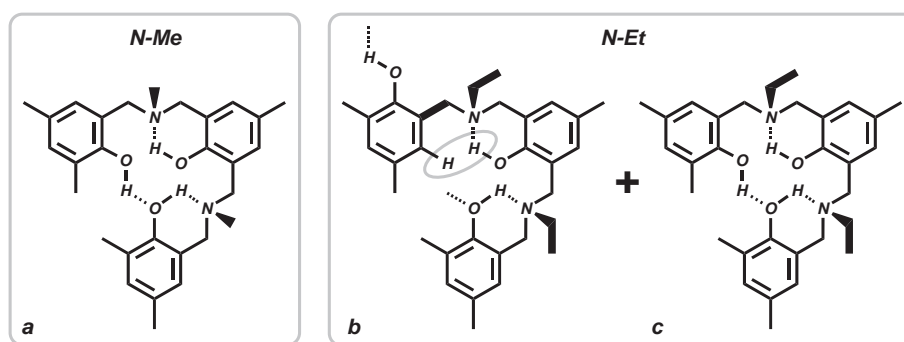
Figure 5.40: *Suggested structures of the (a) methyl and (b,c) ethyl trimers.*

Chapter 6

Related Benzoxazine Systems

In Chapter 4 the effect of ring-substituents on supramolecular structure was investigated for N-Me N-Pr and N-Cy amine-substituted model dimers. The important role of the amine-substituent was further observed in Chapter 5, where dimers and trimers of N-Me and N-Et systems were compared. In this chapter other systems structurally related to those previously examined will be presented. These can be split into two general categories: further model compounds similar in structure to the dimers of Chapter 4 and polybenzoxazines based on diamine containing monomers.

Of the three compounds related to the dimers, one was based on aniline leading to a phenyl amine-substituent (Figure 6.1a), and two possessed only one substituted aromatic ring. The latter systems are hereafter referred to as asymmetric-dimers (Figure 6.1b).

For the diamine based polybenzoxazines a number of systems based on linear-diamine monomers (Figure 6.1c) were studied as well as a single system based on the cyclic-diamine piparazine (Figure 6.1d).
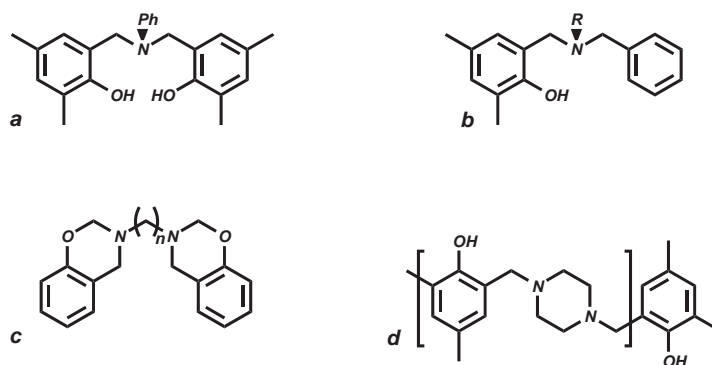
Figure 6.1: *Related benzoxazine systems studied: (a) an aniline based dimer, (b) asymmetric dimers of varying amine-substituent, cross-linked linear-diamine polymers based on (c) linear-diamine monomers of varying length and (d) polymers based on the cyclic-diamine piperazine.*

6.1   An aniline based dimer: Me,Me⁻N⁻Ph

The aniline based model dimer Me,Me⁻N⁻Ph (Figure 6.2) was first prepared as a model for phenolic resins formed by bifunctional benzoxazine monomers based on bisphenol-A and aniline [Kim 01]. A similar phenolic resin formed by bifunctional benzoxazine monomers based on bisphenol-A and methylamine was also studied, the model for which being the dimer Me,Me⁻N⁻Me. By comparison of solution-state ^{1}H NMR of Me,Me⁻N⁻Me and Me,Me⁻N⁻Ph, dissolved in deuterated chloroform and acetic acid, it was found that only Me,Me⁻N⁻Me interacted with the carboxylic acid solvent. This was detected by deshielding interaction on both the N-CH$_3$ and CH$_2$ protons, caused by the protonation of the amine upon salt formation with the solvent [Ma 65]. With such an interaction not occurring for Me,Me⁻N⁻Ph it was thought that either the intramolecular N··H⁻O hydrogen bond to the amine was too strong to be broken by the addition of acetic acid, or that steric hindrance limited salt formation. Taking into account that hydrogen bonding in such Mannich bases is closely related to the acidity of the parent phenol and alkalinity of the amine [Brycki 91], it was expected that the hydrogen bonding in Me,Me⁻N⁻Me and Me,Me⁻N⁻Ph would be different. However, despite the large difference in basicity in the corresponding amines, surprisingly little difference was seen between FT-IR spectra of Me,Me⁻N⁻Me and Me,Me⁻N⁻Ph in the solid-state [Kim 02]. This was thought to be due to the hydrogen bonding of Me,Me⁻N⁻Ph being strongly affected by the physical packing of molecules, and thus suggested similar crystal structures for Me,Me⁻N⁻Me and Me,Me⁻N⁻Ph.
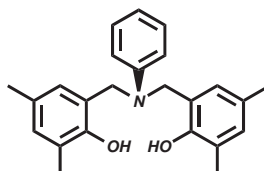
Figure 6.2: The chemical structure of Me,Me⁻N⁻Ph.

As well as intramolecular N··H⁻O and intermolecular O··H⁻O hydrogen bonding, other intramolecular hydrogen bonding interactions via the hydroxyl proton donor were also thought to be possible for Me,Me⁻N⁻Ph. This was supported by the observation of an FT-IR band at 3549 cm^{-1} for Me,Me⁻N⁻Ph that was concentration independent, suggesting an intramolecular X··H⁻O interaction [Kim 02]. This band was also found to be present for Me,Me⁻N⁻Me, Me,Me⁻N⁻Et, Me,Me⁻N⁻Pr and Me,Me⁻N⁻Cy, albeit in much lower concentrations [Kim 03b]. Conformation of this type of interaction was seen through the examination of asymmetric dimers, which possess only a single hydroxyl group (discussed later in Section 6.2). For these systems only intramolecular N··H⁻O hydrogen bonding was observed, with no evidence for intramolecular nor intermolecular O··H⁻O hydrogen bonding [Kim 03b]. These intramolecular X··H⁻O interactions were thought to be non-classical π··H⁻O

hydrogen bonds [Alkorta 98, Steiner 02]. Such interactions occurring between acidic protons and aromatics systems because of the good electron donating ability of delocalised systems [Pimentel 60]. The possible formation of π··H-O hydrogen bonds can be seen when one of the substituted rings of Me,Me-N-Ph is flipped, as in the continuous hydrogen bonding structure (Figure 6.3). In well designed novolac dimers these interactions have been found to be highly affected by molecular conformation, and gave rise to FT-IR bands at 3516 cm^{-1} [Cairns 65]. With proton chemical shift strongly affected by facial interaction with aromatic systems it was hoped that proton solid-state NMR would provide further insight into these interactions.
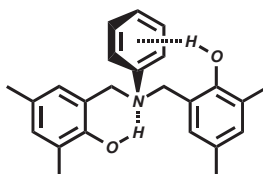
Figure 6.3: The possible formation of intramolecular N··H-O and π··H-O hydrogen bonds in Me,Me-N-Ph.

Relatively high resolution proton solid-state NMR spectra were seen for Me,Me-N-Ph. A high degree of order was also suggested by the physical form of the compound, with white needle-like crystals [Kim 03b]. This was in contrast to all other dimers examined which had only a generic white crystalline form. From a supramolecular perspective, the increased number of aromatic rings was expected to lead to stronger intermolecular interactions, thus a driving force for molecular packing and more supramolecular order. The influence of the extra delocalised electrons was observed for both ^{1}H and ^{13}C NMR spectra, in some cases providing qualitative information regarding proximity and orientation of the ring-substituents.

6.1.1 NMR spectroscopy

Proton spectroscopy

The proton SPE spectrum showed that both N··H‑O and O··H‑O hydrogen bonding was once again present. Multiple aromatic sites were also found to be present, allowing distinction between the four aromatic protons of the two substituted rings and the five protons belonging to the amine-substituent. The difference in chemical shift between the two sites being due to the presence of the nitrogen atom (Figure 6.4). Assignment of the SPE spectrum was in agreement with the relative intensities expected from the chemical structure (Figure 6.2 and Table 6.1).
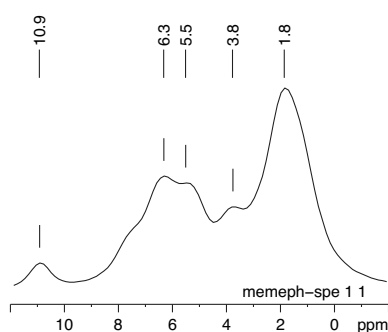
Figure 6.4: ^{1}H SPE spectrum of Me,Me‑N‑Ph.

Table 6.1: Expected (I_n) and deconvoluted (I_f) intensities of Me,Me‑N‑Ph. chemical shifts from 2D spectra shown in parentheses.

	δ_H [ppm]	H_n	I_n [%]	I_f [%]
N··H‑O	10.9	1	3.7	3.1
O··H‑O	(7.6)	1	3.7	3.6
N‑Ar	(6.4)	5	18.5	19.3
R‑Ar	(5.3)	4	14.8	12.3
CH$_2$	3.8	4	14.8	5.7
CH$_3$	1.8	12	44.4	56.0

Table 6.2: Approximate proton T_1 relaxation time constants for Me,Me‑N‑Ph as determined by the inversion-recovery method.

	δ_H [ppm]	T_1 [s]
N··H‑O	10.9	23
N‑Ar	6.3	23
CH$_2$	3.6	25
CH$_3$	1.7	24

Although accurate measurements of ^{1}H T_1 relaxation times for each site were not possible, due to the dense spin-systems facilitating rapid spin-diffusion between resolvable sites, approximate values were determined. Even at 30 kHz MAS spin-diffusion was not fully suppressed and the system relaxed with a single global relaxation time. Thus a single spin-lattice relaxation time of 23–25 s was observed for all resolvable sites (Table 6.2). With no evidence for the system being in the fast-motion regime, the dominance of proton spin-diffusion and relatively long apparent T_1 further suggested a highly crystalline from. The pathway of the dipolar mediated proton spin-diffusion was seen by dipolar-exchange spectroscopy with different mixing times (Figure 6.5).
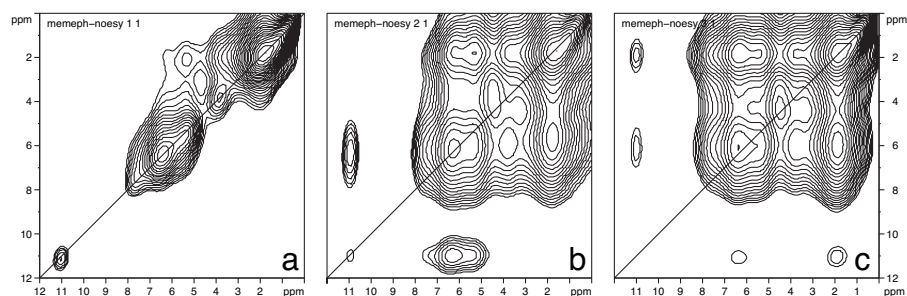
Figure 6.5: *Dipolar exchange spectra of Me,Me-N-Ph: $\tau_{mix} =$ (a) 500 µs, (b) 50 ms and (c) 500 ms.*

With a mixing time of 500 µs ($15 \cdot \tau_r$ at $\omega_r/2\pi = 30$ kHz) little spin-diffusion was observed with most magnetisation remaining on the excited spins (Figure 6.5a). A weak cross-peak was however seen between the aromatic protons of the substituted ring and their neighbouring methyl groups. Favourable conditions for spin-diffusion were the most likely cause due to the relatively short inter-nuclear distance, and thus strong dipolar-coupling between these sites. When the mixing time was increased to 50 ms, cross-peaks involving the hydrogen bonding protons were seen, this indicated a weaker dipolar coupling to the aromatic protons than between aromatic and aliphatic protons (Figure 6.5b). With the longest mixing time of 500 ms all possible cross-peaks were observed, however those involving the N··H-O and O··H-O hydrogen bonding protons were relatively weak (Figure 6.5c). At short mixing-times of $\tau_{mix} = 50$ µs negative cross-peaks were observed between the mobile methyl groups and the N··H-O protons (Figure 6.6), as previously seen for a number of the dimers in Chapters 4 and 5.
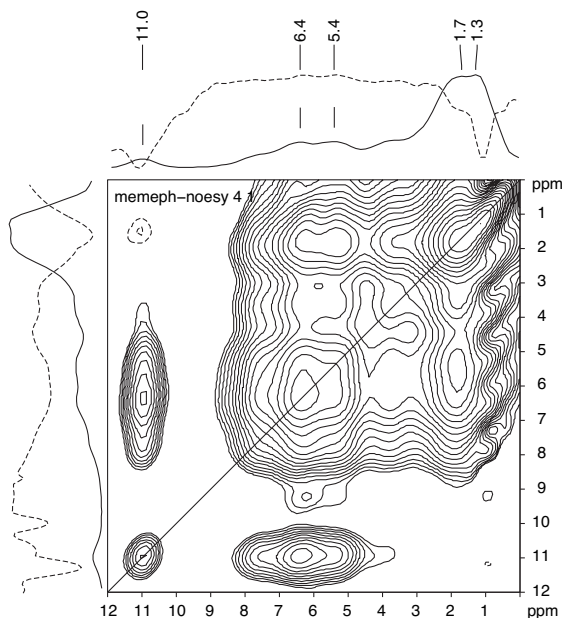
Figure 6.6: *Dipolar exchange spectrum of Me,Me-N-Ph $\tau_{mix} = 50$ µs. Positive (solid) and negative (dashed) projections shown illustrating negative cross-peaks.*

Unlike the systems where this interaction had previously been encountered, flexible ethyl or propyl groups were not present for Me,Me-N-Ph. Thus the DQ cross-relaxation mechanism responsible for the negative cross peaks, was also possible between N··H-O protons and methyl groups alone. Due to the geometric constraints of Me,Me-N-Ph this was most likely an intermolecular interaction.

Proton double-quantum spectroscopy provided a further gain in resolution, with sites with weaker dipolar-couplings revealed with longer recoupling times (Figure 6.7).
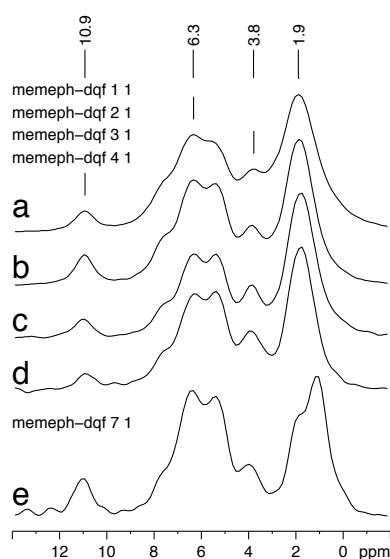
Figure 6.7: *Double-quantum filtered spectra of Me,Me-N-Ph with $\tau_{exc/rec}$ = (a) 1·τ_r, (b) 2·τ_r, (c) 3·τ_r, (d) 4·τ_r and (e) 6·τ_r. Increased resolution with longer recoupling.*
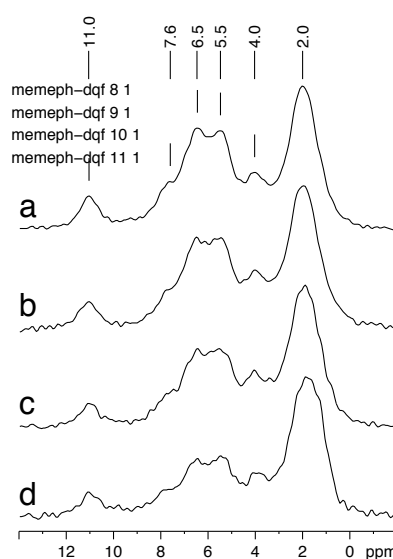
Figure 6.8: *Double-quantum filtered spectra of Me,Me-N-Ph with $\tau_{exc/rec}$ = 2 · τ_r, with varying recycle-delays and number of scans (s/#): (a) 10/16, (b) 5/32, (c) 2/80 and (d) 1/160.*

With six rotor periods of recoupling a second aliphatic peak was shown, albeit at the cost of overall signal intensity (Figure 6.7e). A factor of twelve increase in number of scans was needed to achieve a signal-to-noise comparable to that of the $\tau_{exc/rec} = 1 \cdot \tau_r$ spectrum. The resolution achieved was also found to depend on the recycle delay, or more precisely on how close to the equilibrium state the spin system was allowed to relax back to before subsequent excitation. Greater signal-to-noise per unit time was seen using longer recycle-delays (Figure 6.8). This was possible justification for the use of longer than expected recycle-delays when observing protons in the solid-state, and therefore measuring the equilibrium state as opposed to the steady state.

As with the other dimers investigated, most information regarding the supramolecular structure of Me,Me-N-Ph was gained from ^{1}H–^{1}H DQ correlation spectra. As with the DQ filtered 1D spectra, extended recoupling times gave further resolution in the aromatic region (Figure 6.9).
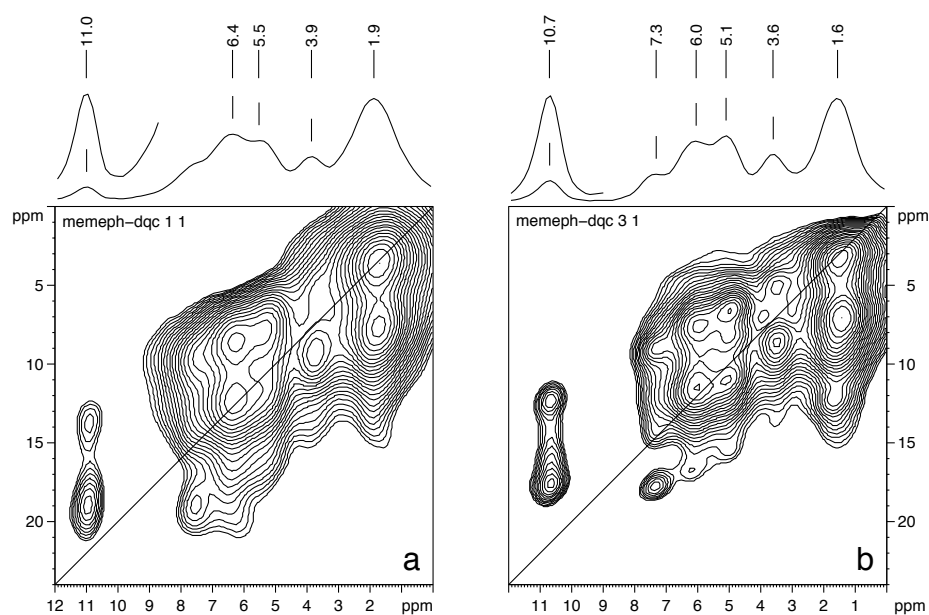
Figure 6.9: DQ spectra of Me,Me-N-Ph: (a) $\tau_{exc/rec} = 1 \cdot \tau_r$ and (b) $\tau_{exc/rec} = 2 \cdot \tau_r$.

The N··H-O protons showed a strong correlation with O··H-O protons and indicated a high likelihood of a regular supramolecular structure. Considering the similarity of FT-IR spectra of Me,Me-N-Ph and Me,Me-N-Me found by Kim *et al.* [Kim 01, Kim 02, Kim 03b] this was suspected to be the dimeric hydrogen bonding form (Figure 6.10). Evidence for the dimeric hydrogen bonding structure was seen in the $\tau_{exc/rec} = 2 \cdot \tau_r$ DQ spectrum, with a relatively strong auto peak found between two O··H-O proton sites (Figure 6.9b). As with the other dimers, weak DQ coherences were also seen between aromatic and N··H-O protons, suggesting that this system could also partially exist in the continuous structure (Figure 6.11). For Me,Me-N-Ph a second possibility also arises, due to the aromatic protons of the amine-substituent at ≈ 6.4 ppm being in close proximity to the N··H-O protons. However, the stronger DQC was seen between the aromatic protons of the substituted rings at ≈ 5 ppm.
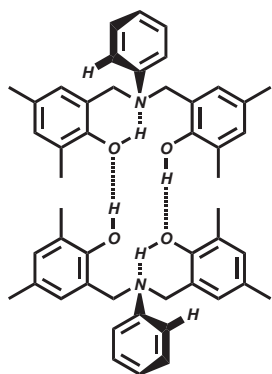
Figure 6.10: Illustration of the proximity of O··H-O protons in the dimeric hydrogen bonding structure of Me,Me-N-Ph.
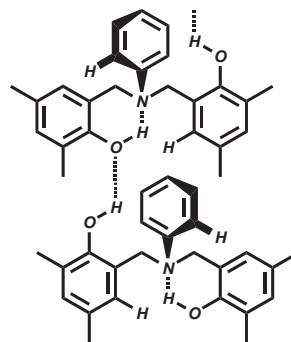
Figure 6.11: Illustration of the proximity of the aromatic protons to N··H-O proton in the continuous hydrogen bonding structure of Me,Me-N-Ph.

Heteronuclear spectroscopy

Heteronuclear experiments were constrained due to the limited quantity of sample available. This resulted in 12k scans being needed to obtain a ^{1}H–^{13}C CP MAS spectrum with reasonable signal-to-noise (Figure 6.12). Although technically possible, heteronuclear dipolar recupling methods were not found to be efficient and resulted in a low signal-to-noise ratio even after 5k scans. This made two-dimensional heteronuclear spectroscopy not feasible (Figure 6.13).
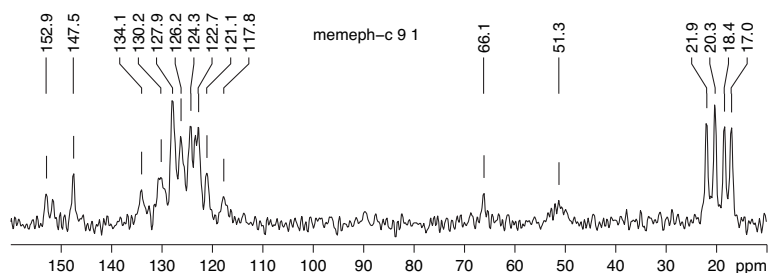
Figure 6.12: *^{1}H–^{13}C CP MAS spectrum of Me,Me-N-Ph.*
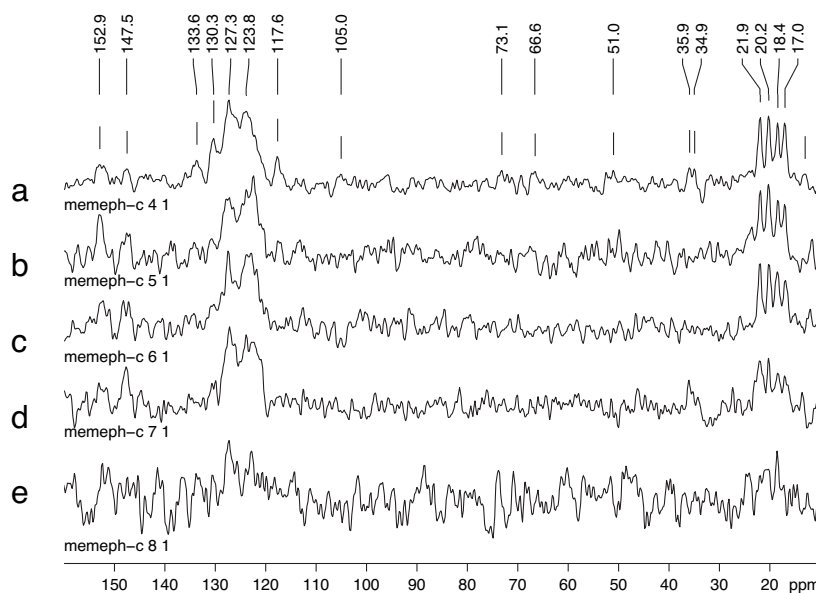
Figure 6.13: *REREDOR spectra of Me,Me-N-Ph: $\tau_{exc/rec}$ = (a) 1·τ_r, (b) 2·τ_r, (c) 3·τ_r and (d) 4·τ_r using 5k scans and 10 s recycle delay. (e) Equivalent $\tau_{exc/rec}$ = 1·τ_r spectrum recorded with 2 s recycle delay.*

As with some of the dimers in Chapter 4, two aromatic C-OH sites were observed at 152.9 and 151.3 ppm. This indicated crystallographic inequivalence of the two substituted aromatic rings. This was confirmed by the presence of four methyl peaks of approximately equal intensity between 17.0–21.9 ppm, as well as multiple aromatic peaks between 117–253 ppm. The aromatic carbon directly bonded to the amine was assigned to the peak at 147.5 ppm. In general, the narrow line widths and observation of crystallographic inequivalence again suggested a highly crystalline system.

6.1.2 Ab-Initio electronic structure calculations

Due to aromatic rings being strong supramolecular structure dictating moieties, the presence of a further ring in Me,Me-N-Ph was expected to impart a higher degree of order. Thus for this dimer a stronger driving force for the formation of supramolecular interactions was thought to be present. Proton DQ correlation spectra had shown that both N··H-O and O··H-O hydrogen bonding interactions were indeed present, confirming the observations of Kim *et al.* [Kim 02, Kim 03b]. With the absence of any strong evidence for the continuous hydrogen bonding structure it was concluded that Me,Me-N-Ph had a high probability of existing in the dimeric structure. Geometry optimisation and chemical shift calculations were undertaken for Me,Me-N-Ph using the crystal structure of Me,Me-N-Me for initial geometry constraints. Unfortunately, modelling of the possible intramolecular π··H-O interaction [Calhorda 00] did not lead to stable geometries or meaningful results.
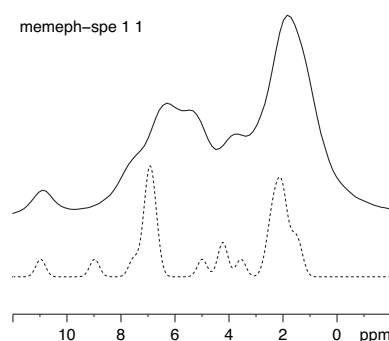
Figure 6.14: *Comparison of experimental (solid) and simulated (dashed) ^{1}H NMR spectra of Me,Me-N-Ph in the dimeric hydrogen bonding structure.*

Comparison of experimental and simulated spectra showed very good agreement for the N··H-O hydrogen bond protons (Figure 6.14). However, the intramolecular O··H-O hydrogen bonds were found to be overestimated in strength, with a chemical shift of 9.0 ppm as compared to 7.6 ppm seen by experiment (Table 6.3). This suggested that the two dimers did not form such a tightly bonded dimeric unit as simulated. This could be explained by the stronger packing interactions, neglected in the geometry optimisation, that could possibly encourage a larger separation of dimers or possible π··H-O interactions and shielding. When compared to Me,Me-N-Me similarity can be seen between the experimental chemical shifts, with both having a $\Delta\delta_H$ between 3.3–3.8 ppm. However, when the calculated chemical shifts were considered stronger deviation from experiment was seen for Me,Me-N-Ph with a $\Delta\Delta\delta_H$ of 1.3 ppm, as opposed to 0.5 ppm for Me,Me-N-Me (Table 6.3).

Table 6.3: *Comparison of chemical shifts of Me,Me-N-Me and Me,Me-N-Ph. (Calculated values in parentheses).*

δ_H [ppm]	N··H-O	O··H-O	$\Delta\delta_H$	$\Delta\Delta\delta_H$
Me,Me-N-Me	11.2 (12.92/12.93)	7.4 (8.65/8.61)	3.8 (4.27/4.32)	0.47/0.52
Me,Me-N-Ph	10.9 (10.99/10.96)	7.6 (8.98/8.98)	3.3 (2.01/1.98)	1.29/1.32

From the optimised geometry it can be seen that the phenyl amine-substituents lie perpendicular to one of the substituted aromatic rings (Figure 6.15). This conformation was also seen in the crystal structure of H,Me-N-Cy (Section 4.3.3). The remaining substituted aromatic ring, that is responsible for the intermolecular O··H-O hydrogen bonding, interlocks with its opposing counterpart. When the hydrogen bond lengths were measured the N··H inter-nuclear distances were found to be 180 pm, longer than the 171 pm simulated for Me,Me-N-Me (Table 6.4). However, these were still comparable to the 195 pm experimentally determined by Goward *et al.* for Me,Me-^{15}N-Me [Goward 01]. The change in simulated N··H-O hydrogen bond length was thought to be due to either steric constraints, imposed by the extra bulk of the phenyl amine-substitutent, or an inherent difference in hydrogen bond strength relating to the pK_a of the associated phenol and amine groups of the Mannich base [Brycki 91]. When the pK_a of aniline is compared to that of all other amines and phenols herein encountered, a significant difference is seen. Thus, an inherent difference in N··H-O hydrogen bond strength/length was to be expected for Me,Me-N-Ph as compared to Me,Me-N-Me and the other dimers of Chapters 4 and 5.

Figure 6.15: *Optimised geometry of Me,Me-N-Ph.*

Table 6.4: *Comparison of hydrogen bond lengths from the optimised geometries of Me,Me-N-Me and Me,Me-N-Ph.*

r_{jk} [pm]	N··H	O··H
Me,Me-N-Me	171/171	182/183
Me,Me-N-Ph	180/180	181/181
Δr_{jk}	9/9	1/2

Table 6.5: *Comparison pKa values of amines and phenols associated with the model dimers [Dean 72].*

	compound	pK_a
amines	methylamine	10.66
	ethylamine	10.71
	n-propylamine	10.61
	n-butylamine	10.64
	t-buthyamine	10.69
	cyclohexylamine	10.69
	aniline	4.63
phenols	2,4-dimethylphenol	10.58
	4-methylphenol	10.26

6.1.3 Summary

As with the other dimers studied in Chapter 4 and Chapter 5, evidence of N··H-O and O··H-O hydrogen bonding was seen in Me,Me-N-Ph.

The presence of a high degree of molecular order, first suggested by the needle-like crystals, was confirmed by the relative ease with which DQ spectra with relatively long recoupling times were able to be recorded. Heteronuclear spectroscopy provided strong evidence of a regular crystalline state with multiple examples of crystallographic inequivalence. Unfortunately, much like the other samples of known high crystallinity, coherent heteronuclear methods were not found to be efficient.

The most likely cause for such long-range order in Me,Me-N-Ph was the ability of the phenyl amine-substituent, as well as the two substituted aromatic rings, to form intermolecular interactions. With π-stacking having already been seen in the crystal structure of H,Me-N-Cy, such interactions were deemed highly probable for Me,Me-N-Ph, although no shielding interactions were observed to support this.

Negative cross peaks in the dipolar exchange spectra were also seen between the N··H-O and aliphatic protons. However, unlike the other dimers, ethyl and propyl substituents were not present and thus can be solely attributed to interactions with the methyl ring substituents. From the DQ spectra the methyl group of higher chemical shift was attributed to this interaction, but as to whether this site is ortho or para to the hydroxyl is still unknown.

Evidence for the dimeric hydrogen bonding structures was seen with proton DQ correlation spectroscopy. With only a weak DQC seen between aromatic and N··H-O protons it was indicated that Me,Me-N-Ph predominantly existed in the dimeric form. It was also suggested that when in the continuous hydrogen bonding structure the aromatic amine-substituent also lies in a closer proximity to the N··H-O protons, with both N··H-O/aromatic DQCs of similar intensity. No evidence for π··H-O interactions were seen.

Simulation of Me,Me-N-Ph showed good absolute agreement regarding N··H-O hydrogen bonding, but overestimated the strength of the O··H-O hydrogen bonds. This could suggest possible π··H-O interaction with shielded protons. For such a system containing a large number of aromatic rings packing effects were thought to be highly important and thus the accuracy of in-vacuo simulation was limited. From the optimised geometry the N··H-O hydrogen bond length was found to be longer than initially expected. However, such a difference was rationalised by considering the pK_a of aniline as compared to that of the other amines previously encountered.

6.2   Asymmetric dimers

All dimers investigated up until this point have been chemically symmetric about the amine. Recently, a number of related asymmetric dimers have been prepared with ring-substituents on only one of the two aromatic rings [Kim 02, Kim 03b]. More specifically, the substituted aromatic ring was similar to that of the Me,Me symmetric dimers, and the other forming a benzyl amine-substituent (Figure 6.16). Such asymmetric dimers allow distinction between intramolecular and intermolecular O··H-O hydrogen bonding due to only a single intramolecular N··H-O *or* intermolecular O··H-O hydrogen bond being able to be formed. This was in contrast to the symmetric dimers which could form an intermolecular or intramolecular O··H-O hydrogen bond, as well as an intramolecular N··H-O hydrogen bond. No evidence for intermolecular O··H-O hydrogen bonding, nor π··H-O hydrogen bonding, was found by FT-IR between 3500–3700 cm^{-1} by Kim *et al.* for the asymmetric dimers [Kim 02, Kim 03b]. Thus only intramolecular N··H-O hydrogen bonding was expected in the asymmetric dimers.

Depending on the amine-substituent, the asymmetric dimers were mostly[†] viscous liquids at room temperature (Table 6.6). However, two systems were solid under these conditions. These were those with cyclohexyl and tertiarybutyl amine-substituents. Although the tertiarybutyl system was reported to be a solid by Kim *et al.* the cyclohexyl system was reported as a pale yellow liquid [Kim 03b]. However, ^{1}H solution-state NMR confirmed the structure to be that of a 2,4-dimethyl-phenol based asymmetric dimer with benzyl and cyclohexyl amine-substituents. It was thus concluded that either upon further purification a solid resulted, or that a misprint had occurred in the initial publication. It had previously been shown that in the molten state detection of hydrogen bonding in the symmetric dimers was not possible by NMR [Schnell 98a], despite the presence of both N··H-O and O··H-O hydrogen bonding being shown by FT-IR and Raman in the melt [Dunkers 95] and in solution [Kim 03b, Kim 03b, Kim 03c]. Thus further characterisation of those systems liquid at room temperature was not undertaken. For simplicity, the two solid asymmetric dimers investigated are hereafter referred to as N-Bz-N-Cy and N-Bz-N-^{t}Bu, reflecting the two amine-substituents.
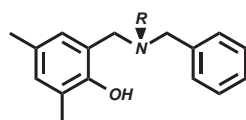
Figure 6.16: *General structure of asymmetric dimers.*

Table 6.6: *Asymetric dimers and their states.*

R	name	state
Me	N-Bz-N-Me	liquid
Et	N-Bz-N-Et	liquid
Pr	N-Bz-N-Pr	liquid
Ph	N-Bz-N-Ph	liquid
^{t}Bu	N-Bz-N-^{t}Bu	solid
Cy	N-Bz-N-Cy	solid

[†]Similar N-Me asymmetric dimers with varying ring-substituents were also reported to be mostly solid at room temperature, however these systems were not available for study [Kim 03b].

6.2.1 NMR spectroscopy of N‑Bz‑N‑Cy

Proton spectroscopy

When compared to the other spectra of the symmetric dimers investigated in this and previous chapters the SPE spectrum of this compound seemed relatively feature-less (Figure 6.17). However, the presence of a resolved peak at 10.2 ppm indicated the presence of hydrogen bonding. Due to only a single proton-donating hydroxyl group being present this was either due to an intramolecular N··H‑O or intermolecular O··H‑O hydrogen bond.

Figure 6.18: Possible structure of N‑Bz‑N‑Cy show-ing an intramolecular N··H‑O hydrogen bond.

Figure 6.17: SPE spectrum of N‑Bz‑N‑Cy

With the chemical shift of the protons involved in hydrogen bonding lying between that of the N··H‑O (10.8–12.4 ppm) and O··H‑O (8.4–9.7 ppm) protons of the N‑Cy dimers of Chapter 4, distinction of the type of hydrogen bonding was problem-atic. However, due to the stability of the six-membered ring formed, intramolecular N··H‑O hydroden-bonding was thought most probable. From 2D proton dipolar ex-change spectroscopy (shown later) a total of two aromatic and three aliphatic sites were distinguished. Deconvolution of the SPE spectra, based on the chemical shifts obtained from 2D spectroscopy, aided assignment (Table 6.7).

Table 6.7: *Expected (I_n) and deconvoluted (I_f) ^{1}H intensities of N‑Bz‑N‑Cy. Brackets indicate chemi-cal shifts taken from two dimensional spectra.*

	δ_H [ppm]	H_n	I_n [%]	I_f [%]
X··H‑O	10.2	1	3.6	2.1
Bz‑Ar	(6.4)	5	17.9	14.3
R‑Ar	(5.6)	2	7.1	17.0
CH$_2$	(2.8)	4	14.3	8.7
Cy‑CH$_2$	(1.0)	10	35.7	37.6
CH$_3$	(-0.5)	6	21.4	20.2

Table 6.8: *Approximate proton T_1 relaxation times of the three resolved sites of N‑Bz‑N‑Cy as measured by the inversion-recovery method.*

	δ_H [ppm]	T_1 [s]
X··H‑O	10.9	51
H‑Ar	6.3	60
CH$_n$	1.7	60

Although relatively large differences were seen between the expected (I_n) and de-convoluted (I_f) intensity distributions of the two aromatic protons of the substituted ring (R-Ar) and CH$_2$ sites, good agreement was seen for all other sites. This was particularly surprising considering the broad nature of the spectrum. Of particular importance was the good agreement seen for protons involved in, as yet unassigned, hydrogen bonding using one hydrogen bonding proton per-molecule. This suggested either a continuous intermolecular O··H-O hydrogen bonding network or discrete intramolecular N··H-O hydrogen bonding (Figure 6.19).
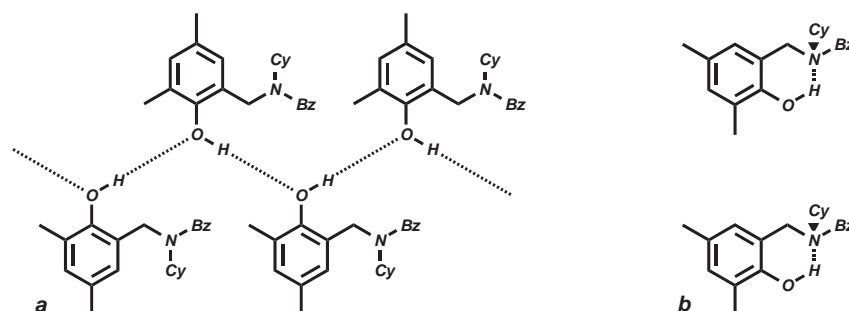
Figure 6.19:   *The (a) continuous intermolecular O··H-O hydrogen bond network or (b) discrete N··H-O hydrogen bonds possible for N-Bz-N-Cy. Both structure having one hydrogen bonding proton per molecule.*

The saturation-recovery method was used to estimate the T_1 relaxation times of each peak seen in the SPE spectra. It was found that all T_1 times were of the the same order of magnitude and ranged from 51–60 s (Table 6.8). It was thought that this relatively long T_1 was due to high crystallinity within the system, with no other signs of high mobility being seen.

As previously mentioned, two aromatic and three aliphatic sites were identified from 2D dipolar exchange spectroscopy (Figure 6.20a). The two aromatic sites at 5.6 and 6.4 ppm were attributed to the substituted and unsubstituted aromatic rings respectively. This assignment was further confirmed by the strong cross-peaks observed between the substituted aromatic ring and methyl protons, and unsubstituted ring and N··H-O protons. The aliphatic region was shown to have three contributions. The CH$_2$ peak at 2.8 ppm, which was only seen as a weak shoulder in the SPE spectra, became more resolved. The broad 1.1 ppm peak of the SPE spectra became resolved into two peaks at 1.1 and 0.4 ppm, these were associated with the methyl and cyclohexyl protons respectively on the basis of the methyl aromatic correlation. The cyclohexyl protons show the effect of shielding, with a lower than expected chemical shift of 0.7 ppm. This was attributed to a facial interaction of the cyclohexyl groups with one of the aromatic rings, as was seen in Chapter 4 for the cyclohexyl amine-substituent in the crystal structure of H,Me-N-Cy (Figure 4.75).
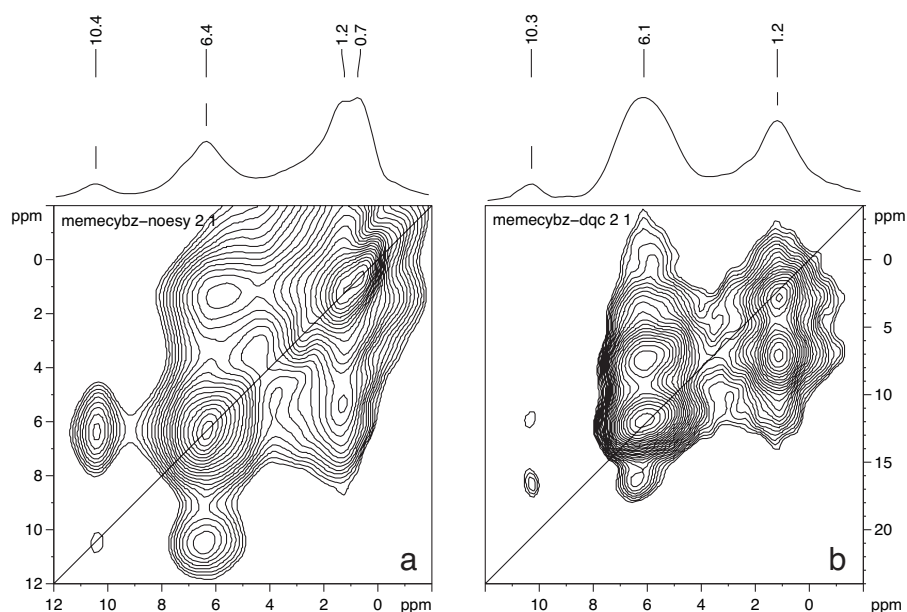
Figure 6.20: *(a) Dipolar-exchange and (b) DQ spectra of N-Bz-N-Cy. $\tau_{mix} = 10$ ms and $\tau_{exc/rec} = 2 \cdot \tau_r$ respectively.*

The DQ correlation spectra of N-Bz-N-Cy confirmed the assignment of the aromatic sites and allowed the nature of the single hydrogen bond to be determined. A clear interaction was seen between the unsubstituted aromatic ring protons (6.4 ppm) and the protons involved in hydrogen bonding (10.2 ppm) (Figure 6.20b). A similar DQC was also seen between the methyl protons and the hydrogen bonding protons. The close proximity of these sites to the hydrogen bonding proton suggested intramolecular N··H-O hydrogen bonding. This was in agreement with the findings of Kim *et al.*, who also observed no evidence for intermolecular O··H-O hydrogen bonding by FT-IR [Kim 02, Kim 03b]. As with the 'bridge' CH_2 protons, the cyclohexyl protons did not appear in the DQ spectra.

Heteronuclear spectroscopy

As with Me,Me-N-Ph, with only small amounts of sample available heteronuclear methods were generally problematic, with coherent methods not found to be efficient. However, from the CP MAS spectrum a number of observations were made (Figure 6.21).
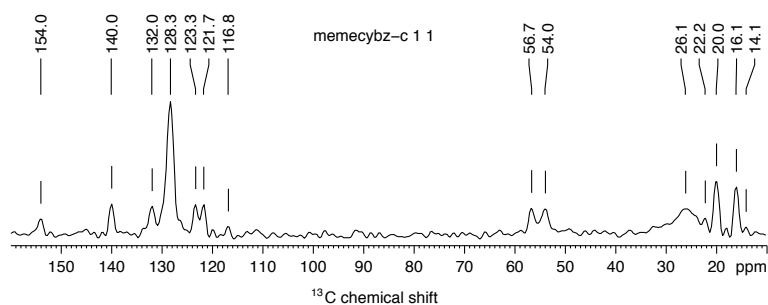
***Figure 6.21**: ^{13}C CP MAS spectrum of N-Bz-N-Cy.*

A single aromatic C-OH site was seen at 154 ppm, and the C-CH$_2$ site of the benzyl group at 140 ppm (Figure 6.22). The strong aromatic peak at 128.3 ppm was assigned to the other aromatics of the unsubstituted ring, with the remaining aromatics attributed to unassigned sites on the substituted ring. The two CH$_2$ groups had chemical shifts of 56.7 and 54.0 ppm, with the higher attributed to the benzyl group. Unlike the dimers no crystallographic inequivalence of the CH$_2$ groups was observed. The CH$_2$ groups of the cyclohexyl ring were seen as a broad peak at 26.1 ppm. This possibly suggested a high number of orientations open to this group, resulting in chemical shift distribution. The ortho and para methyl groups were resolved at 16.1 and 20.0 ppm respectively. It is currently unknown why the N-CH site of the cyclohexyl amine-substituent was not seen in the CP MAS spectrum. This carbon was expected to have a chemical shift of ≈ 60 ppm and should have been clearly resolved.
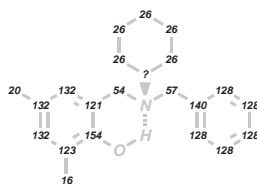
***Figure 6.22**: ^{13}C assignment of N-Bz-N-Cy.*

6.2.2 NMR spectroscopy of N⁻Bz⁻N⁻^{t}Bu

Proton spectroscopy

The proton SPE spectrum of N⁻Bz⁻N⁻^{t}Bu clearly showed the presence of protons involved in N··H⁻O hydrogen bonding at 11.7 ppm, 1.5 ppm higher than that of N⁻Bz⁻N⁻Cy (Figure 6.23). In contrast to the three peaks seen for N⁻Bz⁻N⁻Cy, five distinct peaks and two shoulders were observed for N⁻Bz⁻N⁻^{t}Bu. As expected from the chemical structure the strongest signal arose from the methyl protons of the tertiary-butyl group (Figure 6.24).
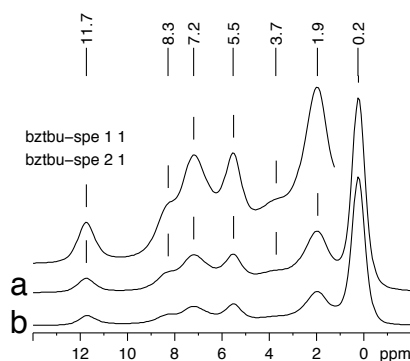
Figure 6.23: (a) SPE and (b) Hahn echo spectra of N⁻Bz⁻N⁻^{t}Bu showing N··H⁻O hydrogen bonding.
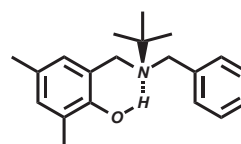
Figure 6.24: Structure of N⁻Bz⁻N⁻^{t}Bu.

The chemical shift of 0.2 ppm for these tertiary-butyl methyl groups indicated the presence of shielding interactions. As with the shielded cyclohexyl protons of N⁻Bz⁻N⁻Cy, a facial orientation to an aromatic ring was suggested. The methyl ring-substituents were resolved at 1.9 ppm and the CH₂ protons were seen as a shoulder at 3.7 ppm. Unlike N⁻Bz⁻N⁻Cy, aromatic protons from both substituted and unsubstituted aromatic rings were resolved in the SPE spectrum, without the need to consult 2D spectra, at 5.5 and 7.2 ppm respectively. The relatively high resolution seen within this system was most likely caused by the mobility imparted by the tertiarybutyl amine-substituent. The general mobility seen within N⁻Bz⁻N⁻^{t}Bu can be demonstrated by the high proportion of magnetisation refocused by a Hahn echo as compared to the SPE spectra (Figure 6.23b).

Upon first inspection the shoulder at ≈ 8.3 ppm was thought to indicate protons involved in O··H⁻O hydrogen bonding. However, a minimum of two molecules would be needed for both N··H⁻O and O··H⁻O hydrogen bonding to occur, with only a single proton donor present for each molecule. Thus an intermolecular N··H⁻O and intermolecular O··H⁻O hydrogen bond would be formed. This would be equivalent to a single N··H⁻O and O··H⁻O proton site for every two molecules. Comparison of the experimental intensity ratios obtained by deconvolution (I_f) and expected ratios for such a configuration (I_A) showed this form to be unlikely (Table 6.9). Only when both 11.7 and 8.3 ppm sites were considered to be present for every molecule

was good agreement between expected (I_B) and experimental intensity ratios found. The only discrepancy was that of the unsubstituted aromatic ring protons Bz-Ar. The assignment of the site responsible for the peak at 8.3 ppm was only achieved by a combination of ^{1}H DQ and ^{13}C–^{1}H HSQC spectroscopy (shown later). This revealed the site to be a single strongly deshielded proton from the unsubstituted aromatic ring.

Table 6.9: *Expected (I_a, I_b) and deconvoluted experimental (I_f) proton intensity ratios of N-Bz-N-^{t}Bu with the 8.3 and 11.7 ppm sites assigned as both being present for every two molecules (A) or every individual molecule (B). Brackets indicate chemical shifts values taken from 2D spectra.*

	δ_H [ppm]	A	B	I_A [%]	I_B [%]	I_f [%]
N··H-O	11.7	1	1	1.9	3.6	3.2
?	(8.3)	1	1	1.9	3.6	3.2
Bz-Ar	(7.1)	10	5	18.5	21.4	14.9
R-Ar	5.5	4	2	7.4	7.1	8.4
CH$_2$	(3.9)	8	4	14.8	14.3	9.5
CH$_3$	2.0	12	6	22.2	21.4	21.3
^{t}Bu-CH$_3$	0.2	18	9	33.3	32.1	39.5

The approximate ^{1}H T_1 relaxation times for all sites were found to be 2.06 ± 0.01 s by inversion recovery. It was thought that a combination of spin-diffusion between all sites and the rapid motion of the tertiarybutyl group lead to such a uniform relaxation behaviour.
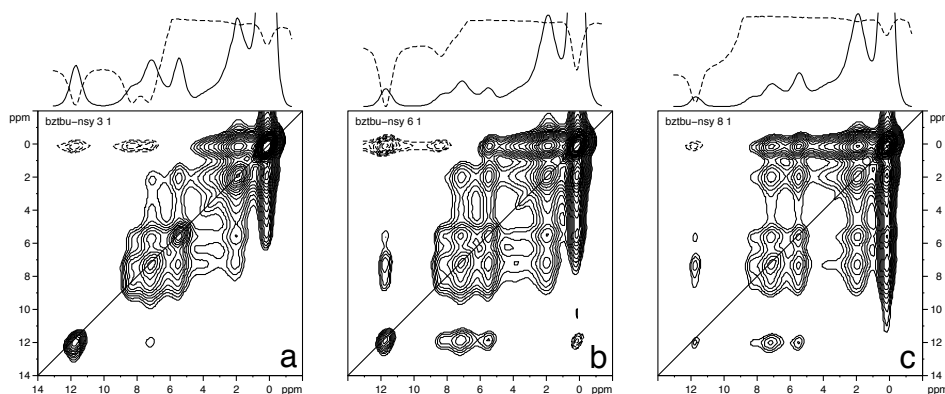
Figure 6.25: *Dipolar exchange spectra of N-Bz-N-^{t}Bu: (a) $\tau_{mix} = 2$ ms, (b) 10 ms and (c) 50 ms. Positive (solid) and negative (dashed) projections shown illustrating negative cross-peaks.*

Dipolar-exchange spectra again showed negative cross-peaks between the shielded methyl protons of the tertiarybutyl group and the isolated N··H-O protons (Figure 6.25). Negative cross-peaks were also seen between the tertiarybutyl protons and the aromatic protons of the unsubstituted ring at 7.1 and 8.3 ppm (Figure 6.25). As compared to the symmetric dimer systems, where such interactions have also been observed, for N-Bz-N-^{t}Bu this phenomenon was observed over a large range of mixing times, i.e at $\tau_{mix} = 50$ ms negative cross-peaks were still present. This was probably due to the mobility of the tertiarybutyl amine-substituent. As with N-Bz-N-Cy, the aromatic protons of the substituted ring (5.5 ppm) showed a stronger interaction to the methyl ring substituents allowing assignment (Figure 6.25a).
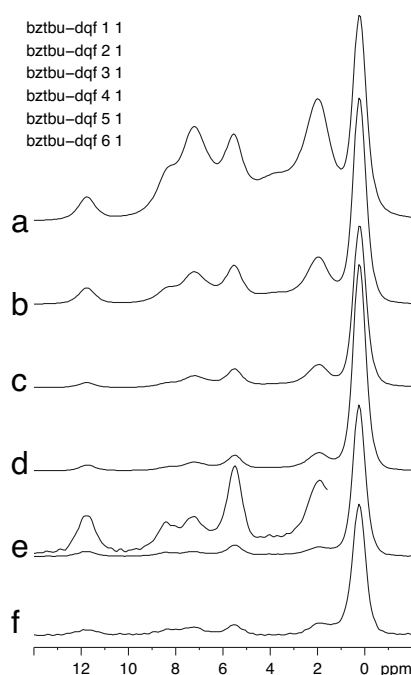
Figure 6.26: *DQ filtered spectra of N-Bz-N-^{t}Bu with 32 scans: (a–d) $\tau_{exc/rec} = 1$–$4 \cdot \tau_r$, (e) $6 \cdot \tau_r$ and (f) $8 \cdot \tau_r$.*
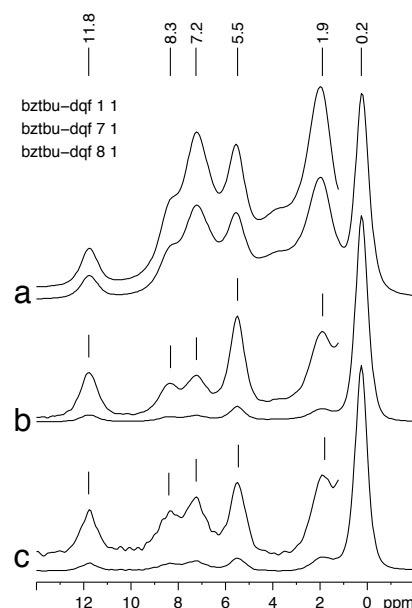
Figure 6.27: *DQ filtered spectra of N-Bz-N-^{t}Bu with variable $\tau_{exc/rec}$ and number of scans (#): (a) $1 \cdot \tau_r$ (32), (b) $6 \cdot \tau_r$ (128) and (c) $8 \cdot \tau_r$ (128).*

The dynamics of the tertiarybutyl amine-substituent were more clearly seen in the 1D DQ filtered spectra, where significant magnetisation was still present even with $\tau_{exc/rec} = 8 \cdot \tau_r$ (Figure 6.26a–f). Relatively high intensities at longer recoupling times were also seen for the other sites, as compared to the systems studied previously. Under longer recoupling the shoulder at 8.3 ppm was further resolved (Figure 6.27b).

A strong similarity was seen between the 2D DQ correlation spectra of the symmetric dimers and N-Bz-N-^{t}Bu (Figure 6.28). From these spectra the assignment of the two aromatic sites was confirmed. The aromatic protons of the unsubstituted ring were found to have a stronger auto-peak at 5.5 ppm, whereas only a weak auto-peak at 7.2 ppm was seen for the substituted ring. Due to the DQC between the two aromatic sites, relatively close proximity was suggested. The N··H-O protons were also observed to be close to both the methyl groups of the tertiarybutyl amine-substituent and the methyl ring-substituents. The DQC intensities reflected the relative intensities of the two methyl sites (Figure 6.28a). A weak DQC was also seen between the N··H-O protons and the unsubstituted ring protons. However, unlike the symmetric dimers this was not indicative of a ring flip, due to the different chemical structure.
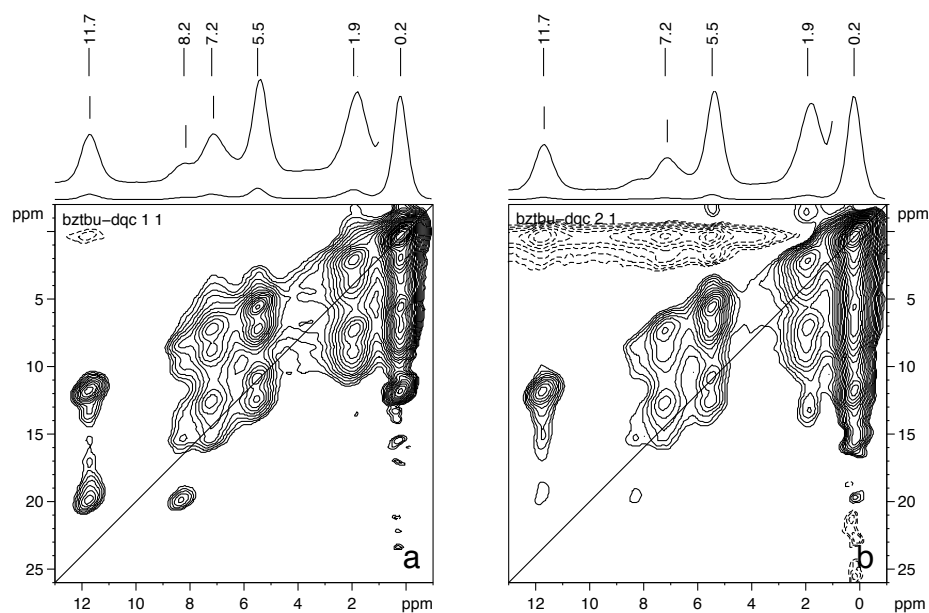
Figure 6.28: *DQ spectra of N-Bz-N-^{t}Bu with (a) $\tau_{exc/rec} = 2 \cdot \tau_r$ and (b) $4 \cdot \tau_r$. Note negative dipolar-exchange-like cross-peaks c.f. Figure 6.25.*

Of more interest were the interactions with the protons at 8.3 ppm. As with the O··H-O protons of the dimers these were in close proximity to the N··H-O protons. However they were also found to interact relatively strongly with the tertiarybutyl and aromatic protons of the unsubstituted ring (Figure 6.28b). Further weak interactions were also observed with the methyl ring substituents and the aromatic protons of the substituted ring.

As was seen with the dipolar-exchange spectra, dipolar-exchange-like negative cross-peaks were also present between the ^{t}Bu and N··H-O sites in the DQ spectra (Figure 6.28). With longer recoupling negative cross-peaks were also seen between ^{t}Bu and aromatic sites, as for dipolar exchange spectra with longer mixing times (Figure 6.25). This provided further support for the negative cross-peaks being caused by cross-relaxation via the double-quantum pathway, as also suggested by the N-Pr dimers in Chapter 4 (Section 4.2.1).

Heteronuclear spectroscopy

Coherent heteronuclear methods were partially successful for this system, with re-coupling using REPT found to be relatively efficient. As with the DQ filtered proton spectra dipolar oscillations were observed with increasing recoupling time before the onset of relaxation phenomena (Figure 6.29). Unfortunately, rotor-encoding side-band experiments were only possible for the aromatic sites, and thus provided no further structural information. Methods based on REREDOR were not found to be successful, with the low efficiency of the initial cross-polarisation step being the most likely cause.
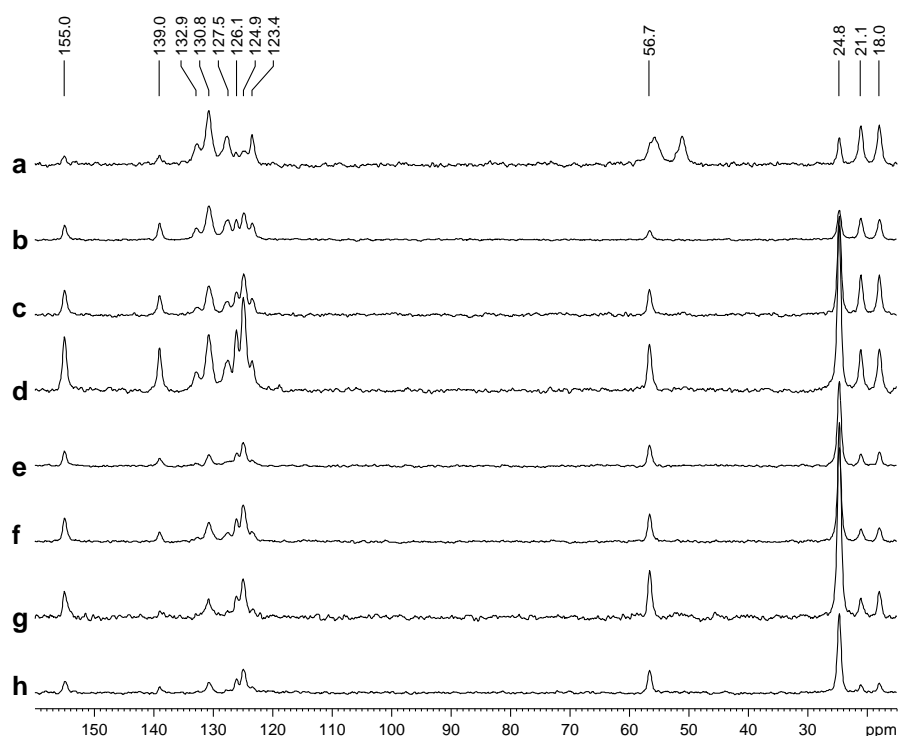
Figure 6.29: *1D REPT specta of N-Bz-N-^{t}Bu: (a–h)* $\tau_{exc/rec} = 1$–$8 \cdot \tau_r$

From the 1D REPT spectra a single C-OH aromatic site was seen at 155.0 ppm. The maximum intensity for this, and most other sites, was achieved with $\tau_{exc/rec} = 4 \cdot \tau_r$ (Figure 6.29d). The unprotonated aromatic carbon of the unsubstituted ring (N-CH$_2$-C) was seen at 139.0 ppm, with a further six aromatic sites attributed to both aromatic rings resolved between 123–133 ppm. The quaternary and methyl carbons of the tertiarybutyl group were found at 56.7 and 24.8 ppm respectively, with the para and ortho methyl ring-substituents observed at 21.1 and 18.0 ppm respectively. The CH$_2$ carbons at 55.0 and 45.4 ppm were only seen with short recoupling times of $\tau_{exc/rec} = 1 \cdot \tau_r$ and were assigned to the unsubstituted and substituted sides of the molecule respectively (Figure 6.29a).

As with the 1D spectra, heteronuclear correlations to the CH$_2$ carbons were only seen in the HSQC spectra with short recoupling times (Figure 6.30). The different proton chemical shifts of the methyl groups associated to the tertiarybutyl and substituted aromatic ring can be clearly seen (Figure 6.30b). The methyl ring-substituents showed a weak interaction with aromatic protons. The the methyl carbons of the tertiarybutyl group showed a weak interaction with protons at 9.5 ppm (Figure 6.30c). Due to the weak nature of these correlations, and the chemical shift of 9.5 ppm not being previously observed in 1D or 2D proton spectra, it was concluded that these peaks were artefacts.
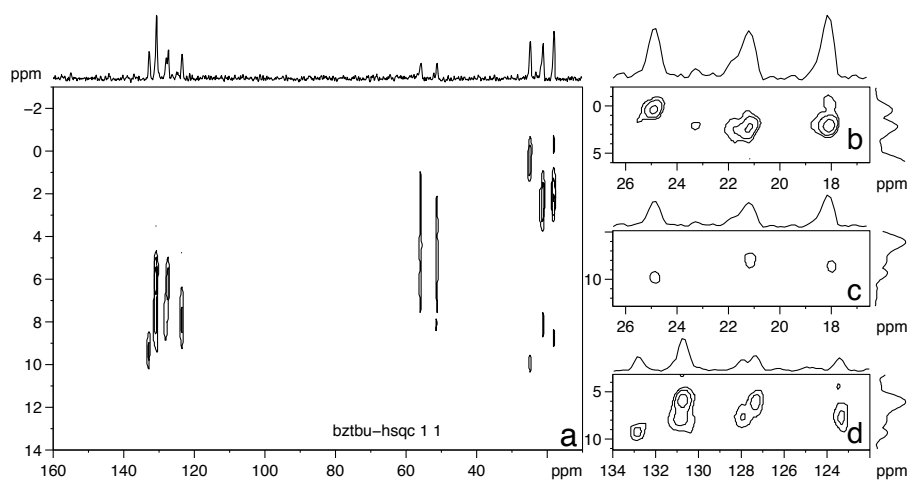
Figure 6.30: *REPT HSQC spectrum of N-Bz-N-^{t}Bu with $\tau_{exc/rec} = 1 \cdot \tau_r$. (a) full (a–b) methy and (c) aromatic regions*

Further assignment of the aromatic carbons was made on the basis of the associated proton chemical shifts, with the substituted and unsubstituted aromatic protons found at 7.1 and 5.5 ppm respectively (Figure 6.30d). Of the five aromatic carbons observed in the $\tau_{exc/rec} = 1 \cdot \tau_r$ HSQC spectrum all but one site could be assigned to one of the aromatic rings on this basis. The remaining aromatic carbon, with a chemical shift of 132.9 ppm, was seen to interact with the as yet unassigned protons at ≈ 9 ppm. With only covalently bound ^{13}C–^{1}H spin-pairs typically observed at such short recoupling times, the proton at ≈ 9 ppm was suggested to be a strongly deshielded aromatic proton. This deshielded proton was thought to be the same as that seen in the proton SPE and DQ spectra at 8.3 ppm, with the difference in observed chemical shift due to the overlap of the peak with the aromatic protons at 7.2 ppm (Section 6.23). Thus the site, previously thought to be involved in O··H-O hydrogen bonding, at 8.3 ppm was shown to be a strongly deshielded aromatic proton.

Upon recalculation of the expected intensities, a much better agreement was seen when the deshielded aromatic proton was assigned to the benzyl group as opposed to the substituted ring (Table 6.10). Thus, as suggested by the chemical structure and FT-IR spectroscopy [Kim 03b] only N··H-O hydrogen bonding was present.

Table 6.10: *Expected (I_S, I_U) and deconvoluted experimental (I_f) proton intensity ratios of of N-Bz-N-^{t}Bu with the deshielded aromatic proton at 8.3 ppm assigned to the substituted (S) and unsubstituted (U) aromatic rings.*

	δ_H [ppm]	S	U	I_S [%]	I_U [%]	I_f [%]
N··H-O	11.7	1	1	3.7	3.7	3.2
?-Ar	8.3	1	1	3.7	3.7	3.2
Bz-Ar	7.1	5	4	18.5	14.8	14.9
R-Ar	5.5	1	2	3.7	7.4	8.4
CH$_2$	3.9	4	4	14.8	14.8	9.5
CH$_3$	2.0	6	6	22.2	22.2	21.3
^{t}Bu-CH$_3$	0.2	9	9	33.3	33.3	39.5

Weaker long-range interactions were observed with recoupling times of $\tau_{exc/rec} = 4 \cdot \tau_r$ (Figure 6.31). As previously seen for the symmetric dimers in Chapter 4, the aromatic C-OH carbons (155.0 ppm) showed a strong interaction with the N··H-O protons (11.7 ppm). However, unlike previous systems another aromatic carbon at 124.9 ppm also showed a weak interaction with these protons (Figure 6.31d).
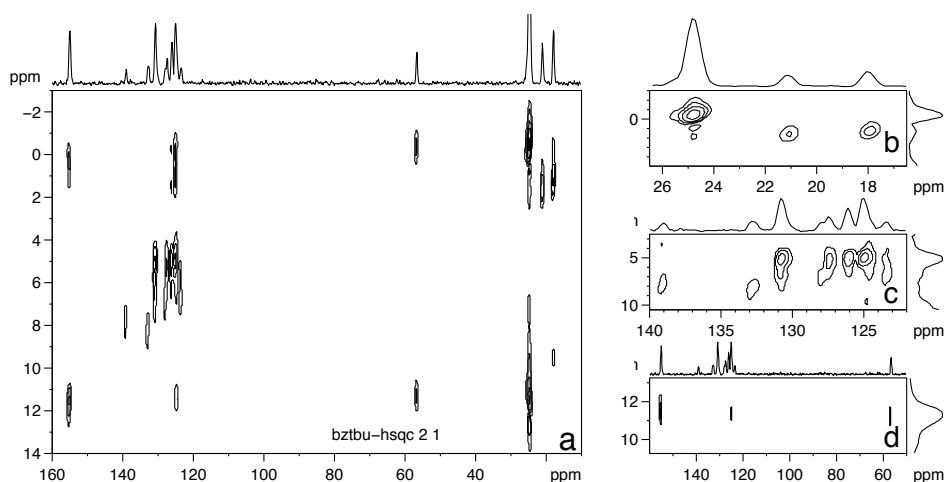
Figure 6.31: *^{13}C–^{1}H REPT HSQC spectrum of N-Bz-N-^{t}Bu with $\tau_{exc/rec} = 4 \cdot \tau_r$. (a) Full (b) methy (c) aromatic and (d) N··H-O regions are shown.*

This carbon was assigned to the unsubstituted aromatic ring by its interaction with the protons at 5.5 ppm, this indicating a close proximity of both aromatic rings to the protons involved in N··H-O hydrogen bonding (Figure 6.31c). Interaction with the strongly deshielded aromatic proton at 8.3 ppm was observed for both the protonated (132.9 ppm) and unprotonated (139.0 ppm) sites of the unsubstituted ring. This suggested the deshielded proton was directly attached to the 123.9 ppm carbon and was relatively close in space to the carbon at 139 ppm.

As well as the two aromatic sites, both the methyl and quaternary carbons of the tertiarybutyl group showed interactions with the N··H‑O protons, indicating their close proximity. The methyl protons of the tertiarybutyl group were also observed to interact with the aromatic C‑OH carbons of the substituted ring, as well as the C‑H carbon of the unsubstituted ring at 124.9 ppm (previously associated with the N··H‑O protons). This lead to the conclusion that the tertiarybutyl group, N··H‑O hydrogen bond and aromatic site on the unsubstituted ring were all within close proximity to each other (Figure 6.32).
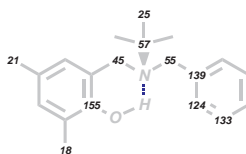
Figure 6.32: *^{13}C chemical shift assignment of N‑Bz‑N‑^{t}Bu.*

6.2.3   Summary

Upon analysis of the solid asymmetric dimers, both N‑Bz‑N‑Cy and N‑Bz‑N‑*t*Bu showed evidence for N··H‑O hydrogen bonding. Unlike the hydrogen bonding seen in the symmetric-dimers of Chapter 4 and Chapter 5 only intramolecular hydrogen bonding was observed. By comparison of the proton chemical shifts the N··H‑O hydrogen bonds in these asymmetric dimers were relatively strong. The higher than expected chemical shift could be explained by the steric bulk of the cyclohexyl and tertiarybutyl groups encouraging shorter N··H‑O hydrogen bonds. This would also explain the higher chemical shift seen for the bulkier tertiarybutyl group (11.7 ppm) as compared to that of cyclohexyl system (10.2 ppm).

The mobility of the tertiarybutyl amine-substituent was also shown to strongly influence the N‑Bz‑N‑*t*Bu, which showed the greatest proton resolution and longest accessible recoupling times of all systems examined. The tertiarybutyl group was shown to be in close proximity to both substituted and unsubstituted aromatic rings, as well as the N··H‑O proton.

On first inspection, with a peak seen at 8.3 ppm, the presence of O··H‑O hydrogen bonding was suggested for N‑Bz‑N‑*t*Bu. However comparison of the deconvoluted intensity ratios proved that to be unlikely. Through heteronuclear ^{1}H–^{13}C correlation spectroscopy the site responsible for this relatively high chemical shift was assigned to a deshielded aromatic proton belonging to the benzyl group. The degree of deshielding suggested both a close proximity, and coplanar arrangement, of two aromatic rings. It was suspected that steric hindrance of the bulky amine-substituent forced the two aromatic rings of N‑Bz‑N‑*t*Bu together, causing such an interaction. Thus, an aromatic proton of the benzyl group experienced not only the ring currents of the ring to which it was attached, but also those of a second aromatic system. Due to the close proximity of both aromatic rings and the N··H‑O hydrogen bond this interaction was thought to be intramolecular in nature.

6.3   Linear-diamine polybenzoxazines

Other than the model dimers and trimers previously discussed a number of macro-molecular polybenzoxazines were also investigated. Unlike the polybenzoxazine oligomers encountered in Chapter 5 these macromolecules were based on diamine-based monomers (Figure 6.33). Two classes of diamine-based polymers were studied: those based on linear-diamines and those based on cyclic-diamines. The latter being discussed separately (Section 6.4).
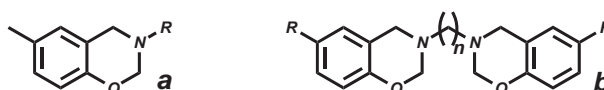
Figure 6.33: Monomers of (a) mono-amine and (b) di-amine based polybenzoxazines.

Due to the multiple functionality of the diamine monomers, polymer-networks may be formed. However, structural characterisation of such cross-linked systems was difficult. For cross-linked polybenzoxazines structural characterisation has gener-ally been undertaken by the analysis of thermal degradation products by TGA, FT-IR and GC-MS [Low 98, Low 99a, Low 99b]. The curing processes of similar cross-linked systems have also been studied by ^{15}N and ^{13}C solid-state NMR [Russell 98a, Russell 98b].

Cross-linked polybenzoxazines with 2, 4, 6 and 12 CH_2 groups separating the amines were investigated (Figure 6.33b). The $n = 2$ systems was available with and without a para-methyl ring-substituent (R). The substituted system being analogous to the H,Me dimers of Chapter 4. All other polymers were only available without ring-substituents (Table 6.11).

Table 6.11: Linear-diamine polymers studied.

$(CH_2)_n$	R	name
12	H	Poly-C_{12}
6	H	Poly-C_6
4	H	Poly-C_4
2	H	Poly-C_2
2	Me	Poly-C_{2p}

As common for many cross-linked systems, the exact chemical structure of the linear-diamine polymer networks in question were unknown. However, from the known reaction pathways available for this system the formation of cross-links, and general structural moieties present, can be illustrated (Figure 6.34).
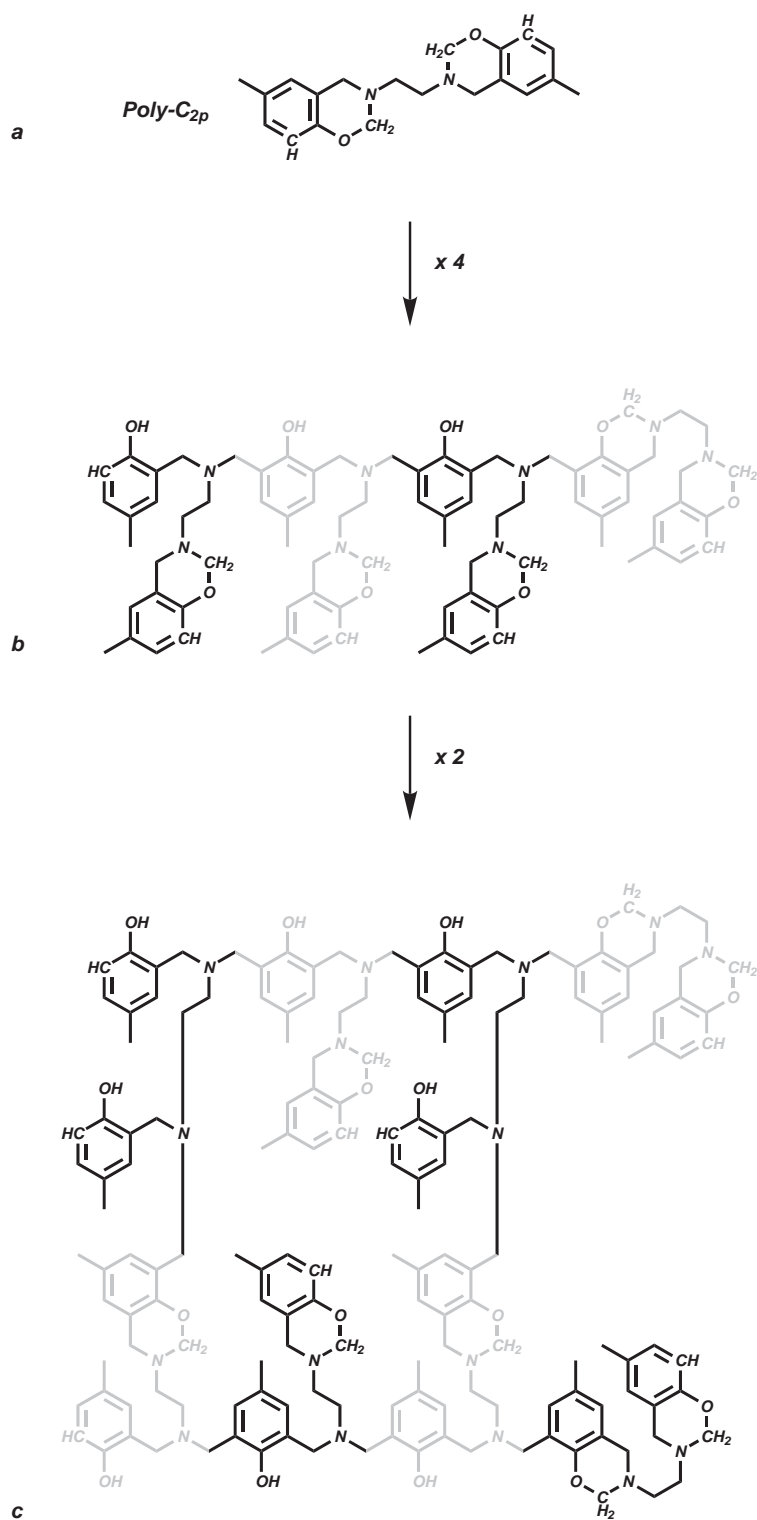
Figure 6.34: *The formation of a cross-linked polybenzoxazine based on the linear-diamine monomer Poly-C$_{2p}$. Aliphatic site capable of forming carbocations (CH$_2$) and aromatic site open to attack by carbocations (CH) are shown illustrating further possible reaction pathways. Segments from the same monomer unit are shaded for clarity.*

6.3.1 NMR spectroscopy

The cross-linked polymeric nature of the compounds was reflected in the broad proton and carbon line-shapes observed, indicative of chemical shift distribution, as compared to the corresponding spectra of the monomers (shown later). No evidence of hydrogen bonding was seen in the monomer due to the lack of a proton-donating functionality.

Proton spectroscopy

Due to the inherent chemical shift distribution present in polymers all proton spectra were relatively featureless, with only resolution of aromatic and aliphatic sites (Figure 6.35). As expected from the chemical structure of the monomers, the aliphatic peak increased in intensity with diamine chain length. The chemical shift of the aliphatic peak also tended to that of CH_2 sites uninfluenced by neighbouring nitrogen sites (Figure 6.35a). For Poly-C_{2p} the chemical shift of the aliphatic peak was strongly influenced by the presence of the para methyl ring-substituents (Figure 6.35e). The chemical shift of the aromatic protons remained approximately constant (6.8 ppm) and was comparable to that of the H,Me-N-Cy and H,Et-N-Cy dimers (Section 4.2.1). The intensity of the aromatic peak also increased slightly with chain length, however this was thought to be due to the broad 'foot' of the aliphatic peak encroaching into the aromatic region. However, this could also be due to greater line narrowing caused by the presence of more motional averaging in systems with longer, more flexible, chains.
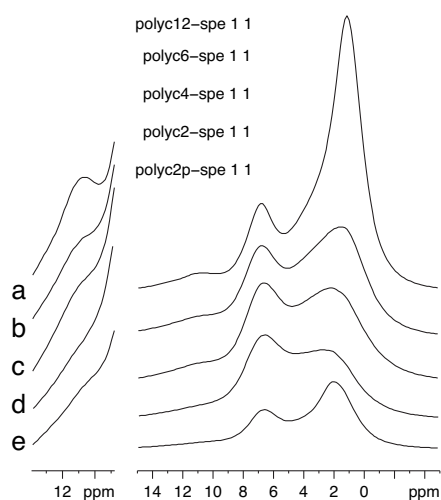
Figure 6.35: *SPE spectra of linear-diamine based polybenzoxazines: (a) Poly-C_{12}, (b) Poly-C_6, (c) Poly-C_4, (d) Poly-C_2 and (e) Poly-C_{2p}.*

Upon closer inspection, a weak peak at 11.5 ppm was observed for Poly-C_{12} and attributed to hydrogen bonding on the basis of its high chemical shift (Figure 6.35a). Similarly, weak shoulders were also seen for some of the other polymers. The intensity of the shoulders were seen to increase with diamine chain length. That is from Poly-C_2, where it is debatable if a shoulder exists, to Poly-C_{12} were a definite peak was seen. The weak shoulder was found to be slightly stronger for Poly-C_{2p} than Poly-C_2, possibly indicating the presence of more hydrogen bonding in Poly-C_{2p}. However, caution should be taken when comparing such weak shoulders in broad peaks.

The chemical shift of 11.5 ppm lies between those observed for the model dimers in Chapter 4, ranging between 11.7–13.0 ppm for the N··H‑O protons and 7.0–9.4 ppm for the O··H‑O protons. Thus, without further investigation this site would be assigned as a weak N··H‑O hydrogen bond. However, DQ spectroscopy revealed another weak peak, not detected in the SPE experiment, at $\approx$13 ppm (shown later). This suggested that rather than having only weak N··H‑O hydrogen bonds both N··H‑O and O··H‑O hydrogen bonds were present. As well as this both types of hydrogen bonding were relatively strong in nature, even if in low concentration. Before the DQ spectra are presented in full, proton relaxation experiments will be briefly discussed.

Although accurate determination of ^{1}H T_1 relaxation times was not possible, especially with the broad overlapping lines present, some structural information was still gained from the approximate relaxation times measured. For most systems a common relaxation time was seen, however for Poly‑C$_{12}$ and Poly‑C$_{2p}$ different relaxation behaviour was measured for each site (Table 6.12). This could imply that for these systems these sites had different degrees of mobility.

Table 6.12: *Approximate proton T_1 relaxation times for the linear-diamine polymers.*

^{1}H T_1 [s]	O··H‑O	Ar‑H	CH$_2$
Poly‑C$_{12}$	2.1	1.6	1.1
Poly‑C$_6$	1.0	1.0	1.0
Poly‑C$_4$	0.9	0.8	0.9
Poly‑C$_2$	–	3.1	3.1
Poly‑C$_{2p}$	–	6.8	5.8

As previously mentioned DQ spectroscopy provided evidence for both N··H‑O and O··H‑O hydrogen bonding in Poly‑C$_{12}$. The DQ filtered spectra with $\tau_{exc/rec} = 2 \cdot \tau_r$, as with the SPE spectra, only showed evidence of O··H‑O hydrogen bonding (Figure 6.36a). However, with longer recoupling of $\tau_{exc/rec} = 4 \cdot \tau_r$ evidence for both N··H‑O and O··H‑O hydrogen bonding was seen (Figure 6.36b).
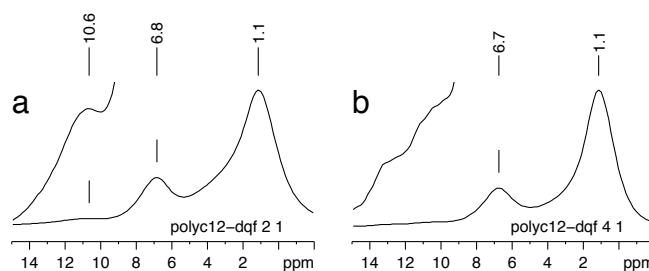
Figure 6.36: *DQ filtered spectra of Poly‑C$_{12}$: (a) $\tau_{exc/rec} = 2 \cdot \tau_r$ and (b) $4 \cdot \tau_r$.*
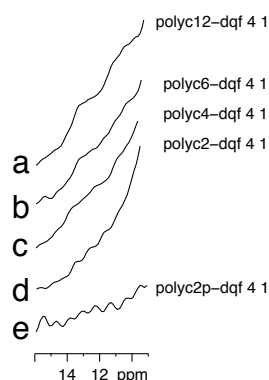
Figure 6.37: *Proton DQ filtered spectra of (a) Poly-C$_{12}$, (b) Poly-C$_6$, (c) Poly-C$_4$, (d) Poly-C$_2$ and (e) Poly-C$_{2p}$.*

Similarly, the DQ filtered spectra of Poly-C$_6$ and Poly-C$_4$ also indicated the possible presence of N··H-O protons. The N··H-O peak, as with the O··H-O peak, also seemed to increase with diamine chain length (Figure 6.37a–c). However, no evidence was found for the presence of N··H-O or O··H-O hydrogen bonding for either Poly-C$_2$ or Poly-C$_{2p}$ (Figure 6.37d–e). This was despite the presence of O··H-O protons having been suggested by the SPE spectra. The presence of O··H-O and N··H-O hydrogen bonding was unambiguously shown by 2D DQ spectroscopy. For Poly-C$_{12}$ both types

of hydrogen bonding were shown to be present with $\tau_{exc/rec} = 2 \cdot \tau_r$ (Figure 6.38a). With longer recoupling the correlations to the N··H-O protons were further resolved (Figure 6.38b).
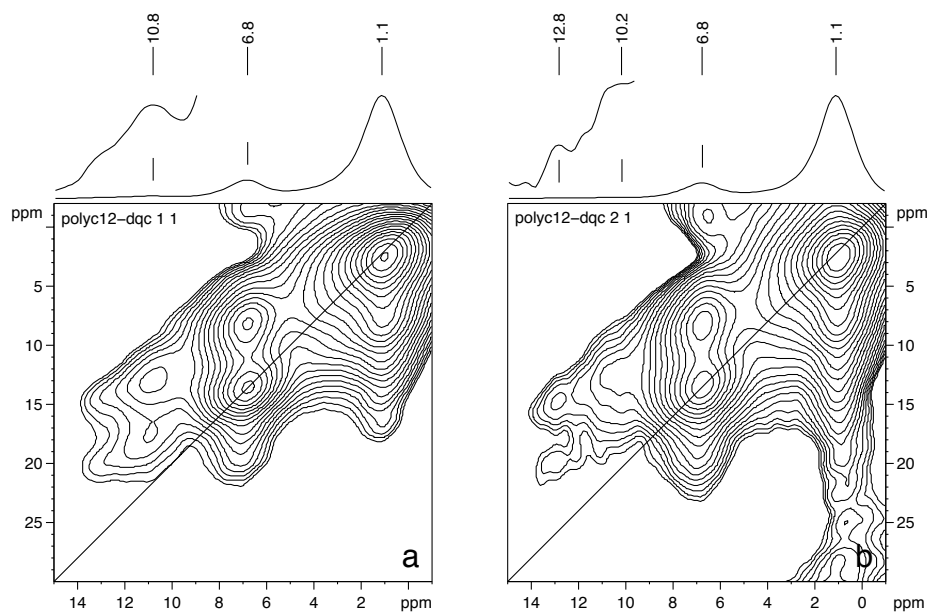
Figure 6.38: *DQ spectra of (a) Poly-C$_{12}$ with (a) $\tau_{exc/rec} = 2 \cdot \tau_r$ and (b) $4 \cdot \tau_r$.*

The 2D DQ spectra of Poly-C_6 and Poly-C_4 also showed signs of the presence of both N··H-O and O··H-O hydrogen bonding (Figure 6.39).
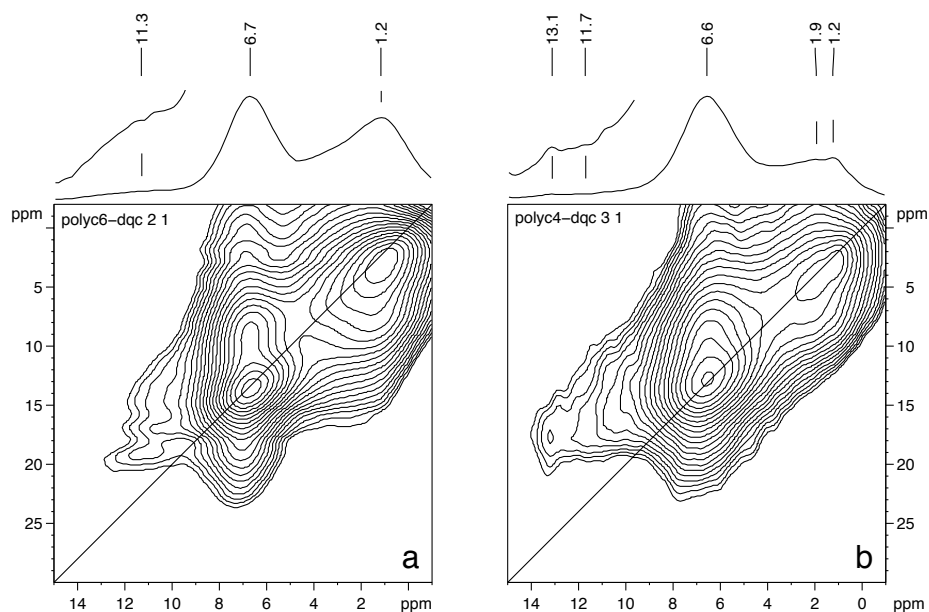
***Figure 6.39**: DQ spectra of (a) Poly-C_6 ($\tau_{exc/rec} = 2 \cdot \tau_r$) and (b) Poly-$C_4$ ($\tau_{exc/rec} = 4 \cdot \tau_r$).*

In contrast, Poly-C_2 and Poly-C_{2p} showed no significant signs of hydrogen bonding (Figure 6.40). This illustrates the problems associated with overinterpretation of weak shoulders in 1D spectra and the power of 2D proton solid-state NMR.
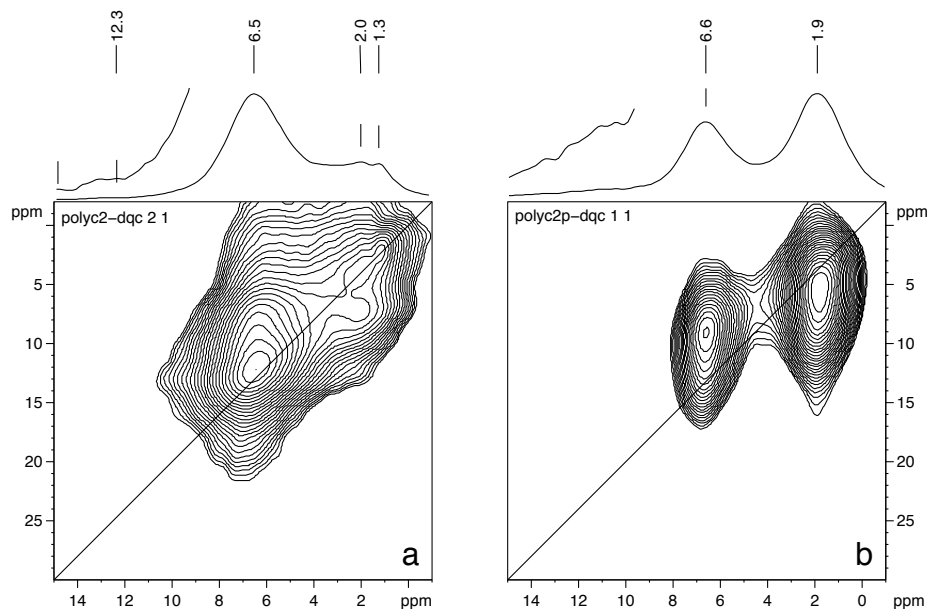
***Figure 6.40**: DQ spectra of (a) Poly-C_2 and (b) Poly-C_{2p} ($\tau_{exc/rec} = 4 \cdot \tau_r$).*

Pulsed field-gradient assisted proton spectroscopy

With hydrogen bonding most prevalent in Poly-C_{12} a complication arises from the spectrometer hardware. Due to the low relative intensity of the N··H-O peak to that of the dominant CH_2 peak, the N··H-O signal is 'driven-into-the-noise' by the receiver needing to be adjusted for the strongest signal. However, by using pulsed-field-gradient (PFG) assisted suppression of the CH_2 signal prior to digitisation, the receiver could be adjusted for the less intense aromatic peak. The gain in resolution, and suppression efficiency, was judged by comparison to a standard Hahn-echo spectrum of Poly-C_{12} (Figure 6.41a).
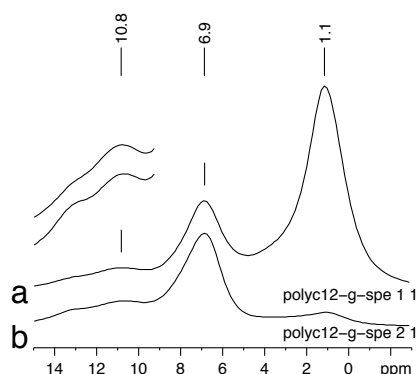
Figure 6.41: (a) Hahn-echo and (b) PFG/watergate spectra of Poly-C_{12}

Combining peak suppression and 2D DQ spectroscopy allowed similar resolution gains to be achieved (Figure 6.42). Although spectral artefacts are present, the resolution gained is consistent with the DQ spectrum acquired without peak suppression.
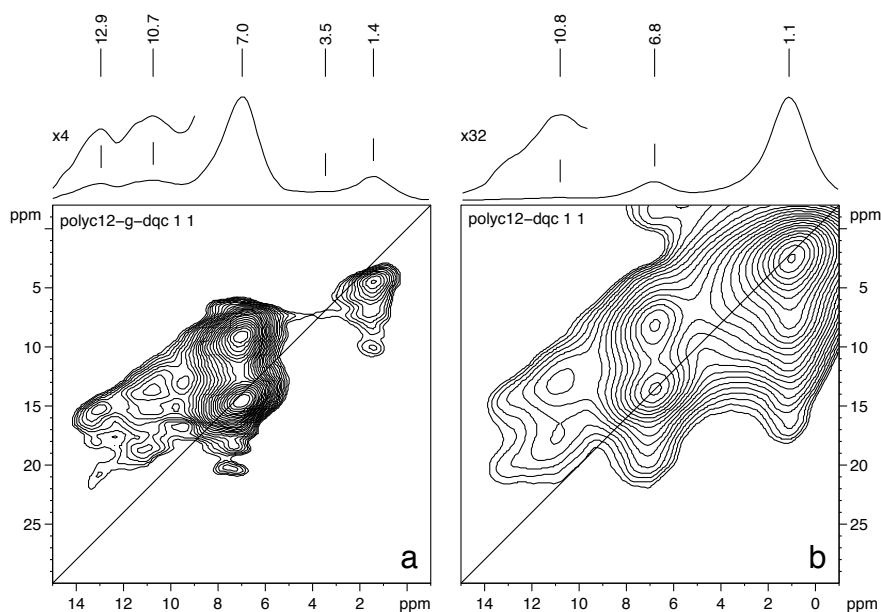
Figure 6.42: DQ spectra of Poly-C_{12} (a) with and (b) without PFG assisted peak-suppression. ($\tau_{exc/rec} = 2 \cdot \tau_r$)

Hetronuclear spectroscopy

Heteronuclear dipolar recoupling methods were not found to be efficient for the linear-diamine based polymers and ^{13}C CP MAS yielded relatively featureless spectra (Figure 6.43a). The broad lines observed were however characteristic of the cross-linked nature of the systems and were comparable to other polybenzoxazines previously investigated by Russell *et al.* [Russell 98b].
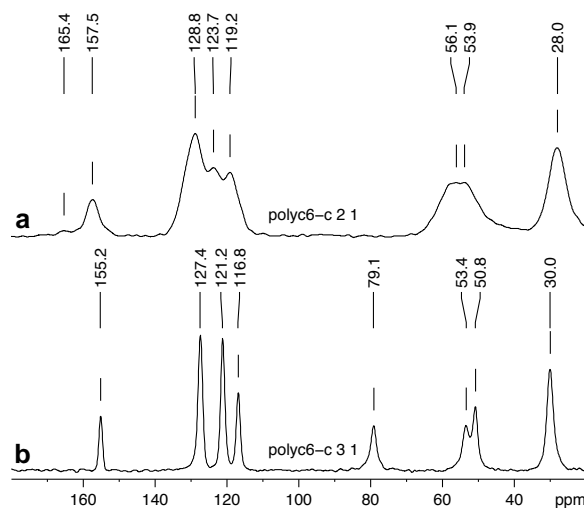
Figure 6.43: ^1H–^{13}C *CP MAS spectra of (a) Poly-C$_6$ and (b) its associated monomer (c.f. Figure 6.33b).*

For all systems, peaks indicating the presence of unreacted benzoxazines, such as the O-C-N carbon at $\approx$ 80 ppm, were not seen (Table 6.13). These sites being clearly observed in the CP MAS spectra of the monomers (Figure 6.43b). For simplicity only the explicit assignment of Poly-C$_6$ is shown (Figure 6.44). As expected, when comparing the spectra of the different length diamines, the chemical shift, and intensity of the CH$_2$ peak varied with chain length.

Table 6.13: ^{13}C *assignment of linear-diamine based polymers.*

δ_C [ppm]	Poly-C$_{12}$	Poly-C$_6$	Poly-C$_4$	Poly-C$_2$
Ar-OH	157.3	157.5	157.1	156.9
m-Ar	129.4	128.8	129.8	128.6
o-Ar	124.8	123.7	123.7	123.5
p-Ar	119.1	119.2	118.7	119.2
N-CH$_2$	57.0	56.1	58.9	59.1
N-CH$_2$-Ar	54.8	53.9	55.1	56.5
CH$_2$	29.5	28.0	28.7	51.6

Figure 6.44: ^{13}C *assignment of (a) Poly-C$_6$ and (b) its associated monomer.*

6.3.2 Summary

Although the exact chemical structure of the linear-diamine based polymers remains unknown, it has been shown that both N··H‑O and O··H‑O hydrogen bonding were still present, albeit in low concentration. The presence of hydrogen bonding was first suggested by weak shoulders in SPE and DQ filtered spectra. Even with the broad proton line-shapes, 2D DQ correlation spectroscopy confirmed the presence of N··H‑O and O··H‑O hydrogen bonding in some of the polymers. For these systems, high-field solid-state NMR was advantageous, with site resolution strongly influenced by the difference in chemical shifts between aliphatic and aromatic sites. The propensity to form hydrogen bonds was found to correlate with the length of the aliphatic chain separating the two amines. The most likely reason for such a correlation was the increased flexibility imparted to the polymer network. Such flexibility would relieve steric constraints and allow the combination of proton donor and acceptor sites.

It has been shown that the detection of weak hydrogen bonding interactions can also be aided by selective peak suppression, when combined with 2D DQ correlation spectroscopy. Although only of significant advantage when the suppressed signal is significantly stronger than that of the site of interest, for other systems where these criteria are met this method could be of interest.

In general, the strong tendency of small molecules containing the basic benzoxazine unit to form N··H‑O and O··H‑O hydrogen bonds has been extended to polymers. Even if the absolute chemical structure can not be determined, the presence of both N··H‑O and O··H‑O hydrogen bonding and thus supramolecular structure in such systems has been shown.

6.4   A cyclic-diamine polybenzoxazine

A single polybenzoxazine based on the cyclic-diamine piperazine [Chutayothin 01][†] was also studied (Figure 6.45).
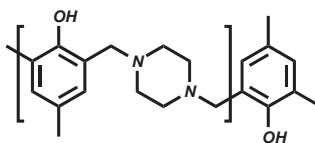
Figure 6.45*: Structure of the cyclic-diamine polybenzoxazine, Poly-P.*

Considering the polymeric nature of this system, relatively narrow proton line-widths were observed indicating low chemical shift distribution and possibly a high degree of order. Upon initial examination resolution in the hydrogen bonding region was also observed suggesting the presence of both N··H-O and O··H-O hydrogen bonds. Unfortunately upon re-examination one year later, and in all subsequent attempts, this resolution was not found to be reproducible. Although the exact reason for such a change was unknown two suggestions can be made. Either absorption of water had disrupted the hydrogen bonding network, or an annealing process had taken place resulting in a structure with less hydrogen bondng. Both of these processes would result in changes in supramolecular structure. The initial state was unable to be recreated by means of recrystallisation, with the process hampered by the small amount of material available (15 mg).

6.4.1   NMR spectroscopy

Proton spectroscopy

In the initial state both N··H-O and O··H-O hydrogen bonding was observed, the N··H-O at 12.1 ppm and the O··H-O existing in two environments at 9.7 and 10.4 ppm (Figure 6.46a). Weak shoulders were also present to the right of both the aromatic and aliphatic peaks in this form, at $\approx$ 5.5 and 1.0 ppm respectively.

Unfortunately, in the current state, evidence for N··H-O hydrogen bonding was no longer found to be present (Figure 6.46b). The O··H-O protons were also only found in one environment at 9.5 ppm, slightly lower than that observed in the initial state. The aromatic protons also had a slightly higher chemical shift of 6.7 ppm, as compared to 6.4 ppm in the initial state. Neither of the weak shoulders were seen in the current state. Such differences were also seen between DQ filtered spectra of the two states (Figure 6.47). In these spectra, as well as the general loss of resolution, a large decrease in aliphatic peak intensity was also seen.

[†]Article [Chutayothin 01] submitted for publication in 2001 but remains hitherto unpublished.
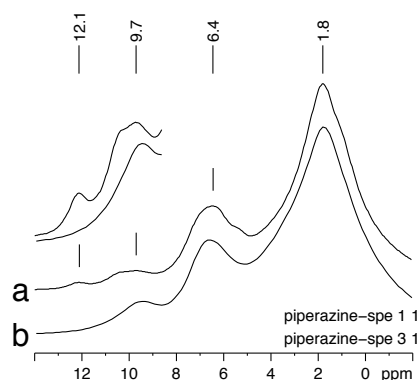
Figure 6.46: *SPE spectra of Poly-P in the (a) initial and (b) current state.*
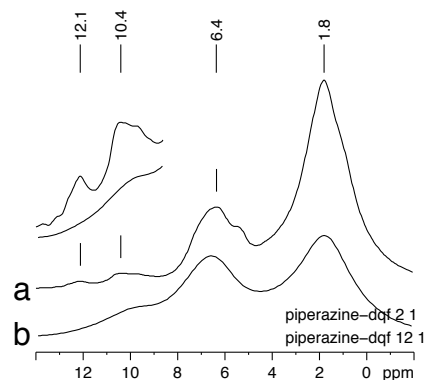
Figure 6.47: *DQ filtered spectra of Poly-P in the (a) initial and (b) current state.* $\tau_{exc/rec} = 2 \cdot \tau_r$

The difference between the two states was most clearly illustrated by 2D DQ correlation spectroscopy (Figure 6.48:a–b). In the initial state the DQ spectra bore a close resemblance to that of the model dimers previously encountered. The resolved DQC between N··H-O and O··H-O protons clearly indicated the close proximity of these two hydrogen bonding sites. In contrast, only broad nondescript peaks, similar to that seen for the linear-diamine polymers (Section 6.3), were observed in the current state. Considering the possible amorphous nature of the polymeric material the latter form would be more expected due to chemical shift distribution. It is thus suggested that a higher degree of order was present in the initial state of Poly-P.
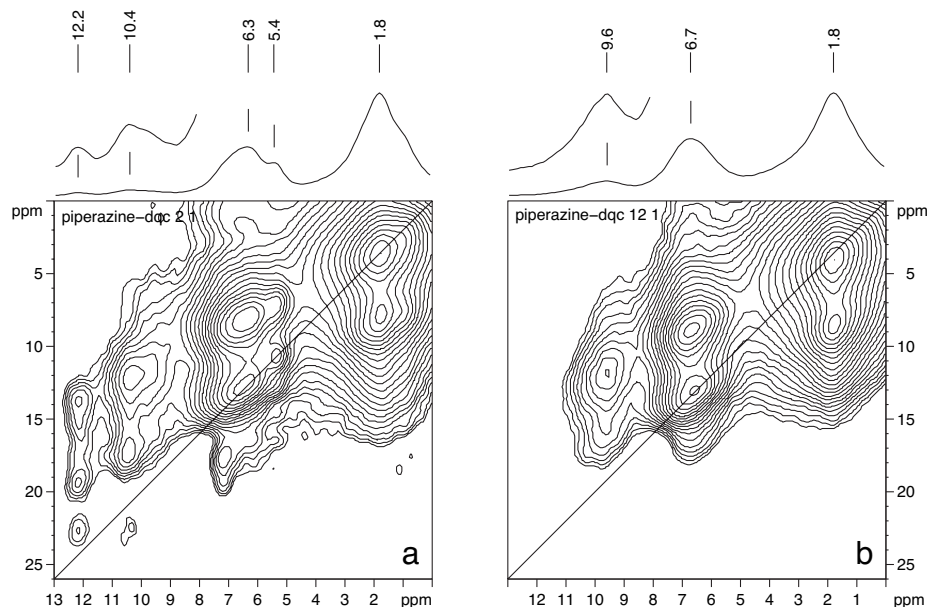
Figure 6.48: *DQ spectra of Poly-P in the (a) initial and (b) current state:* $\tau_{exc/rec} = 2 \cdot \tau_r$

Considering the 2:1 ratio of amine proton acceptors to hydroxyl proton-donors per monomer unit, the O··H-O hydrogen bond was formed in favour of two possible N··H-O hydrogen bonds. The close proximity of the N··H-O and O··H-O protons,

as seen by the DQ spectrum of the initial state, also suggested that both O··H-O and N··H-O hydrogen bonds shared a common oxygen atom. Due to steric constraints the O··H-O interaction was most likely intermolecular in nature (Figure 6.49). With only evidence for O··H-O hydrogen bonding in the current state of Poly-P it is thought that only intermolecular O··H-O hydrogen bonding occurs (Figure 6.50).
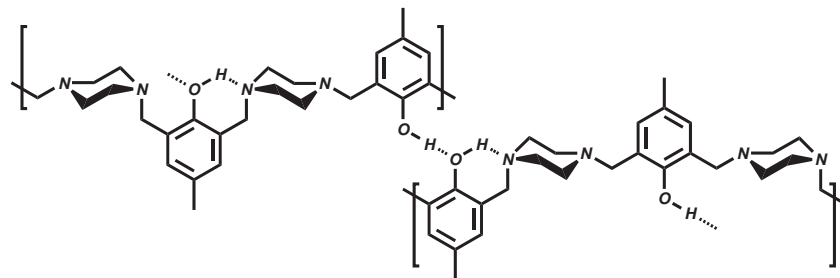
Figure 6.49: *Possible hydrogen bonding in Poly-P: initial state N··H-O and O··H-O protons in close proximity.*
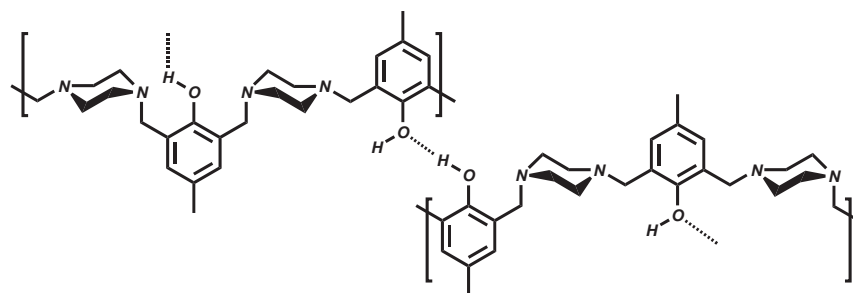
Figure 6.50: *Possible hydrogen bonding in Poly-P: current state only O··H-O hydrogen bonding present.*

Hetronuclear spectroscopy

Coherent polarisation transfer was only possible for the initial state of Poly-P, with broad lines observed indicative of the polymeric nature of the material. With longer recoupling times the aromatic C-OH sites were seen at 153.3 ppm (Figure 6.51).
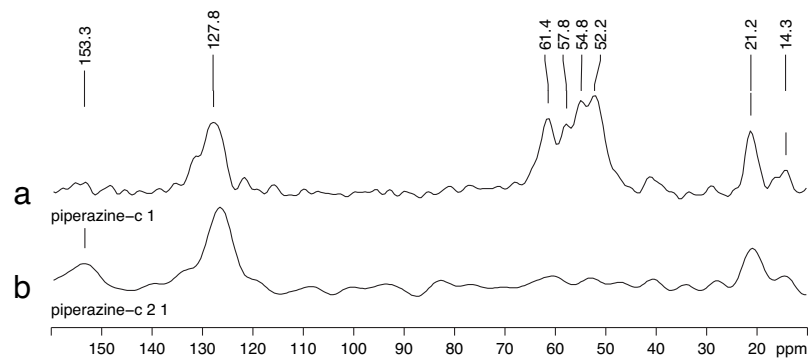
Figure 6.51: $^{13}C-^{1}H$ REPT spectra of Poly-P in the initial state: (a) $\tau_{exc/rec} = 1 \cdot \tau_r$ and (b) $4 \cdot \tau_r$.

As well at the broad aromatic peak at 128 ppm and the para-methyl ring-substituent at 21 ppm, four different CH$_2$ peaks between 52–62 ppm were present. The bridging CH$_2$ groups were assigned to the 52–55 ppm peaks and the 57–62 ppm sites to the CH$_2$ groups of piperazine (Figure 6.52). For both types of CH$_2$ carbons crystallographic inequivalence was seen with $\Delta\delta_c$ between 2.6–3.6 ppm, the larger difference seen for the piperazine sites. With all piperazine CH$_2$ sites chemically equivalent, inequivalent sites were assigned based on the 'chair'-conformation of piperazine (Figure 6.52a). Other structural moieties possible for Poly-P may also be assigned from the weak peaks observed in the carbon spectra (Figure 6.52b–d).
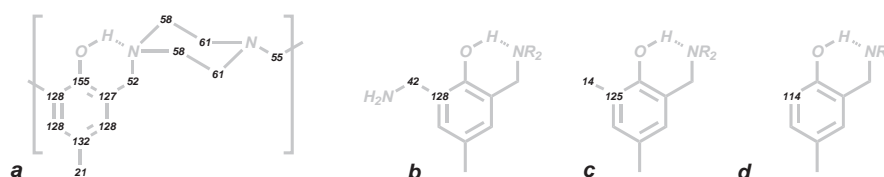
Figure 6.52: ^{13}C assignment of (a) inequivalent CH$_2$ sites and (b–d) less abundante sites of Poly-P.

Unfortunately, heteronuclear correlation spectra were only recorded with a single rotor period of recoupling for the initial state, thus correlation was only seen between directly bound ^1H–^{13}C spin pairs (Figure 6.53). Due to this, little structural information was gained about Poly-P form carbon spectroscopy.
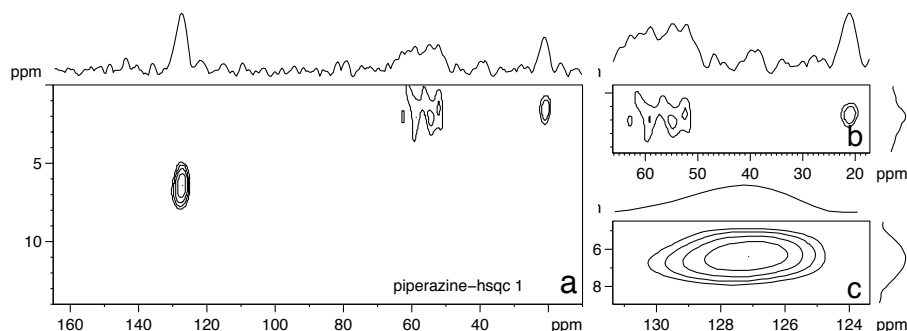
Figure 6.53: ^{13}C–^1HREPT-HSQC spectrum of Poly-P in the initial state with $\tau_{exc/rec} = 1 \cdot \tau_r$: (a) full, (b) aliphatic and (c) aromatic regions.

6.4.2 Summary

Upon initial examination, both N··H-O and O··H-O hydrogen bonding were observed in a polymer based on the cyclic-dimaine piperazine, and thus showed evidence for a highly ordered state. However, upon re-examination at a later date evidence for this state was no-longer present, indicating instability of the supramolecular structure. In contrast to other polybenzoxazines only the weaker O··H-O hydrogen bonding was found to remain [Kim 02]. With limited sample available, and all efforts to regenerate the initial state unsuccessful, further understanding of the processes which lead to such a change was unable to be made.

6.5 Conclusions

In this chapter, it has been shown that hydrogen bonding plays an important role in the structure of many other compounds related to polybenzoxazines, and was not just limited to the model dimers and oligomers of Chapter 4 and Chapter 5.

The hydrogen bonding in Me,Me-N-Ph was shown to be similar to that of Me,Me-N-Me, with the implication that the compound exists in a similar mostly-dimeric supramolecular structure. Heteronuclear spectroscopy also provided strong evidence for a highly ordered state. No evidence of π··H-O interactions were seen for this system as previously suggested by FT-IR [Kim 02, Kim 03b].

The stability of the intramolecular N··H-O hydrogen bond was further illustrated by the asymmetric dimers N-Bz-N-Cy and N-Bz-N-^{t}Bu. For both asymmetric systems relatively strong N··H-O hydrogen bonding was seen, confirming the known stability of the six-memebered ring formed. The strengthening of the N··H-O hydrogen bond was also suggested by the addition of bulky amine-substituents, such as the tertiarybutyl group. The appearance of a strongly deshielded aromatic proton, similar in chemical shift to that of an O··H-O proton, was observed. The higher than expected chemical shift of these sites was rationalised by the combined influence of two sets of aromatic ring currents. As suggested by FT-IR no evidence for O··H-O hydrogen bonding was observed [Kim 03b].

The relevance of the model polybenzoxazines to polymers was demonstrated, with both linear- and cyclic-diamine based polybenzoxazine showing evidence of hydrogen bonding. Both N··H-O and O··H-O hydrogen bonding were seen for some linear-diamine systems. Polymers containing longer aliphatic chains separating the amine groups were found to have a higher likelihood of hydrogen bond formation. The cyclic-diamine system was found to initially exist in a highly ordered state, with both N··H-O and O··H-O hydrogen bonding present. However, over time this system was found to revert to a disordered state with only O··H-O hydrogen bonding present.

In general, through the examination of both small molecule models for polybenzoxazines, and macromolecular polybenzoxazines themselves, information regarding the hydrogen bonding ability of polybenzoxazines was gained.

Chapter 7

Summary & Conclusions

It has been shown that, as with the symmetric Me,Me dimers examined by Schnell *et al.* [Schnell 98a], both the H,Me and H,Et mono ring-substituted systems, as well as the N-Cy symmetric dimers, also posses cooperative hydrogen bonding. Proton solid-state NMR spectroscopy suggested the presence of both intramolecular N··H-O and intermolecular O··H-O hydrogen bonding (Figure 7.1).
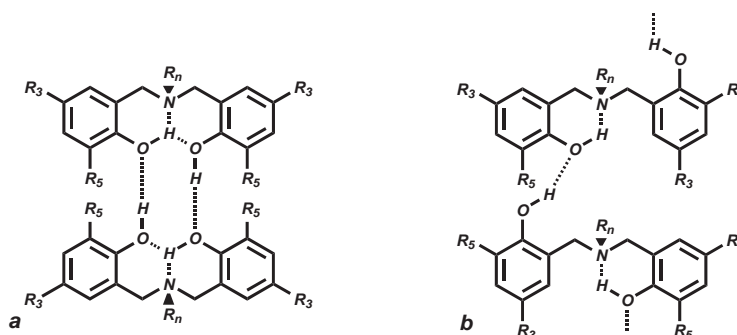
Figure 7.1: The (a) dimeric and (b) continuous hydrogen bonding structure of the dimers [Schnell 98a].

For Me,Me-N-Cy and all other mono ring-substituted dimers the presence of the continuous hydrogen bonding structure was suggested by proton DQ correlation spectroscopy (Figures 7.2–7.4). With the majority of these characteristic DQCs weak in nature polymorphism was suggested, the dimeric hydrogen bonding structure being the more prevalent. In contrast to the findings of Schnell *et al.* Me,Me-N-Et was found to mostly adopt the dimeric hydrogen bonding structure, with only weak indications of the continuous structure found. Despite this, the strongest evidence for polymorphism was observed for Me,Me-N-Et, with two amine sites observed by ^{15}N spectroscopy.
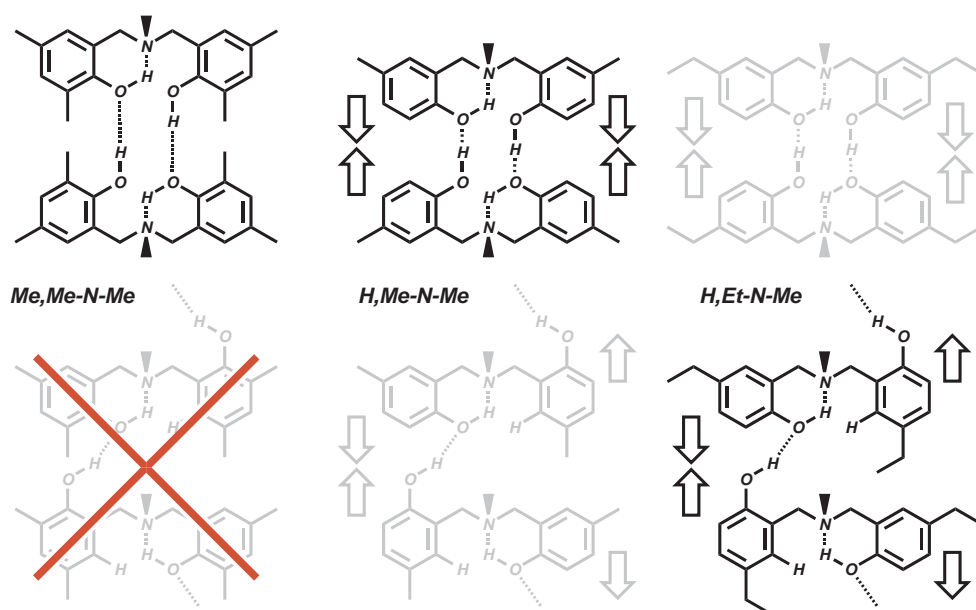
Figure 7.2: Suspected structures of the N‑Me dimers. Less dominant forms shown in grey.
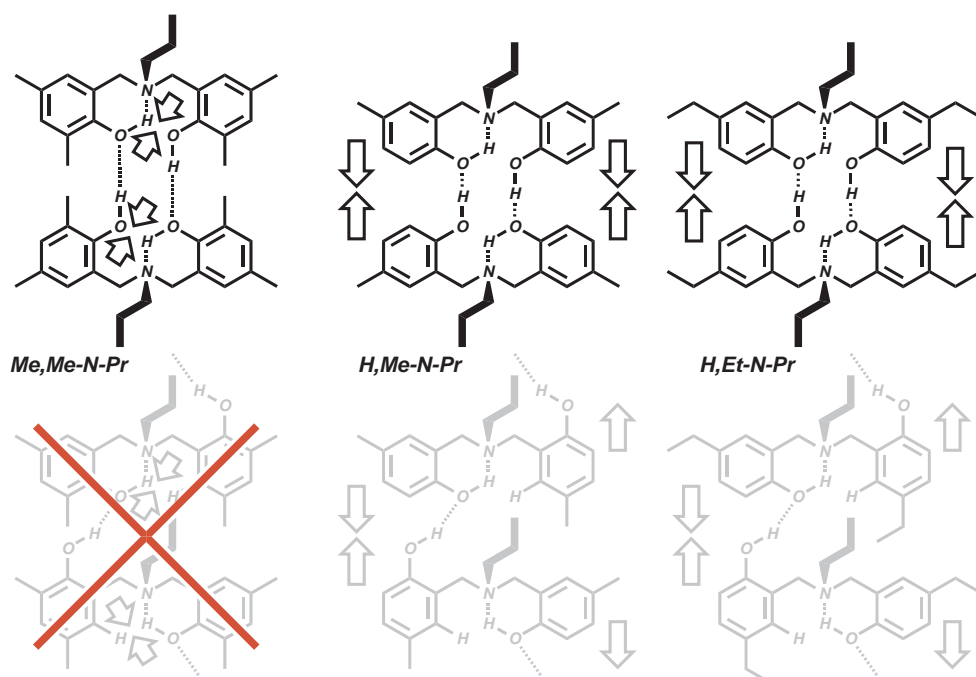
Figure 7.3: Suspected structures of the N‑Pr dimers. Less dominant forms shown in grey.

Ab-initio chemical shift calculations of H,Me‑N‑Cy showed that, even in the dimeric hydrogen bonding structure, aromatic protons could also come into close proximity with the N··H‑O protons. Furthermore, this intermolecular interaction was between the aromatic protons in the 5 positions of the aromatic rings, with such sites only found in the mono ring-substituted dimers. Very good agreement was seen between experimental and calculated proton SPE spectra for H,Me‑N‑Cy and suggested a
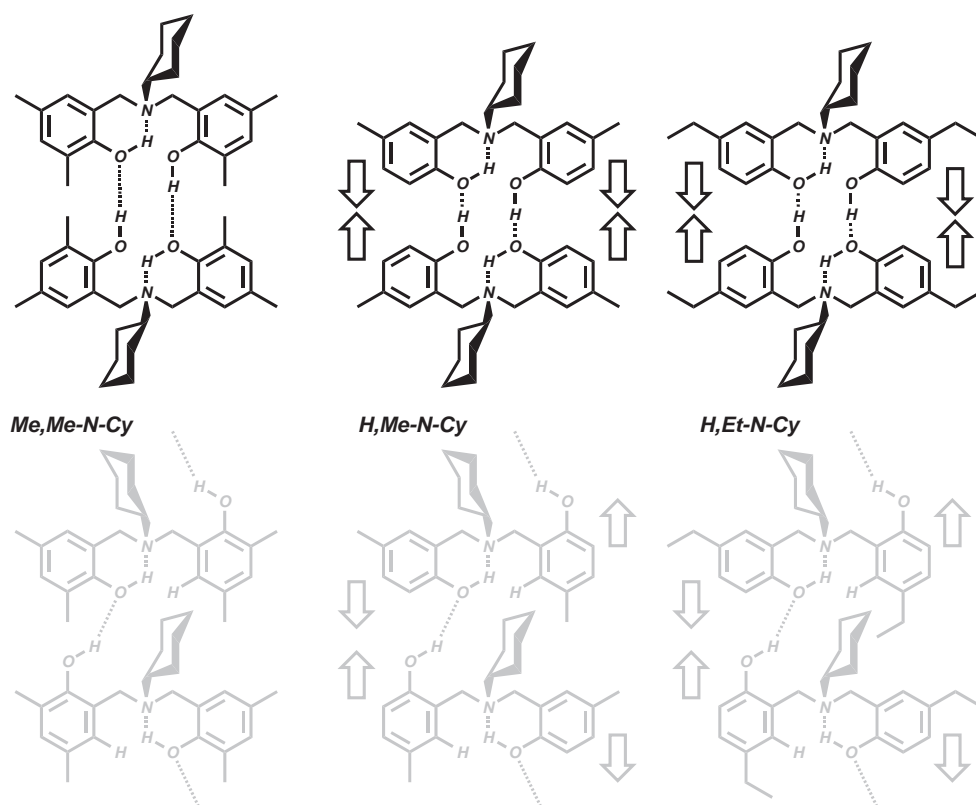
***Figure 7.4**: Suspected structures of the N-Cy dimers. Less dominant forms shown in grey.*

supramolecular structure similar to that of the crystal structure. This placed doubt over the assignment of the continuous hydrogen bonding structure based solely on the DQ correlation between aromatic and N··H-O protons.

Despite FT-IR suggesting intramolecular π··H-O interactions in Me,Me-N-Ph, evidence for such non-classical hydrogen bonding was not found. However, shielding interactions were seen for a number of other systems, thus suggesting their close proximity to the 'face' of an aromatic system. The sites experiencing these interactions were assigned to the flexible terminal methyl groups of the ethyl ring-substituents (H,Et systems) and propyl amine-substituents (N-Pr systems) by ^{13}C–^{1}H HSQC spectroscopy. The crystal structure of H,Me-N-Cy also indicated an intermolecular origin for these interactions.

The intra- and intermolecular nature of hydrogen bonds was studied using the asymmetric dimers, N-Bz-N-Cy and N-Bz-N-^{t}Bu. For both asymmetric systems relatively strong intramolecular N··H-O hydrogen bonding was seen, thus confirming the stability imparted by the formation of a six-membered ring. The strengthening of the N··H-O hydrogen bond was suggested by the addition of bulky amine-substituents. Strongly deshielded aromatic protons, similar in chemical shift to that of O··H-O protons, were also observed for N-Bz-N-^{t}Bu. The higher than expected chemical shift thought to be due to the combined influence of two aromatic rings.

The effects of amine-substituents were further investigated on model trimers, with the cyclic hydrogen bonding structure for the N-Me trimer confirmed. However, from initial investigation the N-Et trimer showed little sign of adopting a similar cyclic structure. Significant differences in both strength and concentration of the two N··H-O hydrogen bonds were seen between the trimers (Figure 7.5).
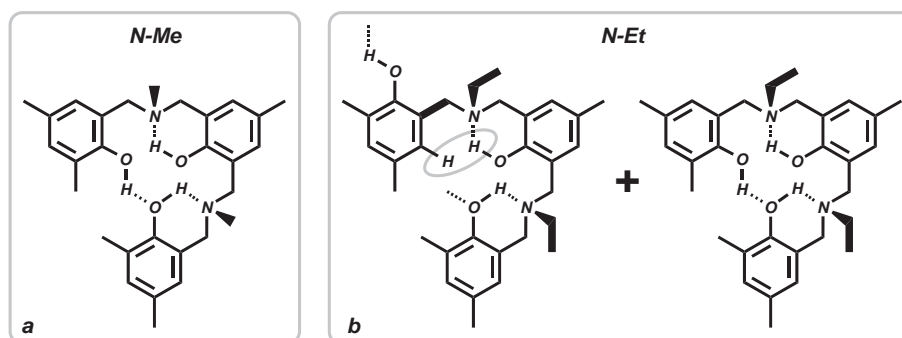
Figure 7.5: Suggested structures of the (a) methyl and (b) ethyl trimers.

The relevance of the model polybenzoxazines to polymers was demonstrated by the observation of hydrogen bonding in both linear- and cyclic-diamine based polybenzoxazine. Linear-diamine based polymers with longer aliphatic chains separating the two amine groups were found to have a higher likelihood of hydrogen bond formation. For these systems both N··H-O and O··H-O hydrogen bonding was seen in relatively low concentrations. Similarly both N··H-O and O··H-O hydrogen bonding was also observed in a cyclic-diamine polybenzoxazine. Although this system was initially present in a highly ordered state, over time it was found to revert to a more disordered state containing only O··H-O hydrogen bonding.

Through the examination of both small-molecule models for polybenzoxazines, as well as polybenzoxazines themselves, proton solid-state NMR has been shown to provide great insight into the hydrogen bonding present within these systems. The combination of solid-state NMR and electronic structure methods combined with chemical shift calculations has also been shown to be a powerful tool for structure elucidation.

All systems examined have been shown to have a high propensity to form both N··H-O and O··H-O hydrogen bonds where possible. The general chemical structure has been shown to not only support strong intramolecular N··H-O hydrogen-bonding, due to 6-membered ring formation, but also impart great flexibility. This flexibility being manifested in the multiple supramolecular structures observed for most of the model systems. Such flexible, strong and abundant hydrogen bonding reinforces the suggestion that the desirable materials properties of polybenzoxazines are due to co-operative hydrogen bonding within the polymer network.

Appendix A

Wigner rotation matrices

For a rotation about an arbitrary angle Ω the elements of the Wigner rotation matrices $\mathcal{D}_{m'm}^{(L)}(\Omega)$ may be given with respect to the Euler angles (α, β, γ) as:

$$\mathcal{D}_{m'm}^{(L)}(\alpha, \beta, \gamma) = d_{m'm}^{(L)}(\beta)\, e^{-im'\alpha}\, e^{-im\gamma} \tag{A.1}$$

where $d_{m'm}^{(L)}(\beta)$ are the so-called reduced matrix elements given by:

$d_{m'm}^{(1)}$		m		
		1	0	-1
	1	$\frac{1}{2}(1 + \cos\beta)$	$-\frac{1}{\sqrt{2}}\sin\beta$	$\frac{1}{2}(1 - \cos\beta)$
m'	0	$\frac{1}{\sqrt{2}}\sin\beta$	$\cos\beta$	$-\frac{1}{\sqrt{2}}\sin\beta$
	-1	$\frac{1}{2}(1 - \cos\beta)$	$\frac{1}{\sqrt{2}}\sin\beta$	$\frac{1}{2}(1 + \cos\beta)$

$d_{m'm}^{(2)}$		m				
		2	1	0	-1	-2
	2	$\frac{1}{4}(1 + \cos\beta)^2$	$-\frac{1}{2}(1 + \cos\beta)\sin\beta$	$\sqrt{\frac{3}{8}}\sin^2\beta$	$-\frac{1}{2}(1 - \cos\beta)\sin\beta$	$\frac{1}{4}(1 - \cos\beta)^2$
	1	$\frac{1}{2}(1 + \cos\beta)\sin\beta$	$\cos^2\beta - \frac{1}{2}(1 - \cos\beta)$	$-\sqrt{\frac{3}{8}}\sin 2\beta$	$-\cos^2\beta + \frac{1}{2}(1 + \cos\beta)$	$-\frac{1}{2}(1 - \cos\beta)\sin\beta$
m'	0	$\sqrt{\frac{3}{8}}\sin^2\beta$	$\sqrt{\frac{3}{8}}\sin 2\beta$	$\frac{1}{2}(3\cos^2\beta - 1)$	$-\sqrt{\frac{3}{8}}\sin 2\beta$	$\sqrt{\frac{3}{8}}\sin^2\beta$
	-1	$\frac{1}{2}(1 - \cos\beta)\sin\beta$	$-\cos^2\beta + \frac{1}{2}(1 + \cos\beta)$	$\sqrt{\frac{3}{8}}\sin 2\beta$	$\cos^2\beta - \frac{1}{2}(1 - \cos\beta)$	$-\frac{1}{2}(1 + \cos\beta)\sin\beta$
	-2	$\frac{1}{4}(1 - \cos\beta)^2$	$\frac{1}{2}(1 - \cos\beta)\sin\beta$	$\sqrt{\frac{3}{8}}\sin^2\beta$	$\frac{1}{2}(1 + \cos\beta)\sin\beta$	$\frac{1}{4}(1 + \cos\beta)^2$

Appendix B

Experimental

B.1 Solid-state NMR hardware

Solid-state NMR was undertaken using a number of dedicated solid-state spectrometers located at Imperial College (IC) London[†], UK, the Max Planck Institute for Polymer Research[‡] (MPIP) Mainz, Germany, and the National Institute of Chemical Physics and Biophysics[§] (NICPB), Tallinn, Estonia. All experiments were carried out on Bruker Avance digital spectrometers. The individual spectrometers, their associated magnets and important Larmor frequencies are summarised in Table B.1.

Table B.1: *Dedicated solid-state NMR Bruker spectrometers used.*

Spectrometer	location	B_0 [T]	bore	ν_{1_H}	ν_{13_C}	ν_{15_N}
Avance 700	MPIP	16.4	narrow	700.13	176.05	70.94
Avance 600	IC	14.7	narrow	600.13	150.91	60.81
Avance 600	NICPB	14.7	narrow	600.16	150.91	60.81
Avance 300	MPIP	7.0	wide	300.23	75.49	30.42

All experiments were undertaken under MAS, unless otherwise stated. For $\omega_r/2\pi < 25$–35 kHz commercial Bruker double-air-bearing probeheads were used with 2.5 mm outer diameter zirconia (ZrO_2) rotors and Vespel® caps. The PFG assisted solid-state NMR experiments were undertaken using a modified 2.5 mm MAS Bruker probehead (MPIP), with the magic-angle field gradient coils wound around each end of the stator. A home-built probehead of the Samoson group (NICP) was used for Fast-MAS $\omega_r/2\pi > 35$ kHz experiments utilising 2 mm outer diameter zirconia rotors. All NMR experiments measured under MAS conditions of $\omega_r/2\pi > 35$ kHz were undertaken at the NICPB by Oivo Manninen of the Samoson research group.

[†]previously known as Imperial College of Science, Technology and Medicine (ICSTM)
[‡]also known as the Max-Planck-Institut für Polymerforschung (MPIP)
[§]also known as the Keemilise ja Bioloogilise Füüsika Instituut (KBFI)

The natural abundance measurements of Chapter 6 were carried out on the DSX300 spectrometer. A commercial Bruker double-air bearing probehead was used for all experiments with 7 mm outer diameter zirconia rotors and Kel-F$^\circledR$ caps. For all measurements $\omega_r/2\pi = 3$ kHz.

The effects of MAS upon sample temperature were not accounted for with all MAS experiments regulated at 300 K. The combination of frictional heating and decompression cooling during MAS have been previously studied [Grey 93, Vanmoorsel 95, Grimmer 97, Köhler 97]. These have a more pronounced effect at higher MAS frequencies [Langer 99]. Under typical experimental conditions used for ¹H solid-state NMR (MAS $\omega_r/2\pi = 30$ kHz, bearing gas pressure of 3600 mBar and drive gas pressure of 1600 mBar) previous temperature calibration for the probeheads used showed the sample temperature to be $\approx 30°$C higher than that of the gas exiting the stator used for temperature monitoring and regulation. Thus the actual sample temperature was thought to be ≈ 330 K or $\approx 57°$C. Previously it has been shown that temperature affected the absolute intensity of the ¹H resonances associated with N··H-O and O··H-O sites in benzoxazine dimers [Schnell 98a] Despite this no change in chemical shift or phase were seen until melting. With the melting points of all systems typically over 100°C (Tables 4.2 and 5.1) the temperature effects of MAS were neglected for reasons of simplicity.

Due to the higher resolution gained at high B_0 fields in dipolar broadened systems, the majority of ¹H solid-state spectra presented in this thesis was acquired on the Avance 700 (MPIP). Similar conclusions could, in most cases, be drawn from the data acquired on the Avance 600 (IC and NICPB).

B.2   Solid-state NMR methodology

The magic angle on all solid-state NMR probeheads was adjusted using the ^{79}Br resonance of KBr under slow MAS (≈ 1 kHz). Upon more accurate adjustment of the magic-angle the weak quadrupolar coupling of ^{79}Br was more accurately refocussed by MAS resulting in more intense rotor echoes after multiple rotor periods. Thus by striving to achieve the observation of higher order spinning-sidebands in the spectrum accurate adjustment of the magic-angle was achieved. Magic-angle adjustment was typically undertaken when a rotor was unable to be ejected and the probehead had to be stripped down, whenever the stator was physically touched or if lower than expected resolution was obtained.

Probehead shimming was undertaken on water before each block of measurement, optimising the shim for the maximum integral of the FID in the time domain, and cross checking the full-width half maximum and peak symmetry in the frequency domain.

Resonance frequency tuning and impedance matching of the probehead was undertaken for each sample at desired MAS frequency, after a period of 5-15 min to allow thermal equilibration of probehead electronics.

Typically 5, 2.5 and 1 μs $\frac{\pi}{2}$ pulses were used on the 7, 2.5 and 2 mm probeheads, corresponding to $\mathbf{B}_1$ fields equivalent to nutation frequencies of 50, 100 and 250 kHz respectively. The power-level required for such nutation pulses was calibrated using the 2π and 4π null points in spectral intensity. Proton power-levels were calibrated on the sample, whereas a ^{13}C labelled *l*-alanine sample was used for carbon power-level determination, and the ^{15}N labelled Me,Me-^{15}N-Me sample used for nitrogen.

Heteronuclear proton decoupling was typically undertaken using the TPPM method, however little difference in decoupling efficiency was seen betweenTPPM and CW decoupling for the systems investigated.

Calibration of the chemical-shift axis was achieved using the external referencing method. The reference compounds and chemical shifts of the various nuclei investigated are summarised in Table B.2.

Table B.2: Compounds used for external chemical-shift referencing.

nucli	compound	site	δ [ppm]
^{1}H	tetrakis-trimethylsilane (TKS)	Si(SiC**H**$_3$)$_4$	0.0
^{13}C	*l*-alanine	NH$_3$**C**HCH$_3$COOH	51.0
^{15}N	ammonium nitrate	**N**H$_4$NO$_3$	0.0

Pulse programs used are explicitly given for Bruker spectrometers in Appendix C and simulation routines used explicitly given for Mathematica in Appendix D.

B.3 Ab-initio electronic structure methods

Ab-initio electronic structure calculations were carried out by Dr Daniel Sebastani and Maxim Zacharov[†] at the MPIP. Calculations were performed in the framework of density functional theory with the BLYP exchange correlation function [Becke 88] using Gaussian98 [Frisch 98] and CPMD [Hutter 95] computer code. A more detailed theoretical description is given in Appendix E.

Specifically, after initial geometry optimisation by MM2 molecular-mechanics the geometry was refined by the PMW1PWG1/6-31G(d,p) ab-initio method. From the final final optimised geometry NMR parameters were calculated using the B3LYP/6-31(d,p) ab-initio method.

With the number of atoms needing to be simulated ranging from 62 (Me,Me-(N-Me)$_2$) to 120 (Me,Me-N-Cy) between 24–48 hours of continuous computation was needed per simulation on a 32 processor 16 node Linux cluster.

[†]currently at the University of Frankfurt, Germany

Appendix C

Pulse Programs

C.1 Homonuclear 1D

C.1.1 SPE

```
1 ze
2 d1
  p1 ph1
  go=2 ph31
  20m wr #0
exit

ph1    =0 2 1 3
ph31   =3 1 0 2
```

C.1.2 Hahn echo

```
"d2=1s*l1/cnst31-p1/2-p2/2"
"d3=1s*l1/cnst31-p2/2-de"
"p2=2*p1"

1 ze
2 d1
  p1 ph1
  d2
  p2 ph2
  d3
  go=2 ph31
  wr #0
exit

ph1 = 0 0 0 0 1 1 1 1 2 2 2 2 3 3 3 3
ph2 = 0 2 1 3 1 3 2 0 2 0 3 1 3 1 0 2
ph31= 0 0 2 2 1 1 3 3 2 2 0 0 3 3 1 1
```

C.1.3 Solid echo

```
"d2=1s*l1/cnst31-p1/2-p2/2"
"d3=1s*l1/cnst31-p2/2-de"
"p2=p1"

1 ze
2 d1
  p1 ph1
  d2
  p2 ph2
  d3
  go=2 ph31
  wr #0
exit

ph0 = 0
ph1 = 0 3 2 1 0 3 2 1
ph2 = 3 2 1 0 1 0 3 2
ph31= 3 2 1 0 3 2 1 0
```

C.1.4 SPE watergate

```
"p2=p1"
"d3=cnst30*((1s/cnst31)/2)"
"cnst29=cnst31/(2*cnst30)"
"d31=1s/cnst29"

1 ze
  d31
2 d1 pl1:f1
  2u fq=cnst10:f1
  p1 ph1
  d17 fq=cnst11:f1
  GRADIENT(cnst21)
  d16 ;pl3:f1
  p2*0.231 ph3
  d3*2
  p2*0.692 ph3
  d3*2
  p2*1.462 ph3
  d3*2
  p2*1.462 ph4
  d3*2
```

```
   p2*0.692 ph4
   d3*2
   p3*0.231 ph4
   d16 fq=cnst10:f1
   GRADIENT(cnst22)
   d17  pl1:f1
   go=2 ph31
   wr #0
exit

ph1=0 2
ph3=0 0 1 1 2 2 3 3
ph4=2 2 3 3 0 0 1 1
ph31=0 2 2 0
```

C.1.5   DQF BABA

```
"d3=1s/(cnst31*2)-p1*2"
"d6=cnst30*(1s/cnst31)"

1 ze
2 d1

3 p1 ph0
   d3
   p1 ph0
   p1 ph1
   d3
   p1 ph3

   p1 ph0
   d3
   p1 ph0
   p1 ph3
   d3
   p1 ph1

   p1 ph2
   d3
   p1 ph2
   p1 ph3
   d3
   p1 ph1

   p1 ph2
   d3
   p1 ph2
   p1 ph1
   d3
   p1 ph3

4 p1 ph10
   d3
   p1 ph10
   p1 ph11
   d3
   p1 ph13

   p1 ph10
   d3
   p1 ph10
   p1 ph13
```

```
   d3
   p1 ph11

   p1 ph12
   d3
   p1 ph12
   p1 ph13
   d3
   p1 ph11

   p1 ph12
   d3
   p1 ph12
   p1 ph11
   d3
   p1 ph13

   d6

   p1 ph30
   go=2 ph31
   wr #0
exit

ph0 = (8) 0 2 4 6
ph1 = (8) 2 4 6 0
ph2 = (8) 4 6 0 2
ph3 = (8) 6 0 2 4
ph10= 0
ph11= 1
ph12= 2
ph13= 3
ph30= 0 2 0 2 1 3 1 3 2 0 2 0 3 1 3 1
ph31= 0 0 0 0 1 1 1 1 2 2 2 2 3 3 3 3
```

C.1.6   Homonuclear Pseudo 2D

C.1.7   Inversion recovery

```
"p2=2*p1"
1 ze
2 d1
   p2 ph1
   vd
   p1 ph2
   go=2 ph31
   20m wr #0 if #0 ivd zd
   lo to 2 times td1
exit

ph1 = 0 2 0 2
ph2 = 0 1 2 3
ph31= 0 1 2 3
```

C.1.8 Saturation recovery

```
1 ze
2 d1
  10u pl1:f1
3 (p1 ph20^):f1
  13m
  (p1 ph21^):f1
  7m
  (p1 ph22^):f1
  1m
  (p1 ph23^):f1
  3m
  lo to 3 times 2
  vd
  (p1 ph1):f1
  go=2 ph31
  1m wr #0 if #0 ivd zd
  lo to 2 times td1
exit

ph1= 0 1 2 3
ph20= 0 1 2 3
ph21= 1 2 3 0
ph22= 2 3 0 1
ph23= 3 0 1 2
ph31= 0 1 2 3
```

C.2   Homonuclear 2D

C.2.1   dipolar-exchange

```
"l30=(cnst31/cnst31)*td1/2"

1 ze
2 d1 pl1:f1
3 p1 ph1
  d0
  p1 ph2
  d6
  p1 ph3
  go=2 ph31
  30m wr #0 if #0
  zd
  ip1
  lo to 2 times 2
  id0
  lo to 2 times l30
exit

ph1 = 0 2 0 2  0 2 0 2  1 3 1 3  1 3 1 3
ph2 = 0 0 0 0  0 0 0 0  1 1 1 1  1 1 1 1
      2 2 2 2  2 2 2 2  3 3 3 3  3 3 3 3
ph3 = 0 0 2 2  1 1 3 3
ph31= 0 2 2 0  1 3 3 1  0 2 2 0  1 3 3 1
      2 0 0 2  3 1 1 3  2 0 0 2  3 1 1 3
```

C.2.2   DQ BABA

```
"d3=1s/(cnst31*2)-p1*2"
"l30=td1/2"
"d8=1s/cnst31"


1 ze
2 d1

  p1 ph0
  d3
  p1 ph0
  p1 ph1
  d3
  p1 ph3

  p1 ph0
  d3
  p1 ph0
  p1 ph3
  d3
  p1 ph1

  p1 ph2
  d3
  p1 ph2
  p1 ph3
  d3
  p1 ph1

  p1 ph2
  d3
  p1 ph2
  p1 ph1
  d3
  p1 ph3
  d0        ;t1
  p1 ph10
  d3
  p1 ph10
  p1 ph11
  d3
  p1 ph13

  p1 ph10
  d3
  p1 ph10
  p1 ph13
  d3
  p1 ph11

  p1 ph12
  d3
  p1 ph12
  p1 ph13
  d3
  p1 ph11

  p1 ph12
  d3
  p1 ph12
  p1 ph11
  d3
  p1 ph13
```

```
3 d8
  lo to 3 times l1
  p1 ph30
  go=2 ph31
  100m wr #0 if #0
  1m zd
  1m ip0
  1m ip1
  1m ip2
  1m ip3
  lo to 2 times 2
  1m id0
  lo to 2 times l30

exit

ph0 = (8) 0 2 4 6
ph1 = (8) 2 4 6 0
ph2 = (8) 4 6 0 2
ph3 = (8) 6 0 2 4
ph10= 0
ph11= 1
ph12= 2
ph13= 3
ph30= 0 0 0 0 1 1 1 1 2 2 2 2 3 3 3 3
ph31= 0 2 0 2 1 3 1 3 2 0 2 0 3 1 3 1
```

C.2.3   TQ BABA

```
"d5=(1s/(cnst31))*cnst30"
"d3=1s/(cnst31*2)-p1*2"
"l30=td1/2"

1 ze
2 d1
  p1 ph1

3 p1 ph0
  d3
  p1 ph0
  p1 ph1
  d3
  p1 ph3

  p1 ph0
  d3
  p1 ph0
  p1 ph3
  d3
  p1 ph1

  p1 ph2
  d3
  p1 ph2
  p1 ph3
  d3
  p1 ph1

  p1 ph2
  d3
  p1 ph2
```

```
  p1 ph1
  d3
  p1 ph3
  lo to 3 times l1
  d0

4 p1 ph10
  d3
  p1 ph10
  p1 ph11
  d3
  p1 ph13

  p1 ph10
  d3
  p1 ph10
  p1 ph13
  d3
  p1 ph11

  p1 ph12
  d3
  p1 ph12
  p1 ph13
  d3
  p1 ph11

  p1 ph12
  d3
  p1 ph12
  p1 ph11
  d3
  p1 ph13
  lo to 4 times l1

  p1 ph13
  d5
  p1 ph30
  go=2 ph31
  100m wr #0 if #0
  zd
  ip0
  ip1
  ip2
  ip3
  lo to 2 times 2
  id0
  lo to 2 times l30
exit

ph0 = (12) 0 2 4 6 8 10
ph1 = (12) 3 5 7 9 11 1
ph2 = (12) 6 8 10 0 2 4
ph3 = (12) 9 11 1 3 5 7
ph10= 0
ph11= 1
ph12= 2
ph13= 3
ph30= 0 2 0 2 0 2 1 3 1 3 1 3
      2 0 2 0 2 0 3 1 3 1 3 1
ph31= 0 0 0 0 0 0 1 1 1 1 1 1
      2 2 2 2 2 2 3 3 3 3 3 3
```

C.2.4 DQ BABA Watergate

```
"p2=p1"
"d3=1s/(cnst31*2)-p1*2"
"l30=td1/2"
"d8=1s/cnst31"
"d4=cnst30*((1s/cnst31)/2)"


1 ze
2 d1 pl1:f1
  2u fq=cnst10:f1

  p1 ph0
  d3
  p1 ph0
  p1 ph1
  d3
  p1 ph3

  p1 ph0
  d3
  p1 ph0
  p1 ph3
  d3
  p1 ph1
  d0        ;t1
  p1 ph10
  d3
  p1 ph10
  p1 ph11
  d3
  p1 ph13

  p1 ph10
  d3
  p1 ph10
  p1 ph13
  d3
  p1 ph11
6 d8
  lo to 6 times l1
  p1 ph30

  d17 fq=cnst11:f1 ;Wgate
  GRADIENT(cnst21)
  d16 pl18:f1
  p2*0.231 ph6
  d4*2
  p2*0.692 ph6
  d4*2
  p2*1.462 ph6
  d4*2
  p2*1.462 ph7
  d4*2
  p2*0.692 ph7
  d4*2
  p3*0.231 ph7
  d16
  GRADIENT(cnst22)
  d17 fq=cnst10:f1
  go=2 ph31
  50m wr #0 if #0
  zd
  ip0
```

```
  ip1
  ip2
  ip3
  lo to 2 times 2
  id0
  lo to 2 times l30
exit


ph0 = (8) 0 2 4 6
ph1 = (8) 2 4 6 0
ph2 = (8) 4 6 0 2
ph3 = (8) 6 0 2 4
ph6 = 0 0 0 0 1 1 1 1 2 2 2 2 3 3 3 3
ph7 = 2 2 2 2 3 3 3 3 0 0 0 0 1 1 1 1
ph10= 0
ph11= 1
ph12= 2
ph13= 3
ph30= 0 0 0 0 1 1 1 1 2 2 2 2 3 3 3 3
ph31= 0 2 0 2 1 3 1 3 2 0 2 0 3 1 3 1
```

C.3 Heteronuclear 1D

C.3.1 SPE DD

```
1 ze
  10u pl1:f1 pl2:f2
2 d1 do:f2
  (p1 ph1):f1
  3u cpd2:f2
  go=2 ph31
  3m do:f2
  wr #0
exit


ph1  =0 1 2 3
ph31 =0 1 2 3
```

C.3.2 Hartmann-Hahn CP

```
1 ze
2 d1 do:f2
  10u pl1:f1 pl2:f2
  (p3 ph1):f2
  2u
3 (p15 ph2):f1 (p15 ph3):f2
  1u pl12:f2
  1u cpd2:f2
  go=2 ph31
  1m do:f2
  wr #0
exit

ph1=1 3
ph2=0 0 1 1 2 2 3 3
ph3=0
ph31=0 2 1 3 2 0 3 1
```

C.3.3 Ramp CP

```
1 ze
2 d1 do:f2
  10u pl1:f1 pl2:f2
  (p3 ph1):f2
  2u ph10:f2
  (p15 ph2):f1 (p15:sp0):f2
  1u pl12:f2
  1u cpd:f2
  go=2 ph31
  1m do:f2
  wr #0
exit


ph0= 0
ph1= 1 3
ph2= 0 0 2 2 1 1 3 3
ph3= 1 1 3 3 2 2 0 0
ph10= 0
ph31= 0 2 2 0 1 3 3 1
```

C.3.4 REPT

```
"l2=l1"
"p2=2*p1"
"d4=(0.5s/cnst31)-p1*2" ; l31 = nu_R / 10
"d11=(0.5s/cnst31)-p1*1.5"

1 ze
2 d1 do:f2
  10u pl1:f1 pl2:f2

3 (p1 ph20^):f1
  13m
  (p1 ph21^):f1
  7m
  (p1 ph22^):f1
  1m
  (p1 ph23^):f1
  3m
  lo to 3 times 16

  d5

  (p1 ph1):f2
  d4
4 (p2 ph6):f1
  d4
  (p2 ph7):f1
  d4
  lo to 4 times l1
5 (p2 ph6):f1
  d4
  lo to 5 times l0
  (p2 ph8):f2
6 d4
  (p2 ph6):f1
  d4
  (p2 ph7):f1
 lo to 6 times l1
```

```
7 d4
  (p2 ph6):f1
 lo to 7 times l0

  d11
  (p1 ph2):f1 (p1 ph3):f2
  d11

8 (p2 ph6):f2
  d4
  (p2 ph7):f2
  d4
  lo to 8 times l2
9 (p2 ph6):f2
  d4
  lo to 9 times l0
  (p2 ph9):f1
  d4
10 (p2 ph6):f2
  d4
  (p2 ph7):f2
  d4
  lo to 10 times l2
11 (p2 ph6):f2
  d4
  lo to 11 times l0
  (p1 ph4):f1

  d6 pl12:f2
  (p1 ph5):f1
  go=2 ph31 cpd2:f2
  2m do:f2
  30m wr #0
  exit


ph1= 0 2 1 3 2 0 3 1  2 0 3 1 0 2 1 3
ph2= 1 3 2 0 3 1 0 2
ph3= 1 1 2 2 3 3 0 0
ph4= 2 2 3 3 0 0 1 1
ph5= 0 0 1 1 2 2 3 3 2 2 3 3 0 0 1 1
ph6= 0
ph7= 1
ph8= 1 3 2 0 3 1 0 2
ph9= 2 0 3 1 0 2 1 3
ph31= 1 1 2 2 3 3 0 0
ph20= 0 1 2 3
ph21= 1 2 3 0
ph22= 2 3 0 1
ph23= 3 0 1 2
```

C.3.5   REREDOR

```
"p2=p1*2"
"d4=(0.5s/cnst31)-p1*2"
"l1=l2"

1 ze
2 d1
  3u pl2:f2
  (p3 ph11):f2
  2u pl3:f2
  (p15:sp0 ph13):f2 (p15 ph12):f1
  4u
  2u pl1:f1
  (p1 ph14):f1 (p3 ph15):f2
  d5 pl2:f2

  (p1 ph1):f1
  d4
4 (p2 ph6):f2
  d4
  (p2 ph7):f2
  d4
  lo to 4 times l1
5 (p2 ph6):f2
  d4
  lo to 5 times l0
  (p2 ph9):f1
6 d4
  (p2 ph6):f2
  d4
  (p2 ph7):f2
  lo to 6 times l1
7 d4
  (p2 ph6):f2
  lo to 7 times l0
  d4

  d0      ;1st t1

  d4
8 (p2 ph6):f2
  d4
  (p2 ph7):f2
  d4
  lo to 8 times l2
9 (p2 ph6):f2
  d4
  lo to 9 times l0
  (p2 ph10):f1
  d4
10 (p2 ph6):f2
  d4
  (p2 ph7):f2
  d4
  lo to 10 times l2
11 (p2 ph6):f2
  d4
  lo to 11 times l0

  d0      ;2nd t1

  (p1 ph8):f1
  d6 pl12:f2
```

```
  (p1 ph30):f1
  2u cpd2:f2
  go=2 ph31
  2u do:f2
  30m wr #0 ;if #0
exit
```

```
ph1 = 0 2 1 3
ph8 = 0 0 1 1 2 2 3 3
ph6 = 0
ph7 = 1
ph9 = 1 1 2 2
ph10= 1 1 2 2
ph11= {1}*8 {3}*8
ph12= 0
ph13= 0
ph14= 1
ph15= 3
ph30= {0 0}*8 {2 2}*8
ph31= 0 2 0 2 2 0 2 0  2 0 2 0 0 2 0 2
      2 0 2 0 0 2 0 2  0 2 0 2 2 0 2 0
```

C.4   Heteronuclear 2D

C.4.1   REPT HSQC

```
"l2=l1"
"p2=p1*2"
"d4=(0.5s/cnst31)-p1*2"
"d11=(0.5s/cnst31)-p1*1.5"

1 ze
2 d1 do:f2
  10u pl1:f1 pl2:f2

3 (p1 ph20^):f1
  13m
  (p1 ph21^):f1
  7m
  (p1 ph22^):f1
  1m
  (p1 ph23^):f1
  3m
  lo to 3 times 8

  d5

  (p1 ph1):f2
  d4
4 (p2 ph6):f1
  d4
  (p2 ph7):f1
  d4
  lo to 4 times l1
5 (p2 ph6):f1
  d4
  lo to 5 times l0
  (p2 ph8):f2
6 d4
  (p2 ph6):f1
```

```
  d4
  (p2 ph7):f1
  lo to 6 times l1
7 d4
  (p2 ph6):f1
  lo to 7 times l0
  d11

  d0       ;t1

  (p1 ph2):f1 (p1 ph3):f2
  d11
8 (p2 ph6):f2
  d4
  (p2 ph7):f2
  d4
  lo to 8 times l2
9 (p2 ph6):f2
  d4
  lo to 9 times l0
  (p2 ph9):f1
  d4
10 (p2 ph6):f2
  d4
  (p2 ph7):f2
  d4
  lo to 10 times l2
11 (p2 ph6):f2
  d4
  lo to 11 times l0
  (p1 ph4):f1

  d6 pl12:f2
  (p1 ph5):f1
  go=2 ph31 cpd2:f2
  2m do:f2
  30m wr #0 if #0
  id0
  ip3
  zd
  lo to 2 times td1
  exit

ph1= 0 2 1 3 2 0 3 1  2 0 3 1 0 2 1 3
ph2= 1 3 2 0 3 1 0 2
ph3= 1 1 2 2 3 3 0 0
ph4= 2 2 3 3 0 0 1 1
ph5 = 0 0 1 1 2 2 3 3  2 2 3 3 0 0 1 1
ph6= 0
ph7= 1
ph8= 1 3 2 0 3 1 0 2
ph9= 2 0 3 1 0 2 1 3
ph31= 1 1 2 2 3 3 0 0
ph20= 0 1 2 3
ph21= 1 2 3 0
ph22= 2 3 0 1
ph23= 3 0 1 2
```

C.4.2 REPT-HDOR

```
"d0=(1s/cnst31)-p1"
"l2=l1"
```

```
"p2=p1*2"
"d4=(0.5s/cnst31)-p1*2" ; l31 = nu_R / 10
"d11=(0.5s/cnst31)-p1*1.5"

1 ze
2 d1 do:f2
  10u pl1:f1 pl2:f2

3 (p1 ph20^):f1
  13m
  (p1 ph21^):f1
  7m
  (p1 ph22^):f1
  1m
  (p1 ph23^):f1
  3m
  lo to 3 times 8

  d5

  (p1 ph1):f2
  d4
4 (p2 ph6):f1
  d4
  (p2 ph7):f1
  d4
  lo to 4 times l1
5 (p2 ph6):f1
  d4
  lo to 5 times l0
  (p2 ph8):f2
6 d4
  (p2 ph6):f1
  d4
  (p2 ph7):f1
  lo to 6 times l1
7 d4
  (p2 ph6):f1
  lo to 7 times l0
  d11
  (d0 p1 ph2):f1  (p1 ph3):f2     ; t1

  d11
8 (p2 ph6):f2
  d4
  (p2 ph7):f2
  d4
  lo to 8 times l2
9 (p2 ph6):f2
  d4
  lo to 9 times l0
  (p2 ph9):f1
  d4
10 (p2 ph6):f2
  d4
  (p2 ph7):f2
  d4
  lo to 10 times l2
11 (p2 ph6):f2
  d4
  lo to 11 times l0
  (p1 ph4):f1

  d6 pl12:f2
```

```
  (p1 ph5):f1
  go=2 ph31 cpd2:f2
  2m do:f2
  30m wr #0 if #0
  id0
  zd
  lo to 2 times td1
  exit
```

```
ph1= 0 2 1 3 2 0 3 1  2 0 3 1 0 2 1 3
ph2= 1 3 2 0 3 1 0 2
ph3= 1 1 2 2 3 3 0 0
ph4= 2 2 3 3 0 0 1 1
ph5= 0 0 1 1 2 2 3 3  2 2 3 3 0 0 1 1
ph6= 0
ph7= 1
ph8= 1 3 2 0 3 1 0 2
ph9= 2 0 3 1 0 2 1 3
ph31= 1 1 2 2 3 3 0 0
ph20= 0 1 2 3
ph21= 1 2 3 0
ph22= 2 3 0 1
ph23= 3 0 1 2
```

C.4.3 REREDOR

```
"p2=p1*2"
"d4=(0.5s/cnst31)-p1*2"
"l2=l1"

1 ze
2 d1

  3u pl2:f2
  (p3 ph11):f2
  2u pl3:f2
  (p15 :sp0 ph13):f2 (p15 ph12):f1
  4u
  2u pl1:f1
  (p1 ph14):f1 (p3 ph15):f2

  d5 pl2:f2

  (p1 ph1):f1
  d4
4 (p2 ph6):f2
  d4
  (p2 ph7):f2
  d4
  lo to 4 times l1
5 (p2 ph6):f2
  d4
  lo to 5 times l0
```

```
  (p2 ph9):f1
6 d4
  (p2 ph6):f2
  d4
  (p2 ph7):f2
  lo to 6 times l1
7 d4
  (p2 ph6):f2
  lo to 7 times l0
  d4

  d0      ;1st t1

  d4
8 (p2 ph6):f2
  d4
  (p2 ph7):f2
  d4
  lo to 8 times l2
9 (p2 ph6):f2
  d4
  lo to 9 times l0
  (p2 ph10):f1
  d4
10 (p2 ph6):f2
  d4
  (p2 ph7):f2
  d4
  lo to 10 times l2
11 (p2 ph6):f2
  d4
  lo to 11 times l0

  d0      ;2nd t1

  (p1 ph8):f1

  d6 pl12:f2

  (p1 ph30):f1
  2u cpd2:f2
  go=2 ph31
  2u do:f2
  30m wr #0 if #0
  zd
  id0
  lo to 2 times td1
exit
```

```
ph1 = 0 2 1 3
ph8 = 0 0 1 1 2 2 3 3
ph6 = 0
ph7 = 1
ph9 = 1 1 2 2
ph10= 1 1 2 2
ph11= {1}*8 {3}*8
ph12= 0
ph13= 0
ph14= 1
ph15= 3
ph30= {0 0}*8 {2 2}*8
ph31= 0 2 0 2 2 0 2 0  2 0 2 0 0 2 0 2
      2 0 2 0 0 2 0 2  0 2 0 2 2 0 2 0
```

Appendix D

Sideband Simulations

Usage examples for:

$$
\begin{aligned}
D_{CH}/2\pi &= 10\,\text{kHz} \\
\tau_{exc/rec} &= 2 \cdot \tau_r\,\text{s} \\
\omega_r/2\pi &= 30\,\text{kHz}
\end{aligned}
$$

D.1 BABA-HH

```
baba[X_, unit_, nR_, MAS_] :=

Block[{omegaR, tmax, dw,
nbeta, ngammamax, powder, t, angles,
alpha, beta, PreFac, Deltagamma,
Deltabeta, Signal, PowderSignal},

angles = {};
int = {};
powder = 0;

tmax = 20;
dw = N[(1/MAS)/tmax];
t = Range[0, tmax - 1]dw;
PowderSignal = t*0;

nbeta = 30 - 1;
Deltabeta = N[pi/(2nbeta)];
ngammamax = 4 nbeta;
omegaR = N[2 pi MAS];

Switch[unit,
khz, dij = 2 pi 1000 X,
k  , dij = 2 pi 1000 X,
h  , dij = 2 pi X,
hz , dij = 2 pi X,
a  , dij = 754664/(X^3),
A  , dij = 754664/(X^3),
pm , dij = 754664/(X/100)^3];

PreFac = (3 2^(1/2) nR dij)/omegaR;
```

```
For[beta = 0, beta < 90 degrees,
  Sin2beta = Sin[2beta];
  Sinbeta2 = Sin[beta]^2;
  Wngamma = Round[N[Sin[beta] ngammamax]];
  Deltagamma = N[360 degrees/Wngamma];

  For[gamma = 0, gamma < 360 degrees,
    Signal =
      Sin[
        PreFac Sin2beta
        Sin[gamma]
      ]
      Sin[
        PreFac Sin2beta
        Sin[gamma + (omegaR t)]
      ];

    PowderSignal = Signal + PowderSignal;
    angles = Append[angles, {beta, gamma}];
    powder++,
  gamma += Deltagamma],
beta += Deltabeta];

PowderSignal =
PowderSignal/Max[PowderSignal];

FID = ListPlot[
  Transpose[{t/(2pi/omegaR)), PowderSignal}
  ],
PlotRange -> {{0, 1}, {-1, 1}},
PlotJoined -> True, AspectRatio -> 0.8,
DisplayFunction -> Identity];

rep = 50;
lambda = 5;
td = tmax rep;
CatPowderSignal = Flatten[
Table[PowderSignal, {rep}]];
gauss = Table[Exp[-(t^2) lambda],
  {t, 0, 2pi - (2pi/td), (2pi/td)}];
GaussCatPowderSignal =
gauss CatPowderSignal;
respec = Re[Join[
Take[Fourier[GaussCatPowderSignal], -td/2],
Take[Fourier[GaussCatPowderSignal],  td/2]
]];
respec = respec/Max[respec];
```

```
For[i = 1, i <= 10, i++,
  int =
  Append[int,
  N[Round[100 Max[Partition[Drop[
    respec,
    (Length[respec]/2)
  - (Length[respec]/40)],
 Length[respec]/20] [[i]] ]]/100]]
];

scale = 0.02(Range[1, td] -td/2);
sim = Transpose[{scale,respec}];
SSB = ListPlot[sim,
PlotRange -> {-5, 5}, {0, 1.05},
PlotJoined -> True, Axes -> {True, False},
AspectRatio -> N[10/13],
Ticks -> {Range[-9, 9, 2], {}},
PlotStyle -> RGBColor[1, 0, 0],
DisplayFunction -> Identity];

Print[
"R_ij = ", N[(754664/dij)^(1/3), 3],"Ang ",
"D_ij = ", N[dij/(1000 2 pi), 4], " kHz ",
"tau_exc = ", nR, "tau_r ",
"tau_rec = ", nR, "tau_r ",
"omega_r = ", N[MAS/1000, 3], "kHz ",
"D_ij:omega_r = ", N[dij/omegaR, 5], "/n",
"crystalites = ", powder, "\n",
"SSB Ratio = 1 : ", int[[2]],
" : ", int[[3]],
" : ", int[[4]],
" : ", int[[5]],
" : ", int[[6]],
" : ", int[[7]],
" : ", int[[8]],
" : ", int[[9]],
" : ", int[[10]]
];

Show[GraphicsArray[{FID, SSB}],
  DisplayFunction -> $DisplayFunction,
  Frame -> True];
]

baba[10, k, 2, 30000]
```

D.2   REPT-CH

```
hdor[X_, unit_, nR_, MAS_] :=

Block[{a, b, c, d, omegaR, tmax, dw,
nbeta, ngammamax, powder, t, angles,
alpha, beta, PreFac, Deltagamma,
Deltabeta, Signal, PowderSignal},

angles = {};
int = {};
powder = 0;

tmax = 20;
dw = N[(1/MAS)/tmax];
```

```
t = Range[0, tmax - 1]dw;
PowderSignal = t*0;

nbeta = 30 - 1;
Deltabeta = N[pi/(2nbeta)];
ngammamax = 4 nbeta;
omegaR = N[2 pi MAS];

Switch[unit,
khz, dij = 2 pi 1000 X,
k  , dij = 2 pi 1000 X,
h  , dij = 2 pi X,
hz , dij = 2 pi X,
a  , dij = 189734/(X^3),
A  , dij = 189734/(X^3),
pm , dij = 189734/(X/100)^3];

PreFac = (2 2^(1/2) nR dij)/omegaR;


For[beta = 0, beta < 90 degrees,
  Sin2beta = Sin[2beta];
  Sinbeta2 = Sin[beta]^2;
  Wngamma = Round[N[Sin[beta] ngammamax]];
  Deltagamma = N[360 degrees/Wngamma];

  For[gamma = 0, gamma < 360 degrees,
    Signal =
      Sin[
        PreFac Sin2beta
        Sin[gamma]
      ]
      Sin[
        PreFac Sin2beta
        Sin[gamma + (omegaR t)]
      ];

    PowderSignal = Signal + PowderSignal;
    angles = Append[angles, {beta, gamma}];
    powder++,
  gamma += Deltagamma],
beta += Deltabeta];


PowderSignal =
PowderSignal/Max[PowderSignal];

FID = ListPlot[
  Transpose[{t/(2pi/omegaR)), PowderSignal}
  ],
PlotRange -> {{0, 1}, {-1, 1}},
PlotJoined -> True, AspectRatio -> 0.8,
DisplayFunction -> Identity];

rep = 50;
lambda = 5;
td = tmax rep;
CatPowderSignal = Flatten[
Table[PowderSignal, {rep}]];
gauss = Table[Exp[-(t^2) lambda],
  {t, 0, 2pi - (2pi/td), (2pi/td)}];
GaussCatPowderSignal =
```

```
gauss CatPowderSignal;
respec = Re[Join[
Take[Fourier[GaussCatPowderSignal], -td/2],
Take[Fourier[GaussCatPowderSignal],  td/2]
]];
respec = respec/Max[respec];

For[i = 1, i <= 10, i++,
  int =
  Append[int,
  N[Round[100 Max[Partition[Drop[
    respec,
    (Length[respec]/2)
  - (Length[respec]/40)],
 Length[respec]/20] [[i]] ]]/100]]
];

scale = 0.02(Range[1, td] -td/2);
sim = Transpose[{scale,respec}];
SSB = ListPlot[sim,
PlotRange -> {-5, 5}, {0, 1.05},
PlotJoined -> True, Axes -> {True, False},
AspectRatio -> N[10/13],
Ticks -> {Range[-9, 9, 2], {}},
PlotStyle -> RGBColor[1, 0, 0],
DisplayFunction -> Identity];

Print[
"R_ij = ", N[(189734/dij)^(1/3), 3],"Ang ",
"D_ij = ", N[dij/(1000 2 pi), 4], " kHz ",
"tau_exc = ", nR, "tau_r ",
"tau_rec = ", nR, "tau_r ",
"omega_r = ", N[MAS/1000, 3], "kHz ",
"D_ij:omega_r = ", N[dij/omegaR, 5], "/n",
"crystalites = ", powder, "\n",
"SSB Ratio = 1 : ", int[[2]],
" : ", int[[3]],
" : ", int[[4]],
" : ", int[[5]],
" : ", int[[6]],
" : ", int[[7]],
" : ", int[[8]],
" : ", int[[9]],
" : ", int[[10]]
];

Show[GraphicsArray[{FID, SSB}],
  DisplayFunction -> $DisplayFunction,
  Frame -> True];
]

hdor[10, k, 2, 30000]
```

D.3   REREDOR-CH

```
reredor[X_, unit_, nR, MAS_] :=

Block[{a, b, c, d, omegaR, tmax, dw,
nbeta, ngammamax, powder, t, angles,
alpha, beta, PreFac1, PreFac2, Deltagamma,
Deltabeta, Signal, PowderSignal},

tmax = 20;
```

```
angles = {};
int = {};
powder = 0;

tmax = 20;
dw = N[(1/MAS)/tmax];
t = Range[0, tmax - 1]dw;
PowderSignal = t*0;

nbeta = 30 - 1;
Deltabeta = N[pi/(2nbeta)];
ngammamax = 4 nbeta;
omegaR = N[2 pi MAS];

Switch[unit,
khz, dij = 2 pi 1000 X,
k  , dij = 2 pi 1000 X,
h  , dij = 2 pi X,
hz , dij = 2 pi X,
a  , dij = 189734/(X^3),
A  , dij = 189734/(X^3),
pm , dij = 189734/(X/100)^3];

PreFac1 = (2 2^(1/2) nR dij)/omegaR;
PreFac2 = dij/(2 omegaR);

For[beta = 0, beta < 90 degrees,
  Sin2beta = Sin[2beta];
  Sinbeta2 = Sin[beta]^2;
  Wngamma = Round[N[Sin[beta] ngammamax]];
  Deltagamma = N[360 degrees/Wngamma];

  For[gamma = 0, gamma < 360 degrees,

    a = + PreFac1 Sin2beta
          (
          Sin[gamma];
          )

    b = -(1/2) PreFac2 Sinbeta2
          (Sin[2 omegaR t + 2 gamma]
           - Sin[2 gamma])
        + 2^(1/2) PreFac2 Sin2beta
          (Sin[omegaR t + gamma]
           - Sin[gamma]);

    c = - PreFac1 Sin2beta
          (Sin[(omegaR t) + gamma]);

    d = +(1/2) PreFac2 Sinbeta2
          (Sin[4 omegaR t + 2 gamma]
           - Sin[2 omegaR t + 2 gamma])
        - 2^(1/2) PreFac2 Sin2beta
  (Sin[2 omegaR t + gamma]
           - Sin[omegaR t + gamma]);

    Signal = Cos[a + b + c + d];

    PowderSignal = Signal + PowderSignal;
    angles = Append[angles, {beta, gamma}];
    powder++,
  gamma += Deltagamma],
beta += Deltabeta];
```

```
                                           " : ", int[[8]],
PowderSignal =                             " : ", int[[9]],
PowderSignal/Max[PowderSignal];            " : ", int[[10]]
                                           ];


FID = ListPlot[                          Show[GraphicsArray[{FID, SSB}],
  Transpose[{t/(2pi/omegaR)), PowderSignal}   DisplayFunction -> $DisplayFunction,
  ],                                        Frame -> True];
PlotRange -> {{0, 1}, {-1, 1}},          ]
PlotJoined -> True, AspectRatio -> 0.8,
DisplayFunction -> Identity];            hdor[10, k, 2, 3, 30000]

rep = 50;
lambda = 5;
td = tmax rep;
CatPowderSignal = Flatten[
Table[PowderSignal, {rep}]];
gauss = Table[Exp[-(t^2) lambda],
  {t, 0, 2pi - (2pi/td), (2pi/td)}];
GaussCatPowderSignal =
gauss CatPowderSignal;

respec = Re[Join[
Take[Fourier[GaussCatPowderSignal], -td/2],
Take[Fourier[GaussCatPowderSignal],  td/2]
]];
respec = respec/Max[respec];

For[i = 1, i <= 10, i++,
  int =
  Append[int,
  N[Round[100 Max[Partition[Drop[
    respec,
    (Length[respec]/2)
  - (Length[respec]/40)],
 Length[respec]/20] [[i]] ]]/100]]
];

scale = 0.02(Range[1, td] -td/2);
sim = Transpose[{scale,respec}];
SSB = ListPlot[sim,
PlotRange -> {-8, 8}, {0, 1.05},
PlotJoined -> True, Axes -> {True, False},
AspectRatio -> N[10/13],
Ticks -> {Range[-9, 9, 2], {}},
PlotStyle -> RGBColor[1, 0, 0],
DisplayFunction -> Identity];

Print[
"R_ij = ", N[(189734/dij)^(1/3), 3],"Ang ",
"D_ij = ", N[dij/(1000 2 pi), 4], " kHz ",
"tau_exc = ", nR1, "tau_r ",
"tau_rec = ", nR2, "tau_r ",
"omega_r = ", N[MAS/1000, 3], "kHz ",
"D_ij:omega_r = ", N[dij/omegaR, 5], "/n",
"crystalites = ", powder, "\n",
"SSB Ratio = 1 : ", int[[2]],
" : ", int[[3]],
" : ", int[[4]],
" : ", int[[5]],
" : ", int[[6]],
" : ", int[[7]],
```

Appendix E

Ab-initio Calculation of NMR Properties

In the following appendix the calculation of NMR properties in condensed matter by electronic structure methods will be briefly presented. Emphasis is placed on the extension of well-established approaches for the calculation of linear magnetic response to extended systems described under periodic boundary conditions.

E.1 Treatment of magnetic fields by perturbation theory

For the numerical calculation the linear electronic response to a magnetic field can be described using second order perturbation theory [Gonze 89, Putrino 00]. The exact Hamiltonian ($\hat{\mathcal{H}}$), its energy eigenvalues (ε_i) and the wavefunctions (φ_i) all being expanded as powers of the perturbing interaction B, the strength of the applied magnetic field B_0. The Schrödinger equation, or equivalently the variational principle, is considered separately for each of these orders in perturbation theory.

In magnetic perturbation theory, the situation is slightly more complex, since there are actually *two* independent perturbations. In addition to the external magnetic field B_0, an internal magnetic field, created by the magnetic moments of the nuclear spins μ_I, also has to be considered. Thus, apart from the purely dipolar spin interaction, quadratic in μ_I, the second order expression of the total energy contains two terms, one bilinear in B and μ_I and another quadratic in B. The latter term, quadratic in B, represents the interaction of the induced electronic current with the external magnetic field, this is characterised by the magnetic susceptibility tensor $\chi_{\alpha\beta}^m$ of the sample:

$$\chi^m_{\alpha\beta} = \frac{\partial^2 E}{\partial B_\alpha \partial B_\beta} \tag{E.1}$$

The former term, bilinear in B and μ_I, represents the interaction of the induced electronic current with the nuclear spins, this gives rise to the chemical shielding tensor $\sigma_{\alpha\beta}(I)$ of a nuclear spin I:

$$\sigma_{\alpha\beta}(I) = \frac{\partial^2 E}{\partial B_\alpha \partial \mu_{I,\beta}} + 1 = -\frac{\partial B^{ind}_\beta(R_I)}{\partial B_\alpha} \tag{E.2}$$

In order to calculate this, the perturbing effect of an external magnetic field on the electronic degrees of freedom is considered. Using Equation E.1 and Equation E.2 $\chi^m_{\alpha\beta}$ and $\sigma_{\alpha\beta}(I)$ can be calculated from the linear response of the electrons.

E.2   Density functional theory (DFT) implementation

Within density functional perturbation theory the DFT energy functional in the Kohn-Sham (KS) scheme [Hohenberg 64, Kohn 65] is denoted $\mathcal{E}_{KS}$, this is modified by a small additional term $\mathcal{E}_B$ describing the effect of an external magnetic field:

$$\mathcal{E}_{KS} \mapsto \mathcal{E}_{KS} + \mathcal{E}_B. \tag{E.3}$$

Compared to $\mathcal{E}_{KS}$ this additional contribution is very small and may be treated by perturbation theory. Thus, Equation E.3 can be expanded in powers of the strength of the magnetic field:

$$\mathcal{E}_{KS} + \mathcal{E}_B = \mathcal{E}^{(0)} + B\mathcal{E}^{(1)} + \frac{1}{2}B^2\mathcal{E}^{(2)} + \dots \tag{E.4}$$

Similarly, the Hamiltonian and KS orbitals can be written as such a series:

$$\mathcal{H} = \mathcal{H}^{(0)} + B\mathcal{H}^{(1)} + \frac{1}{2}B^2\mathcal{H}^{(2)} + \dots \tag{E.5}$$

$$|\varphi_i\rangle = |\varphi_i^{(0)}\rangle + B|\varphi_i^{(1)}\rangle + \frac{1}{2}B^2|\varphi_i^{(2)}\rangle + \dots \tag{E.6}$$

Inserting Equation E.5 and Equation E.6 into Equation E.4, and applying variational principle to all orders, a series of equations is obtained. At zeroth order this yields the usual Kohn-Sham equations with KS energy eigenvalues ε_i:

$$\mathcal{H}^{(0)}|\varphi_i^{(0)}\rangle = \varepsilon_i|\varphi_i^{(0)}\rangle \tag{E.7}$$

The response of the electrons to the magnetic field is represented by the first order perturbation wavefunctions obtained from the second order expansion of Equation E.4:

$$\sum_j \left(\mathcal{H}^{(0)} \delta_{ij} - \varepsilon_{ij} \right) |\phi_j^{(1)}\rangle \;=\; \left(1 - \sum_j |\phi_j^{(0)}\rangle \langle \phi_j^{(0)}| \right) \mathcal{H}^{(1)} |\phi_i^{(0)}\rangle \tag{E.8}$$

where ε_{ij} are the Lagrange multipliers:

$$\varepsilon_{ij} = \langle \phi_j^{(0)} | \mathcal{H}^{(0)} | \phi_i^{(0)} \rangle \tag{E.9}$$

Within this formalism the magnetic field is represented as the magnetic vector potential A. The magnetic vector potential is defined to satisfy the relationship:

$$B = \nabla \times A(\mathbf{r}) = B_0. \tag{E.10}$$

The form of $A(\mathbf{r})$ is discussed in more detal later (Section E.2.1). Using the magnetic vector potential a generalised momentum operator $\hat{\pi}$ is generated:

$$\hat{\pi} \;=\; \hat{p} - eA(\hat{r}) \tag{E.11}$$

The Hamiltonians of which are given by:

$$\mathcal{H}^{(1)} \;=\; -\frac{e}{m} \hat{p} \cdot A(\hat{r}) \tag{E.12}$$

$$\mathcal{H}^{(2)} \;=\; \frac{e^2}{2m} A(\hat{r})^2 \tag{E.13}$$

Inserting Equation E.10 into Equation E.12 and solving Equation E.8 results in the first order perturbation orbitals $|\phi_j^{(1)}\rangle$ being obtained. These are then used to compute the quantum-mechanical current density distribution $j(\mathbf{r})$ induced by the magnetic field using:

$$\mathbf{j}(\mathbf{r}') \;=\; \frac{e}{2m} \sum_j \langle \varphi_j | \left(\hat{\pi} |\mathbf{r}'\rangle\langle\mathbf{r}'| + |\mathbf{r}'\rangle\langle\mathbf{r}'|\hat{\pi} \right) |\varphi_j\rangle \tag{E.14}$$

$$\;=\; \frac{e}{2m} \Re \sum_j \langle \varphi_j^{(0)} | \left[\hat{\mathbf{p}}|\mathbf{r}'\rangle\langle\mathbf{r}'| + |\mathbf{r}'\rangle\langle\mathbf{r}'|\hat{\mathbf{p}} \right] |\varphi_j^{(1)}\rangle +$$

$$\frac{e^2}{m} \sum_j \mathbf{A}(\mathbf{r}') \left| \varphi_j^{(0)}(\mathbf{r}') \right|^2 + \mathcal{O}(B^2) \tag{E.15}$$

From this the induced magnetic field $\mathbf{B}^{ind}$ can be obtained using:

$$\mathbf{B}^{ind}(\mathbf{r}) \quad = \quad \frac{\mu_0}{4\pi} \int d^3 r' \, \frac{\mathbf{r}' - \mathbf{r}}{|\mathbf{r}' - \mathbf{r}|^3} \times \mathbf{j}(\mathbf{r}'). \tag{E.16}$$

From the induced magnetic field the chemical shielding tensor can be calculated according to Equation E.2 respectively. To allow comparison with experimental data the trace of the chemical shielding tensor is calculated relative to a reference compound, e.g. tetramethylsilane for ^1H , thus yielding the isotropic chemical shift δ^{iso}:

$$\delta^{iso}(I) \quad = \quad \text{Tr} \, \sigma^{ref}_{\alpha\beta}(I) - \text{Tr} \, \sigma_{\alpha\beta}(I). \tag{E.17}$$

E.2.1 The gauge origin problem

When constructing the magnetic vector potential $A(\mathbf{r})$ for a given magnetic field B_0 a fundamental degree of freedom is introduced. If the vector potential is constructed according to:

$$A(\mathbf{r}) \quad = \quad -\frac{1}{2}\mathbf{r} \times B_0 + \nabla\Phi(\mathbf{r}) \tag{E.18}$$

an arbitrary scaling function $\Phi(\mathbf{r})$ is introduced. More importantly, variation of this function does not influence the magnetic field created by A. Among these so-called *gauge functions*, one example is particularly illustrative:

$$\Phi(\mathbf{r}) = \frac{1}{2}\mathbf{r} \cdot R_g \times B_0 \tag{E.19}$$

Using this guage function the vector potential becomes:

$$A(\mathbf{r}) \quad = \quad -\frac{1}{2}(\mathbf{r} - R_g) \times B_0 \tag{E.20}$$

Thus the gauge function manifests itself as a choice of origin of the position operator $\hat{\mathbf{r}}$. In principle the choice of such a property is arbitrary, as the gauge origin R_g is cyclic, with all physical observables theoretically being gauge-invariant. However, in practice this is normally not the case for numerical reasons. The expression for the electronic current density, Equation E.15, contains two contributions; the paramagnetic contribution, the first term proportional to $\varphi_j^{(1)}$, and the diamagnetic current, the second term proportional to A. In practice these two terms have opposite signs and thus have a tendency to cancel. Furthermore, both the paramagnetic and diamagnetic terms are approximately linearly dependent on the gauge origin R_g. Thus, the correct choice of gauge origin is crucial for any actual implementation since it

can dramatically influence the numerical quality of the results.

The gauge origin problem represented a major difficulty in early quantum chemical calculations. It is related to the incomplete nature of the basis set used to represent the electronic wavefunctions.

E.2.2   Pioneering theoretical foundations

One of the earliest formulations of linear magnetic response was presented by Ramsey [Ramsey 50a, Ramsey 50b, Ramsey 52], and the contributions of the diamagnetic and paramagnetic terms to the chemical shielding presented. The gauge origin problem was discussed but no practical solution to address this problem was presented.

Later, along with the rise of computer power, many approaches for the calculation of NMR parameters for isolated molecules were formulated. These mostly proposed different solutions to the gauge origin problem [Helgaker 99]. Of these methods some deserve particular recognition: individual gauges for localized orbitals (IGLO) [Kutzelnigg 90], continuous set of gauge transformations (CSGT) [Keith 93], individual gauges for atoms in molecules (IGAIM) [Keith 92] and gauge including atomic orbitals (GIAO) [Ditchfield 72]. Several review articles have investigated the performance and different implementations of those methods [Magyarfalvi 03, Gregor 99].

Recently, computational chemistry has tended towards increasingly more accurate electronic structure methods. Similarly the precision of NMR chemical shielding predictions has also significantly increased [Munzarova 99, Vaara 98, Auer 03]. Presently, the absolute values of NMR chemical shieldings can be computed to an accuracy of a fraction of a ppm. However, this is only true for very small systems and does not yet allow for heavy (relativistic) atoms.

However, for relativistic atoms important progress has been made in the last decade. The investigation of relativistic effects, such as spin-orbit coupling on magnetic properties, has been investigated in great detail [Vaara 01, Malkina 00, Malkina 98, Kaupp 98].

E.3 Magnetic response under periodic boundary conditions

Although Ramsey had first described the interaction of magnetic fields with electrons on a theoretical level fifty years ago, problems associated with periodic boundary conditions were only addressed much later. The position operator **r**, already problematic because of its choice of origin, is intrinsically not periodic. The first possible theoretical formulation for dealing with this problem was presented by Kobayashi and Tsukada [Kobayashi 88]. This aproach assumed the external magnetic field was modulated with a small, but finite, wavevector $\boldsymbol{q} = (q, -q, 0)$. Using this special magnetic field the magnetic vector potential can be defined as being periodic in space:

$$\boldsymbol{A}(\mathbf{r}) = \frac{1}{2q} \sin(\boldsymbol{q} \cdot \mathbf{r}) \begin{pmatrix} B \\ B \\ 0 \end{pmatrix} \tag{E.21}$$

The use of this vector potential also results in an oscillation of the external magnetic field:

$$\boldsymbol{B}(\mathbf{r}) = \nabla \times \boldsymbol{A}(\mathbf{r}) = \cos(\boldsymbol{q} \cdot \mathbf{r}) \begin{pmatrix} 0 \\ 0 \\ B \end{pmatrix} \tag{E.22}$$

By the use of such a vector potential electronic structure calculations under periodic boundary conditions are possible. However, in order to obtain the physically relevant situation of a static magnetic field the limit $q \to 0$ needs to be evaluated numerically [Mauri 96b]. The first realization of this method was achieved by Mauri *et al.* who implemented it into a pseudopotential plane wave scheme [Mauri 96b, Mauri 96a]. It was shown that the calculation of magnetic electronic response within DFT was possible under periodic boundary conditions in a formally exact way. Their results were in good agreement with experimental data.

An alternate approach is also possible, this not requiring the static external magnetic field to be replaced by an oscillating field. It relies on localising the canonical Kohn-Sham wavefunctions $|\varphi_i\rangle$ in space by means of a unitary transformation $\mathcal{U}$ producing Wannier orbitals $|\omega_i\rangle$ [Wannier 37, Berghold 00]:

$$|\omega_i\rangle = \sum_j \mathcal{U}_{ij} |\varphi_j\rangle \tag{E.23}$$

It has been shown that in insulators such Wannier orbitals exponentially decay in space [Wannier 37], in contrast to their canonical counterparts which in general exhibit extended character i.e. Bloch wavefunctions. With this type of orbital a new

position operator can be defined, this being the periodic continuation of an orbital-specific saw-tooth operator. For a given orbital of this type, in the localisation region the operator behaves exactly like the standard position operator. However, the unrealistic discontinuity is located in a region of space in which the wavefunction of the orbital is zero. Thus, the effective magnetic field felt by an individual orbital is homogeneous within the localisation region.

Using the redefinition of the standard vector potential (Equation E.20), and perturbation Hamiltonian (Equation E.12), allow the KS-orbitals to be properly applied under periodic boundary conditions. From here the corresponding perturbation theory equations can be solved in a linear response scheme working under periodic boundary conditions [Putrino 00]. This approach was developed by Sebastiani *et al.*[Sebastiani 01] and implemented recently in the Car-Parrinello Molecular Dynamic package (CPMD) [Hutter 04].

Several algorithmic complications arise due to the orbital-specific character of the perturbation Hamiltonian, but it has been shown how such problems can be resolved in an efficient manner [Sebastiani 03a].

Both approaches have been successfully applied to many systems, showing the potential of ab-initio NMR calculations for condensed phases without the problem of cluster boundary conditions. Applications have ranged from crystalline and amorphous systems [Mauri 97, Yoon 98, Mauri 99, Buda 00, Mauri 01, Goward 02, Sebastiani 02a, Goward 03, Alam 03] to different liquid phases [Pfrommer 00, Piana 01, Romero 02, Sebastiani 02b, Sebastiani 03b].

E.4   Extensions to core electrons and relativistic effects

The aforementioned methods are in principle applicable to any kind of system that can be treated within electronic structure theory. However, their implementation was first achieved in a pseudo-potential plane wave framework. Such a framework considers only the chemically relevant valence electrons. In order to achieve a good description of valence properties, with a modest size of plane wave basis set, the core electrons are neglected and replaced by a pseudo-potential. By doing so the shape of the valence wavefunctions in the core region is also neglected.

This approximation of ignoring the core electrons, and the true nodal structure of the electrons at the core, works very well for all valence-determined properties such as total energies, bond lengths, bond angles as well as vibration and excitation spectra. More subtle effects, such as hydrogen bonding, can also be described with a quality close to quantum chemical precision using this approximation.

Concerning electronic magnetic properties the approximation is, in general, somewhat more problematic since the wavefunctions are not exact in the region where the

nuclear spin is located. However, for first-row atoms ($Z \leq 10$) such problems are less severe. Although correction needs to be applied to compensate for the use of pseudopotentials, the experimentally relevant trends and differences are obtained with a good precision. It has also been demonstrated that the core contributions to NMR chemical shifts are actually constant, such that the application of simple additive correction constants recovers most of the effect of the pseudopotential approximation [Gregor 99]. For magnetic response properties of heavier elements, however, the explicit incorporation of core orbitals is required. The extension of the magnetic linear response method beyond the pseudopotential framework was done recently by Pickard *et al.* [Pickard 01] They developed a combination of the GIAO technique for the gauge origin problem and the projector augmented wave method (PAW) for the reconstruction of the all-electron orbitals within the pseudopotential scheme. This extended method has already been used with great success for the calculation of ^{17}O and ^{29}Si chemical shifts in order to determine the atomic structure of icosahedral boron carbide (B_4C) and to investigate several SiO_2 polymorphs [Ohno 97, Mauri 00, Profeta 03].

For heavier elements, relativistic corrections start to play a non-negligible role. Also, such effects were not taken into account in the first implementations of the linear magnetic response methods previously described. Recently, Yates *et al.* presented the first implementation of the ZORA approach within this GIAO-PAW method [Wolff 99, Bouten 00]. This approach was applied to a range of Se and Te compounds and showed that relativistic corrections are clearly significant and that it was possible to obtain NMR chemical shifts of very heavy elements with very good precision [Yates 03].

E.5   Perspectives

The combination of condensed matter ab-initio calculations with solid-state NMR spectroscopy for the interpretation of packing effects and hydrogen bonding in the condensed phase is an emerging field. Significant speed increases, and thus range of application, of this approach are expected by the use of hybrid quantum mechanical/molecular mechanics (QM/MM) and electronic structure methods with linear scaling [Sebastiani 03b, Sebastiani 04b]. In particular, macromolecules and supramolecular assemblies, which pose problems for standard diffraction techniques, are challenging candidates for the combined approach of experimental solid-state NMR and ab-initio calculation of structural and spectroscopic properties [Rapp 03].

Appendix F

Reported Crystal Structure of the Continuous Form

With the crystal structure of Me,Me‑N‑Me definitive proof was gained regarding the formation of intramolecular N··H‑O and intermolecular O··H‑O hydrogen bonding [Dunkers 96]. Evidence for the continuous hydrogen bonding structure was presented with the subsequent solid-state proton NMR analysis of Me,Me‑N‑Me, Me,Me‑N‑Et and Me,Me‑N‑Pr by Schnell *et al.* [Schnell 98a]. In the follow-up work of Goward *et al.* reference was made to an X-ray diffraction crystal structure of Me,Me‑N‑Pr confirming the continuous hydrogen bonding structure first predicted by solid-state NMR [Goward 01, Goward 03]. Although multiple reference had been made, no such information was found to have been published. Chronologically, reference was first made to an article submitted for publication in the Journal of the American Chemical Society [Chirachanckai 01][†], and later to an article accepted for publication in Macromolecular Symposia [Kim 03a]. When published, neither citation contained any reference to the continuous hydrogen bonding structure [Laobuthee 01, Kim 03c]. In a later review article, which encompassed the work of Schnell and Goward *et al.*, unpublished research was cited for the crystallographic evidence for the continuous hydrogen-bonding structure in [Schnell 04a] as [Chirachanckai 02][†]. Further attempts to gain access to the elusive crystal structure showing the continuous hydrogen-bonding structure proved unsuccessful [Ishida 03, Schnell 04b, Chirachanchai 04].

[†]Authors name misspelt, should have read Chirachanc**h**ai *not* Chirachanc**k**ai.

Bibliography

[Abragam 61]   A. Abragam. The Principles of Nuclear Magnetism. Oxford Univ. Press, Oxford (1961). [Cited on: p33, 50, 64]

[Abramowitz 72]   M. Abramowitz, I. A. Stegun. Handbook of Mathematical Functions. Dover Publications, Inc., New York (1972). [Cited on: p93]

[Ajayaghosh 01]   A. Ajayaghosh, S. J. George. First phenylenevinylene based organogels: Self-assembled nanostructures via cooperative hydrogen bonding and pi-stacking. *J. Am. Chem. Soc.* **123**(21), 5148–5149 (2001). [Cited on: p31]

[Alam 03]   T. M. Alam, T.A. Friedmann, P. A. Schultz, D. Sebastiani. Low-temperature annealing in tetrahedral amorphous carbon thin films observed by ^{13}C NMR spectroscopy. *Phys. Rev. B* **67**, 245309 (2003). [Cited on: p262]

[Alkorta 98]   I. Alkorta, I. Rozas, J. Elguero. Non-conventional hydrogen bonds. *Chem. Soc. Rev.* **27**, 163–170 (1998). [Cited on: p198]

[Andrew 58]   E. R. Andrew, A. Bradbury, R. G. Eades. Nuclear Magnetic Resonance Spectra from a Crystal Rotated at High Speed. *Nature* **182**, 1659 (1958). [Cited on: p33, 65]

[Auer 03]   A. A. Auer, J. Gauss, J. F. Staton. Quantitative prediction of gas-phase 13C nuclear magnetic shielding constants. *J. Chem. Phys.* **118**, 10407 (2003). [Cited on: p260]

[Becke 88]   A. D. Becke. Density-functional Exchange-energy Approximation with Correct Asymptotic-Behavior. *Phys. Rev. A* **38**, 3098–3100 (1988). [Cited on: p242]

[Becker 96]   E. D. Becker. Encyclopedia of Nuclear Magnetic Resonance, Chapter: Hydrogen bonding, pp 2409–2415. Wiley, Chichester (1996). [Cited on: p31]

[Benedict 98]   H. Benedict, H. H. Limbach, M. Wehlan, W. P. Fehlhammer, N. S. Golubev, R. Janoschek. Solid state N-15 NMR and theoretical studies of primary and secondary geometric H/D isotope effects on low-barrier NHN- hydrogen bonds. *J. Am. Chem. Soc.* **120**(12), 2939–2950 (1998). [Cited on: p35, 147]

[Bennett 95]   A. E. Bennett, C. M. Rienstra, M. Auger, K. V. Lakshmi, R. G. Griffin. Heteronuclear Decoupling in Rotating Solids. *J. Chem. Phys.* **103**, 6951–6958 (1995). [Cited on: p73]

[Berghold 00]   G. Berghold, C.J. Mundy, A.H. Romero, J. Hutter, M. Parrinello. General and efficient algorithms for obtaining maximally localized Wannier functions. *Phys. Rev. B* **61**, 10040 (2000). [Cited on: p261]

[Berglund 80]   B. Berglund, R. W. Vaughan. Correlations between Proton Chemical Shift Tensors, Deuterium Quadrupole Couplings, and Bond Distances for Hydrogen Bonds in Solids. *J. Chem. Phys.* **73**, 2037–2043 (1980). [Cited on: p34, 154]

[Berl 02]   V. Berl, M. Schmutz, M. J. Krische, R. G. Khoury, J. M. Lehn. Supramolecular polymers generated from heterocomplementary monomers linked through multiple hydrogen-bonding arrays - Formation, characterization, and properties. *Chemistry-A European Journal* **8**(5), 1227–1244 (2002). [Cited on: p29]

[Bernstein 02]   J. Bernstein. Polymorphism in molecular crystals. Oxford University Press, Oxford (2002). [Cited on: p32]

[Bielecki 89]   A. Bielecki, A. C. Kolbert, M. H. Levitt. Frequency-Switched Pulse Sequences: Homonuclear Decoupling and Dilute Spin NMR in Solids. *Chem. Phys. Lett.* **155**, 341–346 (1989). [Cited on: p33]

[Bielecki 90]   A. Bielecki, A.C Kolbert, H.J.M. de Groot, R.G. Griffin, M.H. Levitt. Frequency-Switched Lee-Goldburg Sequences in Solids. *Adv. Magn. Reson.* **14**, 111 (1990). [Cited on: p33]

[Bloembergen 53] N. Bloembergen, T. J. Rowland. On the Nuclear Magnetic Resonance in Metals and Alloys. *Acta Metall.* **1**, 731–746 (1953). [Cited on: p58]

[Blümich 90]   B. Blümich, A. Hagemeyer, D. Schaefer, K. Schmidt-Rohr, H. W. Spiess. Solid State NMR Spectroscopy in Polymer Science. *Adv. Mater.* **2**, 72–81 (1990). [Cited on: p80]

[Bouten 00]   R. Bouten, E. J. Baerends, E. van Lenthe, L. Visscher, G. Schreckenbach, T. Ziegler. Relativistic Effects for NMR Shielding Constants in Transition Metal Oxides Using the Zeroth-Order Regular Approximation. *J. Phys. Chem. A* **104**, 5600 (2000). [Cited on: p263]

[Brinkmann 00]   A. Brinkmann, M. Edén, M. H. Levitt. Synchronous Helical Pulse Sequences in Magic-angle Spinning Nuclear Magnetic Resonance. *J. Chem. Phys.* **112**, 8539–8554 (2000). [Cited on: p36, 80]

[Brinkmann 01]   A. Brinkmann, M. H. Levitt. Symmetry principles in the nuclear magnetic resonance of spinning solids: Heteronuclear recoupling by generalized Hartmann-Hahn sequences. *J. Chem. Phys.* **115**(1), 357–384 (2001). [Cited on: p37]

[Brown 99]   S. P. Brown, I. Schnell, J. D. Brand, K. Müllen, H. W. Spiess. An Investigation of $\pi - \pi$ Packing in a Columnar Hexabenzocoronene by Fast Magic-Angle Spinning and Double-Quantum ^{1}H Solid-State NMR Spectroscopy. *J. Am. Chem. Soc.* **121**, 6712–6718 (1999). [Cited on: p31]

[Brown 00]   S. P. Brown, I. Schnell, J. D. Brand, K. Müllen, H. W. Spiess. The Competing Effects of $\pi - \pi$ Packing and Hydrogen Bonding in a Hexabenzocoronene Carboxylic Acid Derivative: A ^1H Solid-state MAS NMR Investigation. *Phys. Chem. Chem. Phys.* **2**, 1735–1745 (2000). [Cited on: p36]

[Brown 01a]   S. P. Brown, T. Schaller, U. P. Seelbach, F. Koziol, C. Ochsenfeld, F. G. Klarner, H. W. Spiess. Structure and dynamics of the host-guest complex of a molecular tweezer: Coupling synthesis, solid-state NMR, and quantum- chemical calculations. *Angew. Chem. Int. Ed.* **40**(4), 717–720 (2001). [Cited on: p35]

[Brown 01b]   S. P. Brown, H. W. Spiess. Advanced Solid-state NMR Methods for the Elucidation of Structure and Dynamics of Molecular, Macromolecular and Supramolecular systems. *Chem. Rev.* **101**, 4125–4155 (2001). [Cited on: p28, 31, 33, 35, 79]

[Brown 01c]   S. P. Brown, X. X. Zhu, K. Saalwachter, H. W. Spiess. An investigation of the hydrogen-bonding structure in bilirubin by H-1 double-quantum magic-angle spinning solid-state NMR spectroscopy. *J. Am. Chem. Soc.* **123**(18), 4275–4285 (2001). [Cited on: p35, 36, 91, 94]

[Brown 02a]   S. P. Brown. Personal communication. Proton chemical shifts of hydrogen bonded protons varied by batch from Ishida. (2002). [Cited on: p33]

[Brown 02b]   S.P. Brown, M. Perez-Torralba, D. Sanz, R.M. Claramunt, L. Emsley. The Direct Detection of a Hydrogen Bond in the Solid State by NMR Through The Observation of a Hydrogen-Bond Mediated ^{15}N-^{15}N J Coupling. *J. Am. Chem. Soc.* **124**, 1152 (2002). [Cited on: p45]

[Bruker 97]   Bruker. Commercial MAS probeheads capable of $\omega_r/2\pi = 35$ kHz. Rapport technique, Bruker GMBH, Karlsruhr, Germany (1997). [Cited on: p34, 65, 109]

[Brunet 97]   P. Brunet, M. Simard, J. D. Wuest. Molecular tectonics. Porous hydrogen-bonded networks with unprecedented structural integrity. *J. Am. Chem. Soc.* **119**(11), 2737–2738 (1997). [Cited on: p31]

[Brunsfeld 01]   L. Brunsfeld, B. J. B. Folmer, E. W. Meijer, R. P. Sijbesma. Supramolecular Polymers. *Chem. Rev.* **101**, 4071–4097 (2001). [Cited on: p31]

[Brunsveld 02]   L. Brunsveld, J. A. J. M. Vekemans, J. H. K. K. Hirschberg, R. P. Sijbesma, E. W. Meijer. Hierarchical formation of helical supramolecular polymers via stacking of hydrogen-bonded pairs in water. *Proceedings Of The National Academy Of Sciences Of The United States Of America* **99**(8), 4977–4982 (2002). [Cited on: p31]

[Brycki 91]   B. Brycki, H. Maciejewska, B. Brzezinski, G. Zundel. Preparation and NMR characterisation of hydrogen bonding in 2- and 2,6-bis-(N,N-diethylaminomethyl)-4R-phenols. *J. Mol. Struct.* **246**, 61–71 (1991). [Cited on: p197, 205]

[Buda 00]   F. Buda, P. Giannozzi, F. Mauri. Density functional theory study of the structure and C-13 chemical shifts of retinylidene iminium salts. *J. Phys. Chem. B* **104**, 9048–9053 (2000). [Cited on: p262]

[Cairns 65]   T. Cairns, G. Eglinton. Hydrogen bonding in phenols. Part II. Alkyl substituted bis(hydroxyphenyl)alkanes (dinuclear novolaks). *J. Chem. Soc.*pp 5906–5913 (1965). [Cited on: p198]

[Calhorda 00]   M. J. Calhorda. Weak hydrogen bonds: theoretical studies. *Chem. Commun.*pp 801—809 (2000). [Cited on: p204]

[Carravetta 00]   M. Carravetta, M. Edén, X. Zhao, A. Brinkmann, M. H. Levitt. Symmetry Principles for the Design of Radiofrequency Pulse Sequences in the Nuclear Magnetic Resonance of Rotating Solids. *Chem. Phys. Lett.* **321**, 205–215 (2000). [Cited on: p73, 80]

[Castellano 98]   R. K. Castellano, J. Rebek. Formation of discrete, functional assemblies and informational polymers through the hydrogen-bonding preferences of calixarene aryl and sulfonyl tetraureas. *J. Am. Chem. Soc.* **120**(15), 3657–3663 (1998). [Cited on: p31]

[Chino 01]   K. Chino, M. Ashiura. Themoreversible cross-linking rubber using supramolecular hydrogen-bonding networks. *Macromolecules* **34**(26), 9201–9204 (2001). [Cited on: p29]

[Chirachanchai 01]   S. Chirachanchai, A. Laobuthee, K. Tashiro. Article in preparation. Cited as reference to further crystal structure of H,Me-N-pr and H,Et-N-Cy dimers. (2001). [Cited on: p106, 155]

[Chirachanchai 04]   S. Chirachanchai. Personal communication. Crystal structures of H,Me-N-Cy, H,Et-N-Cy and H,Me-N-Pr reported in chirachanckai01a but only H,Me-N-Cy avalable. (2004). [Cited on: p106, 155, 264]

[Chirachanckai 01]   S. Chirachanckai, A. Laobuthee, H. Ishida, K. Tashiro. Submitted for publication. *J. Am. Chem. Soc.* (2001). [Cited on: p264]

[Chirachanckai 02]   S. Chirachanckai, A. Laobuthee, H. Ishida, K. Tashiro. Unpublished. Cited as reference to further crystal structure of dimers. (2002). [Cited on: p155, 264]

[Christopher 92]   E.A. Christopher, R.K. Harris, R.A. Fletton. Assignments of solid-state 13C resonances for polymorphs of cortisone acetate using shielding tensor components. *Solid State NMR* **1**, 93–101 (1992). [Cited on: p32]

[Chuang 96]   I.-S. Chuang, G. J. Maciel. Probing Hydrogen Bonding and the Local Environment of Silanols on Silica Surfaces via Nuclear Spin Cross Polarization Dynamics. *J. Am. Chem. Soc.* **118**, 401–406 (1996). [Cited on: p32]

[Chutayothin 01]   P. Chutayothin, H. Ishida. ^{31}P NMR Spectroscopy in Mannich Chemistry - Monofunctional Benzoxazine Polymerization and Polymerization of p-Cresol, Formaldehyde, and Piperazine. Never published (2001). [Cited on: p230]

[Davis 76]   J. H. Davis, K. R. Jeffrey, M. Bloom, M. I. Valic, T. P. Higgs. Quadrupolar Echo Deuteron Magnetic Resonance Spectroscopy in Ordered Hydrocarbon Chains. *Chem. Phys. Lett.* **42**, 390–394 (1976). [Cited on: p76]

[De Paëpe 03]   G. De Paëpe, D. Sakellariou, P. Hodgkinson, S. Hediger, L. Emsley. Heteronuclear Decoupling in NMR of Liquid Crystals Using Continuous Phase Modulation. *Chem. Phys. Lett.* **368**, 511–522 (2003). [Cited on: p72]

[De Paul 00]   S.M De Paul, K. Saalwächter, R. Graf, H. W. Spiess. Sideband Patterns from Rotor-Encoded Longitudinal Magnetization in MAS Recoupling Experiments. *J. Magn. Reson.* **146**, 140–156 (2000). [Cited on: p96]

[Dean 72]   J. A. Dean (Hrsg.). Lange's Handbook of Chemistry. McGraw-Hill, New York (1972). [Cited on: p26, 205]

[deAzevedo 99]   E. R. deAzevedo, W.-G. Hu, T. J. Bonagamba, K. Schmidt-Rohr. Centerband-Only Detection of Exchange: Efficient Analysis of Dynamics in Solids by NMR. *J. Am. Chem. Soc.* **121**, 8411–8412 (1999). [Cited on: p80, 81]

[Detken 02]   A. Detken, E. H. Hardy, M. Ernst, B. H. Meier. Simple and Efficient Decoupling in Magic-angle Spinning Solid-state NMR: the XiX Scheme. *Chem. Phys. Lett.* **356**, 298–304 (2002). [Cited on: p73]

[Ditchfield 72]   Robert Ditchfield. Gauge including atomic orbitals. *J. Chem. Phys.* **56**, 5688 (1972). [Cited on: p260]

[Dunkers 95]   J. Dunkers, H. Ishida. Vibrational Assignments of 3,5-Dimethyl-bis(2-hydroxybenzyl)methylamine. *Spectrochim. Acta* **51A**(5), 855 (1995). [Cited on: p30, 38, 207]

[Dunkers 96]   J. Dunkers, E. A. Zarate, H. Ishida. The Crystal Structure and Hydrogen Bonding Characteristics of N,N-Bis(3,5-Dimethyl-2-hydroxybenzyl)methylamine, A Benzoxazine Dimer. *J. Phys. Chem.* **100**, 13514–13520 (1996). [Cited on: p30, 38, 149, 155, 175, 264]

[Dusold 00]   S. Dusold, A. Sebald. Annual reports on NMR spectroscopy, Band 41, Chapter: Dipolar Recoupling under Magic-Angle Spinning Conditions, pp 185–264. Academic Press (2000). [Cited on: p72, 80]

[Elena 04]   B. Elena, G. De Paëpe, L. Emsley. Direct spectral optimisation of proton-proton homonuclear dipolar decoupling in solid-state NMR. *Chem. Phys. Lett.* **398**(4-6), 532–538 (2004). [Cited on: p34]

[Ernst 87]   R. R. Ernst, G. Bodenhausen, A. Wokaun. Principles of Nuclear Magnetic Resonance in One and Two Dimensions. Clarendon Press, Oxford (1987). [Cited on: p35, 64, 77, 117]

[Ernst 01]   M. Ernst, A. Samoson, B. H. Meier. Low-power Decoupling in Fast Magic-angle Spinning NMR. *Chem. Phys. Lett.* **348**, 293–302 (2001). [Cited on: p72]

[Ernst 03]   M. Ernst. Heteronuclear Spin Decoupling in Solid-state NMR under Magic-angle Sample Spinning. *J. Magn. Reson.* **162**, 1–34 (2003). [Cited on: p72, 73]

[Ezuhara 99]   T. Ezuhara, K. Endo, Y. Aoyama. Helical coordination polymers from achiral components in crystals. Homochiral crystallization, homochiral helix winding in the solid state, and chirality control by seeding. *J. Am. Chem. Soc.* **121**(14), 3279–3283 (1999). [Cited on: p29]

[Feike 96a]   M. Feike, D. E. Demco, R. Graf, J. Gottwald, S. Hafner, H. W. Spiess. Broadband Multiple-Quantum NMR Spectroscopy. *J. Magn. Reson. A* **122**, 214–221 (1996). [Cited on: p83, 86]

[Feike 96b]   M. Feike, R. Graf, I. Schnell, C. Jäger, H. W. Spiess. Structure of Crystalline Phosphates from ^{31}P Double-Quantum NMR Spectroscopy. *J. Am. Chem. Soc.* **118**, 9631–9634 (1996). [Cited on: p35]

[Fischbach 02]   I. Fischbach, K. Saalwächter, T. Pakula, P. Minkin, A. Fechtenkötter, K. Müllen, H. W. Spiess. Structure and Dynamics in Columnar Dis-

cotic Materials: A Combined X-ray and Solid-State NMR Study of Hexabenzocoronene Derivatives. *J. Phys. Chem. B* **106**, 6408–6418 (2002). [Cited on: p143]

[Friedrich 98]   U. Friedrich, I. Schnell, S. P. Brown, A. Lupulescu, D. E. Demco, H. W. Spiess. Spinning-sideband patterns in multiple-quantum magic-angle spinning NMR spectroscopy. *Mol. Phys.* **95**, 1209–1227 (1998). [Cited on: p85, 91, 94]

[Frisch 98]   M. J. Frisch, G. W. Trucks, H. B. Schlegel, P. M. W. Gill, B. G. Johnson, M. A. Robb, J. R. Cheeseman, T. Keith, G. A. Petersson, J. A. Montgomery, K. Raghavachari, M. A. Al-Laham, V. G. Zakrzewski, J. V. Ortiz, J. B. Foresman, C. Y. Peng, P. Y. Ayala, W. Chen, M. W. Wong, J. L. Andres, E. S. Replogle, R. Gomperts, R. L. Martin, D. J. Fox, J. S. Binkley, D. J. Defrees, J. Baker, J. P. Stewart, M. Head-Gordon, C. Gonzalez, J. A. Pople. Gaussian 98. Computer Code (1998). [Cited on: p242]

[Fung 00]   B. M. Fung, A. K. Kithrin, K. Ermolaev. An Improved Broadband Decoupling Sequence for Liquid Crystals and Solids. *J. Magn. Reson.* **142**, 97–101 (2000). [Cited on: p73]

[Gan 97]   Z. Gan, R. R. Ernst. Frequency- and Phase-modulated Heteronuclear Decoupling in Rotating Solids. *Solid State NMR* **8**, 153–159 (1997). [Cited on: p73]

[Geen 94]   H. Geen, J.J. Titman, J. Gottwald, H.W. Spiess. Solid-state proton multiple-quantum NMR spectroscopy with fast magic angle spinning. *Chem. Phys. Lett.* **227**, 79–86 (1994). [Cited on: p35, 91]

[Geen 95]   H. Geen, J. J. Titman, J. Gottwald, H. W. Spiess. Spinning Sidebands in the Fast-MAS Multiple-Quantum Spectra of Protons in Solids. *J. Magn. Reson. A* **114**, 264–267 (1995). [Cited on: p85, 91]

[Gerstein 77]   B. C. Gerstein, C. Chow, R. G. Pembleton, R. C. Wilson. Utility Of Pulse Nuclear Magnetic-Resonance In Studying Protons In Coals. *J. Phys. Chem.* **81**(6), 565–570 (1977). [Cited on: p33]

[Gonze 89]   X. Gonze, J. P. Vigneron. Density-functional approach to nonlinear-response coefficients of solids. *Phys. Rev. B* **39**, 13120 (1989). [Cited on: p256]

[Gottwald 95]   J. Gottwald, D. E. Demco, R. Graf, H. W. Spiess. High-resolution Double-quantum NMR Spectroscopy of Homonuclear Spin Pairs and Proton Connectivities in Solids. *Chem. Phys. Lett.* **243**, 314–323 (1995). [Cited on: p35, 85]

[Goward 01]   G. R. Goward, I. Schnell, S.P. Brown, H.W. Spiess, H. Kim, H. Ishida. Investigation of an N...H hydrogen bond in a solid benzoxazine dimer by ^{1}H-^{15}N NMR correlation techniques under fast magic-angle spinning. *Magn. Reson. Chem.* **39**(S5-S17) (2001). [Cited on: p10, 15, 28, 30, 37, 39, 105, 109, 131, 143, 145, 146, 148, 152, 162, 170, 172, 174, 205, 264]

[Goward 02]   G. R. Goward, M. F. H. Schuster, D. Sebastiani, I. Schnell, H. W. Spiess. High-resolution solid-state NMR studies of imidazole-based proton conductors: Structure motifs and chemical exchange from ^{1}H NMR. *J. Phys. Chem. B* **106**(36), 9322–9334 (2002). [Cited on: p38, 149, 262]

[Goward 03]   G. Goward, D. Sebastiani, I. Schnell, H. W. Spiess, H.-D. Kim, H. Ishida. Benzoxazine Oligomers: Evidence for a Helical Structure from Solid-State NMR Spectroscopy and DFT-Based Dynamics and Chemical Shift Calculations. *J. Am. Chem. Soc.* **125**(125), 5792–5800 (2003). [Cited on: p10, 28, 30, 35, 37, 38, 39, 105, 149, 161, 175, 177, 187, 189, 262, 264]

[Graf 96]   R. Graf, D. E. Demco, J. Gottwald, S. Hafner, H. W. Spiess. Dipolar couplings and internuclear distances by double-quantum nuclear magnetic resonance spectroscopy of solids. *J. Chem. Phys.* **106**, 885–895 (1996). [Cited on: p85]

[Graf 97]   R. Graf, D. E. Demco, J. Gottwald, S. Hafner, H. W. Spiess. Dipolar couplings and internuclear distances by double-quantum nuclear magnetic resonance spectroscopy of solids. *J. Chem. Phys.* **106**(3), 885–895 (1997). [Cited on: p35]

[Graf 98a]   R. Graf. *Hochauflösende Doppelquanten-NMR-Spektroskopie an amorphen Polymeren*. Dissertation, Universität Mainz (1998). [Cited on: p89]

[Graf 98b]   R. Graf, D. E. Demco, S. Hafner, H. W. Spiess. Selective Residual Dipolar Couplings in Cross-linked Elastomers by ^{1}H Double-quantum NMR Spectroscopy. *Solid State NMR* **12**, 139–152 (1998). [Cited on: p89]

[Gregor 99]   T. Gregor, F. Mauri, R. Car. A comparison of methods for the calculation of NMR chemical shifts. *J. Chem. Phys.* **111**, 1815–1822 (1999). [Cited on: p260, 263]

[Grey 93]   C. P. Grey, A. K. Cheetham, C. M. Dobson. Temperature-Dependent Solid-State ^{119}Sn MAS NMR Of $Nd_2Sn_2O_7$, $Sm_2Sn_2O_7$, and $Y_{1.8}Sm_{0.2}Sn_2O_7$ - 3 Sensitive Chemical-Shift Thermometers. *Journal Of Magnetic Resonance Series A* **101**(3), 299–306 (1993). [Cited on: p241]

[Grimmer 97]   A.-R. Grimmer, A. Kretschmer, V. B. Cajipe. Influence of magic angle spinning on sample temperature. *Magn. Reson. Chem.* **35**, 86 (1997). [Cited on: p241]

[Gu 96]   Z. T. Gu, C. F. Ridenour, C. E. Bronnimann, T. Iwashita, A. J. McDermott. Hydrogen bonding and distance studies of amino acids and peptides using solid state 2D H-1-C-13 heteronuclear correlation spectra. *J. Am. Chem. Soc.* **118**, 822–829 (1996). [Cited on: p32]

[Gullion 89a]   T. Gullion, J. Schaefer. Detection of Weak Heteronuclear Dipolar Coupling by Rotational-Echo Double-Resonance Nuclear Magnetic Resonance. *Adv. Magn. Reson.* **13**, 57–83 (1989). [Cited on: p81]

[Gullion 89b]   T. Gullion, J. Schaefer. Rotational-Echo Double-Resonance NMR. *J. Magn. Reson.* **81**, 196–200 (1989). [Cited on: p37, 80, 81]

[Gullion 90]   T. Gullion, D. B. Baker, M. S. Conradi. New, Compensated Carr-Purcell Sequences. *J. Magn. Reson.* **89**, 479–484 (1990). [Cited on: p96]

[Gullion 97]   T. Gullion. Measurement of Heteronuclear Dipolar Interactions by Rotational-Echo, Double-Resonance Nuclear Magnetic Resonance. *Magn. Reson. Rev.* **17**, 83–131 (1997). [Cited on: p80]

[Gullion 98]   T. Gullion. Introduction to rotational-echo, double-resonance NMR. *Concepts In Magnetic Resonance* **10**(5), 277–289 (1998). [Cited on: p37]

[Hahn 50]   E. L. Hahn. Spin Echoes. *Phys. Rev.* **80**, 580–594 (1950). [Cited on: p76, 123]

[Hamilton 68]   W. C. Hamilton, J. A. Ibers. Hydrogen Bonding in Solids. Benjamin, New York (1968). [Cited on: p31]

[Harris 88]   R. K. Harris, P. Jackson, L. H. Merwin, B. J. Say, G. J. Hagele. Perspectives in High-Resolution Solid-State Nuclear Magnetic-Resonance, with Emphasis on Combined Rotation and Multiple-Pulse Spectroscopy. *J. Chem. Soc. Faraday Trans.* **84**, 3649–3672 (1988). [Cited on: p34, 154]

[Harris 90]   R.K. Harris, A. M. Kenwright, B. J. Say, R.R. Yeung, R. A. Fletton, R.W. Lancaster, G.L. Hardgrove. Cross-polarization/magic-angle spinning NMR studies of polymorphism: Cortisone acetate. *Spectrochim. Acta* **46A**, 927–935 (1990). [Cited on: p32]

[Harte 05]   S. M. Harte, A. Parkin, A. Goeta, C. C. Wilson. Using neutrons and X-rays to study the effect of temperature on the short hydrogen bond in potassium hydrogen phthalate. *J. Mol. Struct.* **741**(1-3), 93–96 (2005). [Cited on: p31]

[Helgaker 99]   Trygve Helgaker, Michal Jaszunski, Kenneth Ruud. Ab initio methods for the calculation of NMR shielding and indirect spin–spin coupling constants. *Chem. Rev.* **99**, 293 (1999). [Cited on: p260]

[Hemvichian 01]   K. Hemvichian, H. Ishida. Thermal decomposition processes in polybenzoxazines investigated by TGA and GC-MS. *Abstracts Of Papers Of The American Chemical Society* **222**, 102–POLY (2001). [Cited on: p106]

[Hemvichian 02a] K. Hemvichian, H. Ishida. Thermal decomposition processes in aromatic amine-based polybenzoxazines investigated by TGA and GC-MS. *Polymer* **43**(16), 4391–4402 (2002). [Cited on: p106]

[Hemvichian 02b] K. Hemvichian, A. Laobuthee, S. Chirachanchai, H. Ishida. Thermal decomposition processes in polybenzoxazine model dimers investigated by TGA-FTIR and GC-MS. *Polymer Degrad. Stabil.* **76**(1), 1–15 (2002). [Cited on: p106]

[Hemvichian 05]   K. Hemvichian, H. D. Kim, H. Ishida. Identification of volatile products and determination of thermal degradation mechanisms of polybenzoxazine model oligomers by GC-MS. *Polymer Degrad. Stabil.* **87**(2), 213–224 (2005). [Cited on: p30, 106, 175]

[Herzfeld 80]   J. Herzfeld, A. E. Berger. Sideband Intensities in NMR Spectra of Samples Spinning at the Magic Angle. *J. Chem. Phys.* **73**, 6021–6030 (1980). [Cited on: p79]

[Hing 92]   A. W. Hing, S. Vega, J. Schaefer. Transferred-Echo Double-Resonance NMR. *J. Magn. Reson.* **96**, 205–209 (1992). [Cited on: p81, 96, 97]

[Hohenberg 64]   P. Hohenberg, W. Kohn. Inhomogeneous Electron Gas. *Phys. Rev.* **136**, B864 (1964). [Cited on: p257]

[Hohwy 98]   M. Hohwy, H. J. Jakobsen, M. Edén, M. H. Levitt, N. C. Nielsen. Broadband dipolar recoupling in the nuclear magnetic resonance of rotating solids: A compensated C7 pulse sequence. *J. Chem. Phys.* **108**, 2686–2694 (1998). [Cited on: p36]

[Hong 00]   M. Hong.   Solid-state NMR Determination of ^{13}Cα Chemical Shift Anisotropies for the Identification of Protein Secondary Structure. *J. Am. Chem. Soc.* **122**, 3762–3770 (2000). [Cited on: p81]

[Hunt 74]   M. J. Hunt, A. L. Mackay.   Deuterium and Nitrogen Pure Quadrupole-Resonance in Deuterated Amino-Acids. *J. Magn. Reson.* **15**, 402–414 (1974). [Cited on: p32]

[Hutter 95]   J. Hutter, P. Ballone, M. Bernasconi, P. Focher, E. Fois, S. Goedecher, M. Parrinello, M. Tucherman.   CPMD Computer Code (1995). [Cited on: p242]

[Hutter 04]   Jurg Hutter et al.   Computer code CPMD, version 3.9 (2004).   Copyright IBM Corp. and MPI-FKF Stuttgart, http://www.cpmd.org. [Cited on: p262]

[Inabe 94]   T. Inabe, I. Luneau, T. Mitani, Y. Maruyama, S. Takeda. *Bull. Chem. Soc. Jpn.* **67**, 843 (1994). [Cited on: p31]

[Ishida 95]   H. Ishida, Y. Rodriguez. Curing Kinetics Of A New Benzoxazine-Based Phenolic Resin By Differential Scanning Calorimetry.   *Polymer* **36**(16), 3151–3158 (1995). [Cited on: p29]

[Ishida 96]   H. Ishida, D. J. Allen. Physical and Mechanical Characterization of Near-Zero Shrinkage Polybenzoxazines. *J. Polym. Sci. Phys. Ed.* **34**, 1019 (1996). [Cited on: p29]

[Ishida 97]   H. Ishida, H. Y. Low.   A Study on the Volumetric Expansion of Benzoxazine-Based Phenolic Resin.   *Macromolecules* **30**, 1099 (1997). [Cited on: p29, 38]

[Ishida 98]   H. Ishida, C. M. Krus. Synthesis and characterization of structurally uniform model oligomers of polybenzoxazine. *Macromolecules* **31**(8), 2409–2418 (1998). [Cited on: p30, 175]

[Ishida 02]   H. Ishida. Personal communication. Me,Me-*N-Et synthesis by same method as Me,Me-^{15}N-Me. (2002). [Cited on: p162]

[Ishida 03]   H. Ishida. Personal communication. Requested X-ray structure of continious hydrogen-bonding structure unavalable. (2003). [Cited on: p264]

[Jakobsen 96]   H. J. Jakobsen. Encyclopedia of Nuclear Magnetic Resonance, Band 1, pp 398. Wiley: Chichester (1996). [Cited on: p34]

[Jaroniec 00]   C. P. Jaroniec, B. A. Tounge, C. M. Riestra, J. Herzfeld, R. G. Griffin. Recoupling of Heteronuclear Dipolar Interactions with Rotational-Echo Double-Resonance at High Magic-Angle Spinning Frequencies. *J. Magn. Reson.* **146**, 132–139 (2000). [Cited on: p95]

[Jeener 71]   J. Jeener. 2D NMR. *Ampère Summer School, Basko Polje, Yogoslavia* (1971). [Cited on: p35, 77]

[Jeener 79]   J. Jeener, B. H. Meier, P. Bachmann, R.R. Ernst. Investigation of exchange processes by two-dimensional NMR spectroscopy. *J. Chem. Phys.* **71**, 4546 (1979). [Cited on: p78]

[Jeffrey 75]   G. A. Jeffrey, Y. Yeon. *Acta Cryst. B* **31**, 2345 (1975). [Cited on: p31]

[Jeffrey 86]   G. A. Jeffrey, Y. Yeon. The Correlation Between Hydrogen-Bond Lengths and Proton Chemical Shifts in Crystals. *Acta Cryst. B* **42**, 410–413 (1986). [Cited on: p31, 34, 110, 150, 154]

[Jeffrey 91]   G.A Jeffrey, W. Saenger. Hydrogen Bonding in Biological Structures. Springer-Verlag: New York (1991). [Cited on: p31]

[Jones 89]   R. O. Jones, O. Gunnarsson. The Density Functional Formalism, Its Applications And Prospects. *Reviews Of Modern Physics* **61**(3), 689–746 (1989). [Cited on: p38]

[Kaupp 98]   M Kaupp, O. L. Malkina. Density functional analysis of C-13 and H-1 chemical shifts and bonding in mercurimethanes and organomercury hydrides: The role of scalar relativistic, spin-orbit, and substituent effects. *J. Chem. Phys.* **108**, 3648–3659 (1998). [Cited on: p260]

[Keith 92]   T. A. Keith, R. W. F. Bader. Calculation of magnetic response properties using atoms in molecules. *Chem. Phys. Lett.* **194**, 1 (1992). [Cited on: p260]

[Keith 93]   T. A. Keith, R. F. W. Bader. Calculation Of Magnetic Response Properties Using A Continuous Set Of Gauge Transformations. *Chem. Phys. Lett.* **210**(1-3), 223–231 (1993). [Cited on: p260]

[Khitrin 03]   A. K. Khitrin, Toshimichi Fujiwara, Hideo Akutsu. Phase-modulated Heteronuclear Decoupling in NMR of Solids. *J. Magn. Reson.* **162**, 46–53 (2003). [Cited on: p72]

[Kim 01]   H-D. Kim, H. Ishida. Study on the chemical stability of benzoxazine-based phenolic resins in carboxylic acids. *J. Appl. Polym. Sci.* **79**(7), 1207–1219 (2001). [Cited on: p29, 197, 202]

[Kim 02]   H-D. Kim, H. Ishida. A Study on Hydrogen-Bonded Network Structure of Polybenzoxazines. *J. Phys. Chem. A* **106**, 3271–3280 (2002). [Cited on: p197, 202, 204, 207, 210, 233, 234]

[Kim 03a]   H-D. Kim, H. Ishida. Accepted for publication. *J. Macromol. Chem. Macromol. Symp.* (2003). [Cited on: p264]

[Kim 03b]   H-D. Kim, H. Ishida. Model Compounds Study on the Network Structure of Polybenzoxazines. *Macromolecules* **36**(22), 8320–8329 (2003). [Cited on: p30, 197, 198, 202, 204, 207, 210, 218, 234]

[Kim 03c]   H-D. Kim, H. Ishida. A study on hydrogen bonding in controlled-structure benzoxazine model oligomers. *Macromol. Symp.* **195**(1), 123–140 (2003). [Cited on: p30, 161, 175, 187, 207, 264]

[Kimura 00]   H. Kimura, A. Shoji, H. Sugisawa, K. Deguchi, A. Naito, H. Saito. Determination of N-H bond lengths of ^{15}N-labeled poly(L-alanines) by ^{1}H CRAMPS NMR. *Macromolecules* **33**(18), 6627–6629 (2000). [Cited on: p34]

[Kobayashi 88]   K. Kobayashi, M. Tsukada. Rigorous theory for chemical shifts in crystals: application to graphite. *Phys. Rev. B* **38**, 8566–8578 (1988). [Cited on: p261]

[Köhler 97]   F.H. Köhler, X. Xie. Vanadocene as a Temperature Standard for ^{13}C and ^{1}H MAS NMR and for Solution-State NMR Spectroscopy. *Magn. Reson. Chem.* **35**, 487–492 (1997). [Cited on: p120, 241]

[Kohn 65]   W. Kohn, L. J. Sham. Self-Consistent Equations Including Exchange and Correlation Effects. *Phys. Rev.* **140**, A1133 (1965). [Cited on: p257]

[Kutzelnigg 90]   W. Kutzelnigg, U. Fleischer, Michael Schindler. NMR basic principles and progress, Band 23, Chapter: The IGLO method, pp 165. Springer-Verlag, Berlin Heidelberg 1990 (1990). [Cited on: p260]

[Lahiri 00]   S. Lahiri, J. L. Thompson, J. S. Moore. Solvophobically driven pi-stacking of phenylene ethynylene macrocycles and oligomers. *J. Am. Chem. Soc.* **122**(46), 11315–11319 (2000). [Cited on: p31]

[Langer 99]   B. Langer, I. Schnell, H. W. Spiess, A.-R. Grimmer. Temperature Calibration under Ultrafast MAS Conditions. *J. Magn. Reson.* **138**, 182–186 (1999). [Cited on: p120, 241]

[Langer 01]   B. Langer. *Untersuchung supramolekularer Ordnungsphänomene mittels* ^{1}*H-MAS-Mehrquanten-NMR-Spektroskopie in festen und in flüssigkristallinen Phasen.* Dissertation, Universität Mainz (2001). [Cited on: p89]

[Laobuthee 01]   A. Laobuthee, S. Chirachanchai, H. Ishida, K. Tashiro. Asymmetric Mono-oxazine: An Inevitable Product from Mannich Reaction of Benzoxazine Dimers. *J. Am. Chem. Soc.* **123**, 9947–9955 (2001). [Cited on: p30, 106, 125, 149, 155, 158, 264]

[Lee 65]   M. Lee, W. I. Goldburg. Nuclear-Magnetic-Resonance Line Narrowing by a Rotating rf Field. *Phys. Rev. A* **140**, 1261–1271 (1965). [Cited on: p33]

[Lee 95]   Y. K. Lee, N. D. Kurur, M. Helmle, O. G. Johannessen, N. C. Nielsen, M. H. Levitt. Efficient Dipolar Recoupling In The Nmr Of Rotating Solids - A Sevenfold Symmetrical Radiofrequency Pulse Sequence. *Chem. Phys. Lett.* **242**(3), 304–309 (1995). [Cited on: p35, 36, 80]

[Lehn 78]   J.-M. Lehn. Cryptates - Inclusion Complexes of Macropolycyclic Receptor Molecules. *Pure Appl. Chem.* **50**, 871–892 (1978). [Cited on: p28]

[Lehn 93]   J. M. Lehn. Supramolecular Chemistry. *Science* **260**, 1762–1763 (1993). [Cited on: p31]

[Lehn 95]   J.-M. Lehn. Supramolecular Chemistry. VCH, Weinheim (1995). [Cited on: p28]

[Lesage 01]   A. Lesage, L Duma, D. Sakellariou, L. Emsley. Improved Resolution in Proton NMR Spectroscopy of Powdered Solids. *J. Am. Chem. Soc.* **123**, 5747–5752 (2001). [Cited on: p34]

[Levitt 01]   M.H. Levitt. Spin Dynamics: Basics of Nuclear Magnetic Resonance. Wiley (2001). [Cited on: p45]

[Low 98]   H. Y. Low, H. Ishida. Mechanistic study on the thermal decomposition of polybenzoxazines: Effects of aliphatic amines. *J. Polym. Sci. Polym. Phys.* **36**(11), 1935–1946 (1998). [Cited on: p221]

[Low 99a]   H. Y. Low, Ishida. H. Structural effects of phenols on the thermal and thermo-oxidative degradation of polybenzoxazines. *Polymer* **40**, 4365–4376 (1999). [Cited on: p221]

[Low 99b]   H. Y. Low, H. Ishida. An investigation of the thermal and thermo-oxidative degradation of polybenzoxazines with a reactive functional group. *J. Polym. Sci. Polym. Phys.* **37**(7), 647–659 (1999). [Cited on: p221]

[Lowe 59]   I. J. Lowe. Free Induction Decays of Rotating Solids. *Phys. Rev. Lett.* **2**, 285–287 (1959). [Cited on: p33, 65]

[Lui 96]   J.P. Lui, H. Ishida. Polymeric Materials Encyclopedia, pp 484–494. CRC Press Florida (1996). [Cited on: p29]

[Ma 65]   J. C. N. Ma, E. W. Warnhoff. On use of nuclear magnetic resonance for detection estimation and characterisation of N-methyl groups. *Can. J. Chem.* **43**, 1849 (1965). [Cited on: p197]

[Macho 01]   V. Macho, L. Brombacher, H. W. Spiess. The NMR-WEBLAB: an Internet Approach to NMR Lineshape Analysis. *Appl. Magn. Res.* **20**, 405–432 (2001). [Cited on: p76]

[Maciel 90]   G. E. Maciel, C. E. Bronnimann, B. L. Hawkins. High-Resolution ^{1}H nuclear magnetic resonance in solids via CRAMPS. *Adv. Magn. Reson.* **14**, 125–150 (1990). [Cited on: p33]

[Macko 00]   J. A. Macko, H. Ishida. Behavior of a Bisphenol-A-based Polybenzoxazine Exposed to Ultraviolet Radiation. *J. Polym. Sci. Polym. Phys.* **38**, 2687 (2000). [Cited on: p29]

[Magyarfalvi 03] G. Magyarfalvi. Assessment of density functional methods for nuclear magnetic resonance shielding calculations. *J. Chem. Phys.* **119**, 1350 (2003). [Cited on: p260]

[Malkina 98]   O. L. Malkina, B Schimmelpfennig, M Kaupp, B. A. Hess, P Chandra, U Wahlgren, VG Malkin. Spin-orbit corrections to NMR shielding constants from density functional theory. How important are the two-electron terms? *Chem. Phys. Lett.* **296**, 93–104 (1998). [Cited on: p260]

[Malkina 00]   O. L. Malkina, J. Vaara, B. Schimmelpfennig, M. Munzarova, V. G. Malkin, M. Kaupp. Density functional calculations of electronic g-tensors using spin-orbit pseudopotentials and mean-field all-electron spin-orbit operators. *J. Am. Chem. Soc.* **122**, 9206–9218 (2000). [Cited on: p260]

[Maricq 79]   M. M. Maricq, J. S. Waugh. NMR in Rotating Solids. *J. Chem. Phys.* **70**, 3300–3316 (1979). [Cited on: p67]

[Marion 83]   D. Marion, K. Wüthrich. Application of Phase Sensitive Two-dimensional Correlated Spectroscopy (COSY) for Measurements of H-1 H-1 Spin-spin Coupling-constants in Proteins. *Biochem. Biophys. Res. Commun.* **113**, 967–974 (1983). [Cited on: p84]

[Marion 89]   D. Marion, M. Ikura, R. Tschudin, A. Bax. Rapid Recording of 2D NMR-Spectra without Phase Cycling- Application to the Study of Hydrogen-Exchange in Proteins. *J. Magn. Reson.* **85**, 393–399 (1989). [Cited on: p84]

[Mason 87]   J. Mason. Multinuclear NMR, Chapter: Nitrogen. Plenum Press, New York (1987). [Cited on: p146, 148, 170]

[Mauri 96a]   Francesco Mauri, Steven Louie. Magnetic Susceptibility of Insulators from First Principles. *Phys. Rev. Lett.* **76**, 4246–4249 (1996). [Cited on: p261]

[Mauri 96b]   Francesco Mauri, Bernd Pfrommer, Stephen Louie. Ab initio Theory of NMR Chemical Shifts in Solids and Liquids. *Phys. Rev. Lett.* **77**, 5300–5303 (1996). [Cited on: p261]

[Mauri 97]   Francesco Mauri, Bernd Pfrommer, S. Louie. Ab initio NMR chemical shift of diamond, chemical-vapor-deposited diamond, and amorphous carbon. *Phys. Rev. Lett.* **79**, 2340 (1997). [Cited on: p262]

[Mauri 99]   F. Mauri, B. Pfrommer, S. Louie. Signature of surface states on NMR chemical shifts: A theoretical prediction. *Phys. Rev. B* **60**, 2941–2945 (1999). [Cited on: p262]

[Mauri 00]   Francesco Mauri, Alfredo Pasquarello, Bernd G. Pfrommer, Young-Gui Yoon, Steven G. Louie. Si-O-Si bond-angle distribution in vitreous silica from first-principles Si-29 NMR analysis. *Phys. Rev. B* **62**, R4786–R4789 (2000). [Cited on: p263]

[Mauri 01]   Francesco Mauri, N. Vast, C. J. Pickard. Atomic structure of icosahedral B_4C boron carbide from a first principles analysis of NMR spectra. *Phys. Rev. Lett.* **88**, 085506 (2001). [Cited on: p262]

[McQuade 97]   D. T. McQuade, S. L. McKay, D. R. Powell, S. H. Gellman. Indifference to hydrogen bonding in a family of secondary amides. *J. Am. Chem. Soc.* **119**, 8528–8532 (1997). [Cited on: p31]

[Medek 00]   A Medek, L Frydman. A multinuclear solid-state NMR analysis of vitamin B12 in its different polymorphic forms. *J. Am. Chem. Soc.* **122**, 684–691 (2000). [Cited on: p32]

[Mehring 83]   M. Mehring. High Resolution NMR of Solids. Springer-Verlag, Berlin (1983). [Cited on: p33, 46, 58, 75]

[Metz 94]   G. Metz, X. Wu, S. O. Smith. Ramped-Amplitude Cross Polarization in Magic-Angle-Spinning NMR. *J. Magn. Reson. A* **110**, 219–227 (1994). [Cited on: p75]

[Monkman 02]   A. P. Monkman, L. O. Palsson, R. W. T. Higgins, C. S. Wang, M. R. Bryce, A. S. Batsanov, J. A. K. Howard. Protonation and subsequent intramolecular hydrogen bonding as a method to control chain structure and tune luminescence in heteroatomic conjugated polymers. *J. Am. Chem. Soc.* **124**(21), 6049–6055 (2002). [Cited on: p29]

[Morris 79]   G. A. Morris, R. Freeman. Enhancement of Nuclear Magnetic Resonance Signals by Polarization Transfer. *J. Am. Chem. Soc.* **101**, 760–761 (1979). [Cited on: p98]

[Munowitz 87]   M. Munowitz, A. Pines. Principles and Applications of Multiple-Quantum NMR. *Adv. Chem. Phys.* **66**, 1–152 (1987). [Cited on: p83]

[Munzarova 99]   M Munzarova, M Kaupp. A critical validation of density functional and coupled-cluster approaches for the calculation of EPR hyperfine coupling constants in transition metal complexes. *J. Phys. Chem. A* **103**, 9966–9983 (1999). [Cited on: p260]

[Naito 96]   A. Naito, K. Nishimura, S. Kimura, S. Tuzi, M. Aida, N. Yasuoka, H. Saito. Determination of the three-dimensional structure of a new crystalline form of N-acetyl-Pro-Gly-Phe as revealed by ^{13}C REDOR, X-ray diffraction and molecular dynamics simulations. *J. Phys. Chem.* **100**, 14995–15004 (1996). [Cited on: p95]

[Naito 98]   A. Naito, S. Tuzi, H. Saito. Solid State NMR of Polymers, Chapter: Dipolar interactions and interatomic distances, pp 23–49. Elsevier, Amsterdam (1998). [Cited on: p95]

[Nakai 89]   T. Nakai, J. Ashida, T. Terao. Influence of small-amplitude motions on two-dimensional NMR powder patterns. Anisotropic vibrations in calcium formate. *Mol. Phys.* **67**, 839–847 (1989). [Cited on: p152]

[Nielsen 94]   N. C. Nielsen, H. Bilsøe, H. J. Jakobsen, M.H. Levitt. Double-quantum Homonuclear Rotary Resonance: Efficient Dipolar Recovery in Magic-angle Spinning Nuclear Magnetic Resonance. *J. Chem. Phys.* **101**, 1805–1812 (1994). [Cited on: p72]

[Ning 94]   X. Ning, H. Ishida. Phenolic Materials Via Ring-Opening Polymerization - Synthesis And Characterization Of Bisphenol-A Based Benzoxazines And Their Polymers. *J. Polym. Sci. Polym. Chem.* **32**(6), 1121–1129 (1994). [Cited on: p29]

[Oas 88]   T. G. Oas, R. G. Griffin, M. H. Levitt. Rotary Resonance Recoupling of Dipolar Interactions in Solid-state Nuclear Magnetic Resonance Spectroscopy. *J. Chem. Phys.* **89**, 692–695 (1988). [Cited on: p72]

[Ochsenfeld 97] C. Ochsenfeld, M. Head-Gordon. A reformulation of the coupled perturbed self-consistent field equations entirely within a local atomic orbital density matrix-based scheme. *Chem. Phys. Lett.* **270**(5-6), 399–405 (1997). [Cited on: p38]

[Ochsenfeld 00] C. Ochsenfeld. An *ab initio* Study of the Relation between NMR Chemical Shifts and Solid-state Structures: Hexabenzocoronene Derivatives. *Phys. Chem. Chem. Phys.* **2**, 2153–2159 (2000). [Cited on: p38]

[Ochsenfeld 01] C. Ochsenfeld, S. P. Brown, I. Schnell, J. Gauss, H. W. Spiess. Structure assignment in the solid state by the coupling of quantum mechanical calculations with NMR experiments: A columnar hexabenzocoronene derivative. *J. Am. Chem. Soc.* **123**, 2597–2606 (2001). [Cited on: p38]

[Ohno 97]   K. Ohno, F. Mauri, S. Louie. Magnetic susceptibility of semiconductors by an all-electron first-principles approach. *Phys. Rev. B* **56**, 1009 (1997). [Cited on: p263]

[Pake 48]   G. E. Pake. Nuclear Resonance Absorption in Hydrated Crystals: Fine Structure of the Proton Line. *J. Chem. Phys.* **16**, 327–336 (1948). [Cited on: p56]

[Parkin 04]   A. Parkin, S. M. Harte, A. E. Goeta, C. C. Wilson. Imaging proton migration from X-rays and neutrons. *New J. Chem* **28**(6), 718–721 (2004). [Cited on: p31]

[Parkinson 58]   C. N. Parkinson. Parkinson's law : or the pursuit of progress. John Murray, London (1958). [Cited on: p288]

[Parkinson 06]   M Parkinson, M Zakharov, D. Sebastiani. Publication in preparation. Comparision of Me,Me-N-Me and H,Me-N-Cy simulations with full periodic boundary conditions. (2006). [Cited on: p158]

[Percec 98]   V. Percec, C. H. Ahn, G. Ungar, D. J. P. Yeardley, M. Moller, S. S. Sheiko. Controlling polymer shape through the self-assembly of dendritic side-groups. *Nature* **391**(6663), 161–164 (1998). [Cited on: p29]

[Percec 02]   V. Percec, M. Glodde, T. K. Bera, Y. Miura, I. Shiyanovskaya, K. D. Singer, V. S. K. Balagurusamy, P. A. Heiney, I. Schnell, A. Rapp, H. W. Spiess,

S. D. Hudson, H. Duan. Self-organisation of Supramolecular Helical Dendrimers into Complex Electronic Materials. *Nature* **419**, 384–387 (2002). [Cited on: p31]

[Pfrommer 00]   B. Pfrommer, F. Mauri, S. Louie. NMR chemical shifts of ice and liquid water: The effects of condensation. *J. Am. Chem. Soc.* **122**, 123–129 (2000). [Cited on: p262]

[Piana 01]   Stefano Piana, Daniel Sebastiani, Paolo Carloni, Michele Parrinello. Ab Initio Molecular Dynamics-Based Assignment of the Protonation State of Pepstatin A/HIV-1 Protease Cleavage Site. *J. Am. Chem. Soc.* **122**, 123 (2001). [Cited on: p262]

[Pickard 01]   Chris J. Pickard, Francesco Mauri. All-electron magnetic response with pseudopotentials: NMR chemical shifts. *Phys. Rev. B* **63**, 245101 (2001). [Cited on: p263]

[Pimentel 60]   G. C. Pimentel, A. L. McClellan. The Hydrogen Bond. Freeman and Company, London (1960). [Cited on: p198]

[Pines 72]   A. Pines, W.-K. Rhim, J. S. Waugh. Homogeneous and Inhomogeneous Nuclear Spin Echos in Solids. *J. Magn. Reson.* **6**, 457–465 (1972). [Cited on: p74]

[Pines 73]   A. Pines, M. G. Gibby, J. S. Waugh. Proton-enhanced NMR of Dilute Spins in Solids. *J. Chem. Phys.* **59**, 569–590 (1973). [Cited on: p74]

[Powles 63]   J. G. Powles, J. H. Strange. Zero Time Resolution Nuclear Magnetic Transients in Solids. *Proc. Phys. Soc. Lond.* **82**, 60 (1963). [Cited on: p76]

[Profeta 03]   M. Profeta, Francesco Mauri, C. J. Pickard. Accurate first principles prediction of O-17 NMR parameters in SiO2: Assignment of the zeolite ferrierite spectrum. *J. Am. Chem. Soc.* **125**, 541–548 (2003). [Cited on: p263]

[Putrino 00]   A. Putrino, D. Sebastiani, M. Parrinello. Generalized variational density functional perturbation theory. *J. Chem. Phys.* **113**, 7102–7109 (2000). [Cited on: p256, 262]

[Ramsey 50a]   N. F. Ramsey. The Internal Diamagnetic Field Correction in Measurements of the Proton Magnetic Moment. *Phys. Rev.* **77**, 567 (1950). [Cited on: p260]

[Ramsey 50b]   N. F. Ramsey. Magnetic Shielding of Nuclei in Molecules. *Phys. Rev.* **78**, 699 (1950). [Cited on: p260]

[Ramsey 52]   N. F. Ramsey. Chemical Effects in Nuclear Magnetic Resonance and in Diamagnetic Susceptibility. *Phys. Rev.* **86**, 243 (1952). [Cited on: p260]

[Rapp 03]   Almut Rapp, Ingo Schnell, Daniel Sebastiani, Steven P. Brown, Virgil Percec, Hans Wolfgang Spiess. Supramolecular Assembly of Dendritic Polymers Elucidated by ^{1}H and ^{13}C Solid-State MAS NMR Spectroscopy. *J. Am. Chem. Soc.* **125**, 13284–13297 (2003). [Cited on: p143, 263]

[Romero 02]   Aldo Humberto Romero, Daniel Sebastiani, Ricardo Ramírez, Miguel Kiwi. Is NMR the tool to characterize the structure of C_{20} isomers? *Chem. Phys. Lett.* **366**, 134–140 (2002). [Cited on: p262]

[Russell 98a]   V. M. Russell, J. L. Koenig, H. Y. Low, H. Ishida. Study of the characteriza-
tion and curing of a phenyl benzoxazine using N-15 solid-state nuclear
magnetic resonance spectroscopy. *J. Appl. Polym. Sci.* **70**(7), 1401–1411
(1998). [Cited on: p221]

[Russell 98b]   V. M. Russell, J. L. Koenig, H. Y. Low, H. Ishida. Study of the characteriza-
tion and curing of benzoxazines using C-13 solid-state nuclear magnetic
resonance. *J. Appl. Polym. Sci.* **70**(7), 1413–1425 (1998). [Cited on: p221,
228]

[Saalwächter 99] K. Saalwächter, R. Graf, H. W. Spiess. Recoupled Polarization Transfer
Heteronuclear Multiple-Quantum Correlation in Solids under Ultra-fast
MAS. *J. Magn. Reson.* **140**, 471–476 (1999). [Cited on: p37, 96]

[Saalwächter 01a] K. Saalwächter, R. Graf, H. W. Spiess. Recoupled Polarization-Transfer
Methods for Solid-State ^{1}H-^{13}C Heteronuclear Correlation in the Limit of
Fast MAS. *J. Magn. Reson.* **148**, 398–418 (2001). [Cited on: p37, 96, 98, 100,
102]

[Saalwächter 01b] K. Saalwächter, H. W. Spiess. Heteronuclear ^{1}H-^{13}C Multiple-spin Corre-
lation in Solid-state Nuclear Magnetic Resonance: Combining Rotational-
echo Double-resonance Recoupling and Multiple-quantum Spectroscopy.
J. Chem. Phys. **114**, 5707–5728 (2001). [Cited on: p37, 81, 96, 97]

[Saalwächter 02] K. Saalwächter, I. Schnell. REDOR-based Heteronuclear Dipolar Corre-
lation Experiments in Multi-spin Systems: Rotor-encoding, Directing and
Multiple Distance and Angle Determination. *Solid State NMR* **22**, 154–187
(2002). [Cited on: p80, 96, 104]

[Sakellariou 00] D. Sakellariou, A. Lesage, P. Hodgkinson, L. Emsley. Homonuclear dipo-
lar decoupling in solid-state NMR using continuous phase modulation.
Chem. Phys. Lett. **319**(3–4), 253–260 (2000). [Cited on: p34]

[Samoson 01a]   A. Samoson, T. Tuherm, Z. Gan. High-field high-speed MAS resolution
enhancement in H-1 NMR spectroscopy of solids. *Solid State NMR* **20**(3-4),
130–136 (2001). [Cited on: p34]

[Samoson 01b]   A. Samoson, T. Tuherm, J. Past. Ramped-speed cross polarization MAS
NMR. *J. Magn. Reson.* **149**(2), 264–267 (2001). [Cited on: p34]

[Samoson 02a]   A. Samoson. Encyclopedia of Nuclear Magnetic Resonance, Band 9,
Chapter: Extended Magic-Angle Spinning, pp 59–64. John Wiley & Sons,
Ltd (2002). [Cited on: p34]

[Samoson 02b]   A. Samoson, T. Tuherm, J. Past. Rotation sweep NMR. *Chem. Phys. Lett.*
365(3-4), 292–299 (2002). [Cited on: p34]

[Samoson 03]   A. Samoson, Tiit Tuherm. High performance MAS. In Poster contribution
at the ENC 2003, Tallinn (2003). [Cited on: p34, 65, 109]

[Samoson 05]   A. Samoson, T. Tuherm, J. Past, A. Reinhold, T. Anupold, N. Hein-
maa. New Techniques In Solid-State Nmr, Band 246 (*Topics In Current
Chemistry*), Chapter: New horizons for magic-angle spinning NMR, pp
15–31. Springer-Verlag, Berlin (2005). ISI Document Delivery No.: BBX89
Review. [Cited on: p34]

[Scheler 81]   G. Scheler, U. Haubenreisser, H. Rosenberger. High-Resolution H-1-Nmr In Solids With Multiple-Pulse Sequences And Magic-Angle Sample Spinning At 270-Mhz. *J. Magn. Reson.* **44**(1), 134–144 (1981). [Cited on: p33]

[Schleyer 96]   P.v.R. Schleyer, C Maerker, A Dransfeld, H Jiao, N.J.R.v.E. Hommes. Nucleus Independent chemical shifts: A simple and efficient aromaticity probe. *J. Am. Chem. Soc.* **118**, 6317–6318 (1996). [Cited on: p61]

[Schmidt-Rohr 94]   K. Schmidt-Rohr, H. W. Spiess. Multidimensional Solid-State NMR and Polymers. Academic Press, London (1994). [Cited on: p33, 58, 76, 91]

[Schmuck 01]   C. Schmuck, W. Wienand. Self-complementary quadruple hydrogen-bonding motifs as a functional principle: From dimeric supramolecules to supramolecular polymers. *Angew. Chem. Int. Ed.* **40**(23), 4363–+ (2001). [Cited on: p31]

[Schnell 96]   I. Schnell. *Doppelquanten-NMR-Spektroskopie an polykristallinen Phosphaten.* Diplomarbeit, Universität Mainz (1996). [Cited on: p89]

[Schnell 98a]   I. Schnell, S. P. Brown, H. Y. Low, H. Ishida, H. W. Spiess. An Investigation of Hydrogen Bonding in Benzoxazine Dimers by Fast Magic-Angle Spinning and Double-Quantum ^{1}H NMR Spectroscopy. *J. Am. Chem. Soc.* **120**, 11784–11795 (1998). [Cited on: p13, 18, 23, 28, 30, 33, 35, 36, 38, 39, 105, 109, 113, 121, 125, 127, 130, 160, 161, 162, 165, 166, 169, 174, 175, 207, 235, 241, 264]

[Schnell 98b]   I. Schnell, A. Lupulescu, S. Hafner, D. E. Demco, H. W. Spiess. Resolution Enhancement in Multiple-Quantum MAS NMR Spectroscopy. *J. Magn. Reson.* **133**, 61–69 (1998). [Cited on: p36]

[Schnell 99]   I. Schnell. ^{1}*H-NMR-Spektroskopie im Festkörper: Schnelle Probenrotation und Mehrquantenkohärenzen.* Dissertation, Universität Mainz (1999). [Cited on: p94]

[Schnell 01a]   I. Schnell, B. Langer, S. H. M. Söntjens, M. H. P. van Genderen, R. P. Sijbesma, H. W. Spiess. Inverse Detection and Heteronuclear Editing in ^{1}H-^{15}N Correlation and ^{1}H-^{1}H Double-quantum NMR Spectroscopy in the Solid State under Fast MAS. *J. Magn. Reson.* **150**, 57–70 (2001). [Cited on: p35, 36, 37, 96, 98]

[Schnell 01b]   I. Schnell, H. W. Spiess. High-resolution ^{1}H NMR Spectroscopy in the Solid State: Very Fast Sample Rotation and Multiple-quantum Coherences. *J. Magn. Reson.* **151**, 153–227 (2001). [Cited on: p12, 35, 36, 80, 86, 88, 89, 94, 159]

[Schnell 01c]   I. Schnell, A. Watts, H. W. Spiess. Double-Quantum Double-Quantum MAS Exchange NMR Spectroscopy: Dipolar-Coupled Spin Pairs as Probes for Slow Molecular Dynamics. *J. Magn. Reson.* **149**, 90–102 (2001). [Cited on: p87]

[Schnell 02]   I. Schnell, K. Saalwächter. ^{15}N-^{1}H Bond Length Determination in Natural Abundance by Inverse Detection in Fast-MAS Solid-state NMR spectroscopy. *J. Am. Chem. Soc.* **124**, 10938–10939 (2002). [Cited on: p37, 96]

[Schnell 04a]   I. Schnell. Dipolar recoupling in fast-MAS solid-state NMR spectroscopy. *Progr. NMR Spectrosc.* **45**(1-2), 145–207 (2004). [Cited on: p35, 86, 94, 155, 264]

[Schnell 04b]   I. Schnell. Personal communication. Unable to provide crystal structure of continious hydrogen bonding structure. (2004). [Cited on: p264]

[Sebastiani 01]   D. Sebastiani, M. Parrinello. A new ab-initio approach for NMR chemical shifts in periodic systems. *J. Phys. Chem. A* **105**(10), 1951–1958 (2001). [Cited on: p38, 262]

[Sebastiani 02a]   D. Sebastiani, G. Goward, I. Schnell, M. Parrinello. NMR chemical shifts in periodic systems from first principles. *Computer Physics Communications* **147**(1-2), 707–710 (2002). [Cited on: p38, 149, 262]

[Sebastiani 02b]   D. Sebastiani, M. Parrinello. Ab-initio study of NMR chemical shifts of water under normal and supercritical conditions. *Chem. Phys. Chem.* **3**(8), 675–679 (2002). [Cited on: p149, 262]

[Sebastiani 03a]   Daniel Sebastiani, Gillian Goward, Ingo Schnell, Hans-Wolfgang Spiess. NMR chemical shifts in proton conducting crystals from first principles. *J. Mol. Struct.* **625**, 283–288 (2003). [Cited on: p262]

[Sebastiani 03b]   Daniel Sebastiani, Ursula Rothlisberger. Medicinal Quantum Chemistry, Band 88 (*Methods and Principles in Medicinal Chemistry, Series Editors: R. Mannhold, H. Kubiny, G. Folkers*), Chapter: Advances in Density Functional Based Modelling Techniques: Recent Extensions of the Car-Parrinello Approach, pp 5–36. Wiley-VCH, Weinheim, Germany (2003). [Cited on: p262, 263]

[Sebastiani 04a]   D Sebastiani. Personal communication. NICS map of benzene (2004). [Cited on: p61]

[Sebastiani 04b]   Daniel Sebastiani, Ursula Rothlisberger. Nuclear Magnetic Resonance Chemical Shifts from Hybrid DFT QM/MM Calculations. *J. Phys. Chem. B* **108**, 2807 (2004). [Cited on: p263]

[Sebastiani 05]   D Sebastiani. Personal communication. Higher degree of symmetry in H,Me-N-Cy makes simulated cell similar to that of Me,Me-N-Me. (2005). [Cited on: p158]

[Shen 96]   S. B. Shen, H. Ishida. Development and Characterization of High-Performance Polybenzoxazine Composites. *Polym. Composites* **17**, 5 (1996). [Cited on: p29]

[Sijbesma 97]   R. P. Sijbesma, F.H. Beijer, L. Brunsveld, B.J.B. Folmer, J.H.K. Hirschberg, R.F.M Lange, J.K.L. Lowe JKL, E.W. Meijer. Reversible Polymers Formed from Self-Complementary Monomers Using Quadruple Hydrogen Bonding. *Science* **278**, 1601 (1997). [Cited on: p31]

[Slichter 96]   C. P. Slichter. Principles of Magnetic Resonance. Springer-Verlag, Berlin (1996). [Cited on: p75]

[Solomon 55]   I. Solomon. Relaxation Processes in a System of two Spins. *Phys. Rev.* **99**(2), 559–565 (1955). [Cited on: p64]

[Sommer 95]   W. Sommer, J. Gottwald, D. E. Demco, H. W. Spiess. Dipolar Heteronuclear Multiple-Quantum NMR Spectroscopy in Rotating Solids. *J. Magn. Reson. A* **113**, 131–134 (1995). [Cited on: p35]

[Sørensen 83]   O. W. Sørensen, G. W. Eich, M. H. Levitt, G. Bodenhausen, R. R. Ernst. Product Operator Formalism for the Description of NMR Pulse Experiments. *Progr. NMR Spectrosc.* **16**, 163–192 (1983). [Cited on: p55]

[Spiess 78]   H. W. Spiess. NMR Basic Principles and Progress, Band 15, Chapter: Rotation of Molecules and Nuclear Spin Relaxation, pp 55–214. Springer-Verlag, Berlin (1978). [Cited on: p59]

[Spiess 81]   H. W. Spiess, H. Sillescu. Solid Echoes in the Slow-Motion Region. *J. Magn. Reson.* **42**, 381–389 (1981). [Cited on: p76]

[Steiner 02]   T. Steiner. The Hydrogen Bond in the Solid State. *Angew. Chem. Int. Ed.* **41**, 48–76 (2002). [Cited on: p198]

[Stejskal 77]   E. O. Stejskal, J. Schaefer, R. A. McKay. High-Resolution, Slow-Spinning Magic-Angle Carbon-13 NMR. *J. Magn. Reson.* **25**, 569–573 (1977). [Cited on: p80]

[Takegoshi 01]   K. Takegoshi, J. Mizokami, T. Terao. ^{1}H Decoupling with Third Averaging in Solid NMR. *Chem. Phys. Lett.* **341**, 540–544 (2001). [Cited on: p73]

[Tishmack 03]   P. A. Tishmack, D. E. Bugay, S. R. Byrn. Solid-State Nuclear Magnetic Resonance Spectroscopy–Pharmaceutical Applications. *J. Pharma. Sci.* **92**(3), 441–474 (2003). [Cited on: p32]

[Vaara 98]   J. Vaara, J. Lounila, K. Ruud, T. Helgaker. Rovibrational effects, temperature dependence, and isotope effects on the nuclear shielding tensors of water: A new O-17 absolute shielding scale. *J. Chem. Phys.* **109**, 8388–8397 (1998). [Cited on: p260]

[Vaara 01]   J. Vaara, O. L. Malkina, H. Stoll, V. G. Malkin, M Kaupp. Study of relativistic effects on nuclear shieldings using density-functional theory and spin-orbit pseudopotenti als. *J. Chem. Phys.* **114**, 61–71 (2001). [Cited on: p260]

[Vanmoorsel 95]   Gjmp Vanmoorsel, E. R. H. Vaneck, C. P. Grey. $Pr_2Sn_2O_7$ And $Sm_2Sn_2O_7$ As High-Temperature Shift Thermometers In Variable-Temperature ^{119}Sn MAS NMR. *Journal Of Magnetic Resonance Series A* **113**(2), 159–163 (1995). [Cited on: p241]

[Vinogradov 99]   E. Vinogradov, P. K. Madhu, S. Vega. High-resolution proton solid-state NMR spectroscopy by phase- modulated Lee-Goldburg experiment. *Chem. Phys. Lett.* **314**(5-6), 443–450 (1999). [Cited on: p34]

[Voelkel 88]   R. Voelkel. High-Resolution Solid-State C-13-NMR Spectroscopy of Polymers. *Angew. Chem. Int. Ed. Engl.* **27**, 1468–1483 (1988). [Cited on: p75]

[Wannier 37]   G.H. Wannier. The Structure of Electronic Excitation Levels in Insulating Crystals. *Phys. Rev.* **52**, 191 (1937). [Cited on: p261]

[Waugh 68]   J. S. Waugh, L. M. Huber, U. Haeberlen. Approach to High-Resolution NMR in Solids. *Phys. Rev.* **20**, 180 (1968). [Cited on: p33]

[Wei 99]   Y. Wei, A. McDermott. Modeling NMR Chemicals Shifts: Gaining Insights into Structure and Environment, Band 732, Chapter: Effects of Hydrogen Bonding on Chemicals Shifts, pp 177–193. ACS Books (1999). [Cited on: p31, 35]

[Weitekamp 82]   D. P. Weitekamp, J. R. Garbow, A. Pines.   Determination of Dipole Coupling Constants Using Heteronuclear Multiple Quantum NMR. *J. Chem. Phys.* **77**, 2870–2883 (1982). [Cited on: p83]

[Wilson 96]   C. C. Wilson, N. Shankland, A. J. Florence.   A single-crystal neutron diffraction study of the temperature dependence of hydrogen-atom disorder in benzoic acid dimers. *J. Chem. Soc. Faraday Trans.* **92**(24), 5051–5057 (1996). [Cited on: p10, 31]

[Wilson 04]   C. C. Wilson, A. E. Goeta. Towards designing proton-transfer systems - Direct imaging of proton disorder in a hydrogen-bonded carboxylic acid dimer by variable-temperature X-ray diffraction. *Angew. Chem. Int. Ed.* **43**(16), 2095–2099 (2004). [Cited on: p31]

[Wirasate 98]   S. Wirasate, S. Dhumrongvaraporn, D. J. Allen, H. Ishida. Molecular Origin of Unusual Physical and Mechanical Properties in Novel Phenolic Materials Based on Benzoxazine Chemistry. *J. Appl. Polym. Sci.* **70**, 1299–1306 (1998). [Cited on: p29]

[Wolff 99]   S. Wolff, T. Ziegler, E. van Lenthe, E. J. Baerends. Density functional calculations of nuclear magnetic shieldings using the zeroth-order regular approximation (ZORA) for relativistic effects: ZORA nuclear magnetic resonance. *J. Chem. Phys.* **110**, 7689 (1999). [Cited on: p263]

[Yamauchi 00]   K. Yamauchi, S. Kuroki, K. Fujii, I. Ando. The Amide Proton Chemical Shift and Hydrogen-bonded Structure of Peptides and Polypeptides in the Solid State as Studied by High-frequency Solid-state NMR. *Chem. Phys. Lett.* **324**, 435–439 (2000). [Cited on: p35]

[Yamauchi 02a]   K. Yamauchi, S. Kuroki, I. Ando. The Amide Proton Chemical Shift and Hydrogen-bonded Structure of Glycine-containing Peptides and Polypeptides in the Solid State as Studied by Multi-pulse-associated High-speed MAS ^{1}H NMR. *J. Mol. Struct* **602**, 9–16 (2002). [Cited on: p35]

[Yamauchi 02b]   K. Yamauchi, J. R. Lizotte, D. M. Hercules, M. J. Vergne, T. E. Long. Combinations of microphase separation and terminal multiple hydrogen bonding in novel macromolecules. *J. Am. Chem. Soc.* **124**(29), 8599–8604 (2002). [Cited on: p31]

[Yates 03]   Jonathan R. Yates, Chris J. Pickard, Mike C. Payne, Francesco Mauri. Relativistic nuclear magnetic resonance chemical shifts of heavy nuclei with pseudopotentials and the zeroth-order regular approximation. *J. Chem. Phys.* **118**, 5746–5753 (2003). [Cited on: p263]

[Yoon 98]   Y. Yoon, B. Pfrommer, F. Mauri, S. Louie. NMR chemical shifts in hard carbon nitride compounds. *Phys. Rev. Lett.* **80**, 3388 (1998). [Cited on: p262]

[Yu 98]   Y. Yu, B. M. Fung. An Efficient Broadband Decoupling Sequence for Liquid Crystals. *J. Magn. Reson.* **130**, 317–320 (1998). [Cited on: p73]

[Zell 99]   M. T. Zell, B. E. Padden, D. J. W. Grant, M. C. Chapeau, I. Prakash, E. J. Munson. Two-dimensional high-speed CP MAS NMR spectroscopy of polymorphs. 1. Uniformly 13 C-labeled aspartame. *J. Am. Chem. Soc.* **121**, 1372–1378 (1999). [Cited on: p32]

[Zhao 01a]   X. Zhao, M. Edén, M. H. Levitt. Recoupling of Heteronuclear Dipolar Interactions in Solid-state NMR Using Symmetry-based Pulse Sequences. *Chem. Phys. Lett.* **342**, 353–361 (2001). [Cited on: p80]

[Zhao 01b]   X. Zhao, J. L. Sudmeier, W. W. Bachovchin, M. H. Levitt. Measurement of NH bond lengths by fast magic-angle spinning solid-state NMR spectroscopy: A new method for the quantification of hydrogen bonds. *J. Am. Chem. Soc.* **123**(44), 11097–11098 (2001). [Cited on: p37]

Acknowledgements

You cannot teach a man anything,
you can only help him to find it for himself.

GALILEO GALILEI 1564–1642 AD

During my postgraduate research I have undertaken an extremely interesting journey of discovery which has not only resulted in academic achievement but has strongly influenced my personal development. To this extent I am indebted to all those who made a direct input to my research or contributed to my general well-being during this period. Thank you. Your time and effort is greatly appreciated.

I would especially like to thank the following people:

- *Dr Rob Law* for my literal introduction into the field of solid-state NMR. His academic supervision, personal advice and most importantly his endless patience.

- *Prof. Hans Wolfgang Spiess* for the opportunity of doing part of my research in Germany and access to the solid-state NMR facilities in Mainz. His numerous suggestions and general exposure to such a passionate scientist.

- *Prof. Hatsui 'Ken' Ishida* for all chemical systems studied, without which my research could not have taken place.

- *Dr Daniel Sebastiani* and *Maxim Zaxharov* for simulating my relatively large hydrogen bonded systems, multiple times and in multiple conformations. Many discussions and general exposure to the field of computational chemistry.

- *Dr Ago Samoson* and *Oivo Manninen* for kindly measuring some of my samples under fast-MAS conditions of $\omega_r/2\pi = 70$ kHz (4.2 million RPM!)

- *Dr Robert Graf* for his general help with both academic and non-academic problems whilst in Mainz. Practical introduction to solving hardware based spectrometer issues, a new appreciation of the intricacies of Bruker consoles and general cat maintenance.

- *Dr Ingo Schnell* for the general wealth of information regarding proton solid-state NMR, help with phase cycles and numerous discussions regarding the interpretation of my results.

- *Dr Gillian Goward* for handing over the benzoxazine project, along with a number of previously unmeasured samples, facilitating all my research culminating in this thesis. Your continued general interest in the project at various conferences was also highly appreciated.

- *Manfred Hehn* and *Hanspeter Raich* for relentless hardware support, and generally fixing all those very expensive things I broke. I learnt so much and can now fix most of my damage myself!

- The *EPSRC* and *Marie Curie Fellowship Association* for providing financial support for the first three years and the fourth year of my PhD respectively.

- All members of the solid-state NMR research groups at IC and the MPIP for their general help and friendship.

- All my various office mates in London and Mainz: RCS1 102; *Andy Hodgson*, *Nisha Sohal* and *Heather Shepherd*, MPIP 1.101; *Mark McCormick, Michael Pollard*, *Marianne Gaborieau* and MPIP 1.102; *Christopher 'Kiki' Klein, Sarah Höfl*, *Thorsten Neidhöfer*.

- *Michael Neidhöfer, Christopher 'Kiki' Klein* and *Ingrid Fischbach* for encouraging me to speak more German and plying me with alcohol to do so. Their friendship and introduction into German social life.

- *Michael Pollard* for that one week stint at *Schick 'n' Schön* (and various other Kneipen in Mainz for that matter). Your ability to have women spontaneously give you their contact information, all that Swiss chocolate and being a very good friend all round.

- *Mark McCormick* for being a good friend and my partner in crime when convincing our German office mate that gullible was not in the English dictionary. The time-machine, all those beer subsidies and generally kicking my butt about you know who!

- *Katja Klimke* for showing that there is indeed a coupling interaction between two weak dipoles, reading and correcting my thesis multiple times and being *meine kleine Raupe Nimmersatt*.

- *Fraser Boyd* for still being a good friend even after prolonged periods of silence and trying to remember what my particular subject is:
  multiple quantum solid-state nuclear magnetic resonance

- *Mum* and *Dad* for their endless love, support and acceptance of my movement across the continent.

Postface

PARKINSON'S LAW
Work expands so as to fill the time available for its completion.

C. NORTHCOTE PARKINSON 1958 AD
[Parkinson 58]